

**NASA CONTRACTOR
REPORT**

NASA CR-2837



NASA CR

0061705



TECH LIBRARY KAFB, NM

**LOAN COPY: RETURN TO
AFWL TECHNICAL LIBRARY
KIRTLAND AFB, N. M.**

**LUBRICANT RHEOLOGY APPLIED TO
ELASTOHYDRODYNAMIC LUBRICATION**

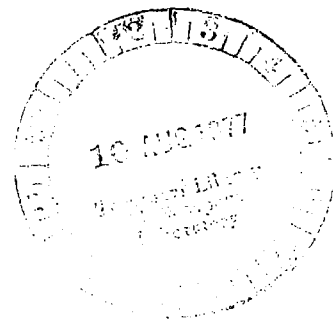
Ward O. Winer and David M. Sanborn

Prepared by

GEORGIA INSTITUTE OF TECHNOLOGY

Atlanta, Ga. 30332

for Lewis Research Center



NATIONAL AERONAUTICS AND SPACE ADMINISTRATION • WASHINGTON, D. C. • MAY 1977



0061705

1. Report No. NASA CR-2837		2. Government Accession No.		3. Recipient's Catalog No.	
4. Title and Subtitle LUBRICANT RHEOLOGY APPLIED TO ELASTOHYDRODYNAMIC LUBRICATION				5. Report Date May 1977	
				6. Performing Organization Code	
7. Author(s) Ward O. Winer and David M. Sanborn				8. Performing Organization Report No. None	
				10. Work Unit No.	
9. Performing Organization Name and Address Georgia Institute of Technology Atlanta, Georgia 30332				11. Contract or Grant No. NGR-11-002-133	
				13. Type of Report and Period Covered Contractor Report	
12. Sponsoring Agency Name and Address National Aeronautics and Space Administration Washington, D. C. 20546				14. Sponsoring Agency Code	
15. Supplementary Notes Final Report. Project Manager, Lavern D. Wedeven, Fluid System Components Division, NASA Lewis Research Center, Cleveland, Ohio					
16. Abstract This is the fifth and final annual report, covering the period March 1975 to April 1976, for NASA Grant NGR 11-002-133. It includes a summary of the research during the previous four years (March 1971 to April 1975) which involved viscosity measurements in a high pressure rheometer, elastohydrodynamic simulator studies (including the development of a temperature measuring technique), and analytical fluid modeling for elastohydrodynamic contacts. The more recent research which is described concerns infrared temperature measurements in elastohydrodynamic contacts and the exploration of the glassy state of lubricants. A correlation, of engineering significance, has been made between transient surface temperature measurements and surface roughness profiles. Measurements of glass transitions of lubricants and the study of the effect of rate processes on materials lead to the conclusion that typical lubricants go into the glassy state as they pass through the contact region of typical elastohydrodynamic contacts.					
17. Key Words (Suggested by Author(s)) Liquid lubricants Elastohydrodynamic lubrication Glass transition Surface temperature			18. Distribution Statement Unclassified - unlimited STAR category 27		
19. Security Classif. (of this report) Unclassified		20. Security Classif. (of this page) Unclassified		21. No. of Pages 213	
				22. Price* A10	

TABLE OF CONTENTS

	Page
I. INTRODUCTION	1
II. SUMMARY OF RESEARCH CONDUCTED DURING 1971-1975	3
A. High Pressure Rheology of Lubricants	3
B. Elastohydrodynamic Simulator Studies	5
C. Analytical Modeling of Ehd Contacts	7
III. EXPERIMENTAL SURFACE TEMPERATURE INVESTIGATIONS IN EHD CONTACTS	10
A. Introduction	10
B. Experimental Equipment and Techniques	13
C. Flash Temperature Measurements for Pure Sliding	15
D. Correlations Between Surface Roughness and Temperature	18
1. Power Spectra	19
2. Autocorrelation Function	21
3. Correlation between Surface Roughness and Temperature Fluctuations	24
4. Discussion of Results of Spectra Correlations between Temperature Fluctuations and Surface Roughness	25
5. Wear Measurements by Ferrographic Analysis	27
E. Experiments in Rolling EHD Contacts	28
1. Film Thickness and Traction Measurements	29
2. Surface Temperature Measurements	30
3. Extension of Flash Temperature Analysis for Sliding and Rolling	32
IV. GLASSY TRANSITIONS AS A FUNCTION OF PRESSURE	37
A. Introduction	37
B. Glass Transition Temperature and the Glassy State	40
C. Experimental Technique	45
1. Light-Scattering Method	45
a. Theory	45
b. Pressure and Temperature Coefficients of the Sound Velocity	51
c. Light Scattering Experimental Apparatus	52
d. High Pressure Equipment	55
e. Glass Formation History	56
f. Data Reduction Technique and the Results for for 5P4E	58
D. Dilatometry Method	62
E. Two Additional Experiments	65

TABLE OF CONTENTS (Continued)

	Page
F. Discussion of Results	66
1. Pressure Dependence of Glass Transition Temperatures in Lubricants	66
2. Relationship of Glass Transition to EHD Conditions	67
a. Traction Measurements	68
b. Side Thrust Measurements	69
c. Contact Temperatures and Pressures	70
G. Conclusions	71
V. ON THE ANALYTICAL DETERMINATION OF PRESSURE DISTRIBUTIONS IN EHD LINE CONTACTS FROM FILM THICKNESS DATA	72
A. Introduction	72
B. Problem Statement	75
C. The Displacement Solutions - The Cylinder	77
1. The Symmetric Solution. $[S_{22}]$	80
2. The Antisymmetric Solution. $[S_{12}]$	83
3. The General Solution	84
D. The Displacement Solutions - The Half-Space	85
1. The Symmetric Solution. $[H_{02}]$	87
2. The Antisymmetric Solution. $[H_{01}]$	88
3. The General Solution	89
E. The Pressure Distribution in the EHD Zone	91
F. Numerical Consideration	93
G. Test Cases and Evaluation	96
H. Summary of Computational Method	100
VI. REFERENCES	115
APPENDICES	
A. Material Specification and Identification	193
B. Publications Resulting from Research Supported Completely or in part by the Grant	202

LIST OF TABLES

Tables		Page
III-1.	Summary of Rolling Experiments Film Thickness and Traction	120
III-2.	Summary of Rolling Experiments Ball Surface Temperature Rises. ($P_H = 1.02 \text{ GN/m}^2$)	121
IV-1.	Frequency Shift and Velocity of Sound as Function of Pressure for 5P4E at 24.4C (76F) (History B) . . .	122
IV-2.	Frequency Shift and Velocity of Sound as a Function of Temperature at 0.40 GPa (59,000 psi) for 5P4E Oil (History A)	123
IV-3.	Least-Square Expressions for Sound Velocity, Temperatures and Sound Velocity at Transition for Different Constant Pressures: 5P4E History A . . .	124
IV-5.	Fluids for Which No. Transition was Observed by the Volumetric Method in the Indicated Temperature and Pressure Ranges (Isothermal Compression)	126
IV-6.	Approximate Yield Shear Strength at Atmospheric Pressure	127

LIST OF FIGURES

Figure	Page
III-1. Schematic of Sliding EHD Contact Simulator	128
III-2. Schematic of the Combined Rolling and Sliding EHD Contact Simulator	129
III-3. Ball Surface Temperature Rise at Contact Center (.011 μm Ra roughness, $1 < \Lambda < 2$ for $P_H = 2.03$ GPa, otherwise $\Lambda > 2$)	130
III-4. Surface Profiles in Direction of Sliding ($P_H = 1.24$ GN/m ² , $V_S = 1.02$ m/s, Hertz Diameter $d = 0.43$ mm, pure sliding)	131
III-5. Power Spectra of the Surface Profiles ($P_H = 1.24$ GN/m ² , $V_S = 1.02$ m/s, Hertz diameter $d = 0.43$ mm, pure sliding.)	132
III-6. Autocorrelation Functions of the Surface Profiles. ($\lambda > 3d$ not included, $P_H = 1.24$ GN/m ² , $V_S = 1.02$ m/s, Hertz diameter $d = 0.43$ mm, pure sliding) . . .	133
III-7. Normalized Histograms of Ball Surface Temperature Fluctuations (.38 μm Ra initial roughness, $P_H = 1.24$ GN/m ² , $V_S = 1.02$ m/s, Hertz diameter $d = 0.43$ mm, pure sliding)	134
III-8. Power Spectra of Ball Surface Temperature Fluctuations (.38 μm Ra initial roughness, $P_H = 1.24$ GN/m ² , $V_S = 1.02$ m/s, Hertz diameter = 0.43 mm, pure sliding)	135
III-9. Debris Concentration Dependence on Λ	136
III-10. Film Thickness as a Function of Slide-Roll Ratio (.011 μm Ra roughness)	137
III-11. Traction Coefficient as a Function of Slide-Roll Ratio (.011 μm Ra roughness)	138
III-12. Film Thickness and Traction Coefficient as a Function of Rolling Velocity ($\Sigma = 0$, .011 μm Ra Roughness, $P_H = 1.02$ GPa)	139
III-13. Ball Surface Temperature Rise as a Function of Slide-Roll Ratio (.011 μm Ra Roughness, $P_H = 1.02$ GPa, $\bar{V} = 0.75$ m/s)	140

LIST OF FIGURES (Continued)

Figure	Page
III-14. Ball Surface Temperature Rise as a Function of Slide-Roll Ratio (.011 μm Ra Roughness, $P_H = 1.02$ GPa, $\bar{V} = 1.0$ m/s)	141
III-15. Ball Surface Temperature Rise as a Function of Rolling Velocity (.011 μm Ra Roughness, $P_H = 1.02$ GPa, $\Sigma = 0$, Maximum T_b Occurs at Contact ^H Center) . .	142
III-16. Ball Surface Temperature Rise Along the Contact Centerline (.011 μm Ra Roughness, $P_H = 1.02$ GPa, $\bar{V} = .75$ m/s)	143
III-17. Ball Surface Temperature Rise Along the Contact Centerline (.011 μm Ra Roughness, $P_H = 1.02$ GPa, $\bar{V} = 1.00$ m/s)	144
III-18. Ball Surface Temperature Rise Along Contact Centerline (.011 μm Ra Roughness, $P_H = 1.02$ GPa, $\Sigma = 0$)	145
III-19. Comparison of Predicted Average and Actual Maximum Ball Surface Temperature Rises for $L > 5$. Combined sliding and rolling as per Equation 21	146
IV-1. Thermal Expansion Coefficient or Specific Heat for a Typical Glassy Material	147
IV-2. Typical Plot of Specific Volume Versus Temperature for a Glassy Material at Different Formation Pressures	148
IV-3. Dependence of the Glass Transition Temperature on the Cooling Rate, K_1 . $L = \text{Liquid}$ and $G = \text{Glass}$	149
IV-4. Bragg Condition of Light Scattered at an Angle Relative to the Incident Light Beam	150
IV-5. Frequency Spectrum of a Naphthenic Base Oil at 24.4C and Atmospheric Pressure	151
IV-6. The Variation of the Brillouin Frequency Shift and the Sound Velocity with Temperature at Atmospheric Pressure for Atactic Polystyrene [53]	152
IV-7. Schematic Arrangement of the Light-Scattering Experiment	153

LIST OF FIGURES (Continued)

Figure		Page
IV-8.	Schematic Arrangement of the Fabry-Perot Interferometer	154
IV-9.	Transmission of the Fabry-Perot Interferometer as a Function of Light Frequency	155
IV-10.	Schematic of Light-Scattering Cell. The Intensifier is Attached Perpendicular to the Paper Plane at the Centerline of the Cell	156
IV-11.	Schematic of Formation Histories Used to Form the Glass. A_1 and B Represent Constant Formation Histories at Pressure P_1 and Room Temperature Respectively	157
IV-12.	Frequency Spectrum for 5P4E Fluid Recorded at 0.19 GPa and 24.4C (History B). B and R represent the Brillouin and Rayleigh Components Respectively . . .	158
IV-13.	Variation of Frequency Shift and Velocity of Sound with Pressure at 24.4C (76 F) for 5P4E Fluid (History B). Arrows Indicate Glass Transition . . .	159
IV-14.	Frequency Spectrum for 5P4E Fluid Recorded at 0.40 GPa (59,000 psi) and 64.4C (148F) (History A). B and R Represent the Brillouin and Rayleigh Components Respectively	160
IV-15.	Variation of Frequency Shift and Velocity of Sound with Temperature at 0.40 GPa (59,000 psi) for 5P4E (History A). Arrows Indicate Glass Transition . . .	161
IV-16.	Frequency Shift Dependence on Temperature at Different Constant Pressures for 5P4E Fluid (History A). Arrows Indicate T_g	162
IV-17.	Velocity of Sound Dependence on Temperature at Different Constant Pressures for 5P4E Fluid (History A). Arrows Indicate T_g	163
IV-18.	Phase Diagram for 5P4E Fluid Based on Light Scattering Experiment. $dT/dP = 183 \text{ C/GPa}$. History A. History B	164
IV-19.	High Pressure Dilatometer (.13 to 1.2 GPa)	165

LIST OF FIGURES (Continued)

Figure	Page
IV-20. Low Pressure Dilatometer. (.014 to .27 GPa)	166
IV-21. Atmospheric Pressure Dilatometer	167
IV-22. Comparison of Glass Transition of 5P4E by Various Methods	168
IV-23. Comparison of Glass Transition of N1 by Various Methods	169
IV-24. Glass Transition by Isothermal Compression from Liquid (Dilatometry)	170
IV-25. Glass Transition by Various Hydrocarbon Oils Determined by Dilatometry	171
IV-26. Dispersion Region in Isothermal Compression by Dilatometry	172
IV-27. Dispersion Region in Isothermal Compression by Dilatometry	173
IV-28. Dispersion Region in Isothermal Compression by Dilatometry	174
IV-29. Shear Stress Between Concentric Cylinders for 5P4E Cooled at 2.75 C/min., Shear Rate $\dot{\gamma} = .435 \text{ sec}^{-1}$. . .	175
IV-30. Heuristic Estimates of the Relationship Between Conditions in an EHD Contact and Glass-Liquid Phase Diagram of Some Lubricants (Lubricant Supply Temperature about 20C)	176
IV-31. The Variation of Apparent Viscosity with Pressure and Temperature	177
IV-32. Comparison of Glass Transition of N1 by Various Methods	178
IV-33. Variation of the Relative Side Thrust with Contact Pressure at 23C and 0.1 m/s [26]	179
IV-34. The Physical State of N1 Lubricant in the Center of a Sliding Contact at Various Speeds and Hertz Pressures (Reference [9]) ----- and ----- Represent the Light-Scattering and the Volumetric Glass Transition Lines Respectively . .	180

LIST OF FIGURES (Continued)

Figure		Page
IV-35.	The Physical State of N1 Lubricant in the Center of a Sliding Contact at Various Speeds and Hertz Pressures .-.-.-.- and -.-.- Represent the Light-Scattering and the Volumetric Glass Transition Lines	181
IV-36.	Ball Surface Temperature Distribution Along the Contact Centerline at Constant Hertzian Pressure of 1.0 GPa and Constant Rolling Speed of 0.75 m/s. (a) and (b) Represent the Physical State of the Lubricant in the Contact Area as Determined by the Light Scattering and Volumetric Transition Data Respectively	182
V-1.	Two Cylinders	183
V-2.	Cylinder Plate	183
V-3.	Decomposition of the EHD Pressure-Cylinder	184
V-4.	Decomposition of the EHD-Pressure-The Plate	185
V-5.	Schematic Diagram of EHD Contact Zone	186
V-6.	Test Case 1 - Uniform Pressure Distribution	187
V-7.	Test Case 2 - Hertzian Contact	188
V-8.	Test Case 3 - Polynomial Pressure Distribution	189
V-9.	Test Case 3 - Random Errors Introduced into Film Thickness Values	190
V-10.	Test Case 3 - Errors Introduced in Location of Inlet Point	191
V-11.	Calculations Based on Experimental Film Thickness Measurements [71]	192

I. INTRODUCTION

This is the fifth and final annual technical report for NASA Grant NGR-11-002-133 (March 1971 - April 1976) "Investigation of Lubricant Rheology as Applied to Elastohydrodynamic Lubrication". A brief summary of the first four years of research is included in Section II. This report is primarily concerned with the research performed during the last year.

During the first four years significant progress was made in three areas; a) rheology of lubricants in a high pressure rheometer, b) observation of lubricant behavior in an elastohydrodynamic simulator, including the development of a temperature measuring technique, and c) the analytical modeling of elastohydrodynamic contacts (isothermal non-linear rheological fluid model and a linear model with thermal effects).

During the past year the research was concerned with elastohydrodynamic simulation and exploration of glassy state lubricant behavior. The ehd simulator research (Section III) is a continuation of the infrared temperature measurements to study the maximum surface temperatures in ehd contacts including rolling contacts with sliding. The effect of roughness on surface temperature and wear has also been studied. Correlations of surface temperature and operating variables have been developed which are suitable for use in engineering design.

Preliminary studies of the glass transition of lubricants were undertaken to determine if typical lubricants in typical ehd contacts pass through a glass transition (Section IV). They clearly indicate that some lubricants do pass into the glassy state in ehd contacts.

These results require further study and will result in a change in thinking regarding ehd lubricant rheology.

As a necessary part of the glassy state studies an analytical procedure was developed which relates the measured ehd film thickness to the pressure distribution. No assumption about lubricant rheology was necessary. This effort is presented in Section V.

Appendix B presents a list of publications which resulted totally or in part from this research.

Some of the research described in this report was jointly supported by NASA and the National Science Foundation (Grant Number ENG 74-21002).

W. O. Winer and D. M. Sanborn were the principal investigators and had overall responsibility. Others were involved in specific aspects of the research: M. A. Alsaad conducted the light-scattering glass transition experiments, which constituted his doctoral research; S. Bair conducted the other glass transition experiments and assisted in the ehd experiments; H. S. Nagaraj conducted the ehd temperature measurement experiments, which constituted a major portion of his doctoral research; and G. M. Rentzepis and R. K. Kunz were responsible for the elasticity analysis of Section V.

II. SUMMARY OF RESEARCH CONDUCTED DURING 1971-1975

A brief summary of research completed during the first four years of this grant is presented in this section. For more complete details in each area the previous annual contract reports or referenced publications should be consulted.

A. High Pressure Rheology of Lubricants

Fifteen fluids have been subjected to high pressure rheological measurements. These include several fluids which consist of pairs of base fluid and base fluid plus an antiwear additive. These measurements were in two categories: 1) determination of the effect of pressure and temperature on the fluid viscosity (and pressure-viscosity coefficients) at relatively low shear stress (approximately 1kPa [1,2], and 2) determination of the effect of high shear stress upon the viscosity at modest pressures and temperature [3,4]. The pressures and temperatures chosen for the latter experiments were those which gave a low shear stress viscosity comparable to the average apparent viscosity observed in the ehd contact simulator under the sliding point contact conditions employed in this laboratory. All fifteen fluids have been subjected to the former type of measurements while six fluids have been subjected to the latter.

The pressure viscosity measurements have shown that the pressure-viscosity coefficient, important in ehd, decreases with increasing temperature in such a manner that the natural logarithm of the pressure-viscosity coefficient is approximately inversely proportional to the temperature [1,2]. Maximum differences of less than a factor of four in pressure-viscosity coefficient were observed among typical lubricants at a temperature of

37.8C (100 F). These differences are reduced considerably at 149C (300 F). Differences in viscosity and viscosity-pressure coefficients between base fluids and base fluids formulated with antiwear additives were found to be minor in all cases [1,2].

The high shear stress measurements performed on six fluids were conducted up to a shear stress within a factor of 3 to 4 of the average shear stress occurring in the sliding point contact ehd simulator employed in this laboratory (5 MPa compared to 14-20 MPa). Repeatable data explainable in terms of viscous heating only were obtained on four of the six fluids throughout the entire range of pressure, temperature and shear stress examined. The other two fluids, a polymer blended mineral oil and a 50 cs dimethyl siloxane, exhibited rheological behavior which could not be explained by viscous heating alone. The polymer blended mineral oil exhibited shear thinning behavior at relatively low shear stress as expected. Both the polymer blended mineral oil and the dimethyl siloxane exhibited "non-liquid" behavior above some characteristic threshold pressure and shear stress. In both cases the apparent viscosity during the non-liquid behavior was higher than expected from Newtonian considerations and generally was neither repeatable nor correlatable with the chronology of the measurement. In retrospect this behavior may be related to glass transition in these materials at the conditions of the experiments.

During the high shear stress measurements the average resident time of a fluid particle in the capillary, hence the time it was subjected to the high shear stress, was short ($4\ \mu\text{s}$) compared to the average time the fluid particle is in an ehd contact ($10^2\ \mu\text{s}$). Although the capillary residence time varied from a minimum of $4\ \mu\text{s}$ up to $10^5\ \mu\text{s}$ no effect of

residence time on viscosity was observed for the four fluids mentioned above suggesting time dependent effects are not important in this range. This is consistent with the oscillatory crystal research of Lamb and co-workers which indicates that the shear relaxation time for fluids in this viscosity range are of the order of 10^{-3} to 10^{-2} μ s.

Viscous dissipation is an important rheological phenomena in the high shear behavior of typical liquid lubricants. This phenomena can be confused with shear thinning pseudoplastic behavior. The utilization of capillaries of different length-to-diameter ratios in performing the experimental measurements is essential in distinguishing between pseudoplastic and viscous heating effects. In addition to interpreting the experimental data, an analysis of the flow of a Newtonian fluid in a capillary including viscous dissipation and temperature dependent viscosity was performed [5]. The results of this analytical model are consistent with the experimental measurements. The analytical model was able to predict the high shear stress behavior of the lubricants whose behavior was measured with a good accuracy up to the highest shear stress measured.

Jakobsen's film thermal-shearing model[6] has been applied to point contacts[7] with emphasis on comparing predictions with existing data from this laboratory. The model appears to have some merit in conditions of high sliding. However, one result of this study has been the recognition of the possible importance of lubricant behavior in the glassy state. This possibility is discussed in Section V of this report.

B. Elastohydrodynamic Simulator Studies

All the fluids that were studied in the high pressure rheometer have also been studied in the ehd simulator where film thickness distribution

and traction were measured. Most of these measurements were at Hertz pressures in the range 1.0 - 2.0 GPa and with sliding speeds in the range 0.02 - 5.0 m/s.

The most significant advancement in these studies has been the development of the infrared emission technique for determining the fluid and ball surface temperature distributions in the ehd contact [8,9,10]. The technique utilizes an indium-antimonide liquid nitrogen cooled detector to measure the IR radiation emitted by the contact region. By suitable filtering, the radiation from the ball surface and the fluid can be separated and with the system calibration each temperature can be determined. At 1GPa Hertz pressure the temperature measurement area resolution is 1% of the contact area. Two principal applications of the technique have been studied. The first was to measure the temperature distribution for a given fluid and then employ these temperatures in an analytical model assuming a given fluid constitutive equation to predict traction which was compared with the measured value [7]. Because of the rheometer measurements mentioned above the linear constitutive model with temperature and pressure dependent viscosity was employed. The second major application of the IR temperature measuring technique was in observing the behavior of an ehd film as the severity of the contact condition increases [9,10]. The objective was to learn about failure of severely loaded ehd contacts. Based on the surface temperature mappings that have been completed to date, temperatures in some regions of the contact are higher than expected when considering viscous dissipation as the only energy source. The analytical model discussed below permits the prediction of the maximum fluid temperature through the film for a given film thickness.

Based on this model the maximum predicted temperature would be in the center of the contact. However, the measured maximum temperature may be in the lobe region and considerably higher than predicted for some operating conditions [9]. The region where measured temperatures exceed the predicted temperatures coincided with the region where the optical film thickness was equal to or less than the composite surface roughness of the surfaces utilized [9]. Thus both the film thickness and temperature measurements suggest the possibility of asperity interaction resulting in energy dissipation in addition to that due to viscous dissipation.

Throughout the experiments performed thus far, ball surface temperatures have been obtained. In addition, the fluid film temperature and ball surface profile have been determined at selected points. The ball surface temperature variations with speed are in close agreement with the results predicted by Jaeger, Blok, and later Archard, for temperature variations of run in surfaces [10]. These correlations are further developed in Section III of this report. Ball temperatures as high as 250 C for a reservoir temperature of 35 C have been observed. The lubricant temperatures have been approximately 40 C above those of the ball surface.

C. Analytical Modeling of Ehd Contacts

Two analytical models of ehd contact behavior have been developed. One was for the complete solution of the isothermal lubrication of rollers with a non-linear viscous fluid covering the load range from the lightly loaded rigid cylinder case to the highly loaded elastic cylinder case [11]. The second model is concerned only with the prediction of traction in highly loaded elastic contacts with viscous dissipation and temperature dependent linear viscosity [6,7].

The complete solution for the isothermal lubrication of rollers with non-linear fluids has been a difficult numerical problem to execute. However, solutions are now available with both linear and non-linear fluids for lightly loaded rigid cylinders and for elastic cylinders [11,12], in which case the solutions have been completed to the limit of the computing capabilities available. When this research was initiated it was thought that shear thinning of lubricants at high shear stress may be an important rheological phenomena. However, the concurrent work mentioned above of the high shear stress measurements of viscosity now indicate that shear thinning probably is not important for most lubricants. Those findings make the results of this analytical modeling less important than originally expected. The results are, however, still expected to be of value for two reasons; a) the numerical technique employed is different from most previous ehd analytical studies and therefore the results can serve as a comparison with other works for the linear fluid case, and b) because of the broad similarities between shear thinning and the effect of viscous heating the results of this model may give some qualitative insight into ehd behavior where viscous heating is present. The results will of course be useful for applications employing non-linear shear thinning fluids, however, this class of lubricants is now believed to be a relatively small portion of liquid lubricants currently employed. There may be wider application of the results to those systems employing greases, however.

The second analytical model developed [6,7] was the result of the high shear stress rheometer measurements which indicated the importance of viscous heating compared to shear thinning at high shear stress. This

model is concerned with predicting traction in the contact given a velocity, film thickness distribution and a rheological constitutive model for the fluid. The constitutive model employed is a linear model with pressure and temperature dependent viscosity. The model also accounts for the thermal effects of viscous energy dissipation. Because of the dependence upon obtaining film thickness independent of the analysis this effort is primarily useful in assessing the validity of rheological constitutive relations. Preliminary application of the model to a sliding ehd contact suggests that a linear viscous model with temperature dependent viscosity and viscous dissipation may be sufficient to describe the behavior of the fluid in an ehd contact with high sliding. However, the model fails to predict the traction as the amount of sliding decreases. This failure of the model may be the result of the lubricant behavior as a glassy solid in low sliding and rolling ehd contacts.

III. EXPERIMENTAL INVESTIGATIONS IN EHD CONTACTS

A. Introduction

The surface temperature data obtained for the case of pure sliding under the previous contract [13] was analyzed and compared to predicted flash temperatures. The surface temperature data is in good agreement with the predicted flash temperature.

Both the surface roughness profile and the AC signal from the infrared detector were analyzed in the frequency domain. It was found that only certain wavelengths in the roughness profile are important as far as asperity interaction is concerned. The parameter $\Lambda(\Lambda = h_c/\sigma)^*$ is shown to be a valuable means of predicting surface interaction in EHD contacts. A new method for determining the surface roughness, σ , is also proposed.

The effect of various amounts of rolling on the film thickness, traction and surface temperature was studied and the results are reported. A correlation study of the influence of sliding and rolling velocity on surface temperature was also undertaken and the results are discussed.

*The nomenclature used in this section is found on the following pages.

NOMENCLATURE

a	Hertzian contact radius, m
C	Auto-correlation function
d	Hertzian contact diameter = $2a$, m
h_c	Film thickness at contact center, m
h_m	Minimum film thickness, m
k	Thermal conductivity, W/(mK)
L	Non-dimensional time parameter = t_1/t_2
ℓ	Length, m
$P(\omega)$	Power spectrum
P_H	Peak Hertz contact pressure, N/m^2 , Pa
\bar{q}	Heat flux, W/m^2
r	Correlation coefficient
R^2	Coefficient of determination
t	Time, s
t_1	Thermal diffusion time = $a^2/2\alpha$, s
t_2	Characteristic resident time = a/V , s
T	Temperature, C
ΔT	Temperature rise, C
T_o	Upstream (bulk) temperature, C
TC	Traction coefficient
V	Surface Velocity, m/s
\bar{V}	Rolling velocity = $1/2(V_b + V_{sa})$, m/s
V_{BP}	Break-point velocity in correlation study, m/s
V_s	Sliding velocity = $V_b - V_{sa}$, m/s
W	Load, N

x	Distance along surface, m
α	Thermal diffusivity, m^2/s
β	Length shift in computing autocorrelation function, m
β^*	Correlation distance, m
K	A constant = $.968 a^{1/2} \alpha^{1/2}/k, \text{m}^{3/2} \text{s}^{1/2} \text{C/N}$
Λ	h_c/σ
λ	Wavelength, m
μ	Viscosity, Ns/m^2
Σ	Slide roll ratio = V_s/\bar{V}
σ	Surface roughness, rms or Ra, m
τ	Time, s
ω	Wave numbers = $1/\lambda, \text{m}^{-1}$

Subscripts

b	ball
f	fluid
sa	sapphire

B. Experimental Equipment and Techniques

Two EHD contact simulators were used in the studies conducted during the past year. The first (Figure III-1) is the apparatus used for film thickness, traction and temperature measurements of EHD contacts in pure sliding. It is the same as the equipment used in pure sliding EHD studies previously conducted in this Laboratory. The new equipment (Figure III-2) differs from the sliding rig primarily in that the sapphire disk may be rotated by a separate drive system to achieve various amounts of slip. The new equipment also has a simplified system for traction measurement. In the pure sliding apparatus, the traction force was isolated from the normal force by using an air bearing under the sphere support. In the new rig, the lateral motion needed to detect the traction force is obtained by mounting the ball support on sheet metal columns. The system is therefore very rigid with respect to the normal load, but is relatively flexible with respect to the traction force. Strain gages are attached to the columns such that bending strain (proportional to traction) can be detected, but compression (proportional to normal load) can not.

In each simulator, the contact is formed using a 31.8 mm diameter 52100 steel ball rotating and loaded against a sapphire flat. Lubricant film thickness was measured for the smooth ball experiments using an optical interference technique. Both monochromatic and dichromatic [14] methods were employed.

Chromium steel balls (AISI 52100) of three different roughness values have been used to study the effects of surface roughness. The

Ra values are 0.011, 0.075 and 0.38 μm and are referred to as smooth, medium rough and rough, respectively. These balls do not have a preferred roughness orientation. Because of the high loads and relatively rough surfaces used in this study, it was not always possible to accurately measure film thickness by an optical technique. The fluid temperature can not be obtained without an accurate film thickness distribution. Rough surfaces give a time dependent film thickness at a given location which prohibits the determination of film temperatures for the rough ball. Therefore, only ball surface temperatures were measured.

The technique for measuring the ball surface temperature distribution in the contact has been described earlier [9,12]. Ball surface temperature measurements are made only at the contact center for the case of smooth and medium rough balls. The center of the EHD contact is easy to locate and also, the temperature at this location is quite close to the maximum. In the experiments with the rough ball, the temperature measured is the maximum in the contact, whether or not it occurs at the contact center. It was necessary to make this procedural change because the contact center could not be located when the rough ball was used. This is due to the disappearance of the interference fringe pattern because of light scattering at the relatively large surface asperities. Therefore, the contact was scanned for the maximum surface temperature in each case.

The infrared radiation emitted at this contact is measured with an infrared radiometric detector having a spot size resolution of 38 μm with a 15X objective and a response time of 8 μs in the A.C. mode of

operation. It was necessary to monitor the oil reservoir temperature with a thermocouple and to hold it constant with a constant temperature bath and an oil circulation system.

A Bendix surface profilimeter has been equipped with a relocation device [13]. This allows the same area of the ball surface to be examined in the profilimeter both before and after use in the EHD simulator.

Fourier analysis of both the surface profile data and the high frequency I-R data was done using Hewlett-Packard Model 5451A Fourier Analyzer System. This equipment is owned by another unit of the Institute but has been made available for use on his project.

The fluid used throughout this investigation is a naphthenic base oil designated N1 in previous studies. A complete description of the fluid is given in the appendix of reference [15].

C. Flash Temperature Measurements for Pure Sliding

Ball surface temperatures for the smooth ball were reported a year ago [13], but a correlation study with existing flash temperature theories has only just been completed. Figure III-3 shows a plot of the ball temperature rise at the contact center above the bath temperature, as a function of sliding velocity for peak Hertz pressures ranging from 0.52 to 2.03 GN/m². For a given Hertz pressure, the data plotted on log-log coordinates falls on one straight line for velocities up to a break-point value and then on another line, of lower slope, for higher velocities. The temperature rise is the difference between the ball surface temperature at the contact center and the lubricant bath temperature as measured with a thermocouple.

The trends shown in Figure III-3 can be predicted using the

techniques of Blok [16], Jaeger [17] and Archard [18]. The energy dissipation rate in the contact is equal to the product $(W \cdot TC \cdot V_b)$. The heat flux to each surface is then proportional to the dissipation rate divided by the area of the contact, or

$$\bar{q} \propto \frac{W \cdot TC \cdot V_b}{\pi a^2} \propto TC \cdot P_H \cdot V_b \quad (1)$$

where the constant of proportionality includes the portion of the total heat flux transferred to the ball. According to Archard [18] the temperature rise on the surface of a solid moving at velocity V_b and subjected to heat flux \bar{q} can be described in terms of a non-dimensional parameter $L = t_1/t_2$. The term $t_1 = a^2/2\alpha_b$ represents the time required for the effect of \bar{q} to penetrate a distance (a) below the surface, whereas $t_2 = a/V$ represents the time required for a point in the contact to move a distance (a). Therefore, for a given fluid and surface, L is proportional to $(P_H \cdot V_b)$. The variation in ΔT (ball surface temperature minus bulk oil temperature) is given as

$$\Delta T \propto \bar{q} \cdot P_H \propto TC \cdot V_b \cdot P_H^2 \quad \text{for } L < .1 \quad (2)$$

and

$$\Delta T \propto \bar{q} \cdot P_H^{1/2} \cdot V_b^{-1/2} \propto TC \cdot V_b^{1/2} \cdot P_H^{3/2} \quad \text{for } L > 5 \quad (3)$$

The parameter L has been plotted in Figure III-3 for the case of $P_H = 1.70 \text{ GN/m}^2$. The values 0.1 and 5 represent points for which the full solution is in good agreement with the limiting cases of equation 2 (stationary heat source solution) and equation 3 (fast moving heat source solution) respectively. Most of the data shown in Figure III-3 has an L between the limiting values.

In order to determine how well the data fits the Jaeger-Archard predictions of equations (2) and (3), a multiple regression analysis of the data shown in Figure III-3 was performed. For each Hertz pressure level, the data was divided into two regions separated by a break-point velocity clearly visible in Figure III-3. This break-point velocity is a function of Hertz pressure and can be described by

$$V_{BP} = 0.53 P_H^{-1} \quad (4)$$

with a correlation coefficient of $r = 0.95$. This results in a value of 3.4 for L at the break point in the experimental data. This is reasonably close to unity which is the theoretically predicted breakpoint [18]. The reason for this discrepancy is the limited amount of experimental data at low values of L . For sliding velocities below V_{BP} ,

$$\Delta T \propto P_H^{2.02} V^{0.53} \quad (5)$$

with $R^2 = .978$. For velocities above V_{BP} ,

$$\Delta T \propto P_H^{1.34} V^{0.34} \quad (6)$$

with $R^2 = .985$.

These relations were obtained neglecting the traction coefficient, since traction data was not obtained during these experiments. However, from equations 1-3 it is apparent that its influence must be included. Based on previously reported data [19,20], the traction coefficient has only a slight positive dependence on P_H in the pressure ranges studied. Furthermore, TC was found to be dependent on sliding velocity to the

power -0.29 with $r = .994$. The data used had $3 \leq L \leq 22$. Including this dependence in equations 5 and 6 results in

$$\Delta T \propto P_H^{2.02} V_b^{.82} V_b^{-.29} \propto P_H^{2.02} V_b^{.82} \cdot TC \quad (7)$$

and

$$\Delta T \propto P_H^{1.34} V_n^{.63} V_b^{-.29} \propto P_H^{1.34} V_b^{.63} \cdot TC \quad (8)$$

Recalling that equations 2 and 3 represent limiting cases, the experimental results appear to be in good agreement with the predicted trends (equations 2 and 3).

D. Correlations Between Surface Roughness and Temperature

In the previous report [13], a method was described wherein the surface roughness profile could be determined at the same location on the ball surface both before and after running in the EHD simulator. During the past year, a significant extension of this work has been undertaken on the frequency or wavelength aspects of the surface profile signal and its influence on surface temperature.

In order to study the ball surface profile in the frequency or wavelength domain, the profilometer output was first recorded on magnetic tape. This was done for samples of balls from the three roughness classifications, both before and after running in the EHD simulator.

The recording of the profilometer trace was transferred to a Hewlett-Packard Fourier Analyzer. The first step in any analysis performed by this instrument is an A/D conversion. After analysis

of the digital representation of the input signal, the results may be printed and/or a D/A conversion can be made and the results plotted or displayed on a CRT.

Figure III-4a shows the surface profile of the unused ball having an initial surface roughness of $0.38 \mu\text{m Ra}$. The trace represents the signal after the A/D and D/A conversions and is an excellent replica of the original signal plotted by the Bendix profilometer. The distance along the ball surface is shown in terms of the Hertzian contact diameter, d . For the conditions of steel on sapphire at 1.24 GN/m^2 peak Hertz pressure, the calculated contact diameter is 0.43 mm .

Figure III-4b shows the same ball after running for 24 minutes in the simulator. The profile traces shown in Figure III-4 were taken in the direction of the sliding motion. No attempt was made to measure the profile at precisely the same location on the ball surface. The traces taken are of sufficient length that they should be representative of any position within the wear track. From the previous report [13], the conditions of 1.24 GN/m^2 and $V_s = 1.02 \text{ m/s}$ should result in a value of $\Lambda < 1$ based on the unused ball surface roughness. The value $\Lambda < 1$ indicates that asperity interaction should be expected. Comparing the two traces in Figure III-4, it is apparent that the 24 minute run-in period has resulted in a smoother surface. The roughness is $.25 \mu\text{m Ra}$ which results in $\Lambda \approx .4$. The 15.9 mm radius of curvature of the ball surface can also be seen.

1. Power Spectra

The primary function of the Fourier Analyzer is to perform the Fast Fourier Transform (FFT) on the time varying input signal. A convenient way of displaying the amplitudes of the component terms in Fourier

series is through the power spectrum. The input to the analyzer is a time varying voltage. After the A/D conversion, the FFT results in a complex amplitude for each of the 127 (plus a constant) terms used in the series. Each of these terms is assigned a pair of channels in the analyzer. The frequency range, and therefore, frequency increment can be selected. The frequency assigned to two adjacent pairs of channels differs by a constant. The resulting plot of the power spectrum is linear in the independent variable, frequency. The value of the ordinate at each center frequency (channel) is the product of the complex amplitude for that frequency and its conjugate. The units are, therefore, V^2 versus Hz. The D/A conversion makes the plotted results appear to be continuous, but all of the data processing was done digitally in terms of the coefficients of the first 127 terms of the Fourier series.

Although the results are plotted on a linear frequency scale, this is not a convenient representation for this study. This is due to the fact that the frequency is influenced by the profilometer stylus scanning speed and differences between magnetic tape recording and play-back speeds. In order to remove these effects, the abscissa has been changed to read wavelength. The unit of wavelength selected is d , the Hertz contact diameter of 0.43 mm. The power spectra of the profiles shown in Figure III-4 are given in Figure III-5.

The first four channels (0-3) were cleared prior to plotting. This is because the values are so large compared to the values in higher channels (see insert), that a plot would show only the very low frequency components. Therefore, only components having wavelengths $< 3d$ have been plotted. In comparing the power spectra for the unused

and run-in ball surface profiles, note the factor of two change of scale in Figure III-5a versus III-5b. The most apparent contrast is the reduction of the components having wavelengths $<2d$. Comparing the tabular data in Figure III-5, it appears that roughness components having wavelengths $>2d$ remain essentially unchanged after the 24 minute run-in period. The nine percent difference in DC level can be attributed to slight differences in signal amplification in obtaining the two surface profiles. The most drastic change occurs for a wavelength of one Hertz diameter. This component has been reduced by more than a factor of eight.

2. Autocorrelation Function

In addition to the power spectrum, the autocorrelation function can be useful in describing the surface profile. In fact, Whitehouse and Archard [21] and Peklinik [22] suggest the description of a real surface in terms of only σ , the rms roughness, and β^* , the correlation distance. Briefly, the autocorrelation function is obtained by comparing a time varying signal, in this case the surface profile measurement, with a replica of itself where the replica is shifted some amount of time (or distance at a given velocity). If the shift along the surface profile is β , then the autocorrelation function $C(\beta)$ becomes

$$C(\beta) = \frac{1}{\ell} \int_0^{\ell} a(x)a(x + \beta)dx \quad (9)$$

where $a(x)$ is the amplitude of the surface profile trace at a distinct x along the surface. For a truly random signal, $C(\beta)$ will be a maximum at $\beta = 0$. If the signal is periodic, $C(\beta)$ will peak whenever β is a

multiple of the wavelength. If a Gaussian distribution of surface roughness amplitudes is considered, equation 9 results in an exponential autocorrelation function when normalized such that $C(0) = 1.0$,

$$C(\beta) = \exp (-\beta/\beta^*) \quad (10)$$

Therefore, when $\beta = 2.3\beta^*$, $C(\beta) = 0.10$. The value 0.10 has been arbitrarily set by Whitehouse and Archard as being sufficiently small that two points on the surface may be regarded as being independent. The power spectrum is the inverse Fourier transform of the autocorrelation function, or

$$P(\omega) = \int_{-\infty}^{\infty} C(\tau) e^{-i\omega\tau} d\tau \quad (11)$$

Substituting equation 10 into 11 results in

$$\begin{aligned} P(\omega) &= 0.5 && \text{for } \lambda = 1/\omega = \beta^* \\ P(\omega) &\approx 0 && \text{for } \lambda = 1/\omega < 0.1\beta^* \\ P(\omega) &\approx 1 && \text{for } \lambda = 1/\omega > 10\beta^* \end{aligned} \quad (12)$$

The wavelength β^* can therefore be thought of as a dividing point between those surface wavelength components having significant amplitudes and the shorter wavelengths which do not. Whitehouse and Archard have shown the model to be in good agreement with a large number of real surface profiles.

Figure III-6 shows the autocorrelation function for the unused and run-in ball surfaces shown in Figure III-4. The position shift β is shown in terms of the Hertz diameter d . If the Whitehouse-Archard

model is applied to the data in Figure III-6, the value of β^* can be found from $C(2.3\beta^*) = 0.1 C(0)$. The correlation distance β^* is .17d (74 μ m) for the unused ball and .33d (142 μ m) for the run-in surface. It is apparent that the exponential model of equation (10) can only be used for $\beta \leq 2.3\beta^*$. The further increase in $C(\beta)$ implies that the profile is not truly random, but has strong periodic components with wavelengths $> d$. This can also be seen from the power spectra shown in Figure III-5.

Figure III-6 also shows that the correlation distance has doubled as a result of the run-in process. From equation 10, a doubling of β^* implies that two points on the surface must be taken twice as far apart after run-in to be considered independent. Because of the interrelationship between the power spectra and autocorrelation function (equations 11 and 12), if the surfaces were in fact random, the half power point would be shifted to a wavelength twice the value of that for the unused surface. This is the case when the high frequency components are reduced much more than the low frequency components (see Figure III-4). This is also consistent with the notion of independent points. Consider, for example, a surface comprised of only two wavelength components $2d$ and $0.2d$. When the $0.2d$ wavelength component is present, the autocorrelation function would have a value of 1.0 for $\beta = 2md$ where m is an integer. However, it would also have sizable peaks for $\beta = 0.2md$ (with drops to near zero between). After run-in, however, the $0.2d$ wavelength component will be substantially reduced. Assuming it to be eliminated, the $C(\beta)$ now peaks only once every $\beta = 2md$ and reaches zero between the peaks. If the correlation distance

is defined as the ten percent point, it is apparent that this distance must be increased if high frequency components are reduced or eliminated.

3. Correlation between Surface Roughness and Temperature Fluctuations

The AC signal from the infrared detector obtained during the run-in process was also recorded and analyzed on the Hewlett-Packard analyzer. However, in order to eliminate noise in the detector signal, a 20 KHz, 3dB filter was used during data acquisition. The noise remaining below 20KHz had a peak power of about $5 \times 10^{-6} \text{V}^2$ whereas the detector signal had a power content on the order of 10^{-4}V^2 . Furthermore, the sampling technique used by the Fourier analyzer tends to average out the random noise while enhancing the signal.

Figure III-7 shows a normalized histogram of the AC signal from the detector obtained at the beginning of the run-in period (Figure III-7a) and after running for eight minutes (Figure III-7b). The figure shows that the voltage distributions are nearly Gaussian. Secondly, it is apparent that the amount of dispersion is decreased by the run-in process. It is interesting that both the high and low extremes in temperature signal have been eliminated as the asperity peaks were removed. The symmetry of the fluctuations supports the argument advanced previously [10] that the peak in the temperature fluctuation signal is due to local heating at an asperity; whereas the minimum signal occurs directly after this maximum and is due to the relatively low local pressure in the region following an asperity.

Figure III-8 shows the power spectra for the same IR detector signals as used in Figure III-7. The abscissa has been replotted in

terms of wavelength in units of d (Hertz diameters). It is apparent from Figure III-8 that the run-in process results in a significant reduction in power at all wavelengths. In both spectra, the peak occurs near $\lambda = 2d$, although the run-in process has reduced the peak magnitude by more than a factor of three. It should be noted that the detector signal was also filtered to remove frequency components less than 500 Hz. This corresponds to wavelengths in Figure III-8 which are greater than $5d$.

4. Discussion of Results of Spectra Correlations between Temperature Fluctuations and Surface Roughness

Based on the results shown in Figures III-5 and III-8, the authors believe that the methods presently used to determine acceptable levels of the R_a or rms surface roughness may not be the most appropriate when surface roughness effects on EHD contact temperature, wear or scuffing are of interest. For example, the rms value for the surface shown in Figure III-4a (unused rough ball) is equal to the square root of the integral of the power spectrum (Figure III-5a). However, the proper limits of integration must be chosen. The Bendix instrument used to obtain the profile shown in Figure III-13a uses an upper limit of .76 mm (through electrical filtering) and has a lower limit set by the stylus radius of $13\mu\text{m}$. If one assumes that the absence of surface temperature fluctuations is indicative of negligible asperity interaction (as shown in the previous report [13]), then as far as asperity interaction is concerned, one can determine the significant wavelengths of the surface profile. For example, Figure III-8a shows that the

temperature spectral power content during asperity interaction drops to about ten percent of its peak value for the wavelengths $\lambda \leq d/4$. However, Figure III-5a shows that there are significant roughness components down to at least $\lambda = .08d$ (the power content is essentially the square of the amplitude). The same figures show that the major components for both the roughness profile and the temperature signal are in the range $d \leq \lambda \leq 2d$. Therefore, whereas the roughness wavelength in the range $d \leq \lambda \leq 2d$ are obviously important in causing temperature fluctuations, wavelengths shorter than $d/4$ appear to have no effect. This, of course, is based on the premise that a temperature fluctuation is caused by an asperity interaction. Based on the power reduction to ten percent of its maximum value, the lower bound for rms determination should be $\lambda \approx d/4$. The upper limit is set at $\lambda = 2d$ because the temperature signal drops off rapidly for $\lambda > 2d$ even though there are roughness components present with wavelengths greater than $2d$ (see Figure III-5).

On the basis of the data taken, it appears that the rms surface roughness to be used in a calculation of $\Lambda (\Lambda = h/\sigma)$ should consider only wavelengths in the range $d/4 \leq \lambda \leq 2d$. For this experiment, $d = 0.43 \text{ mm}$ and the applicable range is then $.11 \leq \lambda \leq .86 \text{ mm}$. A roughness of about $.38\mu\text{m}$ rms was obtained using the Bendix system with limits of about $.013 \leq \lambda \leq .76 \text{ mm}$, and the standard filter (2CR-type). However, by integrating the power spectrum of the surface profile in the Fourier Analyzer between the limits of $0.11 \leq \lambda \leq 0.86 \text{ mm}$ the rms value for the surface roughness was $0.53\mu\text{m}$. This higher value is believed to be due to significant power in range $0.76 \leq \lambda \leq 0.86 \text{ mm}$.

The Bendix instrument also has available cut-offs at .25 mm and .067 mm. The use of either of these values would correspond to rms integration limits of .030d - .58d and .030d - .18d respectively. Since the desired range is .25d - .2d, the resulting rms values from the profilometer using these cutoffs would not be expected to be a reliable measure of surface roughness in predicting surface interaction.

In addition to the possibility of getting a value of surface roughness which cannot reliably predict performance, the fact that wavelengths shorter than 0.25d do not appear to be significant might have an economic impact. For example, under conditions in which the Hertz diameter is relatively large, the final stages in a lapping or polishing process may not be important.

The EHD contact appears to behave like a mechanical filter in which wavelengths outside of a relatively narrow band have a negligible effect on the performance of this system. If relatively thin films are expected during the operation of a highly loaded bearing, an improvement in surface finish should be considered. However, the magnitude of the rms roughness and the processes which might best improve the surface can not be adequately chosen until the Hertz contact diameter is known so a wave length range for measuring surface roughness can be defined.

5. Wear Measurements by Ferrographic Analysis

In order to confirm the dependence of asperity interactions on Λ , a ferrographic analysis of the oil used in the test rig was performed. In ferrographic analysis, solid particles are precipitated from the oil by a magnetic field as the oil flows slowly over a

substrate. Particles are precipitated from the oil at a rate depending on size and magnetic permeability. The resulting ferrogram yields the size distribution and concentrations of particles in the oil sample.

Using special precautions to avoid oil contamination by particles other than contact wear debris, 30 ml samples were taken at various Hertz pressures for 1 m/s sliding. The fluid was the same naphthenic base oil used in the temperature measurement experiments. Knowing the film thickness and surface roughnesses for each of these conditions, the ferrogram results could be interpreted in terms of the Λ parameter. Figure III-9 shows the percent area covered on the ferrogram (proportional to concentration of particles) as a function of Λ . Results are shown for experiments using the rough, medium rough and smooth balls. The two separate curves shown represent positions on the Ferrogram. The upper curve corresponds to relatively large size particles compared to the second curve.

The importance of the parameter Λ is clearly shown. Wear rates for both particle size classes (upper and lower curves) begin to increase rapidly as Λ approaches and then falls below one. Therefore, the onset of asperity interactions predicted by the occurrence of surface temperature fluctuations correlates very well with the results of the Ferrographic analysis. The calculation of the Λ value was based on a roughness cut-off of 0.76 mm, which is reasonably close to $2d$, (0.86 mm), the recommended value.

E. Experiments in Rolling EHD Contacts

Prior to the investigations being reported here, all EHD

experiments conducted in this laboratory were for case of pure sliding. The pure sliding experiments were selected because of their relative simplicity and because the contact temperatures would be higher, thus aiding in the development of the infrared temperature measurement technique. However, since a majority of Hertzian contact conditions occur in devices having relatively small amounts of slip, this condition had to be investigated.

The apparatus shown in Figure III-2 was constructed to allow independent selection of the surface velocity of both the sapphire flat and the steel ball. The results presented here are primarily concerned with the influence of slip on lubricant film thickness, traction and ball surface temperature.

1. Film Thickness and Traction Measurements

The results of the film thickness and traction experiments may be obtained simultaneously, but they cannot be obtained concurrent with the temperature measurements. In addition to requiring two different microscopes (metallurgical and infrared), the film thickness measurement requires a partially reflective coating, which would interfere with the infrared microscope operation.

Table III-1 is a summary of the film thickness and traction experiments. Since only the influence of slip is being studied, a single fluid, the naphthenic oil N1, was investigated. Rolling velocity, slide-roll ratio and peak Hertz pressure were all varied. A slide-roll ratio $\Sigma = 0$ implies pure rolling and a ratio $\Sigma = 2$ implies pure sliding. In all cases, fluid N1 the naphthenic base oil and the smooth ball (.011 μm Ra) were used.

Film thickness and traction have been plotted as a function of Σ in Figures III-10 and III-11 respectively. The effect of the slide/roll ratio on film thickness is small. In fact, both the centerline and minimum film thickness depend on sliding velocity to a power in the range 0 to -0.09 depending on the Hertz pressure and rolling velocity. It is apparent from Figure III-11 that the peak normally obtained in TC vs. Σ experiments in line contacts is not present here. Wedeven's traction data for point contacts [23] also lacks such a peak.

The influence of rolling velocity on film thickness and traction under conditions of zero slip is shown in Figure III-12.

2. Surface Temperature Measurements

Table III-2 shows the results of the ball surface temperature measurements. Because of small changes in the lubricant bath temperature during the course of the experiments, the temperature rise ΔT ($\Delta T = T_b - T_{\text{bath}}$) has been tabulated instead of the absolute temperature of the surface. Also, due to the relatively low infrared detector signal level under conditions of small amounts of sliding, only the high load conditions of those listed in Table III-1 were imposed in the temperature measurement experiments. However, these conditions are the closest to those found in normal practice.

The data from Table III-2 has also been plotted and is shown in Figures III-13-15. Figures III-13 and III-14 show the dependence of temperature rise on slide-roll ratio Σ for rolling velocities of 0.75 and 1.00 m/s respectively. A linear regression analysis of the maximum temperature rise data for both rolling velocities has resulted in

$$\Delta T = 30.3\Sigma + 1.2, \text{ C} \quad (13)$$

with a correlation coefficient of 0.99.

Figure III-15 shows the temperature rise as a function of rolling velocity for the case of pure rolling ($\Sigma = 0$). The data fit the straight line

$$\Delta T = 5.2\bar{V}, \text{ C} \quad (14)$$

with a correlation coefficient of 0.99.

The variation of surface temperature rise with position in the EHD contact is shown in Figures III-16-18 for slide roll ratios in the range 0 to 2.0. The data for $\bar{V} = .75$ m/s (Figure III-16) and $\bar{V} = 1.00$ m/s (Figure III-17) are quite similar and the pure sliding results ($\Sigma = 2.0$) are in good agreement with the data reported previously [13]. It is interesting to note the small amount of inlet heating present under these conditions. For example, at 1.5 Hertz radii upstream of the contact center, the surface temperature is less than 5 °C above the bath temperature. Considering that the ball surface temperature several Hertz radii upstream must be greater than or equal to the bath temperature, the 5 °C value is probably only partially due to heating in the inlet region. This relatively low value is consistent with the film temperature rise in the inlet predicted by Greenwood and Kauzlarich [24].

A second observation from Figures III-16-17 is the movement of the peak in the temperature profile toward the exit as Σ is increased.

Also, Figure III-18, which contains only zero slip data, shows that the peak occurs near the contact center and the temperature at the inlet and exit contact boundaries are nearly equal. The trend toward a symmetric temperature distribution as Σ approaches zero is a result of the primary mechanism of heat generation going from viscous shear when appreciable slip is present, to compression heating at $\Sigma \approx 0$. Viscous shear results in a heat flux present throughout the contact region. If this flux were uniform, the ball surface temperature would continue to rise as it passed through the contact. The fact that the heat flux is very much greater at the contact center results in a temperature reduction as the exit boundary is approached. The faster the heat flux falls off, the lower the exit temperature should be. In the case of nearly pure rolling, the viscous shear component is absent in Hertzian region and the temperature rise is due to shear in the inlet and compressional heating. The latter term is a function of the pressure profile, which is nearly symmetric in the contact. The film and surface temperature should therefore rise and fall with pressure. Therefore, the trends shown in Figures III-16-18 appear to be reasonable.

3. Extension of Flash Temperature Analysis for Sliding and Rolling

The flash temperature analysis done in a previous section can be extended to consider the influence of rolling. The formulation by Archard is followed except that the influence of a second surface must be taken into account. Also, since most of the data in Table III-2 corresponds to $L > 5$, the fast moving heat source limit is applied. It is also assumed that the viscous dissipation takes place in a single

plane. This assumption is reasonable because the dissipation is inversely proportional to viscosity and the shear stress is constant through the film [18]. Since a temperature profile through the film was not calculated, it was further assumed that this adiabatic plane occurred at the center of the film. If the two surface temperatures are not substantially different, this approximation should be reasonable.

The total heat flux \bar{q} is the sum of that transferred to each surface (assuming convection can be neglected). Therefore

$$\bar{q} = \bar{q}_b + \bar{q}_{sa} = \frac{TC \cdot W \cdot V_s}{\pi a^2} \quad (15)$$

Since the dissipation is assumed to occur only on the midplane, the remaining fluid merely conducts the heat to the adjoining surface. This allows a linear temperature profile to be imposed between the midplane and boundary. If T_{\max} is the midplane film temperature (maximum through the thickness) and T_b and T_{sa} are the surface temperatures at the same position in the contact, then the conduction equation reduces to

$$T_{\max} - T_{sa} = \frac{h}{2k_f} \bar{q}_{sa} \quad (16)$$

$$T_{\max} - T_b = \frac{h}{2k_f} \bar{q}_b \quad (17)$$

The average surface temperatures can be obtained from the flash temperature theory of Archard [18]. It should be noted that the location of viscous dissipation is fixed with respect to the IR detector. Therefore, the heat source is moving with respect to points on the two surfaces with velocities equal in magnitude to the absolute surface velocities.

For $L > 5$,

$$T_{sa} - T_{osa} = \frac{K_{sa}}{V_{sa}^{1/2}} \bar{q}_{sa} \quad (18)$$

$$T_b - T_{ob} = \frac{K_b}{V_b^{1/2}} \bar{q}_b \quad (19)$$

where T_o is the bulk temperature assigned to each surface and

$K = .968a^{1/2}c^{1/2}/k$. Equations 15-19 can be combined to yield $\Delta T_b = T_b - T_{ob}$.

The procedure is to eliminate T_{max} from equations 16-17 and then to substitute expressions for \bar{q}_{sa} and \bar{q}_b from equations 18 and 19 into the new equation and equation 15. This results in two equations in the unknowns, T_{sa} and T_b . Eliminating T_{sa} from them results in the following equation

$$\Delta T_b = \frac{\left(\frac{TC \cdot W \cdot V_s}{\pi a^2} \right) \left(\frac{h}{2k_f} + \frac{K_{sa}}{V_{sa}^{1/2}} \right) + (T_{osa} - T_{ob})}{1 + \frac{V_b^{1/2}}{K_b} \left(\frac{K_{sa}}{V_{sa}^{1/2}} + \frac{h}{k_f} \right)} \quad (20)$$

For the conditions used in this study, $(T_{osa} - T_{ob})$ is small compared to the first term in the numerator. Using an average film thickness of $0.16 \mu m$ (Figure III-10) and $W = 67N$, equation 20 can be evaluated for the materials used.

The ball surface temperature rise given in equation 20 assumes only viscous shear as a heat generation mechanism. However, Table III-2 shows that even when $V_s = 0$, $\Delta T_b \neq 0$. In order to account for this additional mechanism, the empirical relation for the pure rolling data

obtained earlier (equation 14) is used. Adding this temperature rise to the rise due to viscous shear (equation 20) results in

$$\Delta T_b = 5.2\bar{V} + \frac{66.7 \text{ TC} \cdot V_s}{\frac{V_{sa}^{1/2}}{5.8V_{sa}^{1/2} + 14.9} + \frac{V_b^{1/2}}{11.8}} \quad (21)$$

Equation 21 has been evaluated using the conditions shown in Table III-2 except for the conditions of pure sliding ($\Sigma = 0$, $V_{sa} = 0$). The simple sliding data was excluded because $L_{sa} = 0$, thus not meeting one of the imposed restrictions. Also, with a stationary sapphire surface, T_b and T_{sa} are likely to be considerably different, resulting in the assumption of the adiabatic plane being at the center of the film being in error. The results are shown in Figure III-19.

It should be remembered that the predicted temperature rise is the average over the contact area whereas the measured temperature rise is the maximum from Figure III-19, it is therefore clear that the predicted values of temperature rise are higher than the measured values.

There are a number of differences in the development of flash temperature theory and the conditions found in the experiments. First of all, the theory is based on a uniform heat flux over the contact area. The heat flux distribution in the EHD contact is probably non-uniform with the maximum occurring near the center. Also because of differences in thermal diffusivities of the materials of the contact, the adiabatic plane of the fluid film may not occur at the film center. Finally, the theory assumes a semiinfinite solid with the free surface being adiabatic except under the concentrated heat flux. This is not

consistent with the conditions of the experiment. The ball and sapphire surfaces outside the contact area are constantly flooded with lubricant. The agreement shown in Figure III-19 should therefore be viewed cautiously.

Because of the apparent agreement shown in Figure III-19, equation 20 can be considered as a predictive equation for the maximum ball surface temperature.

IV. GLASS TRANSITIONS IN LUBRICANTS

A. Introduction

A preliminary investigation into the possible role of glass transition and glassy state behavior of lubricants in EHD contacts was undertaken. Part of this effort requires knowledge of the pressure and temperature distributions in the EHD contact which are the subjects of the previous sections of this report. In this section preliminary results of the glass transition of lubricants as a function of pressure by two methods are presented along with a discussion indicating possible implications of the results to EHD lubrication.

The proposition that the mechanical behavior of lubricants in EHD contacts might not be that of a viscous liquid but of an elastic solid was first presented by Smith [25] in 1960. The results of Johnson and Roberts [26], and Johnson and Cameron [27] suggest that the lubricant film responds as an elastic solid under the conditions of pressure, temperature and shear rate of their EHD experiments.

Lubricating oils contain linear and highly branched hydrocarbons. Thus, a lubricating oil can display both a glass transition which is associated with the non-crystallized (non-linear hydrocarbons) part of the lubricant oil and a phase transition which is associated with the wax in the oil (linear hydrocarbons). Regardless of the wax content in a given oil, the glass transition temperature remains unchanged [28]. When comparing the conditions to which a lubricant is subjected in a typical EHD contact to available glass transition data, it appears quite likely that the lubricant is in or near the glassy state. This appears to be certain for some bulk polymers and polymer solutions and may also

be true for low molecule weight hydrocarbons. If in or near the glassy state, the solidlike behavior and ultimate mechanical properties of the lubricant may be the controlling material characteristics in the large strain and large strain rate conditions that exist in EHD.

A preliminary review of the literature [29,30,31] of glassy solids indicates that the stress and strains occurring in EHD contacts exceed the ultimate stress and strain in many materials. The work performed in this laboratory on the molecular degradation of lubricants in EHD contacts clearly demonstrates that yielding on a molecular level does occur in these applications. The infinitesimal strain work of Lamb [32] and Litovitz and Dill [33] which is being applied to EHD through the efforts of Harrison and Trachman [34] are important in determining the extent to which the lubricant is in the glassy state, but, it seems to us, the important material properties are the ultimate or large strain properties and not the linear viscoelasticity properties.

In the early stages of this research, glass transition temperatures at atmospheric pressure were measured by the technique of Differential Scanning Calorimetry (DSC) for two lubricating oils: naphthenic base oil R-620-15, designated as N1 and five ring polyphenyl ether, 5P4E. The instrument employed was a Perkin-Elmer Model DSC-2. Glass transition temperatures were -59 C for N-1 sample and -21 C for 5P4E. Probably because these values are low compared to the operating temperatures in a typical EHD contact, the occurrence of the glass transition phenomenon and the existence of the glassy state in the contact were not investigated earlier by other researchers in this field. However, because of the fact that the glass transition temperature increases with pressure, and because

of the existence of high pressures in the EHD contacts, the glass transition temperature can be greater than the operating temperature in the contact. The ASME Pressure-Viscosity-Report [35] was used to obtain an estimate of the variation of T_g with pressure. The solidification points indicated in the ASME report were assumed to be approximate glass transition points. Since these are reported as pressures at several different temperatures, they permit an estimate of the change of glass transition temperature with pressure. Also, according to McKinny and Goldstein [36], the glass transition is an isoviscous state. This is apparently because the glass transition is a constant relaxation time state for a given process and the relaxation time is essentially proportional to the viscosity. The change in temperature with pressure required to maintain constant viscosity gives results that are consistent with the results based on solidification. Based on this approach for typical lubricants, the glass transition temperature increases with pressure at a rate ranging from 80 to 350 C/GPa. Thus, it would be expected that some lubricants will be in the glassy state in an EHD contact with average pressures of 0.7 GPa or higher at room temperature. Therefore, it would be expected that many lubricants are in the glassy state for a significant portion of the time they are in the contact.

The temperatures and pressures at which glass transition occurs and the mechanical properties of the lubricant in the glassy state may influence the two most important dependent operating variables of an EHD contact: the film thickness and the traction. Since the relaxation time of a material in the glassy state is long compared to the residence time in the contact, it is possible that once in the glassy state, the

lubricant will remain in the glassy state on the moving surface while the surface moves from one EHD contact to the next. This may happen in spite of the fact that the pressure causing the glassy state formation has been removed. It is also possible that the glassy lubricant does not have time to flow while in the EHD contact but cleaves somewhere in the film so that solid layers of lubricant adhere to the contact surfaces and slide upon each other or the lubricant may undergo large strain like a ductile solid subjected to large stresses.

Therefore, the glass transition temperature as a function of pressure is a significant material property of lubricants. The mechanical and thermal properties of a substance in the glassy state are known to be functions of $T_g(P)$ which in turn is a function of temperature, pressure, and rate of temperature and pressure changes prior to entering the glassy state.

B. Glass Transition Temperature and the Glassy State

Glass transition is characterized by certain experimental observations which occur while the imposed environment of the material is changing. Commonly experiments are performed for isobaric cooling or isothermal compression of the material. At the glass transition, many material properties change in a characteristic manner. As the temperature is reduced in the liquid region, the material contracts and the viscosity increases. If the material is capable of crystallization, a point will be reached where crystallization starts. If crystallization does not occur or can be avoided, the viscosity will continue to increase until some level of 10^7 - 10^{12} Pas is reached [37,38,39]. At this point, the material becomes rigid and the thermal expansion coefficient falls by

about one-half to one-third of its value in the melt or liquid state as shown in Figure IV-1.

Glass transition is also accompanied by a change in the specific heat, c_p , isothermal compressibility, β , and other secondary properties. It corresponds to a change in slope of a plot of specific volume versus temperature as shown in Figure IV-2. Thus, glass transition phenomena are a characteristic of any liquid which can be supercooled to a sufficiently low temperature without crystallization.

Glass transition phenomena are often referred to as an apparent second-order transition since it is characterized by a discontinuous change in the secondary thermodynamic quantities. These changes occur over a range of temperatures and are not strictly discontinuous. Ferry [40] and Haward [29] showed that glass transition phenomena are not true second-order thermodynamic transitions since at T_g the substance is not in thermodynamic equilibrium. This is due to the slowness of molecular rearrangements at this temperature. This absence of thermodynamic equilibrium is part of the definition of the glassy state.

Below T_g , the degree of order will appear fixed and will not vary with temperature or pressure during the time of experimental observation. Because of this, the structural degrees of freedom are said to be frozen-in and therefore, the structural contribution to α , c_p and β are absent in the glassy state.

The effect of pressure on T_g is shown in Figure IV-2. The glass transition temperature shifts upward as the pressure is increased. The increase in T_g with pressure will be sufficient to maintain an isoviscous state. A sufficiently high pressure can induce a transition from the

liquid state to the glassy state without requiring a decrease in the temperature.

The transition temperature of a material is a function of the imposed rate of change of the material's environment, and for a series of constant rate experiments, the transition temperature curve is a constant relaxation time curve. The characteristic time of the experiment is dependent on the observation time employed in the experiment. An approximate value of the relaxation time of the material when transition occurs is the observation time employed in the experiment. The range in the relaxation time of the material as it goes through the transition from liquid to glass is from about 0.1 to 10^2 times the observation time. In the transition region the material exhibits both viscous and elastic behavior relative to the process. The range of the transition region is indicated on Figure IV-1 and 2.

As a result of the non-equilibrium state, the thermodynamic history of a glass forming liquid has considerable influence on the structure, the transition and the properties in the glassy state. The rate of the imposed environmental change effects the transition point and the properties of the glassy substance. Glass transition can be reached by isobaric cooling, isothermal compression, an imposed rate change or a combination of these changes on the material. For example, the influence of the rate of cooling, K , on the shift of the glass transition temperature of poly(vinyl acetate) has been studied over a wide range of rates by Kovacs [41]. The volume-temperature response obtained from different constant rates of cooling of a glass-forming substance is shown in Figure IV-3. Since decreasing the rate of cooling increases the

effective experimental time, the glass transition temperature will be shifted to lower values. Matsouka and Maxwell [42] studied the effect of rate of compression on the compressibility curves of polystyrene at 121 C. Their results indicate that glass transition pressure, P_g , shifts to lower values when a greater rate of pressure application is employed. If the pressure is increased slowly, the molecules of the material will have enough time to rearrange and the glass transition will take place at a higher pressure. On the other hand, if the rate of pressurization is increased, the time for any structural changes is smaller and the glass transition occurs at a lower pressure.

The influence of thermodynamic history on glass transition of poly(vinyl acetate) was studied by McKinney and Goldstein [36] by using three different thermodynamic histories: variable formation history (isobaric cooling at different pressures), and two constant formation histories (cooling at atmospheric pressure or 80 MPa (800 bar) followed by pressure changes in the glassy state).

Several techniques are employed for the determination of the glass transition temperature such as dilatometry [36,38,43], differential scanning calorimetry [28,44,45], thermomechanical analysis (TMA), dielectric [46,47] and light-scattering techniques [48-58]. Depending on the technique used, various methods exist for specifying the glass transition temperature within the transition region. The usual dilatometric technique is to cool the liquid at a constant rate and extrapolate the linear portions of the volume-temperature relation above and below the transition region to their intersection. The

temperature of this intersection [36] is taken as the glass transition temperature as shown in Figure IV-2. If T_g is measured by the change in the expansion coefficient or the specific heat, then T_g is taken as the mid-point in the step-change as measured from the extensions of the glass and liquid base lines as shown in Figure IV-1. While the choice is somewhat arbitrary, and other authors have suggested alternate techniques, the above methods are the most commonly used. Because of these different ways of defining T_g for different experiments, and because of the different inherent rates and histories in the different experiments, different glass transition temperatures may be measured on the same material in different experiments.

The first step in the study of the importance of the glassy state in EHD contacts is to determine if the lubricant is in or near the glassy state while in an EHD contact. This requires the determination of the glass transition temperature as a function of pressure and rate at observation times comparable to that of an EHD contact for typical lubricants. From these data, a phase diagram showing the liquid and the glassy states for the lubricant can be constructed. Based on the temperatures and pressures in the contact inferences can then be made regarding the state of the lubricant in the contact.

Knowing the temperature and pressure distributions in the EHD contact, the phase diagram will permit determination of whether or not the lubricant is in the glassy state, approximately what operating conditions result in the glassy state behavior, and over what fraction of the contact area the glassy state exists.

C. Experimental Technique

The glass transition temperature as a function of pressure based on two different techniques - light scattering and volume dilatometry - is reported. The two techniques are complimentary because the observation times are similar (about 200s) but the characteristic rates of the experiments are quite different - (10^{+2} s^{-1} for dilatometry and 10^{-10} s^{-1} for light scattering). Therefore as the material approaches the amorphous glassy state in the case of the volumetric experiment the material is a viscous liquid while in the light scattering it is behaving as an elastic liquid.

1. Light-Scattering Method

The basic concepts of the light-scattering technique and the description of experimental equipment used for measuring the glass transition temperature are discussed.

a. Theory

When a laser beam passes through a transparent medium, a small portion of the light is scattered in all directions. This light scattering is a result of optical inhomogeneities in the scattering medium. The optical inhomogeneities are the result of fluctuations of the dielectric constant brought about by fluctuations of density due to random thermal motion of the molecules [59].

The dielectric constant, ϵ , of a liquid can be considered as

$$\epsilon = \bar{\epsilon} + \Delta\epsilon \quad (1)$$

where $\bar{\epsilon}$ is the average dielectric constant and $\Delta\epsilon$ represents the fluctuation in ϵ . Assuming the entropy, S , and the pressure, P , are independent variables, one can write $\Delta\epsilon$ as a sum of two terms

$$\Delta\epsilon = \left(\frac{\partial\epsilon}{\partial S}\right)_P \Delta S + \left(\frac{\partial\epsilon}{\partial P}\right)_S \Delta P \quad (2)$$

The first term is the result of entropy fluctuations at constant pressure (isobaric) while the second term is the result of pressure fluctuations at constant entropy (adiabatic). The convenience of this choice of independent variables is obvious if one realizes that thermal sound waves are adiabatic pressure fluctuations. These pressure fluctuations represent random local compressions or rarefactions which, as a consequence of the elastic properties of the medium, do not remain fixed in position but travel throughout the volume of the sample. These adiabatic fluctuations can be described by means of plane sound waves of thermal origin propagating in all possible directions.

The study of the specific heat of a solid lead Debye [60] to the conclusion that the energy which one must have in all $3N$ degrees of freedom associated with the atomic oscillations of the solid can be considered as the energy of $3N$ normal elastic waves. Thus, Debye considered the energy of thermal motion of a solid as the energy of elastic waves. The Debye representation of the energy of thermal motion can also be extended to liquids and dense gases if the damping of thermal waves is small.

A major advancement in the development of light-scattering theory was achieved when Brillouin [61] established the fact that sound waves and the Debye thermal elastic waves were the same phenomena.

Thermal fluctuations do not remain "frozen", but change continuously in time and therefore, they can modulate the scattered light. If we let the modulation function be $\Phi(t)$ and the monochromatic light wave

undergoing modulation be given by

$$E_s(t) = E_o \exp(i\omega_o t) \quad (3)$$

where $E_s(t)$ is the electric field intensity of the scattered light and E_o is its amplitude, the resulting vibration of the scattered light will have the form

$$E'_s(t) = E_s(t) \cdot \Phi(t) \quad (4)$$

Consider the modulation of the scattered light by adiabatic fluctuations of pressure. The change of pressure with time satisfies the wave equation. Neglecting the absorption of the elastic waves, we can write the wave equation in the form [59]

$$\ddot{\Phi} - V^2 \nabla^2 \Phi = 0 \quad (5)$$

where V represent the velocity of propagation of the elastic waves.

The solution of equation (5) is given by

$$\Phi(t) = \Phi_o \cos[\Omega t - \vec{k} \cdot \vec{r}] \quad (6)$$

where Ω is the frequency of the elastic wave and equal to $\vec{V} \cdot \vec{k}$ where \vec{k} is the wave vector of the elastic wave. Thus, the vibration in the scattered light wave with wave vector \vec{k}_s diffracted by the elastic wave with wave vector \vec{k} in the direction of \vec{k}_s is given by

$$E'_s(t) = \frac{\Phi_o E_o}{2} \{ \exp[i(\omega_o + \Omega)t - \vec{k} \cdot \vec{r}] + \exp[i(\omega_o - \Omega)t + \vec{k} \cdot \vec{r}] \} \quad (7)$$

The above result shows that there are two doublets in the spectrum of the scattered light with frequencies $(\omega_o + \Omega)$ and $(\omega_o - \Omega)$

symmetrically located on the two sides of the incident frequency, ω_0 .

All 3N Debye waves in a body propagate in all possible directions. If such a body is irradiated by a parallel light beam with wave vector \vec{k}_i and the scattered light is observed in the direction of the wave vector of the scattered light, \vec{k}_s , making an angle Θ with \vec{k}_i as shown in Figure IV-4, then the maximum intensity of the scattered light along \vec{k}_s will occur when the wave vector \vec{k} of the elastic wave together with the vectors \vec{k}_s and \vec{k}_i satisfy the Bragg condition

$$\vec{k}_i + \vec{k} = \vec{k}_s$$

or

$$|\vec{k}| \equiv k = |\vec{k}_s - \vec{k}_i| = 2n_i k_i \sin \frac{\Theta}{2} \quad (8)$$

where n_i is the refractive index of the scattering medium at the incident wave length. Since the wave number is the reciprocal of the wave length, equation (8) can be rewritten as

$$\Lambda = \frac{\lambda}{2n_i \sin \Theta/2} = \frac{V}{\Omega} \quad (9)$$

where Λ is the wave length of the sound wave and λ is the wave length of the incident light, while V is the sound velocity and Ω the frequency of the sound wave.

Moreover, as a consequence of the sound wave, the frequency of the incident light is altered by the Doppler effect with respect to the original value ω_0 . This shift was first predicted by Brillouin [61] as

$$\omega_B = \pm 2\omega_0 \left(\frac{n_i V}{c} \right) \sin \Theta/2 \quad (10)$$

where c is the speed of light.

Rearranging and using the relation $\lambda = c/\omega_0$ we can write equation (10) as

$$v = \mp \omega_B \cdot \frac{\lambda}{2n_i \sin(\theta/2)} \quad (11)$$

Comparing equations (9) and (11) we obtain the frequency shift, ω_B , equal to the sound frequency, Ω . For scattering angle of 90° and incident light of wavelength of 5145°\AA , the frequency shift in materials having a sound velocity of the order of 3000 m/s. and a refractive index of 1.5 is about 12×10^9 Hz. This result shows that the Brillouin method deals with acoustical phenomena in the gigacycle region (hypersound). This shift represents a frequency change of less than 0.002 percent. The observation of this frequency shift is possible with a gas laser as a monochromatic light source and a Fabry-Perot interferometer as a detector. The two signs in the above equations correspond to the two opposite directions in which the sound wave may travel.

According to Landau and Placzek [62], the scattered light produced by the entropy fluctuations of $\Delta\varepsilon$ does not propagate in normal liquids and these fluctuations are the source of the central unshifted component of the scattered light. The intensity of this component, I_c , is expressed as a function of the total intensity in the Brillouin doublet, $2I_B$, by the Landua-Placzek relation [48,49]

$$\frac{I_c}{2I_B} = \gamma - 1 \quad (12)$$

where γ is the specific heat ratio.

Measurements on Brillouin spectra have been made by a number of workers such as Rank, et al. [48,50], Cummins and Gammons [51], Pinnow et al. [49], and others [52,53] who observed the Brillouin effect by using He-Ne and Argon ion laser as the light source. A typical frequency spectrum of lubricating oils is shown in Figure IV-5. The shift of the Brillouin lines from the laser frequency is of interest since it enables us to calculate the velocity of sound according to equation (11).

For a viscous medium, two types of Brillouin scattering can be observed:

(i) Scattering from longitudinal sound waves which gives a measurement of the longitudinal modulus, M , as

$$M = \rho V_{\ell}^2 \quad (13)$$

where V_{ℓ} is the longitudinal velocity of sound given by

$$V_{\ell} = \omega_{Bl} \frac{\lambda}{2n_i \sin \theta/2} \quad (14)$$

(ii) In highly viscous materials just as in crystals and glasses, a second set of Brillouin lines is often observed in the depolarized spectrum with a shift smaller than that of the longitudinal Brillouin lines (not shown in Figure IV-5). These new shifted components are transverse Brillouin lines due to scattering from propagating thermal transverse waves which can propagate in the medium as it becomes more viscous. Scattering from transverse waves appear in the depolarized spectrum because these waves cause anisotropic fluctuations in the local structure of the material. In lubricants at high viscosities, the material is acting in a glassy manner and the transverse Brillouin

peaks may be detected. The fact that these peaks appear in the frequency spectrum is an indication that the longitudinal waves are no longer purely compressional waves but contain a transverse component also. Scattering from transverse sound waves gives a measurement of the shear modulus, G , as

$$G = \rho V_t^2 \quad (15)$$

where V_t is the transverse velocity of sound given by

$$V_t = \omega_{Bt} \frac{\lambda}{2n_i \sin \theta/2} \quad (16)$$

In low-viscosity liquids, the transverse elastic waves are so weak that the inner Brillouin doublet, which is brought about by the diffraction and modulation of light by the transverse wave, is difficult to observe. In this research only longitudinal frequency shifts and longitudinal sound velocities will be reported.

b. Pressure and Temperature Coefficients of the Sound Velocity

A change in the slope of the sound velocity as a function of temperature and pressure like density or specific heat also defines the glass transition and has been observed by many workers [52-55]. It has been established that the change in the temperature coefficient of the sound velocity is a manifestation of the change in the thermal expansion coefficient that occurs at the glass transition temperature [56-58]. This allows us to detect the glass transition with gigacycle sound waves. Figure IV-6 shows the variation of the sound velocity and frequency shift with temperature for atactic polystyrene [53] where a change in slope

is clearly observed at the glass transition temperature.

The dependence of the velocity of sound on the density, ρ , is seen through the relation

$$V = (M/\rho)^{1/2} \quad (17)$$

where M represents the appropriate modulus of elasticity which is a function of the density. Since the density appears explicitly in the above relation, it is clear that a change must appear in the slope of the velocity-temperature and velocity-pressure curves at the glass transition. A comparison of volume-temperature data with velocity-temperature data taken from literature [56] is consistent with the above observation. However, the expansion coefficient of polystyrene is $2.2 \times 10^{-4} \text{ } ^\circ\text{C}^{-1}$ for $T < T_g$ and $5 \times 10^{-4} \text{ } ^\circ\text{C}^{-1}$ for $T > T_g$ while the velocity coefficient is $8 \times 10^{-4} \text{ } ^\circ\text{C}^{-1}$ for $T < T_g$ and 14×10^{-4} for $T > T_g$ which shows that the dependence of velocity on density is chiefly through the strong dependence of the modulus on density and only to a lesser extent through the explicit appearance of density in equation (17).

c. Light Scattering Experimental Apparatus*

The schematic arrangement of the basic components of the light-scattering experiment is shown in Figure IV-7 and consist of (1) a argon ion laser in single frequency operation and having a power of about 200 milliwatt at $\lambda = 5145 \text{ } ^\circ\text{A}$ (single line operation is accomplished by inserting a wavelength-dispersing element (Prism) into the laser cavity), (2) a high pressure scattering cell containing the

*The assistance of Drs. D. C. O'Shea and F. D. Medina of the Georgia Tech Physics Department for the use of their light scattering equipment and guidance in this work is gratefully appreciated.

lubricant sample to be investigated, and (3) a detector which permits the spectroscopic analysis of the scattered light.

The scattered light from the lubricant sample is collected by a lens and enters a Fabry-Perot interferometer as shown in Figure IV-8. The output of the interferometer, consisting of polarized and depolarized scattered light, is focused on a screen which has a pinhole in front of a photomultiplier tube (PMT). The output signal from the PMT can be processed by a standard counting system and recorded with a multichannel analyser. The spectrum can also be recorded on X-Y recorder and/or punched on paper tape using the output of a ratemeter.

The Fabry-Perot interferometer used in the light-scattering experiment consists of a pair of highly reflective mirrors separated by a specified distance, d . The mirrors can be moved and tilted to ensure exact parallelism between their surfaces. At certain wavelength [63] the amount of light transmitted through the mirrors will be many times larger than expected from the combined transmission for two highly reflective mirrors. This occurs when there is constructive interference between incident light waves with those of different reflections. Only when all the waves from the multiple reflections are in phase will there be high transmission. For incident light normal to the mirror faces, the maximum transmission will occur when

$$\lambda_m = \frac{2d}{m} \quad (18)$$

where m is the order of interference (an integer). In terms of frequency, the above equation can be written as

$$\nu_m = \frac{c}{\lambda_m} = m \frac{c}{2d} \quad (19)$$

The transmitted beams are focused by a lens onto a screen where a series of concentric interference fringes are observed. Only light travelling perpendicular to the plates obey the simple resonance condition. This light is focused to the center of the ring pattern. By placing a pin-hole at this center, only light with frequency $\nu_m = m \frac{c}{2d}$ is allowed to pass through and be detected by a photomultiplier tube. If we plot the transmission of the interferometer as a function of frequency for a monochromatic incident light of frequency f , we would obtain a curve similar to that shown in Figure IV-9. These transmission characteristics enable the device to be used as a tunable filter to display the output frequency of the laser. The frequency range which is transmitted during the Fabry-Perot scan is known as the free spectral range (FSR) which is

$$\text{FSR} = \frac{c}{2d} \quad (20)$$

Since the speed of light is approximated by 3×10^8 m/s, the frequency units can be expressed in cm^{-1} (wave number units). A frequency of 15×10^9 Hz corresponds to 0.5 cm^{-1} . Unless otherwise specified, the frequency units will be reported in cm^{-1} .

In the scanning mode, we observe the spectral content of the scattered light by moving one mirror along the interferometer axis without disturbing the parallelism of the mirrors by applying a ramp (sawtooth) voltage to a piezoelectric transducer (PZT) attached to one of the mirrors.

The temperature inside the Fabry-Perot interferometer is controlled

by a proportional controller and a thermister sensor. Two resistors (20 watt) are glued to each of the bottom and side panels of a box enclosing the interferometer and serve as heaters. The temperature is controlled to about $2-3^{\circ}$ above room temperature.

Since the Rayleigh line intensity is usually several orders of magnitude greater than that of Brillouin lines, a significant improvement of the frequency spectrums can be obtained by operating the Fabry-Perot interferometer in triple pass geometry. This is accomplished by using a pair of corner cubes (Figure IV-8).

In summary, the light-scattering technique enables one to determine the sound velocity at frequency ω_B if a monochromatic beam of light strikes the scattering medium and the frequency shift of the Brillouin scattered light at angle θ is measured. The location of the change in the slope of the sound velocity as a function of temperature and pressure is a measure of the glass transition.

d. High Pressure Equipment

The high pressure equipment consists of a scattering cell, a strain gauge pressure transducer, a 9:1 area ratio intensifier and a hand pump.

The high pressure cell* (3" x 2-3/4" x 1-3/4") is shown schematically in Figure IV-10. It was used to pressures of 0.66 GPa (100,000 psi). The test fluid in the cell was separated from the hand pump oil by an intensifier which was connected to the cell by high pressure tubing. The cell material is Vasco Max 300 CVM alloy.

*The high pressure cell was originally designed by Dr. W. B. Daniels of the University of Delaware.

Heat treatment of the cell was necessary to raise the hardness and increase the strength properties. Aging the cell by heat treatment for six hours at 480 C followed by an air quench raised the hardness to about 52-55 Rockwell "C" and increased the yield strength to 1.9 GPa.

An intensifier with a 9:1 piston area ratio was mounted between the hand pump and the high pressure scattering cell. The test fluid is contained in the high pressure side of the intensifier cavity, the high pressure tubing and the optical cell. The high and low pressure sides of the intensifier piston were sealed with Viton O-rings which were protected by anti-extrusion rings. The intensifier material is the same as that of the optical cell and it was heat treated in the same manner.

The pressure of the lubricant sample contained in the optical cell was measured with a commercial strain gage pressure transducer located as shown in Figure IV-10. The pressure transducer is a Norwood model 114 manufactured by the Advanced Technology Division of American Standard and was used in high pressure viscosity measurements conducted under this grant.

One of the important features of using the pressure transducer is that the lubricant sample pressure is measured directly in the optical cell and thus the influence of intensifier seal friction on pressure measurements is eliminated. However, when the material viscosity increases during glass formation the sample pressure may be different from the transducer pressure because of glass formation in the tube connecting them.

e. Glass Formation History

Because of the dependence of the glass properties on formation history, two standard procedures were adopted to form the glass of the materials investigated. In one formation history (history A), the

pressure was increased from atmospheric to a reference pressure in the liquid region. At the same time, the sample temperature was increased at a rate of 6.1 mC/s (22C per hour) to about 17 C above its assumed glass transition temperature. At this point the pressure and temperature were kept constant for about 30 minutes. The sample was then cooled at constant pressure and frequency spectra were taken at 2.8C (5 °F) intervals. Twenty minutes were allowed for the temperature to reach equilibrium before each spectrum was recorded. Hence, experimental measurements were started in the liquid state and the glassy state was reached by decreasing the temperature at constant pressure as shown in Figure IV-11. This procedure was repeated at different constant pressures and, therefore, the structure of the glass formed varies with the formation pressure.

In the second formation history (history B), the glass was formed by pressurizing the sample at room temperature from atmospheric pressure until the glassy state was reached. Frequency spectra for this case were taken at pressure intervals of about 20 to 27 MPa (3000 to 4000 psi). Again up to twenty minutes was allowed for the sample to reach equilibrium before the spectra were recorded.

In history A, the sample temperature was changed by controlling the voltage input to an electric tape heater wrapped around the intensifier-cell assembly which was enclosed in an oven. By controlling the input voltage to the electric heater, the cell temperature was controlled to better than ± 0.1 C. The temperature was measured with a copper-constantan thermocouple in conjunction with a direct reading digital thermometer. The thermocouple was in a brass well fitted into a hole in the cell body (Figure IV-10).

f. Data Reduction Technique and The Results for 5P4E*

The data on 5P4E will be used to illustrate the data reduction technique. Some results are also available on N1* and the phase diagram for that material based on light-scattering will be presented in the Discussion section.

All frequency spectra of scattered light were obtained at a fixed scattering angle of 90° . The free spectral range for each case investigated was kept constant. This procedure was adopted to minimize the errors in measuring the separation distance of the Fabry-Perot interferometer which in turn minimized the error in the calculated frequency shift. Using the scattering angle of $\theta = 90^\circ$ in equation (9) and (11), one obtains

$$\Lambda = \frac{\lambda}{\sqrt{2} n_i} \quad (21)$$

and

$$V = \omega_B \frac{\lambda}{\sqrt{2} n_i} \quad (22)$$

The recorded spectra were used to measure the frequency shift and to calculate the sound velocity by employing equation (22).

The frequency spectrum of 5P4E recorded at 0.2 GPa (28,200 psi) and 24.4 C (76 F) (formation history B) is shown in Figure IV-12. It contains two successive orders of the interference. The center of the four Brillouin peaks were located at some height where the Brillouin

*See Appendix A for material descriptions.

components appeared to be symmetrical. The separation distance, d , of the Fabry-Perot interferometer was 0.50 cm corresponding to a free spectral range of 30 GHz $\left(\frac{c}{2d}\right)$. The frequency shift obtained from this spectrum is equal to

$$\omega_{B,k} = \frac{\ell}{2L_k} \cdot \frac{c}{2d} \quad (23)$$

where $k = 1, 2$. Two values of ω_B can be calculated, each corresponding to the order of interference. These are (see Figure IV-12)

$$\omega_{B,1} = \frac{\ell}{2L_1} \cdot \frac{c}{2d} = \frac{6.85}{16.50} \times \frac{3 \times 10^{10}}{2 \times 0.50} = 12.45 \text{ GHz}$$

and

$$\omega_{B,2} = \frac{\ell}{2L_2} \cdot \frac{c}{2d} = \frac{6.85}{16.40} \times \frac{3 \times 10^{10}}{2 \times 0.50} = 12.53 \text{ GHz}$$

Each value of ω_B together with the values of n_i (1.6873) and λ (5145 Å) is used in equation (22) to determine the velocity of sound at the indicated pressure and temperature as follow

$$v_1 = \frac{\lambda \omega_{B,1}}{\sqrt{2} n_i} = 12.45 \times 10^9 \times \frac{5145 \times 10^{-10}}{1.6873 \sqrt{2}} = 2685 \text{ m/s}$$

and

$$v_2 = \frac{\lambda \omega_{B,2}}{\sqrt{2} n_i} = 12.53 \times 10^9 \times \frac{5145 \times 10^{-10}}{1.6873 \sqrt{2}} = 2702 \text{ m/s}$$

The average values of $\omega_{B,k}$ and V are reported. Frequency shifts and sound velocities at other pressures and temperatures are calculated in the same manner. The results of these calculations for 5P4E at 24.4 C (76 F) (history B) are shown in Table IV-1 and plotted in Figure IV-13. From this figure, it is seen that the sound velocity and the frequency shift increase with increasing pressure and a change in the slope is apparent at 0.17 GPa (24,700 psi) corresponding to a velocity of sound of 2658 m/s. This change of slope represents the glass transition. The velocities on each side of the transition region can be represented by linear functions of pressure. The two sections of Figure IV-13 were each fit by least squares regression to a linear expression of the form

$$V = A + B P \quad (24)$$

where V is in m/s and P in MPa. The intersection of these lines are interpreted [52-58] as occurring at the glass transition pressure. The least square expression obtained for each section of the velocity-pressure curve shown in Figure IV-13 is

$$V_L = 2098 + 156.3 P$$

and

$$V_g = 2397 + 72.87 P$$

Solving these two equations for their intersection, one obtains

$$P_g = 170.3 \text{ MPa} \quad \text{and} \quad V = 2658 \text{ m/s.}$$

Frequency spectrum of 5P4E obtained by formation history A

(at 0.40 GPa (59,000 psi)) and recorded at 64.4 C (148 F) is reproduced in Figure IV-14. It is typical in general appearance of all frequency spectra obtained. The separation distance, d , was 0.725 cm corresponding to FSR of 20.7 GHz. The frequency shifts and the sound velocities were calculated from the position of the Brillouin peaks as discussed above. The result of these calculations are shown in Table IV-2 and are plotted in Figure IV-15. The sound velocity increases as the temperature is decreased. At the transition region the dependence of sound velocity on temperature changes. This change of slope of the temperature coefficient of the sound velocity was observed at all formation pressures. Once again, the two portions of the sound velocity curves were fit by least square regression to straight lines of the form

$$V = a + b T \quad (25)$$

where V in m/s and T in C.

5P4E was subjected to formation history A at a total of six formation pressures. The resulting material behavior is shown in Table IV-3 and Figures IV-16 and 17.

The least square expressions for both portions of the velocity-temperature curves were solved for their intersection to determine the glass transition temperature at each formation pressure. The glass formation temperature-pressure combinations result in the phase diagram shown in Figure IV-18. The glass transition temperatures and pressures were least square fit with a straight line. The expression obtained is given by

$$T_g = 0.183 P_g - 4.74$$

$$(T_g = 2.27 P_g + 23.5 \text{ with } T_g \text{ in F and } P_g \text{ in kpsi})$$

with T_g in C and P_g in MPa. The glass transition temperature at 24.4 C (76 F) by history B was excluded from the fit due to the different history by which the glass was formed. However, in general, the transition obtained by History B fell near the line obtained by History A.

The scattered light frequency shift was also least square fit with straight lines and the expressions obtained were solved for their intersection to locate the glass transition. The results obtained from the frequency shift did not differ from those obtained from the sound velocity by more than 1.4 MPa (200 psi) for the glass transition pressure (History B, at 24.4 C (76 F)) nor more than 1 C (2 F) transition temperature at any formation pressure for History A. Therefore, the glass transition data were obtained from the sound velocity only.

D. Dilatometry Method

As mentioned in the introduction, dilatometry can be used to measure the glass transition at long observation times. In many respects volume dilatometry is both conceptually and experimentally less complicated than the light scattering method for determining glass transition. Dilatometry is inherently a low rate process and a change in rate shifts the glass transition in a known manner. Therefore, dilatometry data is significant in that any temperature-pressure combination placing the material in the glassy-state by dilatometry measurements will indicate glass formation in an EHD contact because of the

shorter observation time in the EHD contact.

Dilatometry measures the relative volume of the material as a function of temperature and pressure. The compressibility and thermal expansion coefficients of the material differ in the liquid and glass regions and the glass transition is defined by this change as discussed in the introduction and shown in Figures IV-1, 2, and 3.

Three dilatometers were constructed and are shown schematically in Figure IV-19, IV-20, and IV-21. The three devices were made to cover different pressure ranges. Two types of experiments can be conducted: 1) isobaric cooling (History A) and 2) isothermal compression (History B). Both the isobaric cooling and isothermal compression experiments had observation times on the order of 10^2 s to 10^3 s.

The formation histories in the dilatometry experiments were similar in that the material was always taken from the liquid state into the glassy state. For elevated pressure experiments this required heating and pressurizing in the liquid region well above the glass transition to some starting pressure and temperature from which the isobaric cooling or isothermal compression would start. As the experiment progressed the relative specific volume would be obtained as a function of temperature or pressure and the intersection of the curves in the liquid and glassy regions would define the glass transition. These intersections and resulting phase diagrams were obtained in the same manner as that in the section on light-scattering for the sound velocity data.

Experiments have been completed on the materials shown in Table IV-4. The phase diagram for 5P4E obtained with the volumetric method compared with that from the light-scattering is shown in

Figure IV-22. The reason for the difference in the data from the two techniques is not known at this time but the difference is small relative to the temperature and pressure ranges a material is subjected to in an EHD contact. Therefore, if 5P4E is subjected to a temperature-pressure combination in an EHD contact which is to the right of the dilatometry curve on this phase diagram, the material will be in the glassy state in the EHD contact. These data suggest that 5P4E would be in the glassy state in most EHD applications. Figure IV-23 contains similar comparisons for material N1. The same comments made regarding 5P4E are applicable to N1.

Figure IV-24 contains phase diagram data for several materials based on the isothermal compression measurements. The variation in glass forming tendencies of the materials is large. However, the typical mineral oil based lubricants studied have very similar glass forming characteristics as shown in Figure IV-25. The transition regions for the compression experiments are shown in Figures IV-26, IV-27, and IV-28. Because the observation time in these experiments was approximately five minutes the glass transition point is where the material relaxation time is approximately five minutes and the transition region represents the changes in relaxation time (τ_m) from about one tenth that value on the liquid end to about 10^2 times that on the glassy end ($0.5 \leq \tau_m \leq 500$ minutes). In this region the material exhibits both viscous and elastic behavior relative to this experiment. In the liquid region the relaxation time is much less than 0.5 minute and the material can be treated as a viscous liquid in this process. In the glassy region the relaxation time is greater than 50 minutes and the

material can be treated as an elastic solid in this process.

Table IV-5 lists those materials which were studied but for which no glass transition was observed for the volumetric experiments in the pressure and temperature range studied. This implies that the relaxation times of these materials were much less than one half minute in the pressure and temperature range of observation.

E. Two Additional Experiments

Glass transition is accompanied by changes in all the material's physical properties including very large changes in viscosity. In the past glass transition has been defined as the point at which the viscosity of the material reaches a high value (e.g. 10^{11} Ns/m²). Because the approximate shear rates and shear stresses to which the material is subjected in an EHD contact are not consistent with such high viscosities, while the temperatures and pressures indicate it is in the glassy state, two simple shearing experiments were conducted. Both were conducted in a concentric cylinder device. In one experiment the torque (shear stress) was measured continuously at constant shear rate (0.43 s^{-1}) while the 5P4E sample was cooled continuously. In the second experiment a crude indication of the ultimate shear strength of the material in the glassy state was obtained.

The viscosity measurement experiment was conducted in a Haake concentric cylinder viscometer and the results are shown in Figure IV-29. As expected the viscosity increases rapidly with decreasing temperature but the trend begins to change substantially as the glass transition temperature is approached. The glass transition temperature as measured by differential scanning calorimetry is -23 C and is marked on the

figure. The shear stress limit of the instrument is about 3.5 kPa. As the temperature continues to decrease below the glass transition temperature the material effectively becomes a rigid solid.

Once in the glassy state the material has solid-like properties such as sound velocity, thermal expansion coefficient, specific heat, etc., and might also be expected to have an ultimate yield shear strength. To get an estimate of this property at atmospheric pressure, a concentric cylinder device was constructed with a outer diameter of 16 mm, inner diameter of 13 mm and length of 16 mm. The outer cylinder could be held firm and the inner cylinder turned with a torque wrench when the sample was cooled below its glass transition temperature. A thermocouple was inserted into the sample through the inner cylinder and the device cooled by liquid nitrogen. The torque required to break the inner cylinder loose was then an estimate of the yield shear strength of the material. The data are shown in Table IV-6. These results suggest that yield behavior of the material in the glassy state should be studied in conjunction with the study of material behavior in EHD contacts.

F. Discussion of Results

1. Pressure Dependence of Glass Transition Temperatures in Lubricants

The glass transition results presented suggest that glass transition phenomena and rheological behavior in the glassy state are important for some lubricants in some EHD applications.

The volumetric experiments covered the widest range of pressure and temperature. As seen in Figure IV-23 for N1 at low formation pressures (up to about 0.45 GPa), the transition temperature is a linear function of pressure with a slope of about 190 C/GPa. Above 0.45 GPa, the slope

decreased gradually and the glass transition relation became linear again above 0.55 GPa with a slope of about 100 C/GPa. Figure IV-23 also includes the light scattering transition data obtained by history A for fluid N1 (slope = 120 C/GPa). The glass transition temperatures of the light scattering technique are seen to be higher (by about 19 C) than the temperatures based on the volumetric method at all pressures. The reason for this difference is unclear at present.

The glass transition temperature for N1 at atmospheric pressure was also determined by the volumetric measurements and has a value of - 81 C. This value is lower than that obtained by the DSC measurements by about 22 C. The decrease in T_g is due to the different cooling rates (28 C/hr for the volumetric measurements and 1220 C/hr for the DSC measurements) and the different formation history used in each technique.

The volumetric and light scattering transition data for 5P4E are shown in Figure IV-22 and have behavior similar to that discussed above for N1.

From the above discussion, the glass transition determined from the light scattering technique is in general agreement with glass transition measurements obtained with other techniques.

2. Relationship of Glass Transition to EHD Conditions

To obtain an impression of the relationship between glass transition for various lubricants and conditions in EHD contacts, Figure IV-30 has been prepared. Figure IV-30 contains the liquid-glass transitions for three lubricants as measured by the volumetric technique. The three lubricants selected represent a wide range of behavior with respect to glass transition. Above and to the left of each curve is the liquid

region for the material for low rate (long observation time) processes. To the right and below each curve is the glassy region. Based on limited measurements on three other hydrocarbon base oils the curve for N1 is an adequate first approximation for non-polymer containing hydrocarbon base oils. Also indicated in Figure IV-30 are the approximate ranges of pressure in the inlet and the Hertzian zones of an EHD contact. The approximate temperature ranges are also marked for an inlet temperature of about 20 C based on the IR temperature measurements reported elsewhere in this report. What this heuristic depiction shows is that glass transition most probably occurs in many practical applications of EHD contacts with many existing lubricants. The higher the contact pressure the more likely the transition to the glassy state, particularly with rolling and low slip ratio contacts. The glass transition and glassy state behavior is most likely to effect traction but may also effect film thickness if the transition occurs in the inlet zone, which can happen. The above clearly suggests the phenomena of glass transition occurs in EHD and its effects may be observable in EHD data already available.

a. Traction Measurements

Johnson and Cameron [27] measured the traction transmitted by an elastohydrodynamic film in a rolling contact with low sliding speeds and near isothermal conditions. From the traction measurements, the variation in apparent viscosity of their oil* with pressure and temperature is shown in Figure IV-31. The variation of the apparent viscosity with pressure shows a marked change above 10^3 Pas. The

*Shell Vitra 76 similar to N1 but of higher viscosity.

authors [27] remarked that it is tempting to suppose that this change indicates a change in physical properties of the oil at high pressure. To test their remarks, the linear sections of Figure IV-31 were extrapolated to obtain an intersection. Pressures of about 0.57 and 0.88 GPa were obtained at 30 and 70 C respectively. These intersection points fall near the glass transition lines of N1 fluid as shown in Figure IV 23 which is repeated with this data in Figure IV-32. The fact that the intersection points correspond to the measured glass transition points support the authors [27] remark.

b. Side Thrust Measurements

Johnson and Roberts [26] devised a rolling-contact experiment with a small amount of twist. Because of certain kinematic characteristics of their contact, no side thrust will be transmitted if the lubricant behavior is that of a liquid. If the material behaves like a solid, some side thrust will be observed. Figure IV-33 is a plot of the relative side thrust as a function of contact pressure. This transition in the behavior of their oil* is similar to that of specific heat or expansion coefficient of a material passing through a glass transition as discussed earlier. This observation raises the question of whether the behavior shown in Figure IV-33 is a glass transition. The onset of solid like behavior occurs at about 0.5 GPa and 23 C which is plotted on Figure IV-32. When the technique for determining the glass transition temperature for such a physical behavior was used, a midpoint transition pressure (see Figure IV-32) of about 0.7 GPa was obtained at 23 C. These values of pressure are seen to fall in the transition and glassy regions of Figure IV-32. This result agrees with

Johnson and Roberts' conclusion that a transition from viscous to solid behavior occurred above a contact pressure of about 0.5 GPa.

c. Contact Temperatures and Pressures

Fluid and ball surface temperature distributions in a sliding and rolling contact are shown in Section III of this report. Figure IV-34 is a plot of the ball surface temperature at the contact center versus maximum Hertz pressure at three sliding speeds. Figure IV-35 shows the ball surface temperature versus sliding speed at different Hertz pressures. Because both figures have temperature and pressure plotted, we can include the glass transition lines obtained by the light-scattering and the volumetric measurement techniques. As shown in these figures, the lubricant near the ball surface is in the glassy state at a sliding speed of 0.2 m/s. At higher sliding speeds, the glassy state exists only at high pressures. This result was expected since a sliding contact generates frictional heat and thus the temperature levels in the contact are relatively high.

The above discussion suggests the existence of the glassy state in sliding EHD contacts at relatively low speeds or sufficiently high pressures.

Ball surface temperature distributions for fluid N1 at different slide-to-roll ratio ($\Sigma = 2 \frac{(u_2 - u_1)}{(u_2 + u_1)}$) are shown in Chapter III and are repeated in Figure III-36. The speed ratio, Σ , ranged from zero (pure rolling) to 2.0 (pure sliding) at a constant Hertzian pressure of 1 GPa and at constant rolling speed of 0.75 m/s. Based on the measured temperatures, assumed Hertzian pressure distributions, and the glass transition data, it can be estimated what portion of the fluid in contact with the

ball surface will be in the glassy or liquid states. The portions are shown in the bar diagrams included in Figure IV-36. The lubricant near the ball surface is in the glassy state for all speed ratios except that of $\Sigma = 2.0$. At sufficiently low speed ratios, the glassy state occupies all the contact area. This result shows that the lubricant N1 is in the glassy state in a rolling/sliding contact and the glass can occupy all the contact area at low slide-to-roll speed ratios.

G. Conclusions

The glass transition temperatures of lubricants increase sufficiently with pressure to cause glass transition in EHD contacts with many typical lubricants. The glass transition behavior of lubricants of current interest varies considerably. Some, for example 5P4E, undergo glass transition at room temperature at about 0.14 GPa while bis-2-ethyl hexyl sebacate did not undergo a glass transition down to -30°C even up to 1.1 GPa.

It appears that EHD data already available in the literature are consistent with the glass transition observations reported here. Glass transition of lubricants can be expected to influence both the EHD traction and the film thickness depending on the location of the transition in the contact.

The results of the preliminary study reported here clearly suggest that further research into the glass transition of lubricants, rheological behavior of lubricants in the glassy state and further verification of glass transition in EHD contacts are needed. Analytical modeling of the mechanics of EHD contacts with glassy lubricants should be pursued. Also the study of the relationship of chemical structure to glass transition may be useful in future lubricant formulation.

V. ON THE ANALYTICAL DETERMINATION OF PRESSURE
DISTRIBUTION IN EHD LINE CONTACTS FROM FILM
THICKNESS DATA

A. Introduction

The objective of the investigation reported in this section is the determination, by analytic methods, of the pressure distribution to which a film is subjected in an elastohydrodynamic process. The EHD-generated pressures in the film are the surface-tractions on the solid components of the system. In this study the solid components consist of either two elastic cylinders with parallel generators, or an elastic cylinder and an elastic plate.

The interest inherent in the foregoing problem is many-fold. Firstly, the rheological properties of the film are functions of its local pressure and temperature. This dependence becomes more pronounced at the high pressures generated in the EHD-zone. Consequently the integrity of the film is tied to the understanding of this dependence. Secondly, if the intensity of the pressure field becomes large enough there is a distinct possibility that the lubricant's physical state may change. Hence an accurate description of the thermodynamic variables is needed to assess the accuracy of the currently employed theories and hypotheses of the EHD process. Thirdly, the pressure distribution is necessary for the calculation of the stress fields to which the elastic components of the system are subjected. The determination of the stress field could lead to a better understanding of the fatigue and fracture of bearing surfaces. Fourthly, since the determination of the pressure field, as developed here, is independent of

NOMENCLATURE

a	half-width of pressure distribution
$[A]$	cylinder solution corresponding to arbitrarily distributed surface load
$[B_1]$	basic solution to cylinder problem
$C(0, k\theta)$	cosine integral
F_x, F_y	surface forces
h	elastohydrodynamic film thickness
h_o	film thickness in undeformed state
h_n	Fourier coefficient of pressure on half-plane
$[H]$	half-plane solution corresponding to arbitrarily distributed surface load
$[H_{01}]$	symmetric half-plane solution
$[H_{02}]$	antisymmetric half-plane solution
i	$\sqrt{-1}$
J	set of real integers
p	pressure
p_n	Fourier coefficient of pressure
p_o	reference pressure
P	total applied load
r_o	radius of cylinder
r_1, \dots, r_4	radial location of arbitrary interior point z relative to points of application of surface forces
r_i	residual
$[S_{12}]$	antisymmetric cylinder solution
$[S_{22}]$	symmetric cylinder solution
$s(0, k\theta)$	sine integral

u, v	displacement in x- and y-directions respectively
u_1, u_2	surface deformation of bodies 1 and 2
U_i, V_i	coefficient of deformation
x, y	cartesian coordinates
x_0	reference length
\hat{x}	distance along x-axis measured from point of contact in the undeformed state
z	complex variable $x + iy$
z_k	points on surface of body at which forces act
α	angular location of surface force
α_0	angular half-width of pressure distribution on cylinder
β	angular coordinate of arbitrary point on cylinder surface
$\tilde{\beta}$	dimensionless angle, β/α_0
γ	normal approach of two solid bodies
$\theta_1, \dots, \theta_4$	angular location of arbitrary interior point z relative to points of application of surface forces
λ, μ	Lamé elastic constants
ξ	dimensionless coordinate x/a
σ	tangential surface traction
$\tau_{xx}, \tau_{xy}, \tau_{yy}$	stresses
ϕ, ψ	complex potentials
$[\quad]$	stress tensor or displacement tensor fields associated with a particular solution
Superscripts	
(a), (s)	antisymmetric and symmetric solutions, respectively
—	complex conjugate function
'	differentiation with respect to the argument

the state of the lubricant, one may view the EHD-process as a reasonable method for examining the behavior of fluids under high pressures.

B. Problem Statement

As stated previously, the surface tractions*, to which the elastic components of the system are subjected, are caused by the EHD generated pressure field in the thin film separating the solid components of the system. Since the region of the solid elements over which the EHD pressure is acting has dimensions which are very small by comparison to the dimensions of the solid, and furthermore the thickness of the fluid film is orders of magnitude less than its EHD-zone length, it is reasonable to assume that the variation of the EHD-pressure across the thickness of the film is negligible.

Under these circumstances the surface tractions acting on either of the two solid bodies separated by the fluid film are identical, Figures V.1 and V.2. Consequently, the problem under consideration, namely the determination of the pressure distribution in the EHD film, may be decomposed into three simpler problems.

(i) The determination of the displacement field of the first solid body subjected to the EHD-generated pressure field over a region of its surface of the order of magnitude of the EHD-zone.

(ii) The determination of the displacement field of the second solid body subjected to the same pressure field over the same region as the first solid body.

*Surface tractions are the force distributions on the surface of the solid body.

(iii) The calculation of the film thickness as a function of position for a given pressure distribution. This task may be accomplished from the determination of the displacement fields of problems (i) and (ii), the undeformed geometry of the elastic bodies, their normal approach and the total load transmitted across the film. The resulting relationships contain the film thickness and the EHD generated pressure intensity as dependent functions. The complete mathematical description of the EHD problem can be accomplished by deriving the appropriate field equations for the fluid film from the conservation equations of fluid mechanics. However, the coupling of the pressure field with the film thickness and consequently with the elastic displacements makes the resulting equation almost intractable. However, experimental techniques have been developed which make it possible to measure the fluid film thickness in an EHD process. Thus, assuming the availability of film thickness information, the complex complete mathematical problem may be bypassed in favor of the following simpler problem: the calculation of the pressure field in terms of the fluid film thickness. The resulting mathematical problem is much simpler than the complete one associated with the EHD process.

In this investigation an EHD line contact is considered. Hence the elastic bodies bounding the film are either parallel cylinders or a cylinder and a plate. Section C contains the formulation of the boundary value problem of an elastic cylinder subjected to surface tractions over a small portion of its curved boundary, and the determination of the associated displacement field as a function of the EHD-generated pressure field. In Section D the deflection of a

thick plate subjected to normal loading is examined by approximating the plate by the elastic half-space and subjecting it to the same surface tractions employed in Section C. In Sections C and D it is assumed that the length of the cylinder is large enough so that the edge effects may be neglected and that the geometry of the bodies as well as the pressure distribution variations along the axial direction are sufficiently small to be ignored. With the adoption of these assumptions the elastic deformation problem reduces to one of plane elasticity and the complex function approach is employed. The coupling between the pressure distribution and the known film thickness is accomplished in Section E.

The first phase of the problem is approached as a boundary value problem of the first kind (Sections C and D). The result of the first phase is a relationship between the surface tractions and the film thickness. The measured film thickness is then employed in the second phase of the analysis to calculate the pressure distribution (Section E). The numerical approach and its consequences are discussed in Section F. The influence of errors in the measurements of the film thickness on the pressure distribution and the method of minimizing their effect is also presented in Section F. Finally Section G deals with test cases for the evaluation of the whole analytic and numerical approach.

C. The Displacement Solutions - The Cylinder

In this section, the complex representation of the theory of plane elasticity is employed [64,65], for the purpose of formulating the solutions of an elastic cylinder under surface tractions. The surface tractions are assumed independent of the axial direction and the body

forces are ignored. Under these conditions, the stress tensor field and the associated displacement vector field may be represented in terms of two complex holonomic functions [66,67] by

$$\tau_{xx} + \tau_{yy} = 2[\Phi'(z) + \overline{\Phi'(z)}] \quad (C.1)$$

$$\tau_{yy} - \tau_{xx} + 2i\tau_{xy} = 2[\bar{z}\Phi''(z) + \Psi'(z)] \quad (C.2)$$

$$2\mu(u + iv) = \left(\frac{\lambda+3\mu}{\lambda+\mu}\right) \Phi(z) - \overline{z\Phi'(z)} - \overline{\Psi(z)} \quad (C.3)$$

where ' implies differentiation with respect to the argument, — denotes the complex conjugate function, and λ, μ are the Lamé elastic constants.

In the case of an elastic cylinder under surface forces $F_x + iF_y$, the functions $\Phi(z)$ and $\Psi(z)$ are found to be

$$\Phi(z) = \frac{1}{2\pi i} \int \frac{f d\xi}{\xi - z} - \frac{1}{2\pi i} \int \frac{f d\xi}{\xi} - \bar{a} r_0 z \quad (C.4)$$

$$\Psi(z) = \frac{1}{2\pi i} \int \frac{\bar{f} d\xi}{\xi - z} - \frac{1}{z} \Phi'(z) + \frac{a}{z} \quad (C.5)$$

where

$$a = \bar{a} = \Phi'(0)$$

$$f = i \int_{\Gamma} (F_x + iF_y) ds \quad (C.6)$$

If the surface forces consist of n concentrated forces applied at points of the circumference z_k , the stress functions assume the form,

$$\Phi(z) = \frac{1}{4\pi} \sum_{k=1}^n (F_{kx} + iF_{ky}) [2\ln(z_k - z) - z\bar{z}_k] \quad (C.7)$$

$$\Psi(z) = \frac{1}{2\pi} \sum_{k=1}^n \left[(F_{kx} - iF_{ky}) \ln(z_k - z) - (F_{kx} + iF_{ky}) \frac{\bar{z}_k}{z_k - z} \right] \quad (C.8)$$

Employing the above function for the particular case of a pair of equal and opposite forces, parallel to the real axis, acting at $z_1 = r_0 e^{i\alpha}$, $z_2 = r_0 e^{i(\pi-\alpha)}$, one obtains

$$\Phi(z) = \frac{p}{2\pi} \left\{ \ln \frac{z_1 - z}{z_2 - z} + \frac{\bar{z}_1 - \bar{z}_2}{2r_0^2} z \right\} \quad (C.9)$$

$$\Psi(z) = -\frac{p}{2\pi} \left\{ \ln \frac{z_1 - z}{z_2 - z} - \frac{\bar{z}_1}{z_1 - z} + \frac{\bar{z}_2}{z_2 - z} \right\} \quad (C.10)$$

with the associated displacement field

$$u = -\frac{p}{4\pi\mu} \left\{ \frac{2(\lambda+2\mu)}{\lambda+\mu} \ln \frac{r_2}{r_1} + \cos 2\theta_1 - \cos 2\theta_2 - \left(\frac{2\mu}{\lambda+\mu} \right) \frac{x}{r_0} \cos \alpha \right\} \quad (C.11)$$

$$v = -\frac{p}{4\pi\mu} \left\{ \left(\frac{2\mu}{\lambda+\mu} \right) (\theta_1 + \theta_2) - \sin 2\theta_1 - \sin 2\theta_2 - \left(\frac{2\mu}{\lambda+\mu} \right) \frac{y}{r_0} \cos \alpha \right\} \quad (C.12)$$

with $p = F_2 = F_1$ and (r_1, θ_1) , (r_2, θ_2) signifying the location of an arbitrary interior point z of the cylinder relative to the points of application of the surface forces. The displacement field at any point on the surface may now be expressed in terms of the intensity of the load, p , the location of its application, (r_0, α) and the arbitrary point on the surface $Q(r_0, \beta)$

$$u(\beta; \alpha) = - \frac{\lambda + 2\mu}{2\pi(\lambda + \mu)\mu} p \left\{ \ln \frac{\cos \frac{1}{2}(\alpha + \beta)}{\sin \frac{1}{2}(\alpha - \beta)} - \cos \alpha \cos \beta \right\} \quad (C.13)$$

$$v(\beta; \alpha) = - \frac{p}{2\pi(\lambda + \mu)\mu} \left\{ \mu \left(\alpha + \frac{\pi}{2} \right) + \lambda \cos \alpha \sin \beta \right\} \quad (C.14)$$

This solution forms the basis for the subsequent development of the problem and is referred to as solution $[B_1]$. The displacement field $[B_1]$ may be expanded by means of Green's method, to yield the displacement field corresponding to an arbitrarily distributed surface loading of intensity $p(\alpha)$.

In this work, however, the following procedure is adopted. Let $[S_{22}]$ denote the solution corresponding to surface loading symmetric with respect to the x- and y-axes, and $[S_{12}]$ denote the solution corresponding to loading antisymmetric with respect to the x-axis and symmetric with respect to the y-axis. Consequently the sought solution, $[A]$, corresponding to the arbitrarily distributed surface loading is given by

$$[A] = a_1[S_{12}] + a_2[S_{22}] \quad (C.15)$$

with a_1, a_2 being constants and letters in brackets refer to the stress tensor or displacement vector fields associated with this particular solution.

Solutions $[S_{12}]$ and $[S_{22}]$ are subsequently generated by using the "basic" solution $[B_1]$ and employing Green's method with the appropriate choice of loading functions $p(\alpha)$.

1. The Symmetric Solution. $[S_{22}]$

Let two pairs of equal and opposite forces, parallel to the x-axis,

act at points z_1, z_2, z_3 and z_4 of the surface of the cylinder, with the points of application chosen in such a manner as to make the loading symmetric with respect to the x and y-axes. The displacement field associated with this loading is easily obtained from the basic solution $[B_1]$, Figure (V-3a)

$$u(\beta; \alpha) = + \frac{\lambda+2\mu}{2\pi(\lambda+\mu)\mu} p \left\{ \ell n \tan \frac{1}{2} |\alpha + \beta| + \ell n \tan \frac{1}{2} |\alpha - \beta| + 2 \cos \alpha \cos \beta \right\} \quad (C.16)$$

$$v(\beta; \alpha) = - \frac{p}{\pi(\lambda+\mu)} (\pi + 2\alpha) \quad (C.17)$$

The displacement field for distributed loading $p(\alpha)$ over an arc $(-\alpha_0, \alpha_0)$, which adheres to the symmetry imposed in this section, is

$$u(\beta) = \frac{\lambda+2\mu}{\pi(\lambda+\mu)\mu} \int_0^{\alpha_0} p(\alpha) \left\{ \ell n \tan \frac{1}{2} (\alpha + \beta) + \ell n \tan \frac{1}{2} (\alpha - \beta) + 2 \cos \alpha \cos \beta \right\} r_0 d\alpha \quad (C.18)$$

$$v(\beta) = - \frac{1}{\pi(\lambda+\mu)} \int_0^{\alpha_0} p(\alpha) (\pi + 2\alpha) r_0 d\alpha \quad (C.19)$$

Since the intensity $p(\alpha)$ is symmetric with respect to the x-axis, which is the $\alpha = 0$ ray, then $p(\alpha) = p(-\alpha)$. Hence it renders itself to the following representation

$$p(\alpha) = \sum_{n=0}^{\infty} p_n \cos \left(\frac{2n+1}{2\alpha_0} \pi \alpha \right) \quad (C.20)$$

which, in conjunction of Eqs. (C.18) and (C.19) and along with the assumption that the angles α_0 and β are small and the introduction [68,69] of

$$q_n = \frac{2n+1}{2} \pi ; \quad \tilde{\beta} = \frac{\beta}{\alpha_0} \quad (C.21)$$

$$S(0, k\theta) = \int_0^\theta \frac{\sin kx}{x} dx ; \quad C(0, k\theta) = \int_0^\theta \frac{1 - \cos kx}{x} dx$$

yields the displacement field

$$[S_{22}]: \quad u(\beta) = \sum_{n=0}^{\infty} p_n U_n(\beta; \alpha_0) \quad (C.22)$$

$$v(\beta) = \sum_{n=0}^{\infty} p_n V_n(\beta; \alpha_0) \quad (C.23)$$

where

$$U_n(\beta; \alpha_0) = \frac{(\lambda+2\mu)r_0}{\mu(\lambda+\mu)\pi} \left\{ \frac{q_n \alpha_0}{q_n^2 + \alpha_0^2} \sin q_n \cos \alpha_0 \cos \beta \right. \\ + \left(\frac{\alpha_0}{q_n} \right) \left[\sin q_n \left[\ln(1+\tilde{\beta}) + \ln(1-\tilde{\beta}) + 2 \ln \frac{\alpha_0}{2} \right] \right. \\ + \sin q_n \tilde{\beta} \left[\ln(1+\tilde{\beta}) - \ln(1-\tilde{\beta}) + C(0, q_n(1-\tilde{\beta})) \right. \\ \left. \left. - C(0, q_n(1+\tilde{\beta})) \right] - \cos q_n \tilde{\beta} \left[S(0, q_n(1-\tilde{\beta})) + S(0, q_n(1+\tilde{\beta})) \right] \right] \left. \right\} \quad (C.24)$$

$$v_n(\beta, \alpha_0) = - \frac{r_0 \alpha_0}{\pi(\lambda + \mu)} \left\{ (2\alpha_0 + \pi) \frac{\sin q_n \tilde{\beta}}{q_n} - \frac{\alpha_0}{2} \right\} \quad (C.25)$$

2. The Antisymmetric Solution, $[S_{12}]$

The loading in this case consists of two pairs of equal and opposite forces parallel to the x-axis, the $\alpha = 0$ ray. The first pair acts at the points $z_1 = r_0 e^{i\alpha}$ and $z_2 = r_0 e^{i(\pi-\alpha)}$ respectively, while the second pair acts at $z_3 = r_0 e^{-i\alpha}$ and $z_4 = r_0 e^{i(\pi+\alpha)}$ and has its sense reversed with respect to the first pair. Thus the loading is antisymmetric with respect to the x-axis and symmetric with respect to the y-axis (Figure V-3b). Taking advantage of the basic solution $[B_1]$, the displacement field associated with this type loading is found to be

$$u(\beta; \alpha) = \frac{\lambda + 2\mu}{2\pi(\lambda + \mu)\mu} p \ln \left| \frac{\sin(\alpha + \beta)}{\sin(\alpha - \beta)} \right| \quad (C.26)$$

$$v(\beta; \alpha) = - \frac{\lambda}{\pi(\lambda + \mu)\mu} p \cos \alpha \sin \beta \quad (C.27)$$

Subsequently the displacement field for distributed loading over an arc $(-\alpha_0, \alpha_0)$, with $p(\alpha) = -p(-\alpha)$ is simply

$$u(\beta) = \frac{\lambda + 2\mu}{2\pi(\lambda + \mu)\mu} \int_0^{\alpha_0} p(\alpha) \ln \left| \frac{\sin(\alpha + \beta)}{\sin(\alpha - \beta)} \right| r_1 d\alpha \quad (C.28)$$

$$v(\beta) = - \frac{\lambda}{\pi(\lambda + \mu)\mu} \int_0^{\alpha_0} p(\alpha) \cos \alpha \cos \beta r_0 d\alpha \quad (C.29)$$

With the loading intensity $p(\alpha)$ being antisymmetric with α , its expansion is of the form

$$p(\alpha) = \sum_{n=1}^{\infty} p_n \sin \frac{n\pi\alpha}{\alpha_0} \quad (C.30)$$

Substitution of Eq. (C.30) into Eqs. (C.28) and (C.29), and adopting the notation introduced by Eqs. (C.21) along with assumption that α_0 and β are small, yields the results

$$[S_{12}]: \quad u(\beta) = \sum_{n=1}^{\infty} p_n U_n(\beta; \alpha_0) \quad (C.31)$$

$$v(\beta) = \sum_{n=1}^{\infty} p_n V_n(\beta; \alpha_0) \quad (C.32)$$

where

$$\begin{aligned} U_n(\beta; \alpha_0) = & \frac{(\lambda+2\mu)r_0}{2\pi(\lambda+\mu)\mu} \left(\frac{\alpha_0}{q_n} \right) \{ \cos q_n [\ell n(\tilde{\beta}-1) - \ell n(\tilde{\beta}+1)] + (\cos q_n \\ & + \cos q_n \tilde{\beta}) [\ell n(\tilde{\beta}+1) - \ell n(\tilde{\beta}-1) - C(0, q_n(\tilde{\beta}-1)) - C(0, q_n(\tilde{\beta}+1))] \\ & + (\sin q_n \tilde{\beta}) [S(0, q_n(1+\tilde{\beta})) - S(0, q_n(1-\tilde{\beta}))] \} \end{aligned} \quad (C.33)$$

$$V_n(\beta; \alpha_0) = - \frac{\lambda r_0}{\pi(\lambda+\mu)\mu} \left(\frac{q_n}{2 + \alpha_0^2} \sin q_n \right) \cos \alpha_0 \sin \tilde{\beta} \quad (C.34)$$

with $q_n = n\pi$.

3. The General Solution

The displacement field corresponding to an arbitrary pressure distribution is obtained by employing the solutions $[S_{22}]$ and $[S_{12}]$.

Its form is as follows

$$u(\beta) = \sum_{n=0}^{\infty} \left\{ p_n^{(s)} U_n^{(s)}(\beta; \alpha_o) + p_n^{(a)} U_n^{(a)}(\beta; \alpha_o) \right\} \quad (C.35)$$

$$v(\beta) = \sum_{n=0}^{\infty} \left\{ p_n^{(s)} V_n^{(s)}(\beta; \alpha_o) + p_n^{(a)} V_n^{(a)}(\beta; \alpha_o) \right\} \quad (C.36)$$

where superscript (s) refers to the displacement field associated with the symmetric solution $[S_{22}]$, and superscript (a) refers to the displacement field associated with the antisymmetric solution $[S_{12}]$.

D. The Displacement Solutions - The Half-Space

If one of the solid bodies that bounds the EHD zone from above or below is a thick elastic plate, whose dimensions are large by comparison to the EHD zone, then the elastic response of the plate can be represented reasonably by that of the elastic half space. If, furthermore, the other body is a sufficiently long elastic cylinder it can be assumed that the EHD-generated pressure is independent of the coordinate along the axis of the cylinder. Under these circumstances, the thick elastic plate can be substituted by the elastic half-plane. It is this case that is considered in this section and this is consistent with the formulation of the problem of section C.

Again, as in the previous section, the displacement field may be expressed [66] in terms of two complex functions $\phi(z)$ and $\psi(z)$ by

$$2\mu(u + iv) = \left(\frac{\lambda+3\mu}{\lambda+\mu} \right) \phi(z) - z\phi'(z) - \psi(z) \quad (D.1)$$

If the loading over the force boundary is

$$\begin{aligned}\tau_{yy} &= p(x) \\ \tau_{xy} &= \sigma(x)\end{aligned}\quad \text{for } x \in [-a, a] \quad (D.2)$$

it can be shown [66] that the stress functions $\phi(z)$ and $\psi(z)$ are

$$\phi(z) = -\frac{1}{2\pi} \int (\sigma + ip) \ln(t - z) dt \quad (D.3)$$

$$\psi(z) = -\frac{z}{2\pi} \int (\sigma + ip) \frac{dt}{t-z} + \frac{1}{2\pi} \int (\sigma - ip) \ln(t - z) dt \quad (D.4)$$

and the displacement field becomes

$$\begin{aligned}4\pi\mu(u + iv) &= - \int (\sigma + ip) \left[\left(\frac{\lambda+3\mu}{\lambda+\mu} \right) \ln(t-z) + \ln(t-\bar{z}) \right] dt \\ &\quad - (z-\bar{z}) \int (\sigma - ip) \frac{dt}{t-\bar{z}}\end{aligned} \quad (D.5)$$

In this problem it is assumed that the tangential surface tractions are negligible ($\sigma = 0$), thus the displacement eq. (D.5) reduces to

$$\begin{aligned}4\pi\mu(u + iv) &= -i \int_{-a}^a p(t) \left[\left(\frac{\lambda+3\mu}{\lambda+\mu} \right) \ln(t-z) + \ln(t-\bar{z}) \right] dt \\ &\quad + i(z-\bar{z}) \int_{-a}^a p(t) \frac{dt}{(t-\bar{z})}\end{aligned} \quad (D.6)$$

Because any arbitrary loading function $p(x)$ can be expressed as a sum of a symmetric and an antisymmetric component, the corresponding displacement field may be given as a combination of displacements corresponding to symmetric and antisymmetric solutions

$$[H] = a[H_{01}] + b[H_{02}]$$

1. The Symmetric Solution, $[H_{02}]$

Assuming that $p(x) = p(-x)$, $p(x)$ may be expanded in the form,

Figure V-4a

$$p(t) = \sum_{n=1}^{\infty} h_m \cos \frac{m\pi t}{a} \quad m = \frac{2n+1}{2}, \quad n \in J \quad (D.7)$$

And the displacement becomes

$$\begin{aligned} 4\pi\mu(v - iu) = & - \left(\frac{\lambda+3\mu}{\lambda+\mu} \right) \sum_{n=1}^{\infty} h_m \int_{-a}^a \left(\cos \frac{m\pi t}{a} \right) \ln(t-z) dt \\ & - \sum_{n=1}^{\infty} h_m \int_{-a}^a \left(\cos \frac{m\pi t}{a} \right) \ln(t-\bar{z}) dt \\ & + 2iy \sum_{n=1}^{\infty} h_m \int_{-a}^a \left(\cos \frac{m\pi t}{a} \right) \frac{dt}{(t-\bar{z})} \end{aligned} \quad (D.8)$$

Eq. (D.8), after some calculations and evaluating at $y = 0$, the free surface, yields

$$4\pi\mu u = - \sum_{n=1}^{\infty} a h_m \left\{ (\theta_1 + \theta_2) \sin q_m - \left(\frac{2\mu}{\lambda+\mu} \right) \frac{1}{q_m} (\theta_1 - \theta_2) \sin q_m \xi \right\} \quad (D.9)$$

$$4\pi\mu v = - \sum_{n=1}^{\infty} \frac{2a}{q_m} h_m \left(\frac{\lambda+2\mu}{\lambda+\mu} \right) \left\{ (\sin q_m) \ln r_1 r_2 \right.$$

$$\begin{aligned}
& - (\sin q_m \xi) \left[\ln \frac{r_1}{r_2} + C(0, q_m(1+\xi)) - C(0, q_m(1-\xi)) \right] \\
& - (\cos q_m \xi) [S(0, q_m(1+\xi)) + S(0, q_m(1-\xi))] \}
\end{aligned} \tag{D.10}$$

where

$$\theta_1 + \theta_2 = \begin{cases} 0 & \text{for } x > a \\ \pi & \text{for } a > x > -a \\ 2\pi & \text{for } x < -a \end{cases} \tag{D.11}$$

$$\xi = \frac{x}{a}, \quad r_1 = a - x, \quad r_2 = a + x \tag{D.12}$$

$$q_m = m\pi = \frac{2n+1}{2} \pi \quad \text{as in section C.}$$

2. The Antisymmetric Solution - $[H_{01}]$

The antisymmetric solution is characterized by Figure V-4b,

$$p(x) = -p(-x)$$

and consequently submits to the representation

$$p(x) = \sum_{m=1}^{\infty} h_m \sin \frac{m\pi x}{a} \quad m \in J \tag{D.13}$$

Substitution of eq. (D.13) into eq. (D.6) yields

$$\begin{aligned}
4\pi\mu(v - iu) = & - \left(\frac{\lambda+3\mu}{\lambda+\mu} \right) \sum_{m=1}^{\infty} h_m \int_{-a}^a \left(\sin \frac{m\pi t}{a} \right) \ln(t-z) dt \\
& - \sum_{m=1}^{\infty} h_m \int_{-a}^a \left(\sin \frac{m\pi t}{a} \right) \ln(t-\bar{z}) dt \\
& + 2iy \sum_{m=1}^{\infty} h_m \int_{-a}^a \left(\sin \frac{m\pi t}{a} \right) \frac{dt}{(t-\bar{z})}
\end{aligned} \tag{D.14}$$

Performing the indicated operations in eq. (D.14) and evaluating at $y = 0$, the displacement field at the free surface corresponding to the antisymmetric loading becomes

$$4\pi\mu u = - \sum_{m=1}^{\infty} h_m \left\{ \frac{a}{q_m} \left(\frac{2\mu}{\lambda+\mu} \right) (\cos q_m \xi - \cos q_m) (\theta_1 - \theta_2) \right\} \tag{D.15}$$

$$\begin{aligned}
4\pi\mu v = & - \sum_{m=1}^{\infty} h_m \frac{2a}{q_m} \left(\frac{\lambda+2\mu}{\lambda+\mu} \right) \left\{ (\cos q_m \xi - \cos q_m) \ln \frac{r_1}{r_2} \right. \\
& + \cos q_m \xi [C(0, q_m(1+\xi)) - C(0, q_m(1-\xi))] \\
& \left. - \sin q_m \xi [S(0, q_m(1+\xi)) + S(0, q_m(1-\xi))] \right\}
\end{aligned} \tag{D.16}$$

3. The General Solution - [H]

The displacement field corresponding to an arbitrary pressure distribution in $x \in [-a, a]$ is generated from the linear combinations of $[H_{02}]$ and $[H_{01}]$. Thus

$$[H]: \quad u(\xi) = \sum_{n=0}^{\infty} (h_m^{(s)} U_m^{(s)} + h_m^{(a)} U_m^{(a)}) \quad (D.17)$$

$$v(\xi) = \sum_{n=0}^{\infty} (h_m^{(s)} V_m^{(s)} + h_m^{(a)} V_m^{(a)}) \quad (D.18)$$

where $h_m^{(s)}$ is the pressure coefficient corresponding to the symmetric loading, while $h_m^{(a)}$ is the pressure coefficient associated with the anti-symmetric loading, and

$$U_m^{(s)} = -\frac{a}{4\pi\mu} \left\{ (\theta_1 + \theta_2) \sin q_{ms} - \frac{2\mu}{(\lambda+\mu)q_{ms}} (\theta_1 - \theta_2) \sin q_{ms} \xi \right\} \quad (D.19)$$

$$\begin{aligned} V_m^{(s)} = & -\frac{a(\lambda+2\mu)}{2\pi q_{ms} \mu(\lambda+\mu)} \left\{ (\sin q_{ms}) \ln r_1 r_2 \right. \\ & - (\sin q_{ms} \xi) \left[\ln \frac{r_1}{r_2} + C(0, q_{ms}(1+\xi)) - C(0, q_{ms}(1-\xi)) \right] \\ & \left. - (\cos q_{ms} \xi) [S(0, q_{ms}(1+\xi)) + S(0, q_{ms}(1-\xi))] \right\} \quad (D.20) \end{aligned}$$

$$U_m^{(a)} = -\frac{a}{2\pi q_{ma}(\lambda+\mu)} (\cos q_{ma} \xi - \cos q_{ma}) (\theta_1 - \theta_2) \quad (D.21)$$

$$\begin{aligned} V_m^{(a)} = & -\frac{a(\lambda+2\mu)}{2\pi q_{ma}(\lambda+\mu)} \left\{ (\cos q_{ma} \xi - \cos q_{ma}) \ln \frac{r_1}{r_2} \right. \\ & + \cos q_{ma} \xi [C(0, q_{ma}(1+\xi)) - C(0, q_{ma}(1-\xi))] \\ & \left. - \sin q_{ma} \xi [S(0, q_{ma}(1+\xi)) + S(0, q_{ma}(1-\xi))] \right\} \quad (D.22) \end{aligned}$$

and

$$q_{ms} = m\pi = \frac{2n+1}{2} \pi$$

$$n \in J$$

$$q_{ma} = m\pi = n\pi$$

E. The Pressure Distribution in the EHD Zone

If the film thickness in the EHD contact is known from measurements, and the elastic properties and geometric characteristics of the solid bodies are known, it is possible to calculate the pressure distribution in the EHD zone. The film thickness may be expressed as

$$h(x, p(x)) = h_o(x) - \gamma(P) + u_1(x, p(x)) + u_2(x, p(x)) \quad (E.1)$$

where $h(x, p(x))$ is the film thickness; $h_o(x)$ is the film thickness in the undeformed state when the bodies are touching; $\gamma(P)$ is the normal approach of the solid bodies; and u_1 and u_2 are the displacements of the surface of the solid bodies at the EHD zone. The film thickness and the displacements are functions of position and of pressure distribution. The film thickness is known from measurements, and $h_o(x)$ may be calculated from the geometry of the undeformed solid surfaces. In the previous two sections, expressions have been derived that give u_1 and u_2 explicitly in terms of position and the Fourier coefficients of the pressure distribution. It remains, then, to determine the normal approach $\gamma(P)$ and the pressure coefficients.

Specifically, since at any point A in the contact zone or its near neighborhood the film thickness is known, then

$$h(x_A, p(x)) = h_o(x_A) - \gamma(P) + u_1(x_A, p(x)) + u_2(x_A, p(x)) \quad (E.2)$$

where

$$u_1(x_A, p(x)) = \sum_{n=0}^{N-1} p_n^{(s)} U_{1n}^{(s)} + \sum_{m=1}^M p_m^{(a)} U_{1m}^{(a)} \quad (E.3)$$

$$u_2(x_A, p(x)) = \sum_{n=0}^{N-1} p_n^{(s)} U_{2n}^{(s)} + \sum_{m=1}^M p_m^{(a)} U_{2m}^{(a)} \quad (E.4)$$

$U_{1n}^{(s)}$, $U_{1m}^{(a)}$, $U_{2n}^{(s)}$, $U_{2m}^{(a)}$ are the symmetric and antisymmetric coefficients of the deformations of bodies 1 and 2 respectively, corresponding to a pressure distribution of the form

$$p = \sum_{n=0}^{N-1} p_n^{(s)} \cos \frac{2n+1}{2a} \pi x + \sum_{m=1}^M p_m^{(a)} \sin \frac{m\pi}{a} x \quad (E.5)$$

Further information is obtained by observing that the total pressure acting on either of the solid surfaces is equal to the applied load thus

$$P = \int_{-a}^a p(x) dx \quad (E.6)$$

If the film thickness is known at $(N + M)$ points, there are $(N + M + 1)$ equations available $((N + M)$ of the form of Equation (E.2), plus equation (E.6)) to determine the $(N + M + 1)$ unknowns $\gamma(P)$, $p_n^{(s)}$, and $p_m^{(a)}$. The pressure distribution in the EHD zone is then known from equation (E.5).

It is apparent that if the EHD zone is bounded by two cylinders, both u_1 and u_2 will be given by equation (C.35). If one of the boundary

surfaces is a cylinder and the other is a plate, u_1 is obtained from equation (C.35) and u_2 from equation (D.18). The latter case is the one which will be dealt with in the following discussion; treatment of the case of two cylinders is analogous.

Figure V-5 shows the conjunction of the cylinder and the plate. The pressure zone extends from $x = -a$ to $x = a$, and $\beta = -\alpha_0$ to $\beta = \alpha_0$. Because α_0 is very small, $a = r_0 \alpha_0$, and $x = r_0 \beta$. Since the location of the point $x = 0$ is the midpoint of the pressure distribution, it is necessary to specify the points at which the pressure goes to zero (i.e. the inlet and outlet points) in order to determine the location of $x = 0$ and the value of a . An ad hoc procedure for determining these points is discussed in a later section. It should be noted that the origin of the x coordinate in this analysis in general is not the center of the dry Hertzian contact.

F. Numerical Considerations

As developed in the previous section, the problem of determining the pressure distribution in the EHD zone reduces to the problem of solving a set of algebraic equations for the Fourier coefficients of the pressure. Since equations (C.35) and (D.18) for the displacement of the solid surfaces are linear in these coefficients, the set of algebraic equations to be solved is linear. In order to avoid an ill-conditioned numerical system of equations, equation (E.2) is solved for the total displacement,

$$u_1(x_A, p) + u_2(x_A, p) = h(x_A, p) - h_0(x_A) + \gamma(p) \quad A = 1, 2, \dots, n \quad (F.1)$$

where the left-hand side is expressed in terms of the Fourier coefficients

p_i , $i = 1, 2, \dots, m$ by equations (E.3) and (E.4). A trial value of $\gamma(P)$ is assumed, and when $m = n$ the system (F.1) may be solved for p_i . Equation (E.6) is then evaluated to see if the total load condition is satisfied. If not, a different value for γ is selected and the process repeated. Since the system is linear, two iterations are required to find the true value of γ . Because only the right-hand side of equation (F.1) is affected by changing γ , very little extra work is incurred by this iteration scheme. If the film thickness measurements were known to be exact, the film thickness at m points would be sufficient to determine the Fourier coefficients. However, due to unavoidable inaccuracies in the measurements, certain modifications to the solution of the equations must be made.

Since the measurements at each point in the EHD zone are in error, the total error increases as the number of points used, n , increases. At the same time, a sufficient number of points must be used to adequately characterize the shape of the film thickness profile. Furthermore, the number m of Fourier coefficients to be found must be large enough that the truncated Fourier series, equation (E.5) (with $m = N + M$) may accurately represent the true pressure. To alleviate this problem, n and m are chosen, with $n > m$, and the following process used to "smooth out" the errors in the film thickness. The algebraic equations take the form

$$a_{ij} p_j = b_i \quad i = 1, 2, \dots, n, \quad j = 1, 2, \dots, m \quad (F.2)$$

where p_i are the unknown coefficients. Equation (F.2) represents an overdetermined system (that is, there are more equations than unknowns)

for which, in general, there is no exact solution. Accordingly, the residual, r_i , is defined as

$$a_{ij}p_j - b_i = r_i \quad (F.3)$$

The unknowns p_j are then determined so as to minimize the sum of the squares of the residuals, $r_i r_i$. This results in a system of m linear equations [70]. The minimization of the residuals has the effect of smoothing the data while coming as close as possible to solving equations (F.2), recognizing the fact that the data is a best estimate to the true film thickness. The amount of smoothing depends on the degree to which n is greater than m . If the Fourier series for the pressure is to converge to the true pressure, the coefficients must eventually go to zero as m is increased. Once n is selected, the amount of smoothing required is determined by increasing n until the Fourier coefficients begin to increase, causing the series to diverge. As a check on the acceptability of the result the magnitudes of the residuals may be compared to the expected error in film thickness measurements.

It should be noted that the calculations for the pressure are based on the displacement of the surfaces from their undeformed states, rather than on the film thickness itself. From equation (E.1), assuming $h_0(x)$ and $\gamma(P)$ may be found precisely, the magnitude of the error in total displacement, $u_1 + u_2$, is the same as that for the film thickness. Consequently, near the center of the contact where the film thickness is small and the surface deformation is large, a small relative error in film thickness results in a smaller relative error in the displacement. Therefore, the pressure calculated in the part of the

contact where deformations are large is expected to be quite accurate. On the other hand, in the inlet region where the pressure is building up gradually from zero, the film thickness is large due to the initial surface geometry while the displacements are small because of the lower pressure. Hence, a small relative error in film thickness in the inlet region may result in a large relative error in the displacement, so that the pressure calculated in this region is somewhat less reliable. Thus it is often helpful to introduce additional information in this area by requiring that the pressure gradient at $x = -a$ vanish. This is a consequence of the fact that the pressure is generated by the hydrodynamic action of the fluid, and has the effect of introducing an additional equation into the set to be solved. This procedure tends to offset somewhat the increased effect of errors in the inlet region.

Because of the method by which pressures are calculated, an error in film thickness which is constant in magnitude throughout the entire EHD zone has no effect on the computations. Such an error has the character of a rigid-body translation of one of the solid surfaces, and would therefore be absorbed in the normal approach term (γ) of equation (E.1), leaving the displacement and hence the pressure unaffected. Consequently the range of errors encountered, rather than their magnitude, determines the accuracy of the calculated pressure distribution.

G. Test Cases and Evaluation

In order to test the procedures described in the previous section, and to evaluate the effects of certain types of errors in the input data, a number of test cases were run. In the first case,

the following pressure distribution was employed

$$p(\hat{x}) = \begin{cases} 0 & \hat{x} \leq -x_0 \\ p_0 & -x_0 < \hat{x} < x_0 \\ 0 & \hat{x} \geq x_0 \end{cases} \quad (G.1)$$

where $\hat{x} = 0$ is the contact point of the undeformed surfaces. Closed-form solutions for the displacements of the cylinder and the plate for the pressure distribution were found from equations (C.13) and (D.6). These displacements were then used as film thickness data to obtain a series expression for the pressure of the form of equation (E.5), which could be evaluated by comparison with equation (G.1). The calculated pressure curve which resulted is shown in Figure V-6, which represents equation (E.5) with 10 terms, and $a = 1.3 x_0$. The major disagreement with equation (G.1) occurs near $\hat{x} = \pm x_0$ where the pressure is discontinuous; this is to be expected due to the nature of the series, and is not a serious drawback, since pressure discontinuities are not expected in a film. The selection of $a = 1.3 x_0$ results in small negative pressures near the inlet and outlet. This will be discussed later in this section in more detail.

As a second case, the film thickness was taken as zero over the region $-x_0 < \hat{x} < +x_0$; this is the case of two dry bodies in contact over the region, for which the pressure distribution should approximate the Hertzian semi-elliptical distribution. The results are shown in Figure V-7 for nine terms in the series of equation (E.5), with a and $x = 0$ chosen so that the pressure is zero at $\hat{x} = -1.33 x_0$ and $\hat{x} = 1.1 x_0$.

The agreement is good except near $\hat{x} = \pm x_0$, where there is a discontinuity in the pressure gradient. In the presence of such a discontinuity, inaccuracy in the series expansion is to be expected, since equation (E.5) implies continuous derivatives.

A third test case was examined using a pressure distribution expressed by a third-degree polynomial, shown in Figure V-8. As in the first case, a closed-form expression for the displacement of the surfaces was obtainable, and the resulting film thickness profile is also shown in Figure V-8. The values of the total load, elastic constants of the surfaces, cylinder dimensions, and minimum film thickness were selected so as to approximate those in an actual EHD contact [71]. The calculated film thickness was used to obtain a series solution for the pressure as described in the preceding section. When the inlet and outlet points ($x = \pm a$) were specified correctly, the series expression for the pressure showed negligible deviation from the polynomial expression throughout the contact. Because the pressure distribution of Figure V-8 in some ways resembles that expected in an EHD contact, this test case was examined further in order to study the effects of certain types of errors. It was estimated that, using the optical interference method of measuring film thickness, the maximum error in film thickness at a given location is $.025 \mu\text{m}$ ($1 \mu\text{in.}$). Accordingly, three sets of random errors in the range $(-.025, .025) \mu\text{m}$ were introduced into the film thickness data. This was a fairly severe test, because in actuality the errors would most likely be normally distributed, over the range $(-0.025, 0.025 \mu\text{m})$. The pressure distributions calculated from these three error sets are shown in Figure V-9.

Sets 1 and 3 show the largest errors on the side corresponding to the inlet of an EHD contact, as would be expected from the discussion of the previous section. The general shape of the pressure distribution is preserved in all three cases shown in the figure.

The effects of errors in location of the beginning and end of the pressure were also studied. The results of varying the point of zero pressure at the inlet of the EHD zone are shown in Figure V-10. When the inlet point is located too far in, a hump in the calculated pressure appears, and convergence of the series becomes somewhat slower. The presence of these conditions indicates that the inlet point should be moved farther out. When the inlet point was located too far out, the calculated pressure came in at zero up to the true inlet, and blended into the exact distribution almost immediately, resulting in negligible error. When the change in pressure near the inlet is more abrupt, as in Figure V-6, negative pressures may result if the inlet point is set too far out. Since the location of the point of zero pressure is not known ahead of time, these conclusions are helpful in locating the inlet point when calculating the pressure distribution. Similar conclusions may be drawn concerning the location of the outlet point; however, the determination of the location of this point in an actual EHD contact is generally less difficult, since it is known a priori that the pressure goes to zero in the vicinity of the exit constriction of the film.

In addition, small (3%) errors were introduced in the elastic constants, the total load, and the radius of the cylinder. The calculated pressure distribution was found to be relatively insensitive

($\sim 1\%$) to these errors in the elastic constants and the load, and somewhat more sensitive to errors in the radius. This is not a serious drawback, since the radius may be measured to a high degree of precision.

At present, accurate data for the film thickness in an actual EHD line contact are not available to us. Wymer and Cameron [71] show measured line contact film thickness profiles, but from their published figures it is possible to determine the film thickness only to within $2-3 \mu$ in. at a given location in the EHD zone. Nevertheless, a pressure distribution was calculated based on their measurements, and the results shown in Figure V-11 where it is compared with the Hertzian distribution. The figure also shows a comparison between the measured film thickness used as input for the calculations, and the film thickness which would result from the calculated pressure distribution. The difference between the two is the residual, which is quite large near the exit region, as shown in the figure. In this region, the magnitude of the slope of the film thickness profile is quite large, which increases the difficulty in reading the points from the figures. Because of the large residuals near the exit and the inaccuracy of the input data used, the pressure distribution of Figure V-11 should be viewed as a rather rough approximation. In spite of the lack of precise film thickness data for a line contact, accurate data is available for the EHD point contact. Most of the foregoing numerical methods and conclusions concerning probable errors are expected to carry over into this case.

H. Summary of Computational Method

If the film thickness is known from measurements at n points x_A , $A = 1, 2, \dots, n$, in the EHD zone, the set of n equations (F.1) is used

to find the Fourier coefficients of pressure as follows. The film thickness in the undeformed state is known at each point x_A , and an initial estimate for the normal approach $\gamma(P)$ is made. The right-hand side of equations (F.1) is then known. The displacements $u_1(x_A, p)$ and $u_2(x_A, p)$ are expressed in terms of the m unknown Fourier coefficients. The number of Fourier terms used (m) is arbitrary as long $m < n$. For the case of two cylinders, both u_1 and u_2 are given by equation (C.35); for the case of a cylinder and a plate, u_1 is given by equation (C.35) and u_2 by equation (D.18). Equation (F.1) is then a set of n equations in m unknowns. An additional equation is obtained from the requirement that the pressure gradient be zero at the inlet $\left(\frac{dp}{dx}\right)_{x=-a} = 0$ from equation (E.5)}. Because the system is overdetermined ($m < n + 1$) residuals are defined as in Equation F.3. The condition that the sum of the squares of the residuals be a minimum is applied, which results in a system of m equations in m unknowns. This system is solved for the m Fourier coefficients, for use in equation (E.5) for the pressure distribution. The total load P is calculated from equation (E.6), and the result compared with the known value of the load. If they are not the same, a new estimate is made for $\gamma(P)$, and the solution process is repeated. Once equation (E.6) is satisfied, the Fourier coefficients of pressure are known, and the pressure at any point in the EHD contact is determined from equation (E.5).

The calculations require knowledge of the film thickness at n locations in the EHD zone, the total load on the system, the elastic constants of the solid bodies, and the radii of the cylinders. In addition, the number of sine and cosine terms to be used in equation

(E.5) and the locations of the inlet and outlet points must be specified. On the following pages is a listing of the Fortran computer program for calculating the pressure distribution by the above method.

YJJJJJJ

77/02/11. 10.13.50.

GEORGIA TECH CYBER 74.

NOS 1.1-430

USER NUMBER: ME650AC

PASSWORD

TERMINAL: 77, TTY

RECOVER /SYSTEM: BATCH,50000

\$RFL,50000.

/GET,MLSDP

/LNH,F=MLSDP

PROGRAM EHD*(DAT,INPUT,OUTPUT,TAPE5=DAT,TAPE4=INPUT,TAPE6=OUTPUT)

C PROGRAM TO COMPUTE PRESSURE DISTRIBUTION FOR EHD LINE CONTACT

C FROM FILM THICKNESS DATA.

DIMENSION H(30),BETA1(30),BETA2(30),Q(30),A1(30,30),XT(30)

DIMENSION A2(30,30),AS(30,30),X(30),U(30),P(51),XIN(51),XTIN(51)

DIMENSION IPIVOT(30),D(30),SL(30,30),UIN(30)

DIMENSION UC(30),HC(30),RES(30)

REAL K1,K2

C PRELIMINARY DATA:

C SET IFLAG=0 FOR TWO CYLINDERS, =1 FOR CYLINDER + PLATE

C GAM: INITIAL GUESS FOR NORMAL APPROACH OF BODIES (M)

C F: TOTAL LOAD (N)

C M: NO. OF COS TERMS IN SERIES FOR PRESSURE

C N: NO. OF SIN TERMS IN SERIES FOR PRESSURE

C LI: NO. OF FILM THICKNESS DATA POINTS TO BE INPUT

C SP: DESIRED SPACING BETWEEN POINTS AT WHICH PRESSURE

C IS TO BE PRINTED OUT (M)

C X1,X2: INLET, OUTLET POINTS, MEASURED FROM POINT OF CONTACT

C IN UNDEFORMED STATE (M)

```

      READ(5,*) IFLAG, GAM, F
      READ(5,*) M, N, L1, SP
      READ(5,*) X1, Y2
      PI=4.*ATAN(1.)
      A=ABS((X1-X2)/2.)
      OFST=-(X1+X2)/2.
      NN=0
      MM=M-1
      L11=L1+1
      LL=M+N
C     FILM THICKNESS DATA:
C       X(I): DISTANCE OF I-TH DATA POINT FROM POINT OF CONTACT IN
C             UNDEFORMED STATE (M)
C       H(I): FILM THICKNESS AT X(I) (M)
      READ(5,*)(X(I),H(I),I=1,L1)
      DO 13 I=1,L1
      XT(I)=Y(I)+OFST
13  CONTINUE
C     DATA ON BODY 1 - CYLINDER:
C       YM1: MODULUS OF ELASTICITY (N/M**2)
C       PR1: POISSON'S RATIO
C       R1: RADIUS (M)
      READ(5,*) YM1, PR1, R1
      K1=2.*(1.-PR1*PR1)/(PI*YM1)
      ALP1=A/R1
      DO 5 I=1,L1
      BETA1(I)=XT(I)/R1
5  CONTINUE
      CALL CYL(ALP1,BETA1,N,M,L1,A1)
      IF(IFLAG.EQ.0)GO TO 10
C     DATA ON BODY 2: USE IF IFLAG=1
      READ(5,*) YM2, PR2
      K2=2.*(1.-PR2*PR2)/(PI*YM2)
      CALL PLATE(A,XT,N,M,L1,A2)
      PIN=0.0
      GO TO 17

```

```

C      DATA ON BODY 2: USE IF IFLAG=0
10     READ(5,*)YM2,PR2,R2
       K2=2.*(1.-PR2*PR2)/(PI*YM2)
       ALP2=A/R2
       DO 20 I=1,L1
       BETA2(I)=XT(I)/R2
20     CONTINUE
       CALL CYL(ALP2,BETA2,N,M,L1,A2)
       PIN=1./R2
C      COMBINE MATRICES FOR BODIES 1 AND 2. SL(I,J) IS THE MATRIX OF
C      COEFFICIENTS OF THE UNKNOWN FOURIER COEFF. OF PRESSURE.
17     DO 25 I=1,L1
       DO 25 J=1,LL
       SL(I,J)=(A1(I,J)*K1+A2(I,J)*K2)*A/PI
25     CONTINUE
C      INCLUDE CONDITION THAT PRESSURE GRADIENT VANISH AT INLET
       DO 70 I=1,N
       SL(L11,I)=((-1.)*I*I)*(1.E-10)
70     CONTINUE
       DO 71 I=1,M
       SL(L11,N+I)=((-1.)*(I-1)*(2.*I-1.)/2.)*1.E-10
71     CONTINUE
C      FROM SL, FORM MATRIX CORRESPONDING TO MINIMIZATION OF THE NORM
C      OF THE RESIDUAL.
       DO 55 I=1,LL
       DO 55 J=1,LL
       AS(I,J)=0.0
       DO 55 K=1,L11
       AS(I,J)=AS(I,J)+SL(K,I)*SL(K,J)
55     CONTINUE
C      BEGIN PROCEDURE FOR SOLVING THE SET OF LINEAR EQUATIONS FOR THE
C      UNKNOWN FOURIER COEFF.
       DO 1 I=1,LL
       IPIVOT(I)=I
       ROWMAX=0.0
       DO 2 J=1,LL

```



```

2  ROWMAX=AMAX1(ROWMAX,ABS(AS(I,J)))
1  D(I)=ROWMAX
   NM1=LL-1
   DO 3 K=1,NM1
     J=K
     KP1=K+1
     IP=IPIVOT(K)
     COLMAX=ABS(AS(IP,K))/D(IP)
     DO 4 I=KP1,LL
       IP=IPIVOT(I)
       AMIKOV=ABS(AS(IP,K))/D(IP)
       IF(AMIKOV.LE.COLMAX)GO TO 4
     COLMAX=AMIKOV
     J=I
4  CONTINUE
   IPK=IPIVOT(J)
   IPIVOT(J)=IPIVOT(K)
   IPIVOT(K)=IPK
   DO 3 I=KP1,LL
     IP=IPIVOT(I)
     AS(IP,K)=AS(IP,K)/AS(IPK,K)
     RATIO=-AS(IP,K)
     DO 3 J=KP1,LL
3  AS(IP,J)=RATIO*AS(IPK,J)+AS(IP,J)
C  FORM RIGHT-HAND SIDE OF THE EQNS.
90 DO 45 I=1,L1
   UIN(I)=.5*X(I)*X(I)*(1./R1+RIN)-H(I)-GAM
45 CONTINUE
C  FROM UIN AND SL, FORM RHS OF EQNS. CORRESPONDING TO MINIMI-
C  ZATION OF THE NORM OF THE RESIDUAL. CONTINUE SOLN. OF
C  LINEAR EQNS. WITH THIS AS RHS.
   UIN(L11)=0.0
   DO 36 I=1,LL
     U(I)=0.0
     DO 36 J=1,L11
       U(I)=U(I)+UIN(J)*SL(J,I)

```

```

36 CONTINUE
   IP=IPIVOT(1)
   Q(1)=U(IP)
   DO 9 K=2,LL
     IP=IPIVOT(K)
     KM1=K-1
     SUM=0.0
     DO 6 J=1,KM1
6      SUM=AS(IP,J)*Q(J)+SUM
9      Q(K)=U(IP)-SUM
      Q(LL)=Q(LL)/AS(IP,LL)
      K=LL
      DO 7 NPIMK=2,LL
        KP1=K
        K=K-1
        IP=IPIVOT(K)
        SUM=0.0
        DO 8 J=KP1,LL
8          SUM=AS(IP,J)*Q(J)+SUM
C      Q(K): DESIRED FOURIER COEFFICIENTS
7      Q(K)=(Q(K)-SUM)/AS(IP,K)
C      IF NECESSARY, MODIFY VALUE OF GAM TO SATISFY TOTAL LOAD CON-
C      DITION, AND RE-SOLVE THE EQUATIONS WITH NEW RHS.
      FTRIAL=0.0
      DO 34 I=1,M
        T=4.*A*(-1.)**(I-1)/((2.*I-1.)*PI)
34      FTRIAL=FTRIAL+T*Q(N+I)
      F0=FTRIAL-F
      NN=NN+1
      IF(NN.EQ.3)GO TO 100
      IF(NN.EQ.2)GO TO 110
      F1=F0
      GAM1=GAM
      GAM=GAM/2.
      GO TO 90

```

```

110 GAM2=GAM1
    GAM1=GAM
    F2=F1
    F1=F0
    GAM=GAM1-((GAM1-GAM2)*F1)/(F1-F2)
    GO TO 90
C   COMPUTE PRESSURE AT LOCATIONS DESIRED FOR OUTPUT.
100 NP=INT(ABS(X1/SP))+INT(ABS(X2/SP))+3
    XTIN(1)=AMIN1(X1,X2)
    XTIN(2)=INT(XTIN(1)/SP)*SP
    NP1=NP-1
    DO 40 I=3,NP1
        XTIN(I)=XTIN(I-1)+SP
40  CONTINUE
    XTIN(NP)=AMAX1(X1,X2)
    DO 42 L=1,NP
        XIN(L)=XTIN(L)+OFST
        P(L)=0.0
        DO 32 I=1,N
            P(L)=P(L)+Q(I)*SIN(I*PI*XIN(L)/A)
32  CONTINUE
        DO 35 JJ=1,M
            I=JJ-1
            P(L)=P(L)+Q(N+JJ)*COS((2.*I+1.)*PI*XIN(L)/(2.*A))
35  CONTINUE
42  CONTINUE
C   COMPUTE RESIDUALS AT EACH DATA POINT LOCATION.
    TR=0.0
    DO 91 I=1,LI
        UC(I)=0.0
        DO 92 J=1,LL
            UC(I)=UC(I)+SL(I,J)*Q(J)
92  CONTINUE
        HC(I)=.5*X(I)*X(I)*(1./R1+RIN)-UC(I)-GAM
        RES(I)=H(I)-HC(I)
        TR=TR+RES(I)*RES(I)

```

```

91 CONTINUE
C   OUTPUT:
C       FTIRIAL: CALCULATED TOTAL LOAD (N) - USE FOR COMPARISON AS A TEST

C           OF ACCURACY OF THE CALCULATIONS.
C       GAM: NORMAL APPROACH VALUE ARRIVED AT (M)
C       FOURIER COEFF.: COEFFICIENTS OF SIN TERMS LISTED FIRST
C       RESIDUALS: LISTED IN SAME ORDER AS INPUT POINTS (M).
C           LAST VALUE PRINTED IS SUM OF THEIR SQUARES.
C       X: DISTANCE FROM CONTACT POINT IN UNDEFORMED STATE
      WRITE(6,*)FTIRIAL,GAM
      WRITE(6,150)
150  FORMAT(5X,"FOURIER COEFFICIENTS:")
      WRITE(6,*)(Q(I),I=1,LL)
      WRITE(6,250)
250  FORMAT(5X,"RESIDUALS:")
      WRITE(6,*)(RES(I),I=1,L1)
      WRITE(6,*)TR
      WRITE(6,550)
      WRITE(6,450)(XTIN(I),P(I),I=1,NP)
550  FORMAT(10X,"X (M)",10X,"PRESSURE (N/M**2)"/)
450  FORMAT(9X,F10.5,10X,E11.4)
      WRITE(6,650)
C   IF USER WANTS CALCULATED FILM THICKNESS AT EACH INPUT POINT,
C       ENTER 1. OTHERWISE ENTER 0.
650  FORMAT(5X,"ENTER 1 FOR FILM THICKNESS")
      READ(4,*)NP
      IF(NP.NE.1)GO TO 93
      WRITE(6,750)
750  FORMAT(12X,"X (M) ",9X,"FILM THICKNESS (M)"/)
      WRITE(6,450)(X(I),HC(I),I=1,L1)
93  WRITE(6,850)
C   IF USER WANTS CALCULATED FILM THICKNESS AT OTHER POINTS IN OR
C       NEAR CONTACT, ENTER 1. OTHERWISE, ENTER 0.
850  FORMAT(5X,"ENTER 1 FOR ADD'L FILM THICKNESS")
      READ(4,*)NP

```

```

      IF(NP.NE.1)STOP
C      ENTER LOCATION OF DESIRED FILM THICKNESS CALCULATION. TO STOP PROGRAM.
AM,
C      ENTER VALUE > 20.
94 READ(4,*)XX
   IF(XX.GT.20.)STOP
   XT(1)=XX+OFST
   BETA1(1)=XT(1)/R1
   CALL CYL(ALP1,BETA1,N,M,1,A1)
   IF(IFLAG.EQ.0)GO TO 95
   CALL PLATE(A,XT,N,M,1,A2)
   GO TO 96
95 BETA2(1)=XT(1)/R2
   CALL CYL(ALP2,BETA2,N,M,1,A2)
96 DO 97 I=1,LL
   SL(1,I)=(A1(1,I)*K1+A2(1,I)*K2)*A/PI
97 CONTINUE
   UA=0.0
   DO 98 I=1,LL
   UA=UA+SL(1,I)*Q(I)
98 CONTINUE
   HH=.5*XX*XX*(1./R1+RIN)-UA-GAM
   WRITE(6,450)XX,HH
   GO TO 94
   STOP
   END
SUBROUTINE CYL(ALP,BETA,N,MT,L1,A)
C SUBROUTINE TO FILL MATRIX CORRESPONDING TO CYLINDER DISPLACEMENTS

   DIMENSION A(30,30),BETA(30)
   REAL M
   PI=4.*ATAN(1.)
   MM=MT-1
   LL=MT+N
   DO 10 L=1,L1
   NN=0

```

```

      IF(ABS(1.-ABS(BETA(L)/ALP)).LT.1.E-10)NN=1
C    CALCULATE ELEMENTS CORRESPONDING TO ANTISYMMETRIC COMPONENTS
      DO 12 I=1,N
      COEF1=I*PI/ALP
      XL=COEF1*(BETA(L)+ALP)
      CALL SICO(XL,S1,C01)
      XL=COEF1*(BETA(L)-ALP)
      CALL SICO(XL,S2,C02)
      IF(NN.NE.1)GO TO 16
      A1=0.0
      GO TO 15
16  A1=(((-1.)*I-COS(COEF1*BETA(L)))*ALOG(ABS((BETA(L)
      1+ALP)/(BETA(L)-ALP)))
15  B1=SIN(COEF1*BETA(L))*(S2-S1)
      C1=COS(COEF1*BETA(L))*(C01-C02)
      A(L,I)=(1./I)*(A1+B1+C1)
12  CONTINUE
C    CALCULATE ELEMENTS CORRESPONDING TO SYMMETRIC COMPONENTS
      DO 14 JJ=1,MT
      I=JJ-1
      M=(2.*I+1.)/2.
      COEF2=M*PI/ALP
      XL=COEF2*(BETA(L)+ALP)
      CALL SICO(XL,S1,C01)
      XL=COEF2*(ALP-BETA(L))
      CALL SICO(XL,S2,C02)
      A2=(2.*M*(PI)**2/(M**2*PI**2+ALP**2))*
1    SIN(M*PI)*COS(ALP)*COS(BETA(L))
      IF(NN.NE.1)GO TO 20
      B2=SIN(M*PI)*(2.*ALOG(2.*ALP)-ALOG(4.))
      C2=0.0
      GO TO 25
20  B2=SIN(M*PI)*(ALOG(ABS((ALP+BETA(L))*(ALP-
      1BETA(L))))-ALOG(4.))
      C2=SIN(COEF2*BETA(L))*(ALOG(ABS((ALP+BETA(L))/
      1(ALP-BETA(L))))))

```

```

25 D2=SIN(COEF2*BETA(L))*(C02-C01)
   E2=(-1.)*COS(COEF2*BETA(L))*(S2+S1)
   A(L,N+JJ)=A2+1./M*(B2+C2+D2+E2)
14 CONTINUE
10 CONTINUE
   RETURN
   END
   SUBROUTINE PLATE(A,X,N,MT,L1,AN)
C   SUBROUTINE TO FILL MATRIX CORRESPONDING TO PLATE DISPLACEMENTS
   DIMENSION AN(30,30),X(30)
   REAL M
   PI=4.*ATAN(1.)
   MM=MT-1
   LL=MT+N
   DO 10 L=1,L1
   NN=0
   IF(ABS(1.-ABS(X(L)/A)).LT.1.E-10)NN=1
C   CALCULATE ELEMENTS CORRESPONDING TO ANTISYMMETRIC COMPONENTS.
   DO 12 I=1,N
   COEF1=I*PI/A
   XL=COEF1*(A+X(L))
   CALL SICO(XL,S1,C01)
   XL=COEF1*(A-X(L))
   CALL SICO(XL,S2,C02)
   IF(NN.NE.1)GO TO 16
   A1=0.0
   GO TO 15
16 A1=(((-1.))*I-COS(COEF1*X(L)))*ALOG(ABS((A+X(L))/
   1(A-X(L))))
15 B1=(-1.)*SIN(COEF1*X(L))*(S1+S2)
   C1=COS(COEF1*X(L))*(C01-C02)
   AN(L,I)=(1./I)*(A1+B1+C1)
12 CONTINUE
C   CALCULATE ELEMENTS CORRESPONDING TO SYMMETRIC COMPONENTS.
   DO 14 JJ=1,MT
   I=JJ-1

```

```

      M=(2.*I+1.)/2.
      COEF2=M*PI/A
      S=SIN(COEF2*X(L))
      XL=COEF2*(A+X(L))
      CALL SICO(XL,S1,C01)
      XL=COEF2*(A-X(L))
      CALL SICO(XL,S2,C02)
      IF(NN.NE.1)GO TO 20
      A2=ALOG(2.)*(2.*SIN(M*PI))
      B2=0.0
      GO TO 25
20  A2=ALOG(ABS((A-X(L))/A))*(SIN(M*PI)-S)
      B2=ALOG(ABS((A+X(L))/A))*(SIN(M*PI)+S)
25  C2=(-1.)*S*(C01-C02)
      D2=(-1.)*COS(COEF2*X(L))*(S1+S2)
      AN(L,N+JJ)=(1./M)*(A2+B2+C2+D2)
14  CONTINUE
10  CONTINUE
      RETURN
      END
      SUBROUTINE SICO(X,S,C)
C    SUBROUTINE TO EVALUATE SIN AND COS INTEGRALS
      IF(ABS(X).GT.1.E-12)GO TO 25
      S=0.0
      C=0.0
      RETURN
25  IF(ABS(X).LT.0.1)GO TO 26
C    SICI IS A SUBROUTINE IN CDC MATH-SCIENCE LIBRARY.
      CALL SICI(S,C,X)
      S=S+1.570796
      C=.5772157+ALOG(ABS(X))-C
      RETURN
26  S=X
      C=0.0
      N=1
      NC=1

```



```

NS=-1
NTC=0
NTS=0
FACT=1.
COUNT=1.
PROD=X
DO 10 I=2,10
COUNT=COUNT+1.
FACT=FACT*COUNT
PROD=PROD*X
TERM=PROD/(COUNT*FACT)
IF(N.EQ.1)GO TO 15
N=1
IF(NS.EQ.-1)TERM=-TERM
NS=-NS
S=S+TERM
IF(ABS(TERM/S).LT.1.E-5)NTS=1
GO TO 112
15 N=0
IF(NC.EQ.-1)TERM=-TERM
NC=-NC
C=C+TERM
IF(ABS(TERM/C).LT.1.E-5)NTC=1
112 IF(NTS.EQ.0)GO TO 10
IF(NTC.EQ.1)RETURN
10 CONTINUE
RETURN
END
EOI ENCOUNTERED.          1 FILES.

BYE

ME650AC  LOG OFF    10.37.33.
ME650AC  SRU       0.025 UNITS.

```

VI. REFERENCES

1. Bohn, M., Carlson, S., Lee, D., Jakobsen, J., Sanborn, D. M., and Winer, W. O., "Investigations of Lubricant Rheology as Applied to Elastohydrodynamic Lubrication", NASA Grant No. 11-002-133, June 1972.
2. Johnson, R. L., Jones, W. R., Sanborn, D. M., and Winer, W. O., "Viscosity-Pressure Measurements for Several Lubricants to $5.5 \times 10^8 \text{ N/m}^2$ ($8 \times 10^4 \text{ psi}$) and 149 C (300F)", Trans. ASLE, Vol. 97, 1975.
3. Jakobsen, J., and Winer, W. O., "High Shear Behavior of Some Representative Lubricants", Trans. ASME, Journal of Lubrication Technology, Vol. 97, No. 3, 1975, pp. 479-485.
4. Carlson, S., Turchina, V., Jakobsen, J., Sanborn, D. M., and Winer, W. O., "Investigations of Lubricant Rheology as Applied to Elastohydrodynamic Lubrication", NASA Grant No. 11-002-133, October 1973.
5. Jakobsen, J., and Winer, W. O., "Dissipative Heating Effects and End Corrections for Viscous Newtonian Flow in High Shear Stress Capillary Viscometry", Trans. ASME, Journal of Lubrication Technology, Vol. 97, No. 3, 1975, pp. 424-278.
6. Jakobsen, J., "Traction of Elastohydrodynamic Contacts with Thermal Shearing Flow", Trans. ASME, Journal of Lubrication Technology, Vol. 97, No. 3, 1975, pp. 424-429.
7. Kunz, R. K., and Winer, W. O., "Prediction of Traction in Sliding EHD Contacts", Trans. ASME, Journal of Lubrication Technology, Vol. 98, Series F, No. 3, 1975, pp. 362-365.
8. Turchina, V., Sanborn, D. M., and Winer, W. O., "Temperature Measurements in Sliding Elastohydrodynamic Point Contacts", Journal of Lubrication Tehcnology, Trans. ASME, Vol. 96, 1974, pp. 464-471.
9. Ausherman, V. K., Nagaraj, H. S., Sanborn, D. M., and Winer, W. O., "Infrared Temperature Mapping in Elastohydrodynamics Lubrication", Trans. ASME, Journal of Lubrication Technology, Vol. 98F, No. 2, 1976, pp. 236-243.
10. Nagaraj, H. S., Sanborn, D. M., and Winer, W. O., "Effects of Load, Speed and Surface Roughness on Sliding EHD Contact Temperatures", Presented at the Joint ASME-ASLE Lubrication Conference, Boston, Mass., October 1976.
11. Carlson, S. F., and Winer, W. O., "The Viscous Lubrication of Rolling and Sliding Rigid Cylinders", ASME Transactions, Journal of Lubrication Technology, Vol. 97F, No. 2, April 1975, pp. 180-186.

12. Carlson, S., Jakobsen, J., Nagaraj, H. S., Molina-C., M. A., Sanborn, D. M., and Winer, W. O., "Investigations of Lubricant Rheology as Applied to Elastohydrodynamic Lubrication", NASA CR-134730, September 1974.
13. Kunz, R. K., Nagaraj, H. S., Sanborn, D. M., and Winer, W. O., "Investigations of Lubricant Rheology as Applied to Elastohydrodynamic Lubrication", NASA CR-134882, August 1975
14. Foord, C. A., Wedeven, L. D., Westlake, F. J., Cameron, A., "Optical Elastohydrodynamics, Proc. Instr. Mech. Engrs. 184, Part 1, 1969/70.
15. Sanborn, D. M. and Winer, W. O., "Fluid Rheological Effects in Sliding Elastohydrodynamic Point Contacts with Transient Loading: I - Film Thickness", Trans. ASME, Journal of Lubrication Technology, Vol. 93, pp. 262-271, 1971.
16. Blok, H., General Discussion on Lubrication, Vol. 2, Institute of Mechanical Engineers, p. 222, 1937.
17. Jaeger, J. C., "Moving Sources of Heat and the Temperature at Sliding Contacts," Proc. Roy. Soc. N.S.W., Vol. 56, 1942, p. 203.
18. Archard, J. F., "The Temperature of Rubbing Surfaces", Wear, Vol. 2, No. 6, October 1959, pp. 438-455.
19. Sanborn, D. M., "An Experimental Investigation of the Elastohydrodynamic Lubrication of Point Contacts in Pure Sliding", Ph.D. Thesis, University of Michigan, 1969.
20. Sanborn, D. M. and Winer, W. O., "Fluid Rheological Effects in Sliding Elastohydrodynamic Point Contacts: II - Traction, Trans. ASME, Journal of Lubrication Technology, Vol. 93, pp. 342-348, 1971.
21. Whitehouse, D. J. and Archard, J. F., "The Asperities of Random Surfaces of Significance in their Contact", Proc. Roy. Soc. Lond. A., 316, 97-121, 1970.
22. Peklenik, J., "New Developments in Surface Characterization and Measurements by Means of Random Process Analysis", Proc. Inst Mech Engr, Vol. 182, Pt. 3K, 1967-1968.
23. Wedeven, L. D., "Traction and Film Thickness Measurements Under Starved Elastohydrodynamic Conditions", Trans, ASME., Journal of Lubrication Technology, Series F, No. 2, pp. 321-329, April 1975.
24. Greenwood, J. A., and Kauzlarich, J. J., "Inlet Shear Heating in Elastohydrodynamic Lubrication", Journal of Lubrication Technology, Trans. ASME, Series F, Vol. 95, pp. 417-426, October 1973.

25. Smith, F. W., "Lubricant Behavior in Concentrated Contact - Some Rheological Problems", ASLE Transaction, 3, 18, 1960.
26. Johnson, K. L., and Roberts, A. D., "Observation of Viscoelastic Behavior of an EHD Lubricant Film", Proc. Roy. Soc. Lond. A-337, 217, 1974.
27. Johnson, K. L., and Cameron, R., "Shear Behavior of Elastohydrodynamic Oil Films at High Rolling Contact Pressures," Proc. Inst. Mech. Engrs., 182, Pt. 1, 307, 1967-1968.
28. Noel, F., "Thermal Analysis of Lubricating Oils", Thermonica Act., 4, 377, 1972.
29. Haward, R. N., The Physics of Glassy Polymers, New York, Wiley and Sons, Inc.
30. McCrum, N. G., Read, B. E., and Williams, G. E., Anelastic and Dielectric Effects in Polymeric Solids, John Wiley and Sons, New York, 1967.
31. Rosen, Bernard, Fracture Processes in Polymeric Solids - Phenomena and Theory, John Wiley and Sons, Interscience Publishers, New York, 1964.
32. Lamb, John, "Experimental Linear Viscoelastic Measurements for Liquids", ACS Symposium on Lubricant Properties in Thin Lubricating Films, April 1976.
33. Dill, J. F., Drake, P. W., and Litovitz, T. A., "The Study of Viscoelastic Properties of Lubricants Using High Pressure Optical Techniques", ASLE, 18(3), 202, 1975.
34. ASME, Pressure-Viscosity Report, I, II, A Report Prepared by the ASME Research Committee on Lubrication, New York, ASME, 1953.
35. McKinny, J. E., and Goldstein, M., "PVT Relationships for Liquid and Glassy Poly(Vinyl Acetate)", Journal of Research of the NBS-Physics and Chemistry, 78A, 331, 1974.
36. Turnbull, D., Contemp. Phys. 10, 473, 1969.
37. Gee, G., "The Glassy State in Polymers", Contemp. Phys., 11(4).
38. Harrison, G., The Dynamic Properties of Supercooled Liquids, Academic Press, New York 1976.
39. Ferry, J. D., Viscoelastic Properties of Polymers, New York, Wiley and Sons, Inc., 1961.
40. Kovacs, A. J., J. Polym. Sci., 30, 131, 1958.

41. Matsuoka, S., and Maxwell, B., J. Poly. Sci., 32, 131, 1958.
42. Yourtee, J. B., and Cooper, S. L., "Properties of Densified Amorphous Polystyrene", J. Appl. Poly. Sci., 18, 897, 1974.
43. Greet, R. J., and Turnbull, D., "Glass Transition in O-Terphenyl", J. Chem. Phys., 46(4), 1967.
44. Barrall, E. M., II, Porter, R. S., and Johnson, J. F., "Heat of Transition for Some Cholesteryl Esters by Differential Scanning Calorimetry", J. Phys. Chem., 71(5), 1224, 1967.
45. Johari, G. P., and Goldstein, M., "Viscous Liquids and the Glass Transition", J. Chem. Phys., 55(9), 4245, 1971.
46. Yano, O., and Wada, Y., "Dynamic and Dielectric Relaxations of Polystyrene Below the Glass Temperature", J. Poly. Sci., 9(A2), 669, 1971.
47. Rank, D. H., Kiess, E. M., and Fink, U., "Brillouin Spectra of Viscous Liquids", J. Opt. Soc. Am. 56(2), 103, 1966.
48. Pinnow, D. A., Candau, S. J., LaMacchia, I. T., and Litovitz, T. A., "Brillouin Scattering: Viscoelastic Measurements in Liquids", J. Acoust. Soc. Am., 43, 13, 1968.
49. Rank, D. H., Kiess, E. M., Fink, U. and Wiggins, T. A., J. Opt. Soc. Am., 54, 1286, 1964.
50. Cummins, H. Z., and Gammon, R. W., "Rayleigh and Brillouin Scattering in Liquids: The Landau-Placzek Ratio", J. Chem. Phys., 44(7), 2785, 1966.
51. Stevens, J. R., Jackson, D. A., and Champion, J. V., "Evidence for Ordered Regions in Poly(n-butyl) Methacrylate from Light Scattering Studies", Molecular Physics, 29(6), 1893, 1975.
52. Coakley, R. W., Mitchel, R. S., Stevens, J. R., and Hunt, J. L., "Rayleigh-Brillouin Light Scattering Studies on Atactic Polystyrene", A paper presented at the American Physical Society Conference, Atlanta, Georgia, April, 1976.
53. Jackson, D. A., Pentecost, H. T. A., and Powels, J. G., "Hypersonic Absorption in Amorphous Polymers by Light Scattering", Molecular Physics, 23(2), 425, 1972.
54. Romberger, A. B., Eastman, D. P., and Hunt, J. L., "Evidence for Structure in Plastics from Light Scattering", J. Chem. Phys., 51(9), 3723, 1969.

55. Work, Richard N., "On the Discontinuity in the Temperature Coefficient of the Velocity of Ultra Waves in Polymeric Materials", J. Appl. Phys., 27(1), 69, 1956.
56. Mitchell, R. S., and Guillet, J. E., "Brillouin Scattering in Amorphous Polymeric Solid", J. Polymer Sci.: Polymer Phys. Ed., 12, 713, 1974.
57. Friedman, E. A., Ritger, A. J., and Andrews, R. D., "Brillouin Scattering Near the Glass Transition of Polymethyl Methacrylate", J. Appl. Phys., 40(11), 4243, 1969.
58. Fabelinskii, I. L., Molecular Scattering of Light, Plenum Press, New York, 1968.
59. Debye, P., Ann. Physik, 39, 789, 1912.
60. Brillouin, L., Ann. Phys. (Paris) 17, 88, 1922.
61. Landau, L., and Placzek, G., Z. Phys. Sowjetunion, 5, 172, 1934.
62. O'Shea, D. C., Callen, W. R., and Rhodes, W. T., A Laser Textbook-An Introduction to Lasers and their Applications, Georgia Institute of Technology, 1973.
63. Love, A. E. H., A Treatise on the Mathematical Theory of Elasticity, Cambridge University Press, 1927.
64. Timoshenko, S., and Goodier, J. N., Theory of Elasticity, McGraw-Hill Book Company, New York, 1951.
65. Milne-Thomson, L. M., Plane Elastic Systems, Springer-Verlag, Berlin, 1968.
66. Muskhelishvili, N. I., Some Basic Problems of the Mathematical Theory of Elasticity, Noorhoff, Groningen, 1953.
67. Carrier, G. F., Krook, M., Pearson, C. E., Functions of a Complex Variable, McGraw-Hill Book Company, New York, 1966.
68. Jahnke, E., and Ende, F., Tables of Functions, Dover, New York, 1945.
69. Sheid, F., "Theory and Problems of Numerical Analysis", Schaum's Outline Series, McGraw-Hill Book Company, New York, 1968.
70. Wymer, D. G., and Cameron, A., "Elastohydrodynamic Lubrication of a Line Contact", Proc. of the Institute of Mechanical Engineers, Vol. 188, pp. 221-238, 1974.

Table III-1. Summary of Rolling Experiments
Film Thickness and Traction.

\bar{V}	Σ	V_s	P_H	T_{BATH}	h_c	h_m	TC
m/s	-	m/s	GN/m ²	°C	μm	μm	--
0.5	2.00	1.00	0.81	34	.18	.076	.061
"	0.60	0.30	"	37	"	"	.056
"	0.40	0.20	"	38	"	"	.055
"	0.20	0.10	"	38	"	"	.050
"	0.00	0.00	"	39	"	"	.017
"	-.20	-.10	"	38	"	"	--
"	-.40	-.20	"	40	"	"	--
"	-.88	-.44	"	41	"	"	--
0.75	2.00	1.50	"	39	.19	.089	.058
"	1.20	0.90	"	"	.20	"	.058
"	0.67	0.50	"	"	.20	"	.055
"	0.13	0.10	"	"	.22	"	.049
"	0.00	0.00	"	38	.22	"	.024
"	2.00	1.50	0.66	33	.22	.15	.051
"	1.20	0.90	"	34	.24	.18	.051
"	0.67	0.50	"	34	"	"	.051
"	0.19	0.14	"	35	"	"	.051
"	0.00	0.00	"	"	"	"	.014
"	-.10	-.08	"	"	"	"	.041
"	2.00	1.50	1.02	40	.15	.064	.061
"	.27	.20	"	38	.18	.076	.059
"	0.00	0.00	"	37	.22	"	.020
"	-.27	-.20	"	"	.17	"	.057
0.51	0.00	0.00	"	"	.18	"	.020
0.72	0.00	0.00	"	"	.22	"	.023
1.00	0.00	0.00	"	"	.24	.127	.023
1.25	0.00	0.00	"	"	.28	.178	.027

Table III-2. Summary of Rolling Experiments
Ball Surface Temperature Rises.
($P_H = 1.02 \text{ GN/m}^2$)

\bar{V}	Σ	V_s	T_{BATH}	CENTER ΔT	MAX. ΔT
m/s	-	m/s	$^{\circ}\text{C}$	$^{\circ}\text{C}$	$^{\circ}\text{C}$
0.75	2.00	1.50	42	54	64
0.75	1.20	0.90	42	35	36
0.75	0.99	0.74	43	26	26
0.75	0.56	0.42	42	14	15
0.75	0.27	0.20	40	6	6
0.75	0.13	0.10	41	4	4
0.75	0.00	0.00	41	4	4
0.75	-0.27	-0.20	40	6	6
1.00	2.00	2.00	44	53	62
1.00	1.50	1.50	45	42	46
1.00	1.30	1.30	45	37	39
1.00	1.04	1.04	44	36	37
1.00	0.60	0.60	43	21	21
1.00	0.40	0.40	43	10	10
1.00	1.12	0.12	42	6	6
1.00	0.00	0.00	41	5	5
0.50	0.00	0.00	41	2	2
1.25	0.00	0.00	41	7	7

Table IV-1. Frequency Shift and Velocity of Sound
as Function of Pressure for 5P4E at
24.4C (76F) (History B).

Date: December 26, 1975
 Separation Distance - 0.50 cm
 Resulting $P_g = 24,700 \text{ psi}$
 $= 0.17 \text{ GPa}$

Spectrum Number	Pressure kpsi*	Frequency Shift cm^{-1}	Frequency Shift GHZ	Refractive Index	Velocity of Sound, m/s
1	4.78	0.33194	10.00	1.6405	2208
2	7.2	0.34034	10.21	1.6453	2258
3	10,460	0.35364	10.61	1.6518	2337
4	14,250	0.36805	11.04	1.6594	2421
5	16,800	0.37819	11.35	1.6645	2480
6	20,840	0.39429	11.83	1.6726	2573
7	23,125	0.40259	12.08	1.6772	2620
8	26,050	0.41204	12.36	1.6829	2672
9	28,200	0.41642	12.49	1.6873	2695
10	29,950	0.42067	12.62	1.6909	2715
11	31,500	0.42347	12.70	1.6939	2729

* Multiply entry by 6.894×10^{-3} to get pressure units of GPa.

Table IV-2. Frequency Shift and Velocity of Sound as a Function of Temperature at 0.40 GPa (59,000 psi) for 5P4E Oil (History A).

Date: March 2, 1976					
Separation Distance = 0.725 cm					
Resulting: $T_g = 70.3$ C					
Spectrum Number	Temperature C	Frequency Shift cm^{-1}	Frequency Shift GHZ	Refractive Index	Velocity of Sound m/s
64	82	0.43966	13.19	1.7222	2787
65	80	0.44236	13.27	1.7233	2801
66	77	0.44618	13.39	1.7246	2823
67	75	0.44973	13.49	1.7258	2844
68	72	0.65369	13.61	1.7271	2867
69	70	0.45511	13.65	1.7280	2875
70	67	0.45691	13.71	1.7292	2883
71	65	0.45789	13.74	1.7303	2888
72	63	0.45910	13.77	1.7313	2894
73	59	0.46064	13.82	1.7328	2901
74	56	0.46216	13.86	1.7343	2908

Table IV-3. Least-Square Expressions for Sound Velocity, Temperatures and Sound Velocity at Transition for Different Constant Pressures: 5P4E History A.

Formation Pressure, MPa	Range of Measurements C	Least-Square Expression for Sound Velocity	Glass Transition Temperature (T _g) C	Sound Velocity at T _g , m/s
210	48-27	$V_L = 2961 - 7.99T$ $V_g = 2798 - 3.15T$	34	2692
248	49-27	$V_L = 3043 - 7.49T$ $V_g = 2856 - 2.88T$	41	2739
276	58-32	$V_L = 3138 - 7.94T$ $V_g = 2903 - 2.88T$	46	2769
321	68-43	$V_L = 3172 - 6.79T$ $V_g = 2942 - 2.43T$	53	2812
355	72-46	$V_L = 3259 - 6.95T$ $V_g = 3015 - 2.48T$	59	2848
407	82-54	$V_L = 3410 - 7.60T$ $V_g = 3032 - 2.23T$	70	2875

Table IV-4. Experimental Fluids* in Volumetric
Glass Transition Experiments.

5P4E	XRM-177-F4
N1, N2	DN 600
P1	FN 2961
MCS 460	S2-Polybutene
MCS 1218	S1-Diester
Sanotrac 50	S3-DC200-Blend I
Formulated Advanced Ester	DC 200-50

*Detailed descriptions are given in Appendix A.

Table IV-5. Fluids for Which No Transition was Observed by the Volumetric Method in the Indicated Temperature and Pressure Ranges (Isothermal Compression).

SAMPLE	MAXIMUM PRESSURE (GPA)	TEMPERATURE (°C)
DIESTER (S1)	1.13	-3.3
DC 200 BLEND II	** .61	7.2
DC 200 - 50 (S3)	* .92	21.1
ADVANCED ESTER	*1.07	16.9

* PISTON SEIZED

** DISPLACEMENT LIMITED

Table IV-6. Approximate Yield Shear Strength
at Atmospheric Pressure

FLUID	T	T_g	$\approx \tau$ yield, MPa
5P4E	- 60C	- 23C	5.38
N1	< T_g	- 62C	3.24
XRM	< T_g	N.A.	2.96

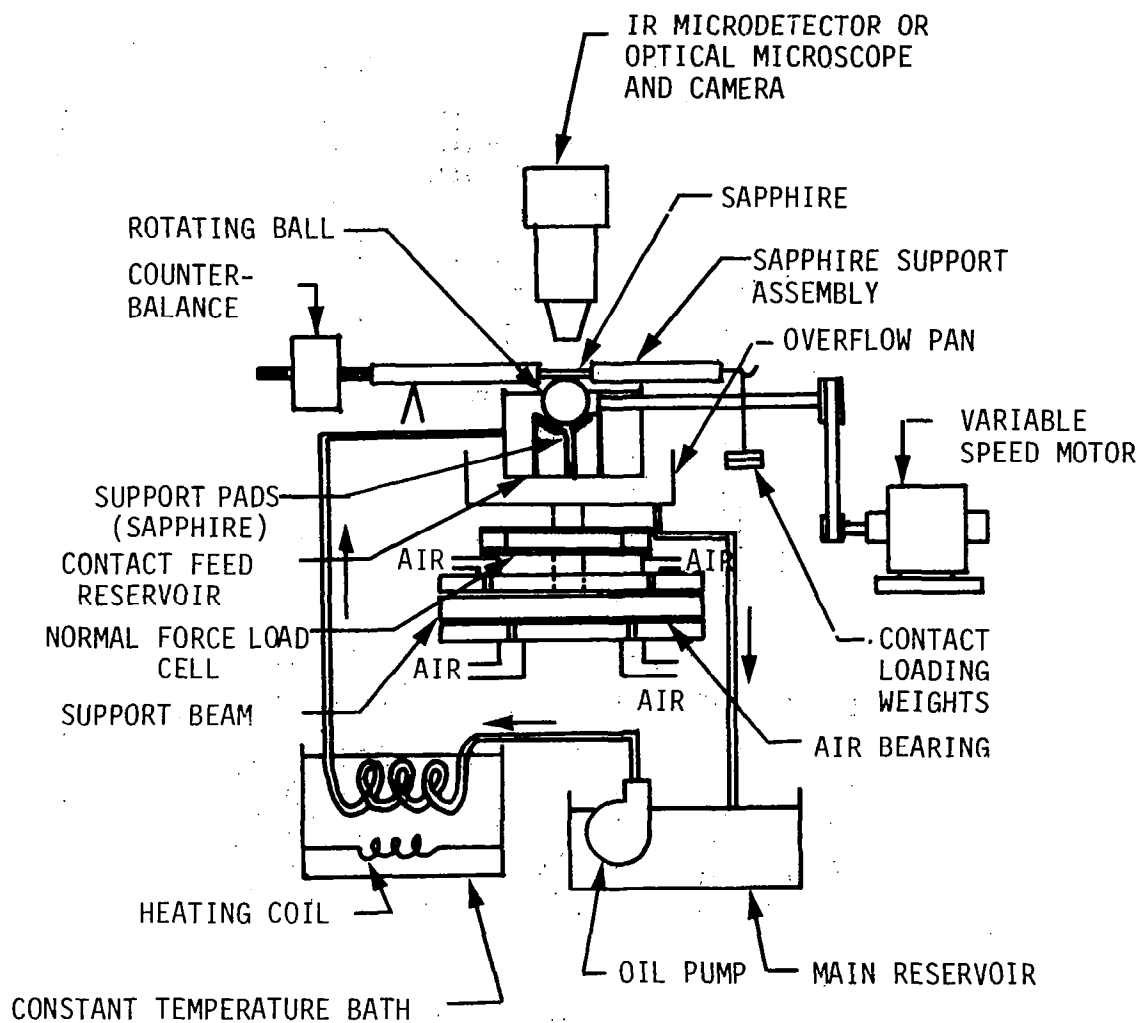


Figure III-1. Schematic of Sliding EHD Contact Simulator.

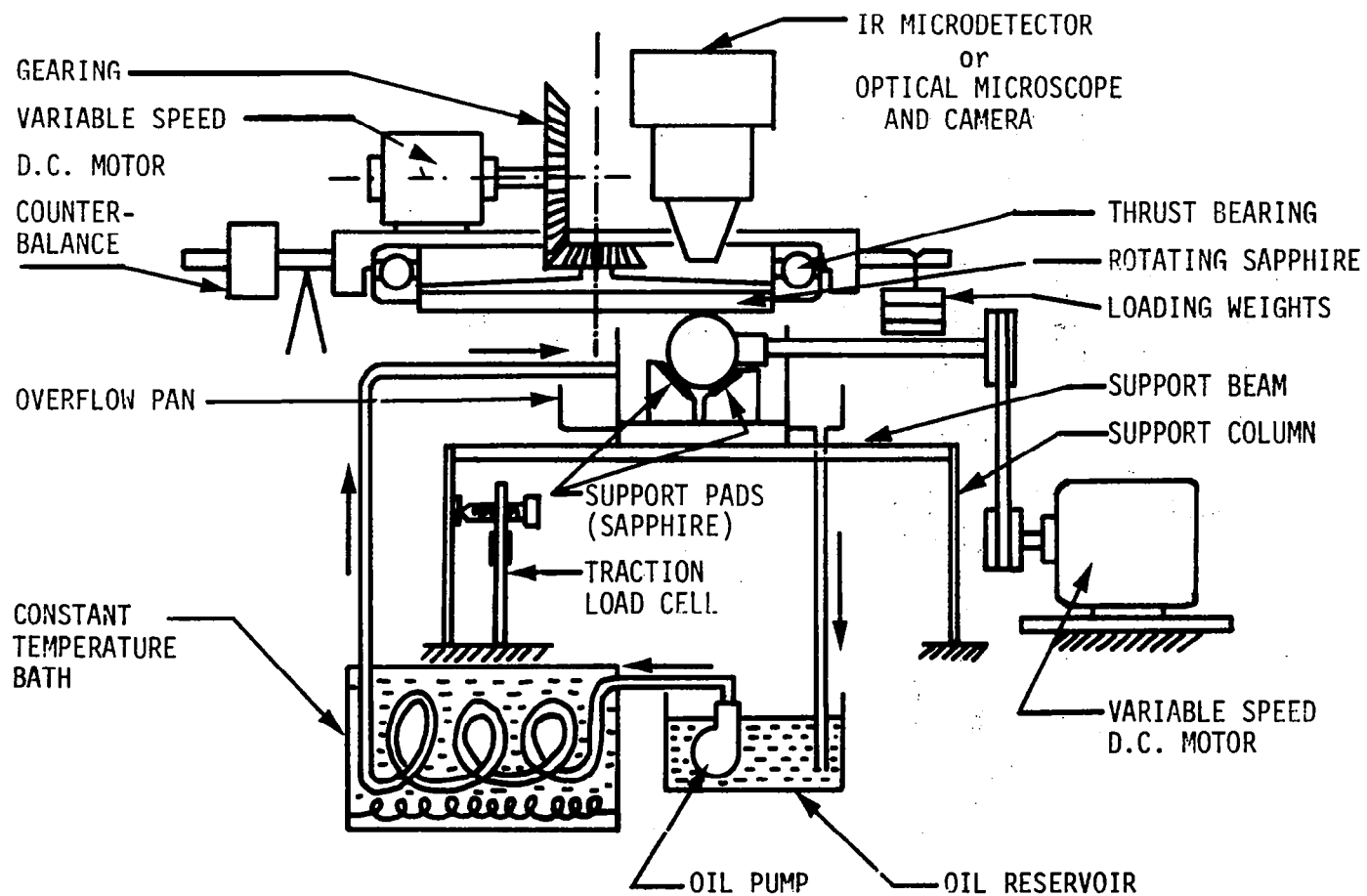


Figure III-2. Schematic of the Combined Rolling and Sliding EHD Contact Simulator.

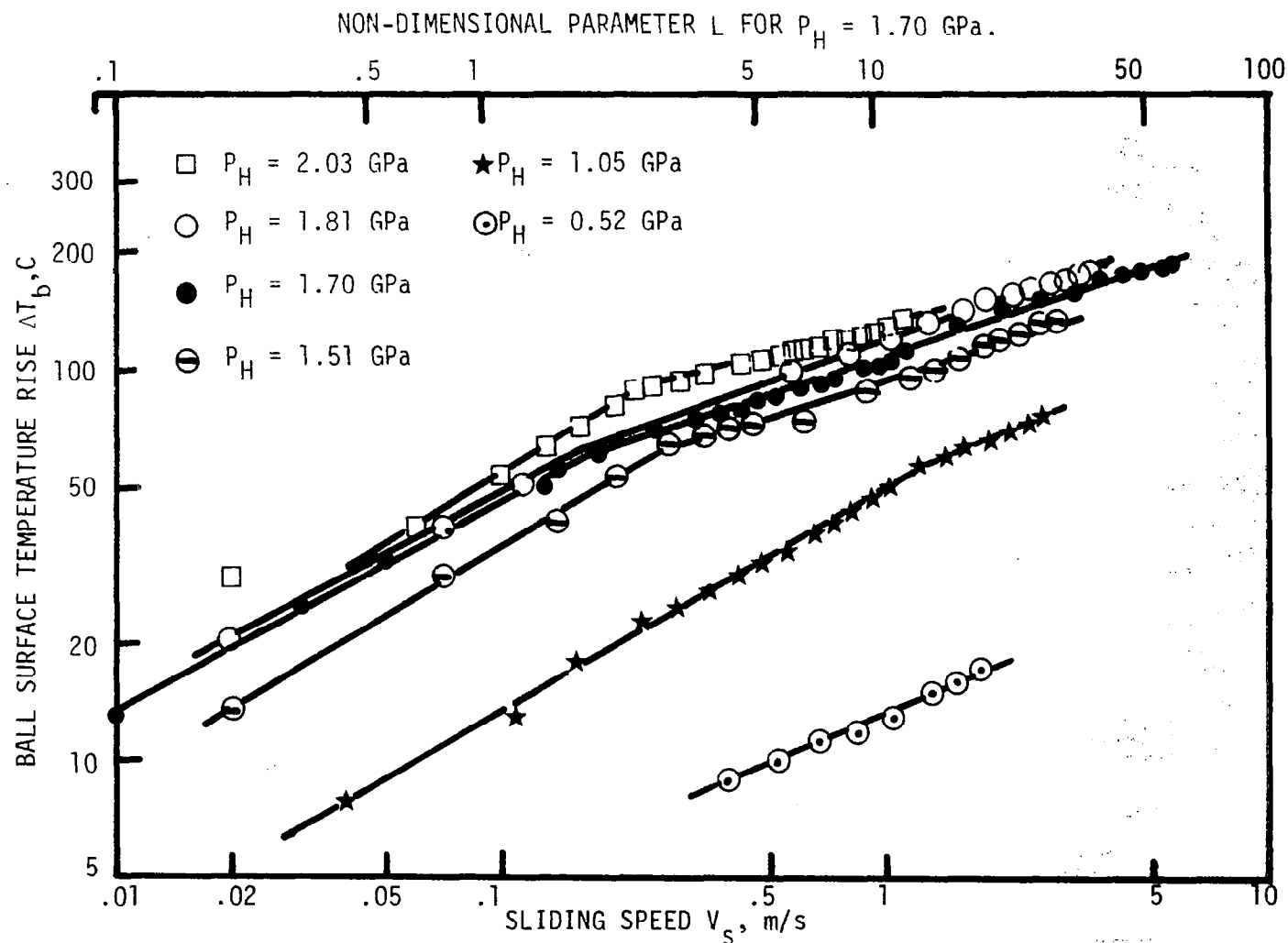
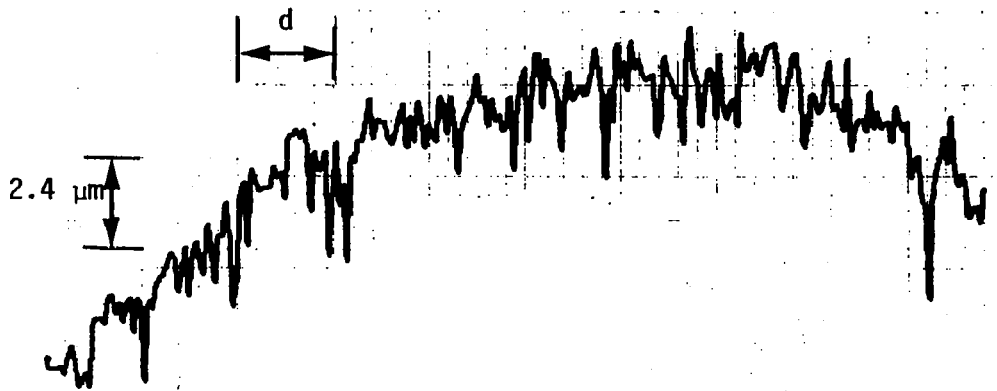
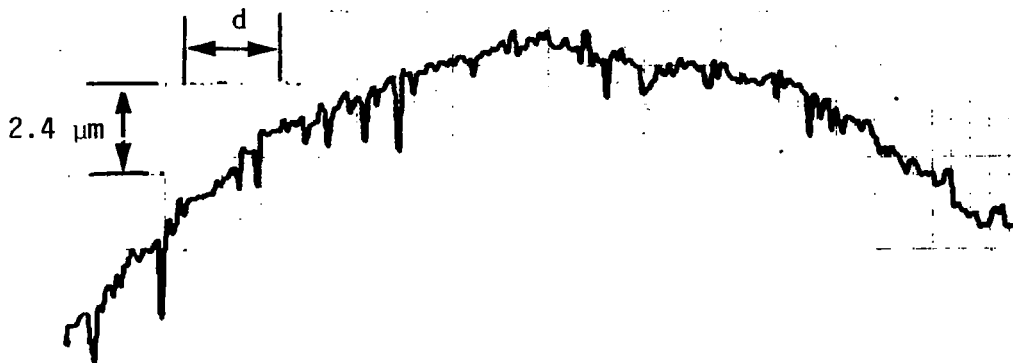


Figure III-3. Ball Surface Temperature Rise at Contact Center ($.011 \mu\text{m}$ Ra roughness, $1 < \Lambda < 2$ for $P_H = 2.03$ GPa, otherwise $\Lambda > 2$).

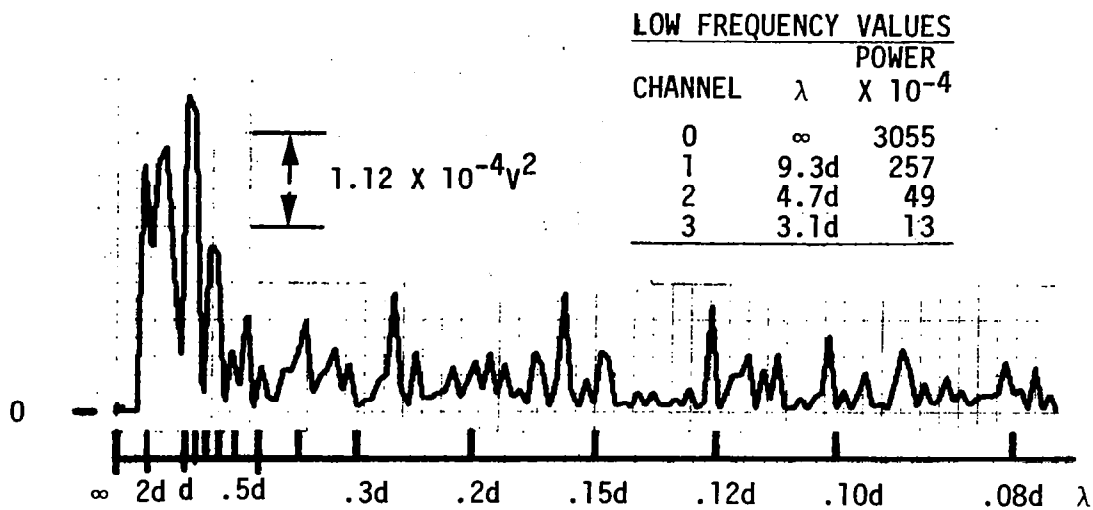


a) Unused ball surface ($.38 \mu\text{m}$ Ra roughness).

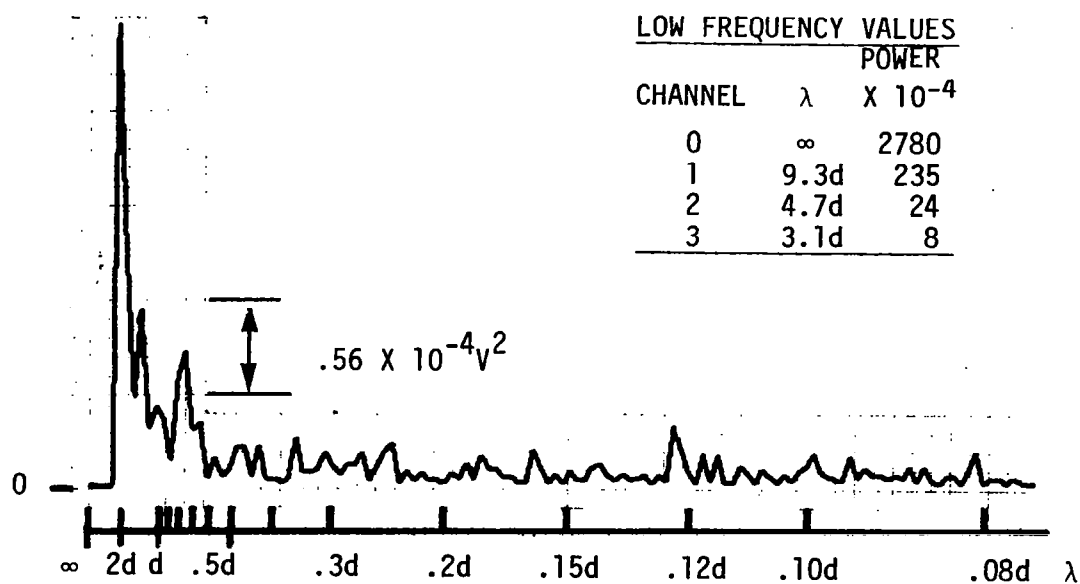


b) Ball surface after running 24 minutes ($.25 \mu\text{m}$ Ra roughness).

Figure III-4. Surface Profiles in Direction of Sliding
 $(P_H = 1.24 \text{ GN/m}^2, V_s = 1.02 \text{ m/s, Hertz}$
 Diameter $d = 0.43 \text{ mm}$, pure sliding).

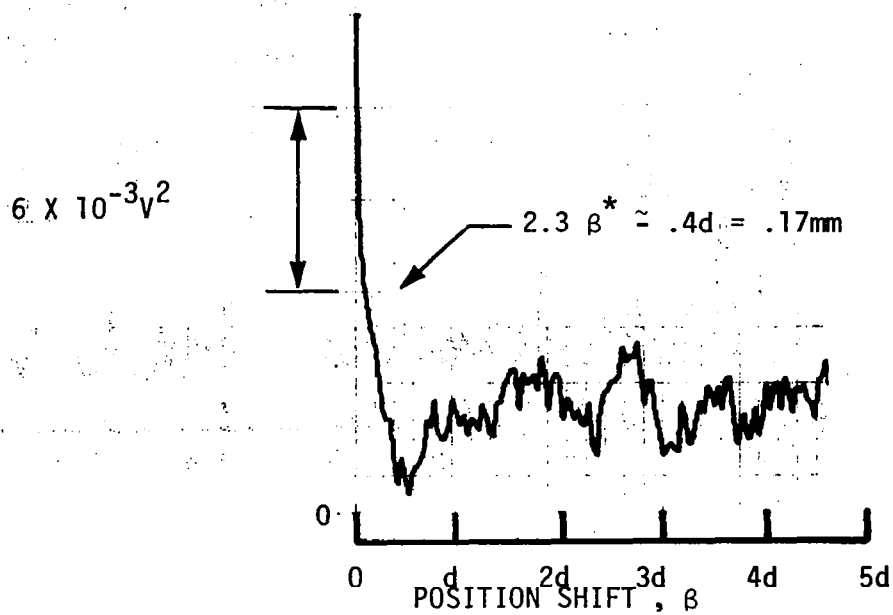


a) Unused ball surface.

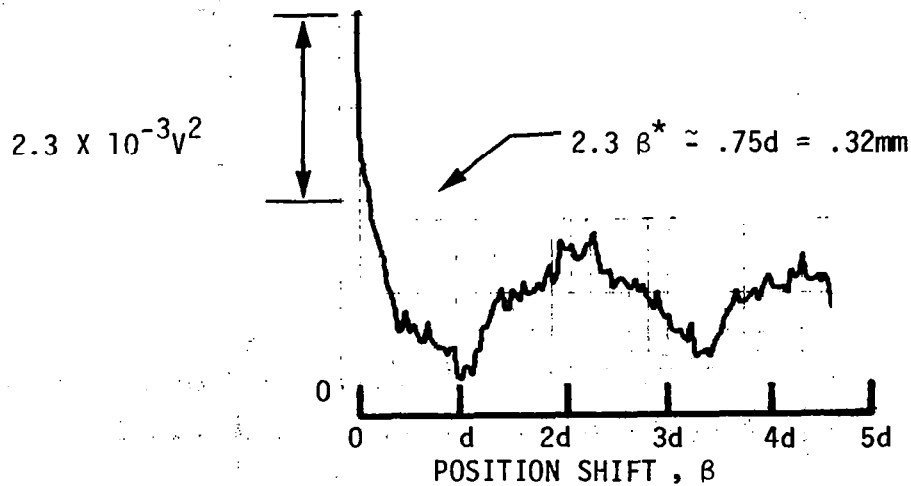


b) Ball surface after running 24 minutes.

Figure III-5. Power Spectra of the Surface Profiles
 ($P_H = 1.24 \text{ GN/m}^2$, $V_s = 1.02 \text{ m/s}$, Hertz
 diameter $d = 0.43 \text{ mm}$, pure sliding.)

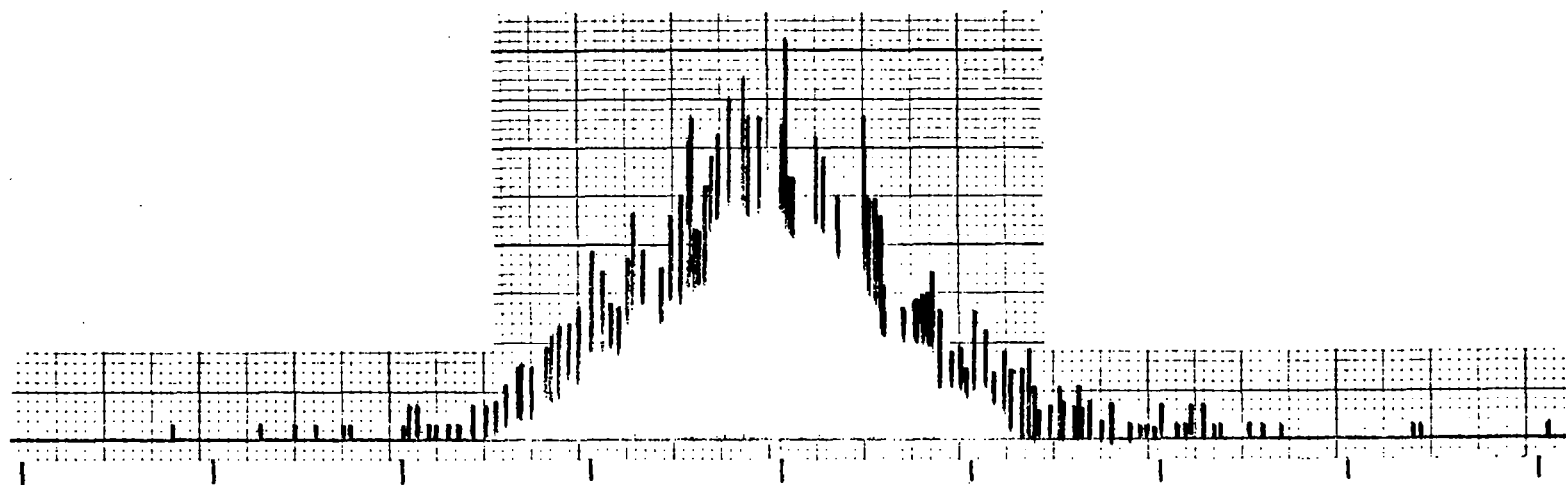


a) Unused ball surface ($.38 \mu\text{m}$ Ra roughness).

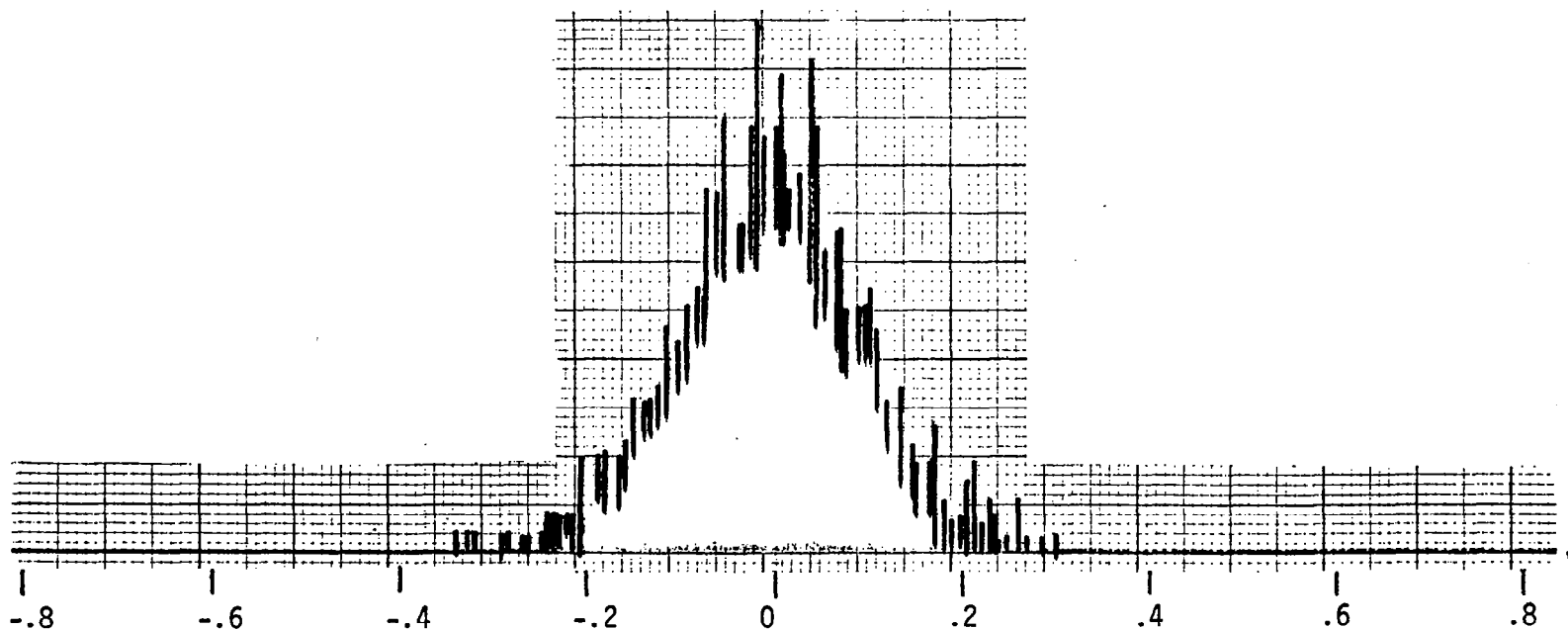


b) Ball surface after running 24 minutes.

Figure III-6. Autocorrelation Functions of the Surface Profiles.
 $(\lambda > 3d$ not included, $P_H = 1.24 \text{ GN/m}^2$, $V_S = 1.02 \text{ m/s}$,
Hertz diameter $d = 0.43 \text{ mm}$, pure sliding)

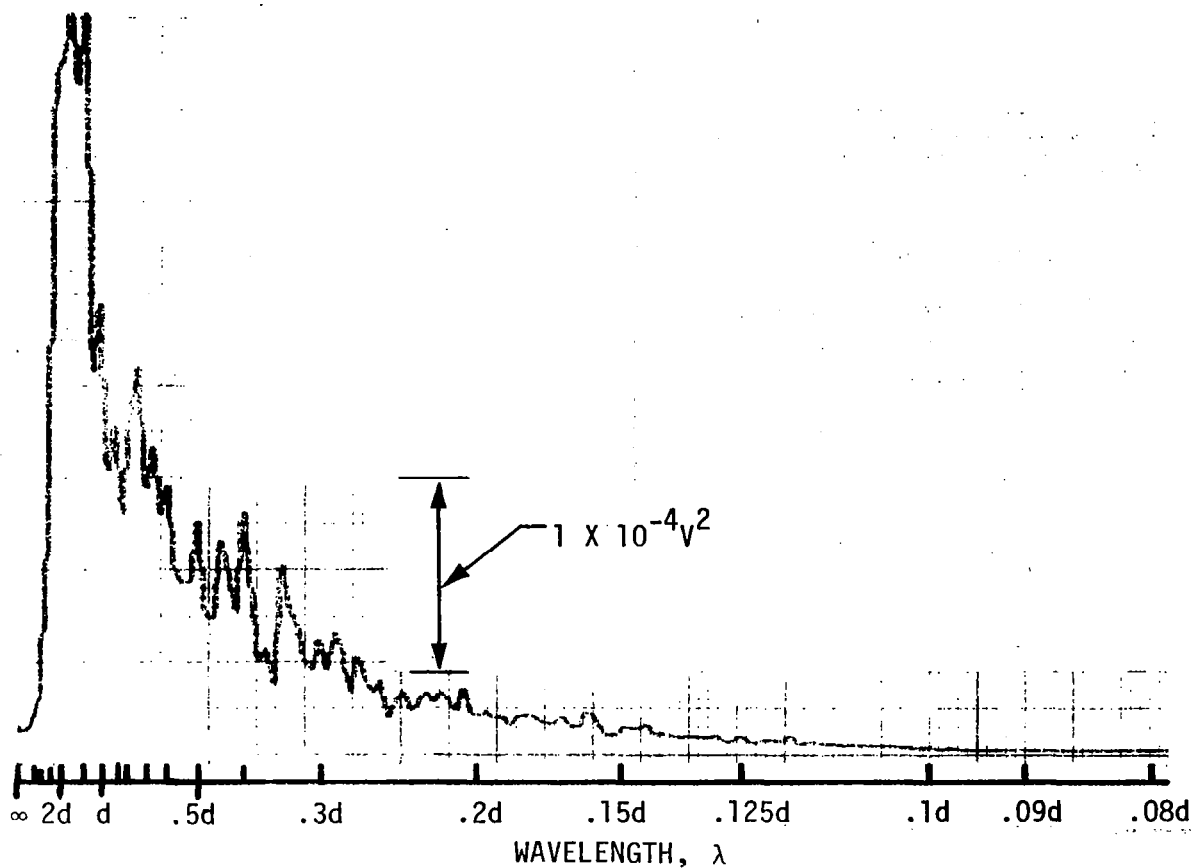


a) Initial Ball Surface Radiation Fluctuations.

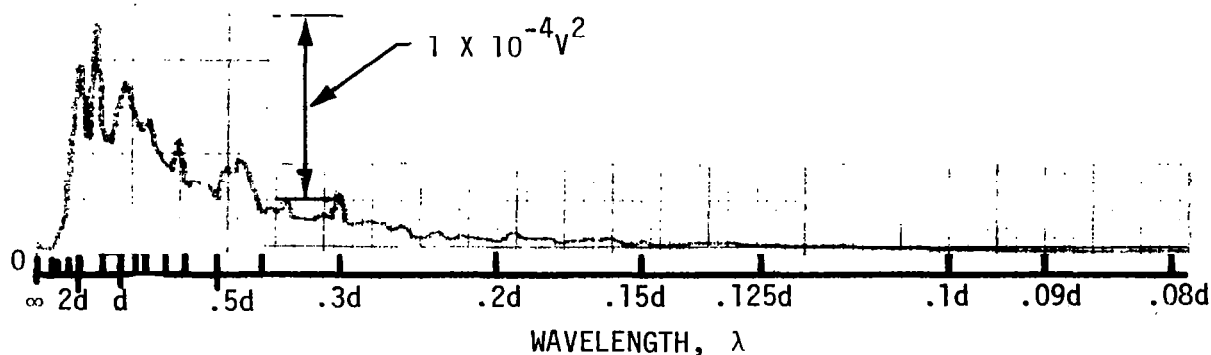


b) Ball Surface Radiation Fluctuations after Running 8 Minutes.

Figure III-7. Normalized Histograms of Ball Surface Radiation Fluctuations
 (.38 μm R_a initial roughness, $P_H = 1.24 \text{ GN/m}^2$, $V_s = 1.02 \text{ m/s}$,
 Hertz diameter $d = 0.43 \text{ mm}$, pure sliding).



a) Ball Surface Temperature Fluctuations at Start of Run-in.



b) Ball Surface Temperature Fluctuations after 8 Minutes Run-in.

Figure III-8. Power Spectra of Ball Surface Temperature Fluctuations
 ($.38 \mu\text{m}$ Ra initial roughness, $P_H = 1.24 \text{ GN/m}^2$,
 $V_s = 1.02 \text{ m/s}$, Hertz diameter = 0.43 mm , pure sliding).

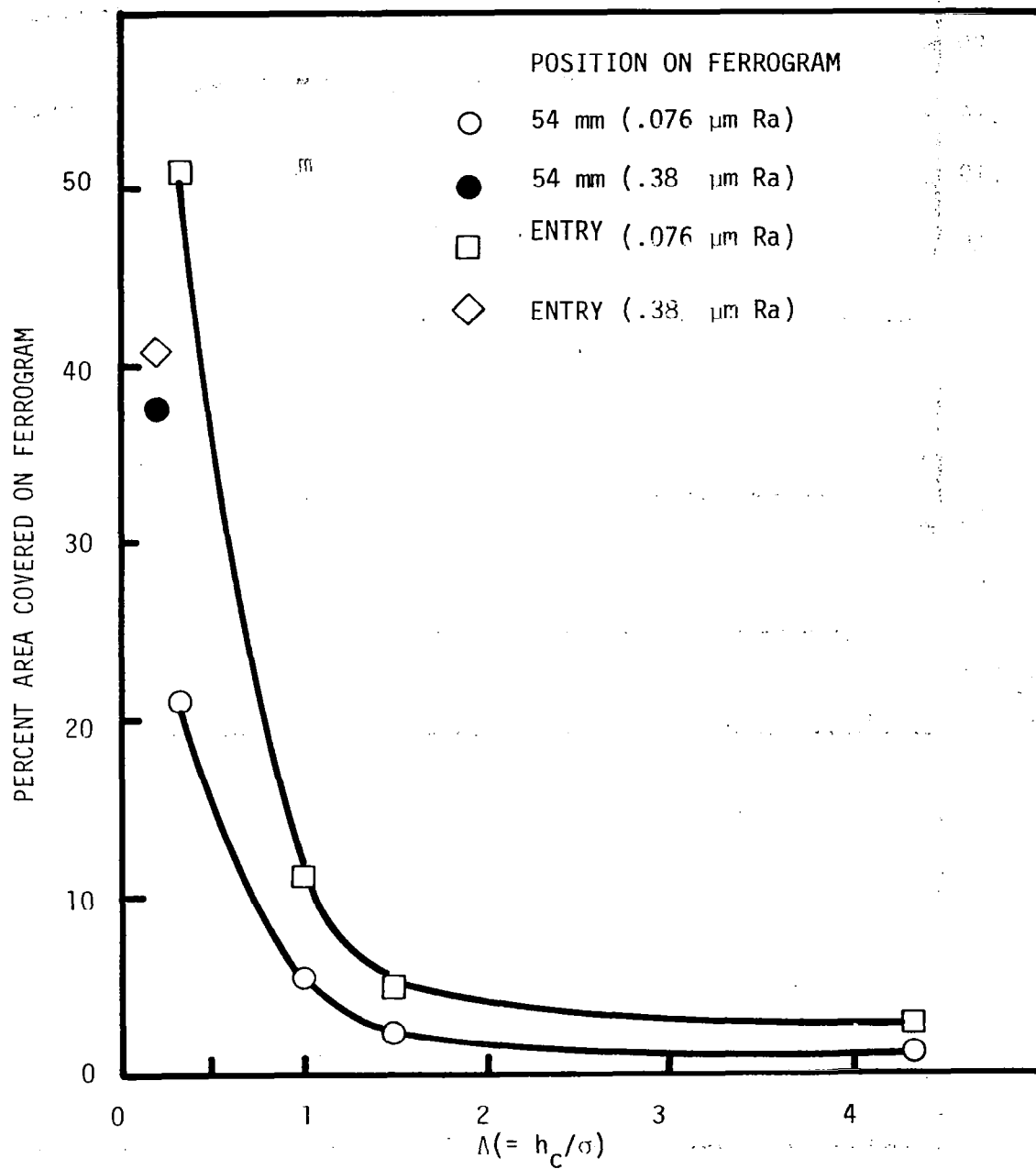


Figure III-9. Debris Concentration Dependence on Λ .

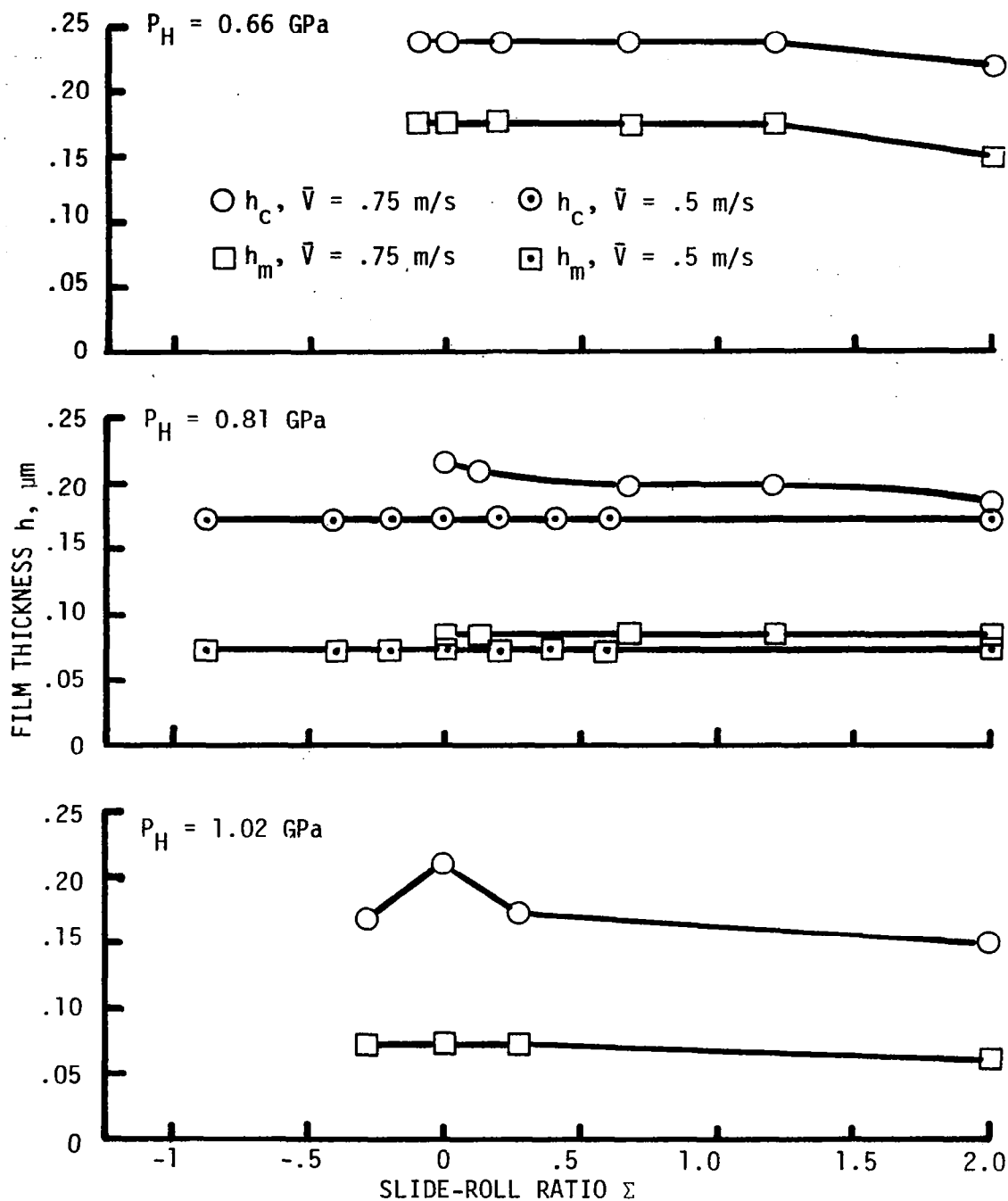


Figure III-10. Film Thickness as a Function of Slide-Roll Ratio ($.011 \mu\text{m}$ Ra roughness).

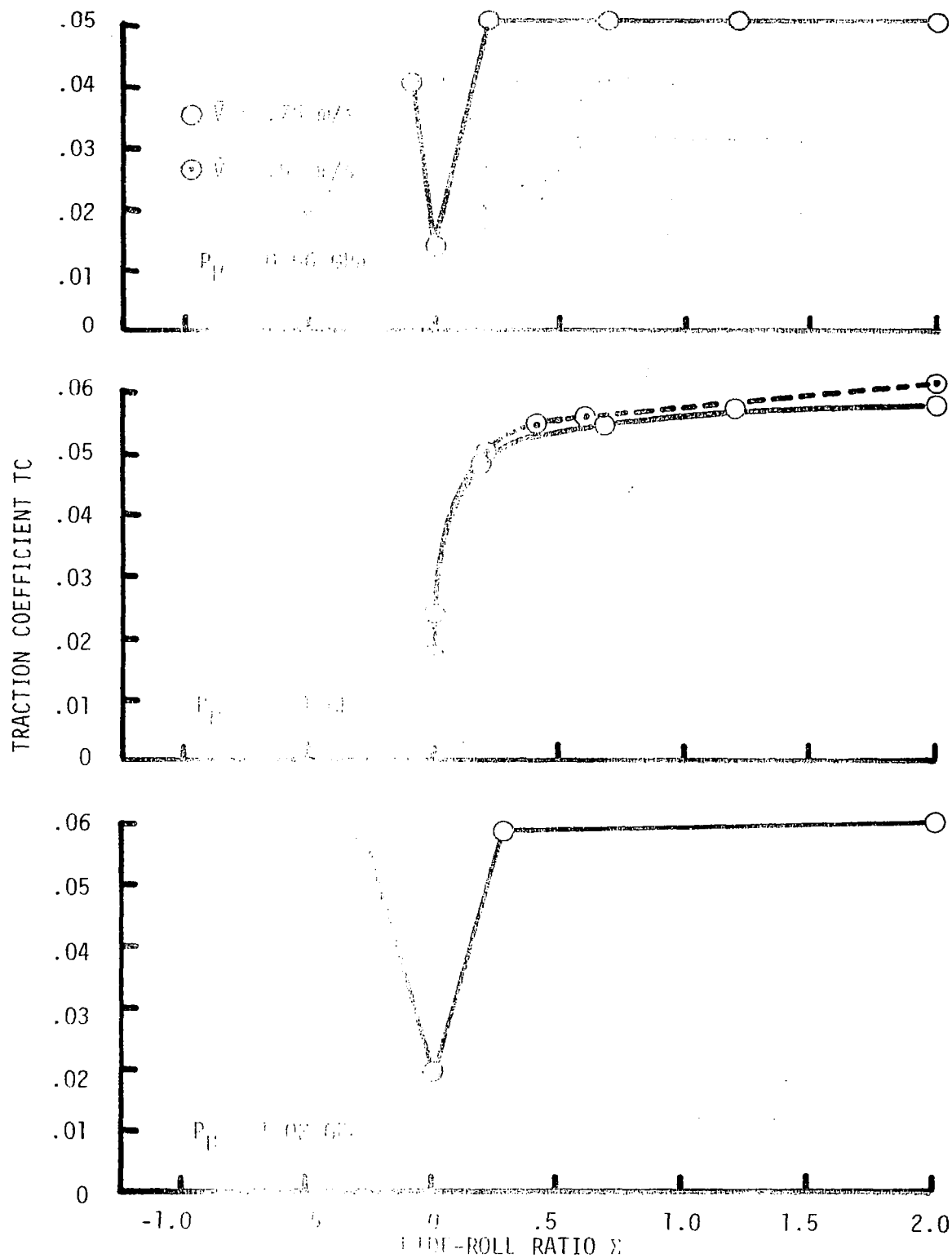


Figure 1.1.11 Traction Coefficient as a Function of Slide-Roll Ratio (0.011 μm Ra roughness).

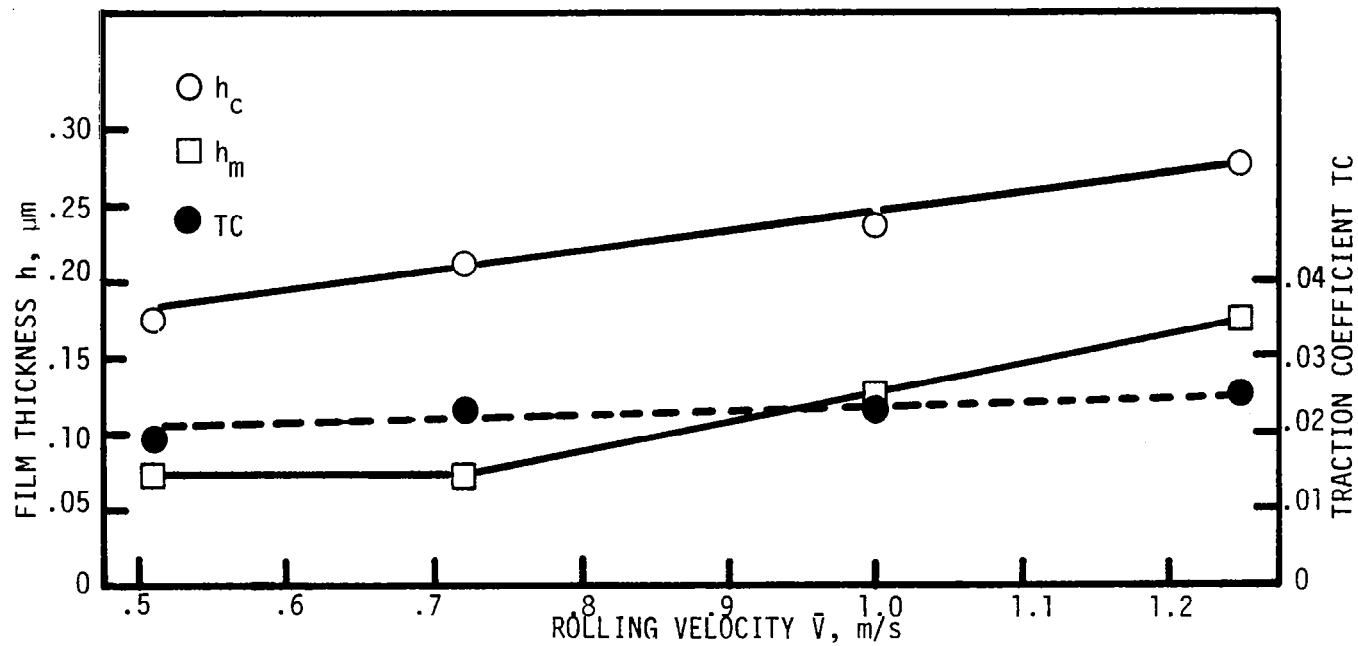


Figure III-12. Film Thickness and Traction Coefficient as a Function of Rolling Velocity ($\Sigma = 0$, $.011 \mu\text{m Ra}$ Roughness, $P_H = 1.02 \text{ GPa}$).

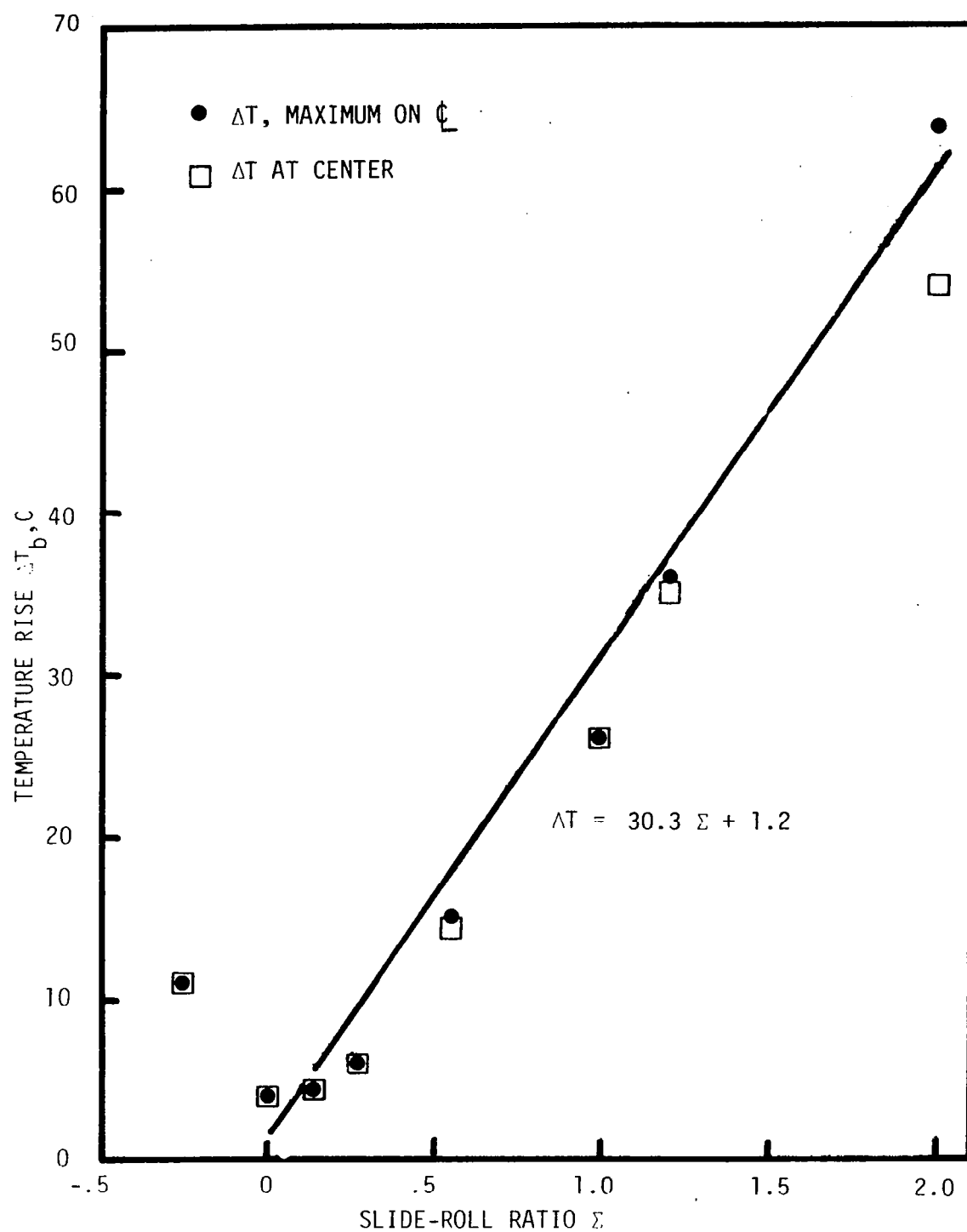


Figure III-13. Ball Surface Temperature Rise as a Function of Slide-Roll Ratio ($.011 \mu\text{m Ra}$ Roughness, $P_H = 1.02 \text{ GPa}$, $\bar{V} = 0.75 \text{ m/s}$).

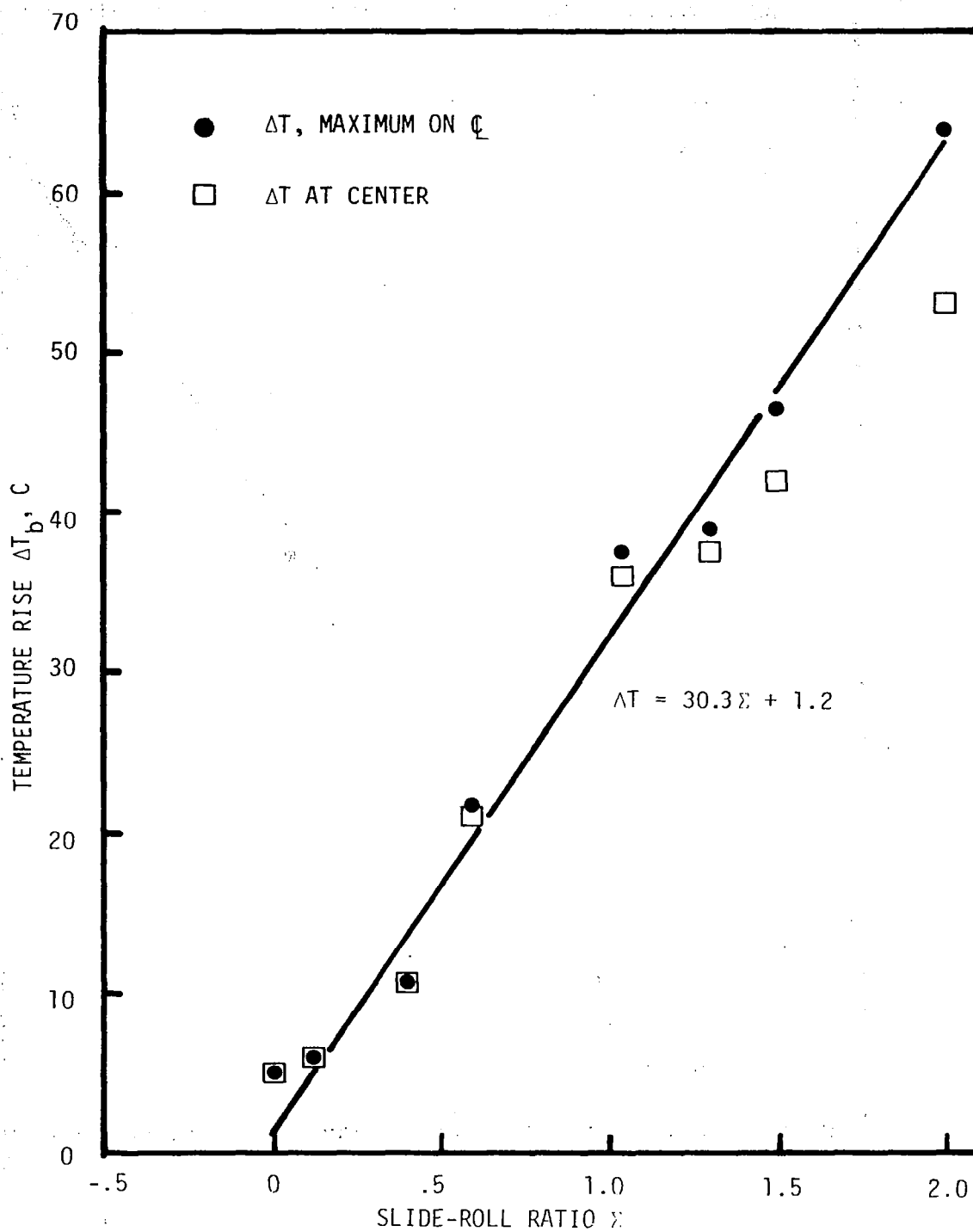


Figure III-14. Ball Surface Temperature Rise as a Function of Slide-Roll Ratio (.011 μm Ra Roughness, $P_H = 1.02$ GPa, $\bar{V} = 1.0$ m/s).

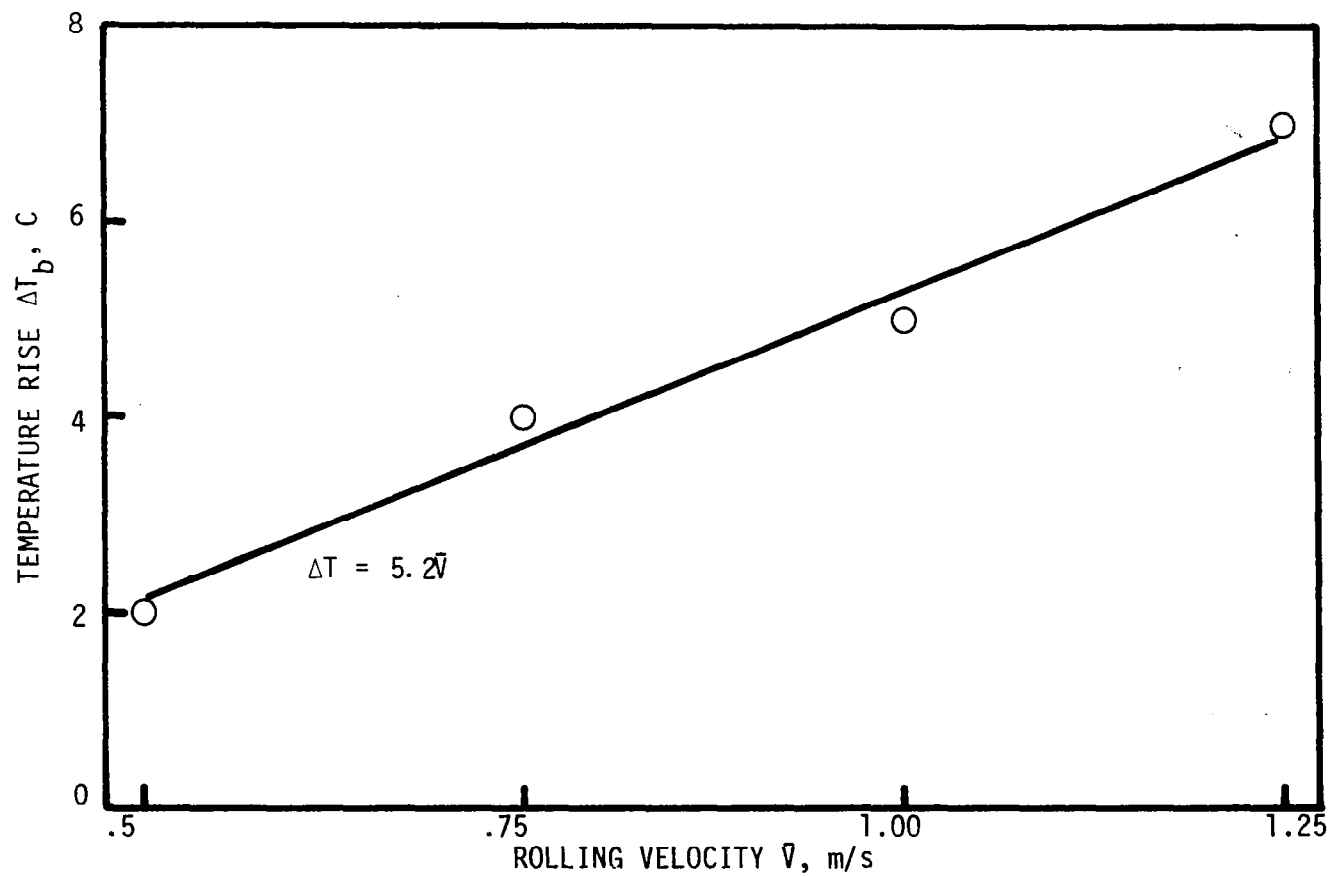


Figure III-15. Ball Surface Temperature Rise as a Function of Rolling Velocity (.011 μm Ra Roughness, $P_H = 1.02$ GPa, $\Sigma = 0$, Maximum ΔT_b Occurs at Contact Center).

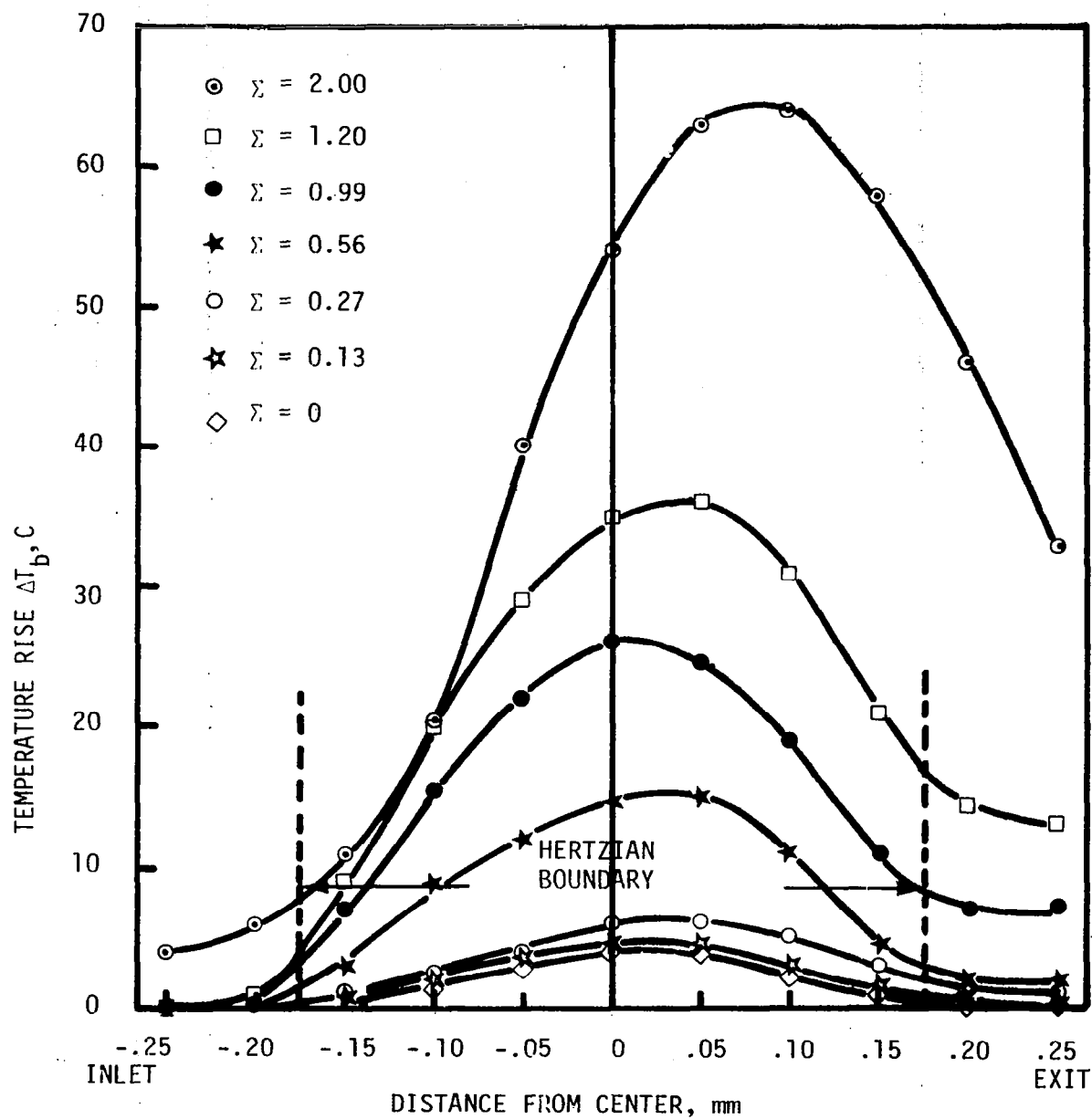


Figure III-16. Ball Surface Temperature Rise Along the Contact Centerline ($.011 \mu\text{m}$ Ra Roughness, $P_H = 1.02 \text{ GPa}$, $\bar{V} = .75 \text{ m/s}$).

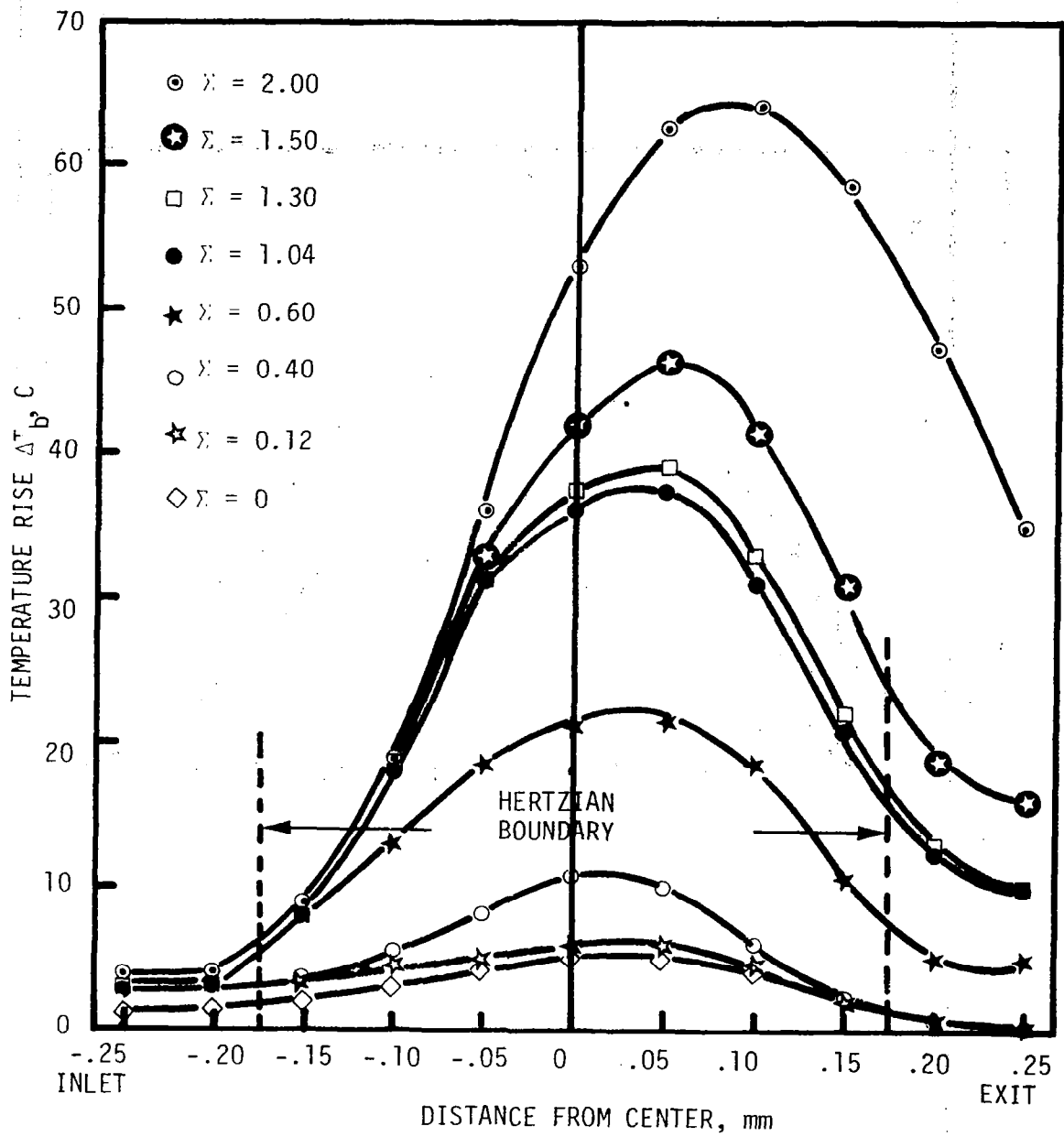


Figure III-17. Ball Surface Temperature Rise Along the Contact Centerline ($.011 \mu\text{m Ra}$ Roughness, $P_H = 1.02 \text{ GPa}$, $\bar{V} = 1.00 \text{ m/s}$).

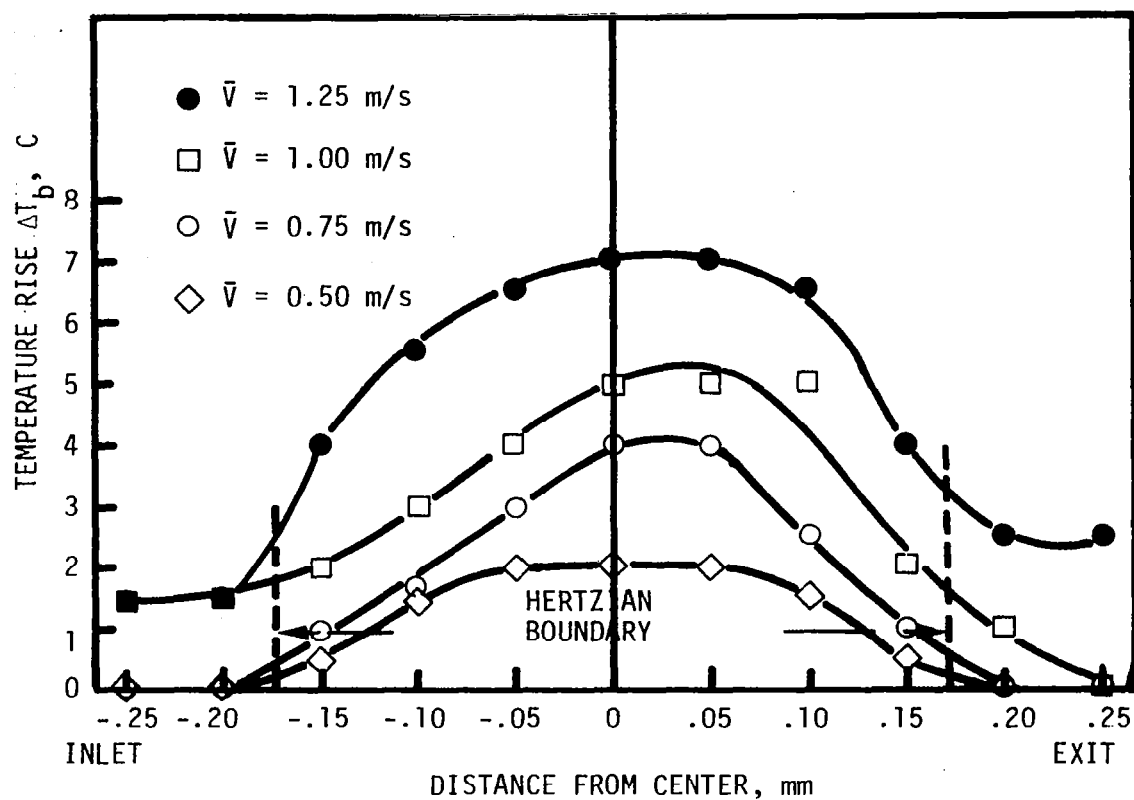


Figure III-18. Ball Surface Temperature Rise Along Contact Centerline ($.011 \mu\text{m}$ Ra Roughness, $P_H = 1.02 \text{ GPa}$, $\Sigma = 0$).

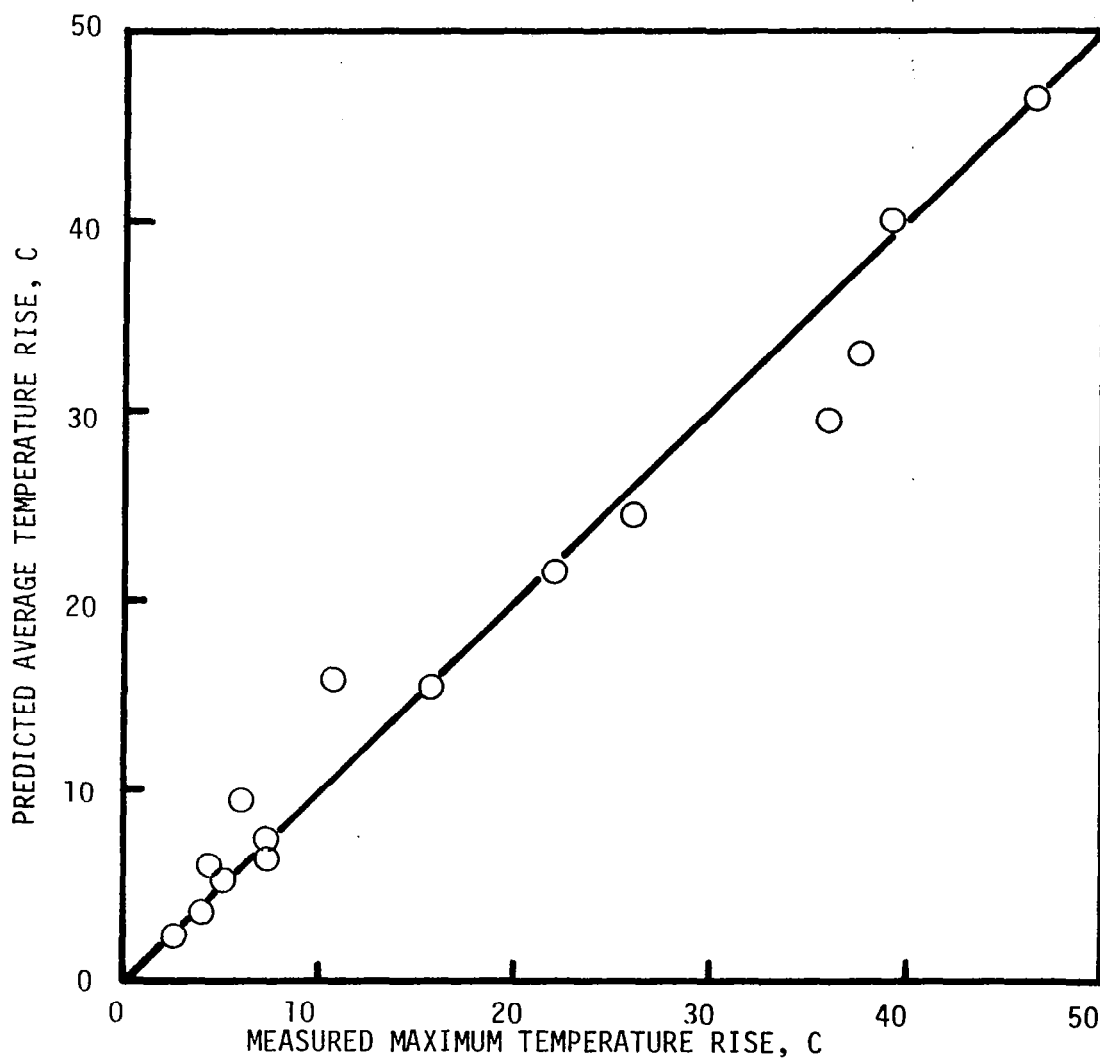


Figure III-19. Comparison of Predicted Average and Actual Maximum Ball Surface Temperature Rises for $L > 5$. Combined sliding and rolling as per Equation 21.

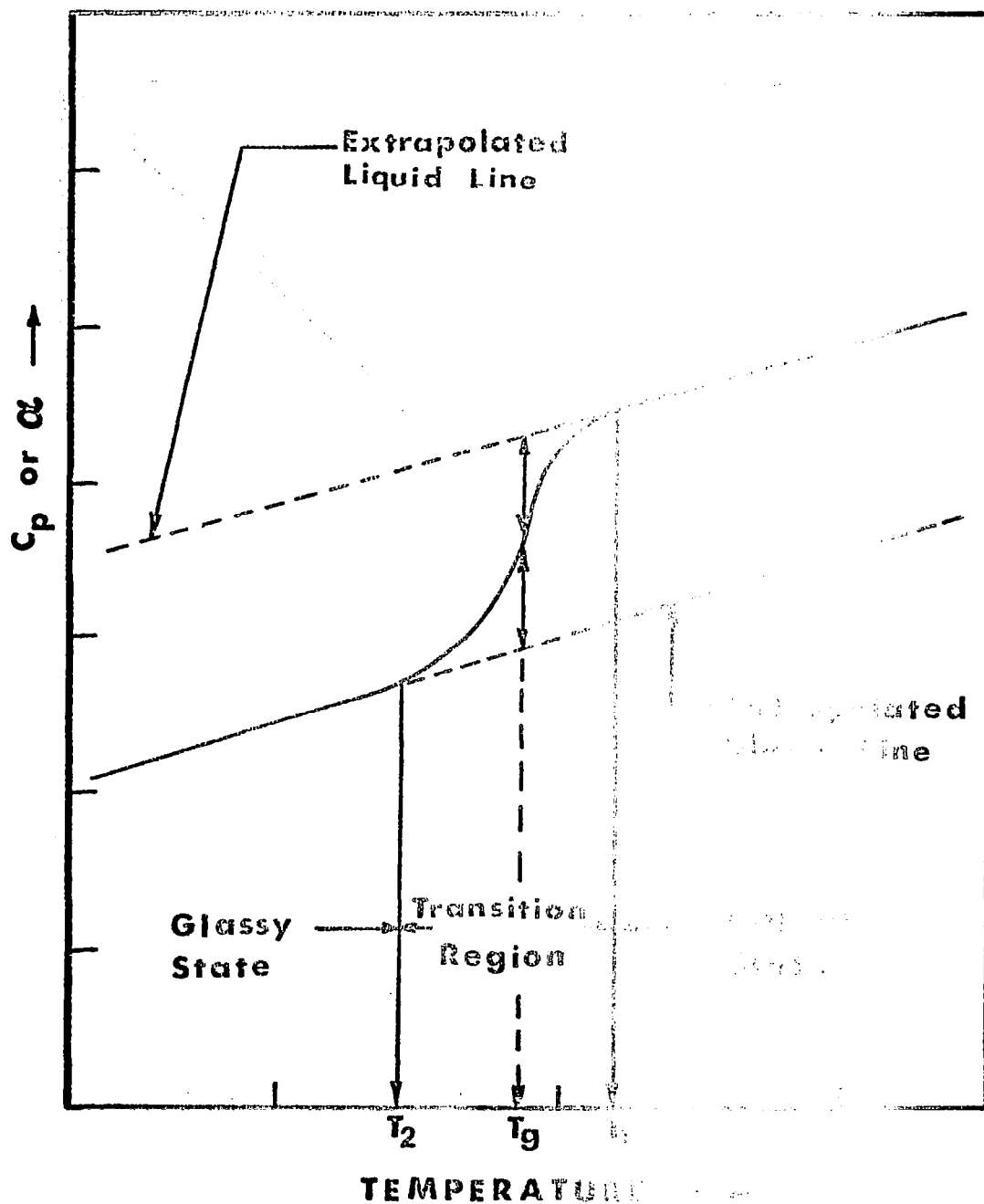


Figure IV-1. Thermal Expansion Coefficient and Specific Heat for a Typical Glassy Material.

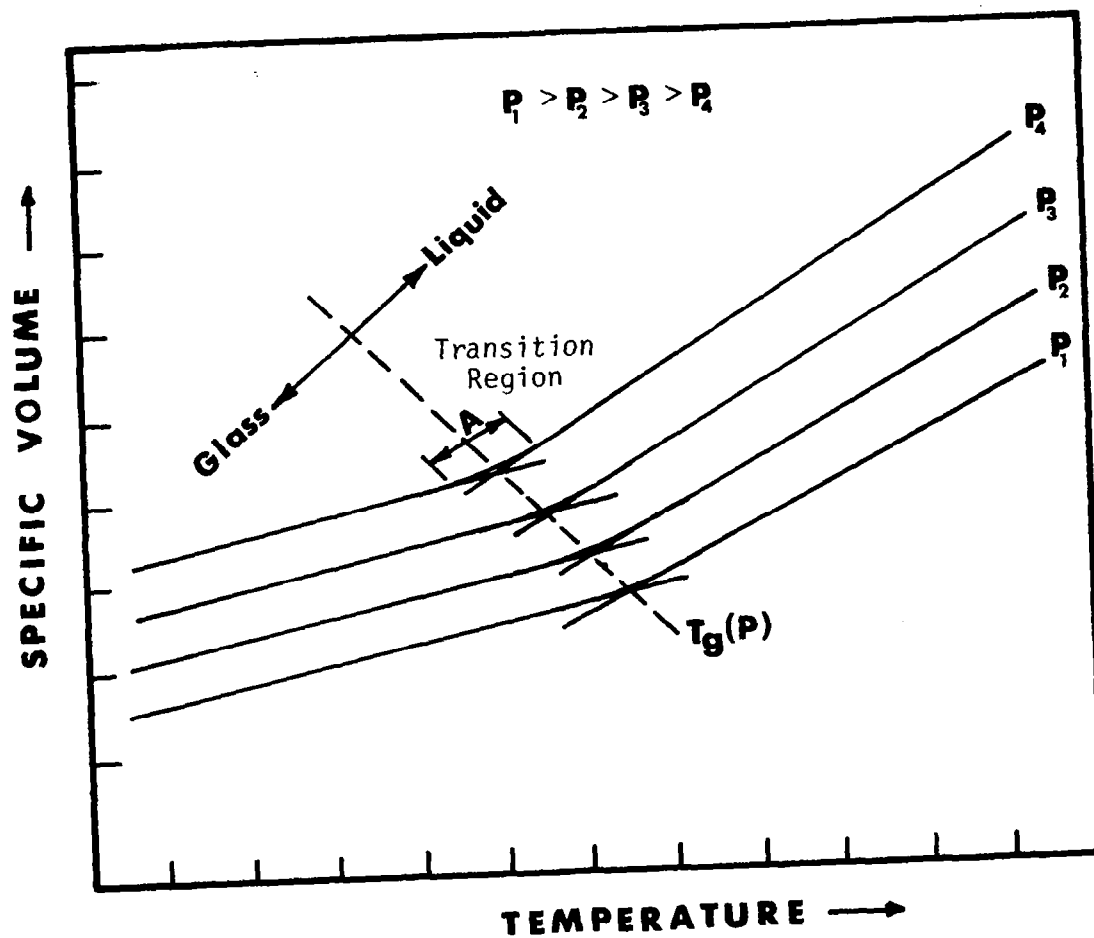


Figure IV-2. Typical Plot of Specific Volume Versus Temperature for a Glassy Material at Different Formation Pressures.

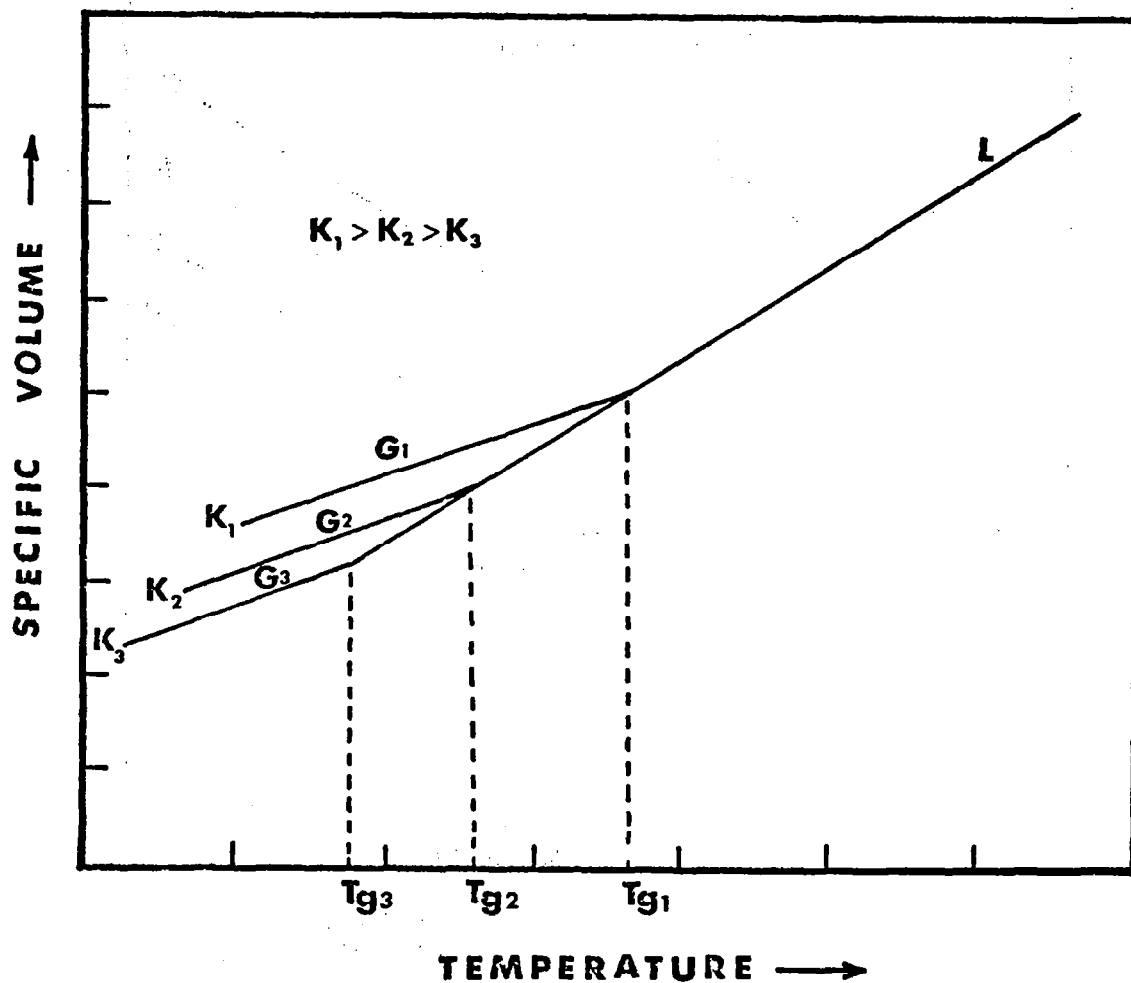


Figure IV-3. Dependence of the Glass Transition Temperature on the Cooling Rate, K_i . L = Liquid and G = Glass.

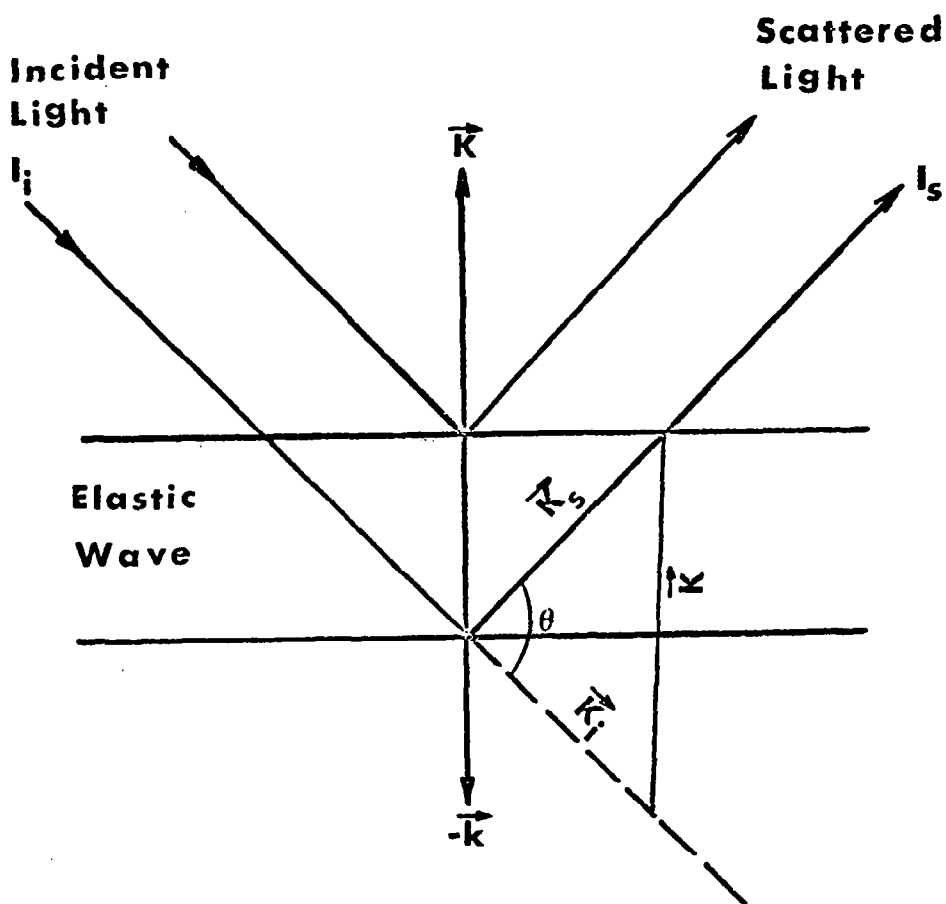


Figure IV-4. Bragg Condition of Light Scattered at an Angle θ Relative to the Incident Light Beam.

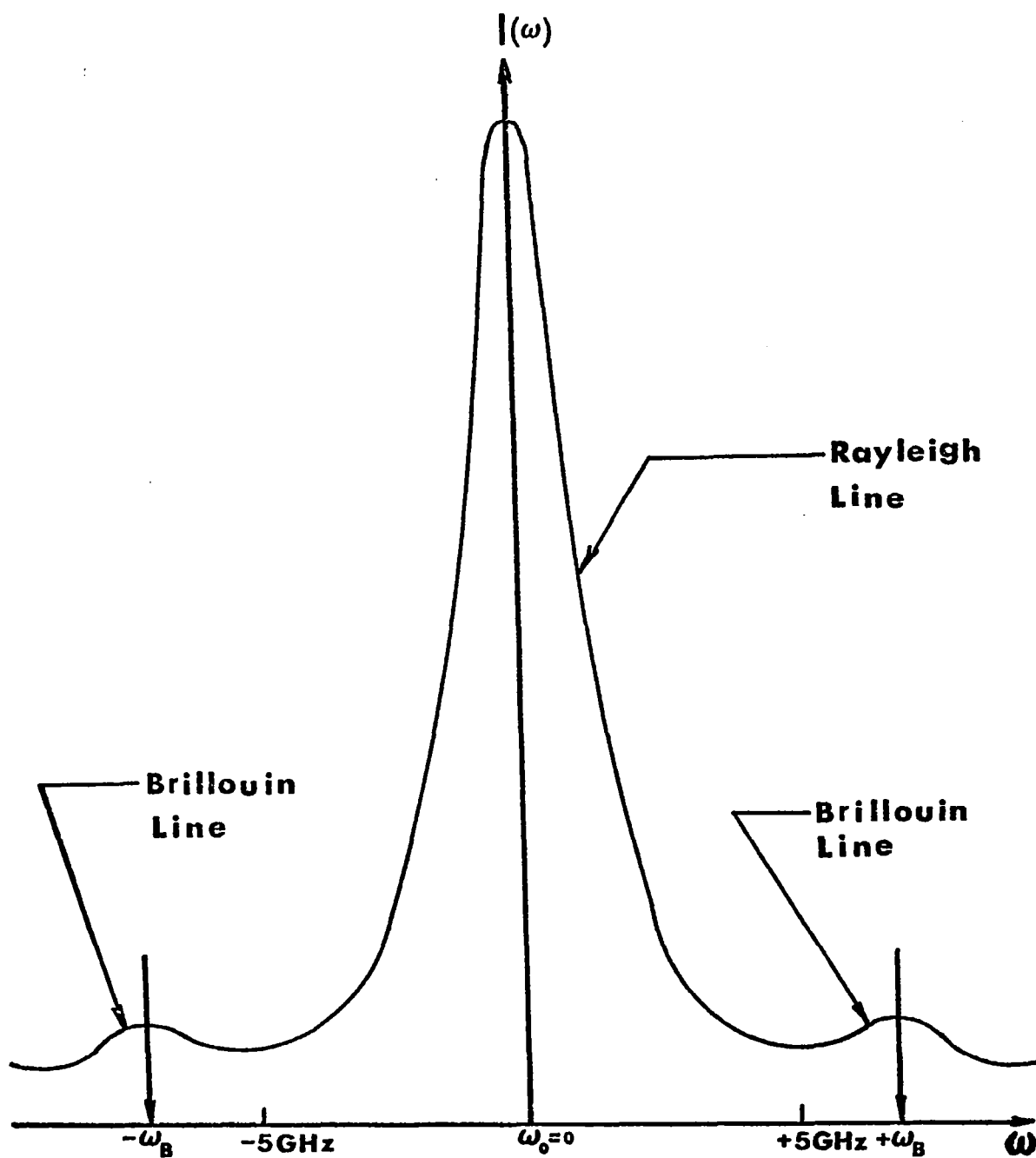


Figure IV-5. Frequency Spectrum of a Naphthenic Base Oil at 24.4°C and Atmospheric Pressure.

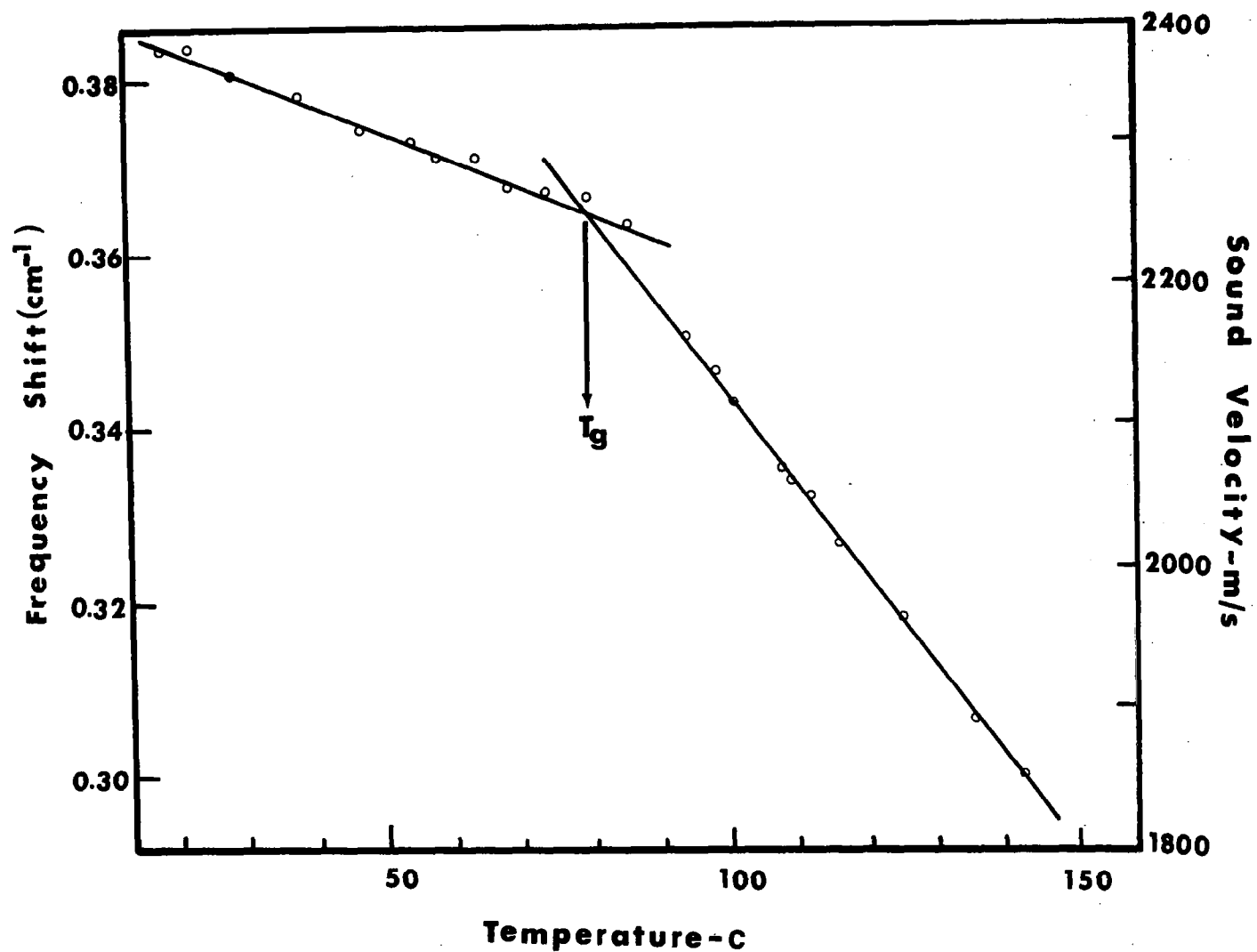


Figure IV-6. The Variation of the Brillouin Frequency Shift and the Sound Velocity with Temperature at Atmospheric Pressure for Atactic Polystyrene [53].

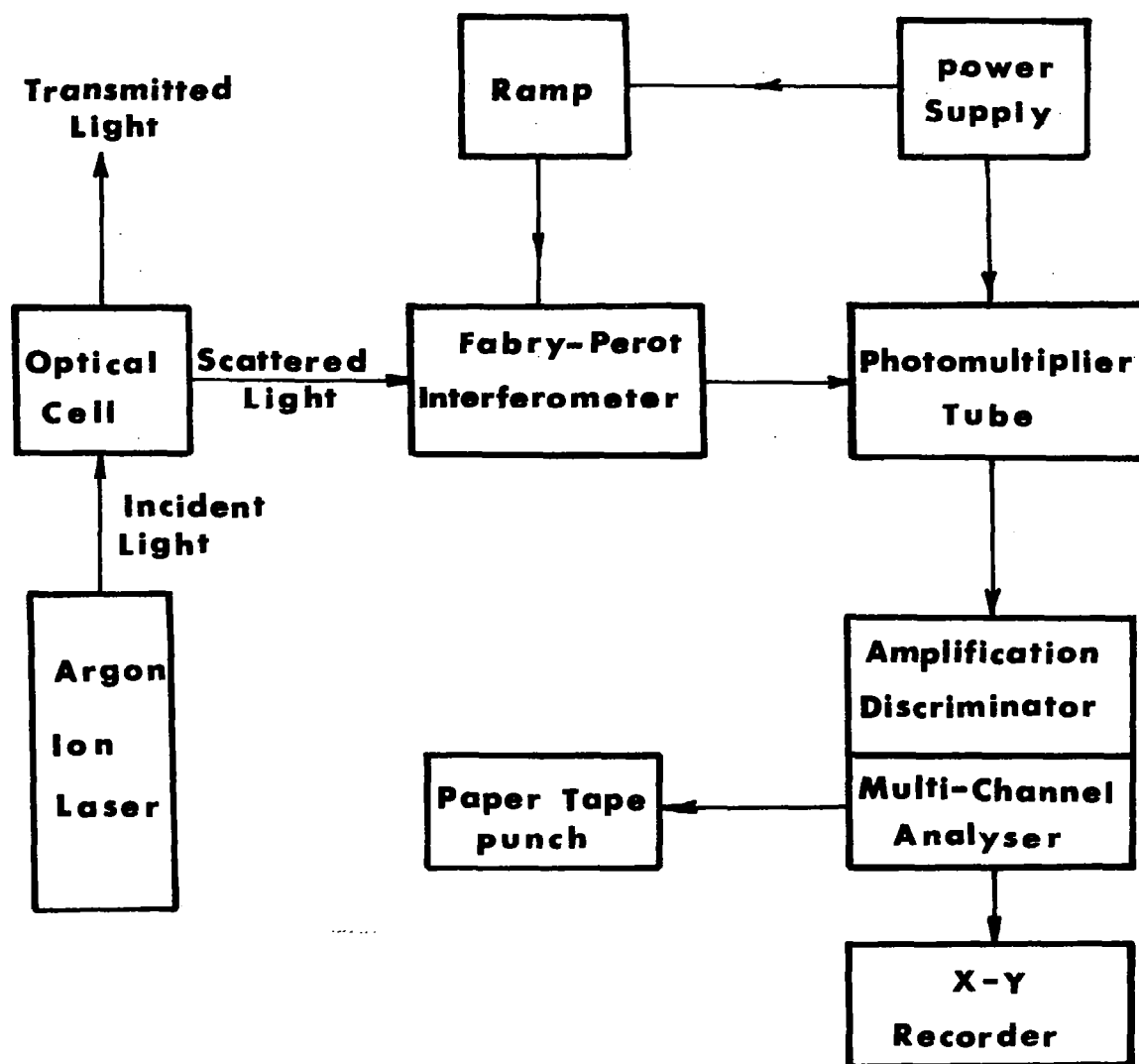


Figure IV-7. Schematic Arrangement of the Light-Scattering Experiment.

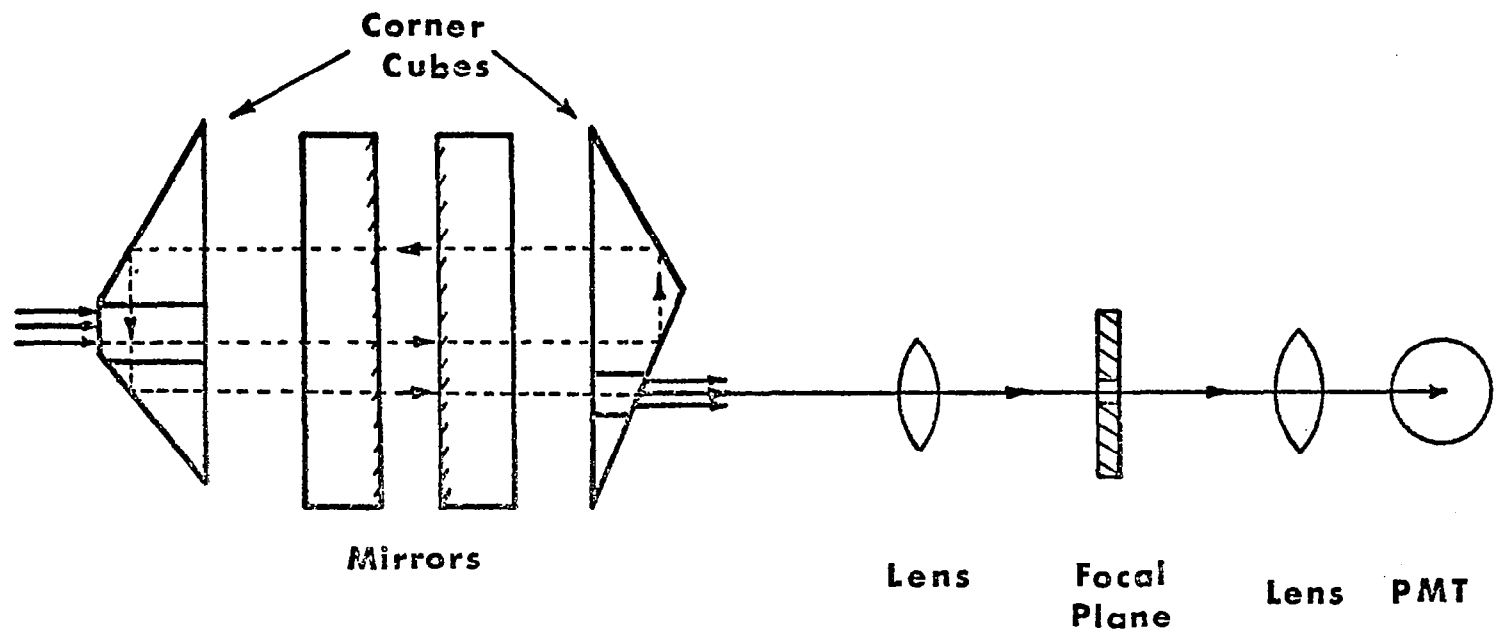


Figure IV-8. Schematic Arrangement of the Fabry-Perot Interferometer.

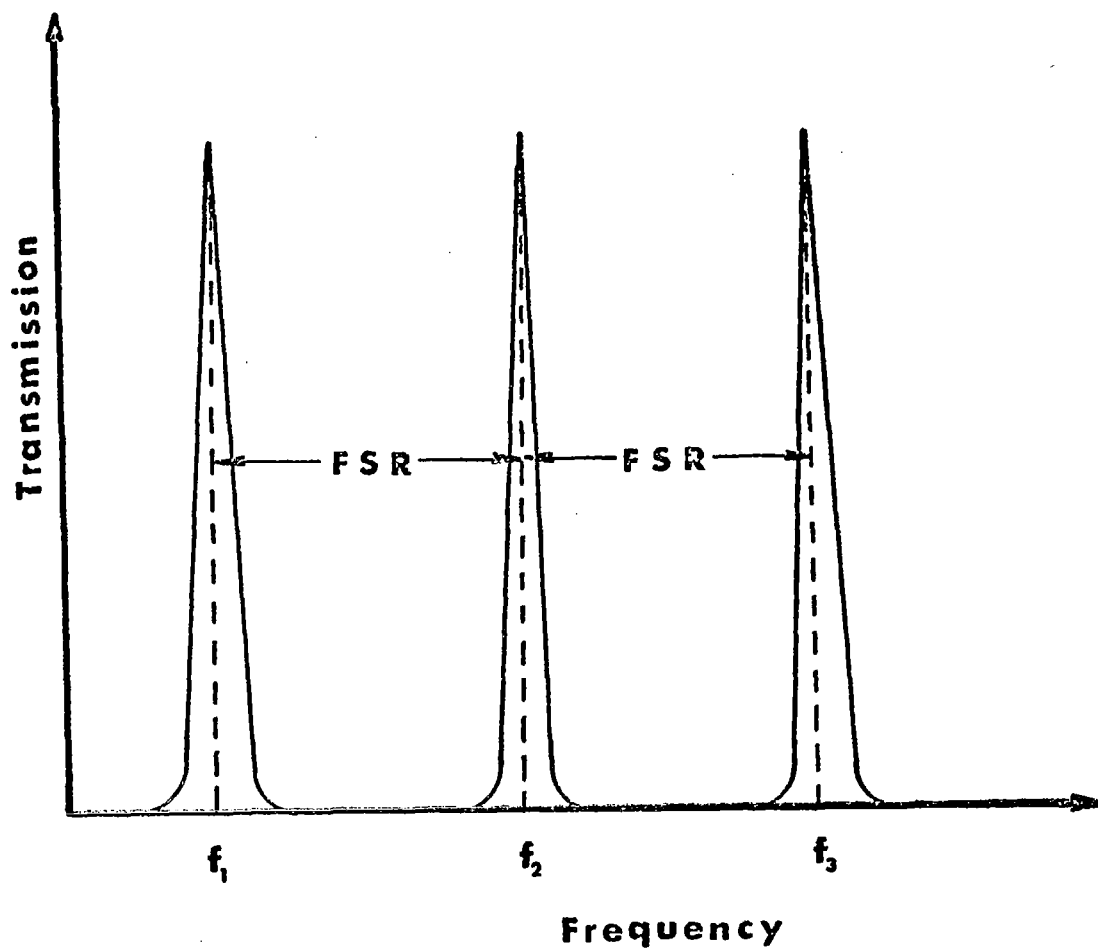


Figure IV-9. Transmission of the Fabry-Perot Interferometer as a Function of Light Frequency.

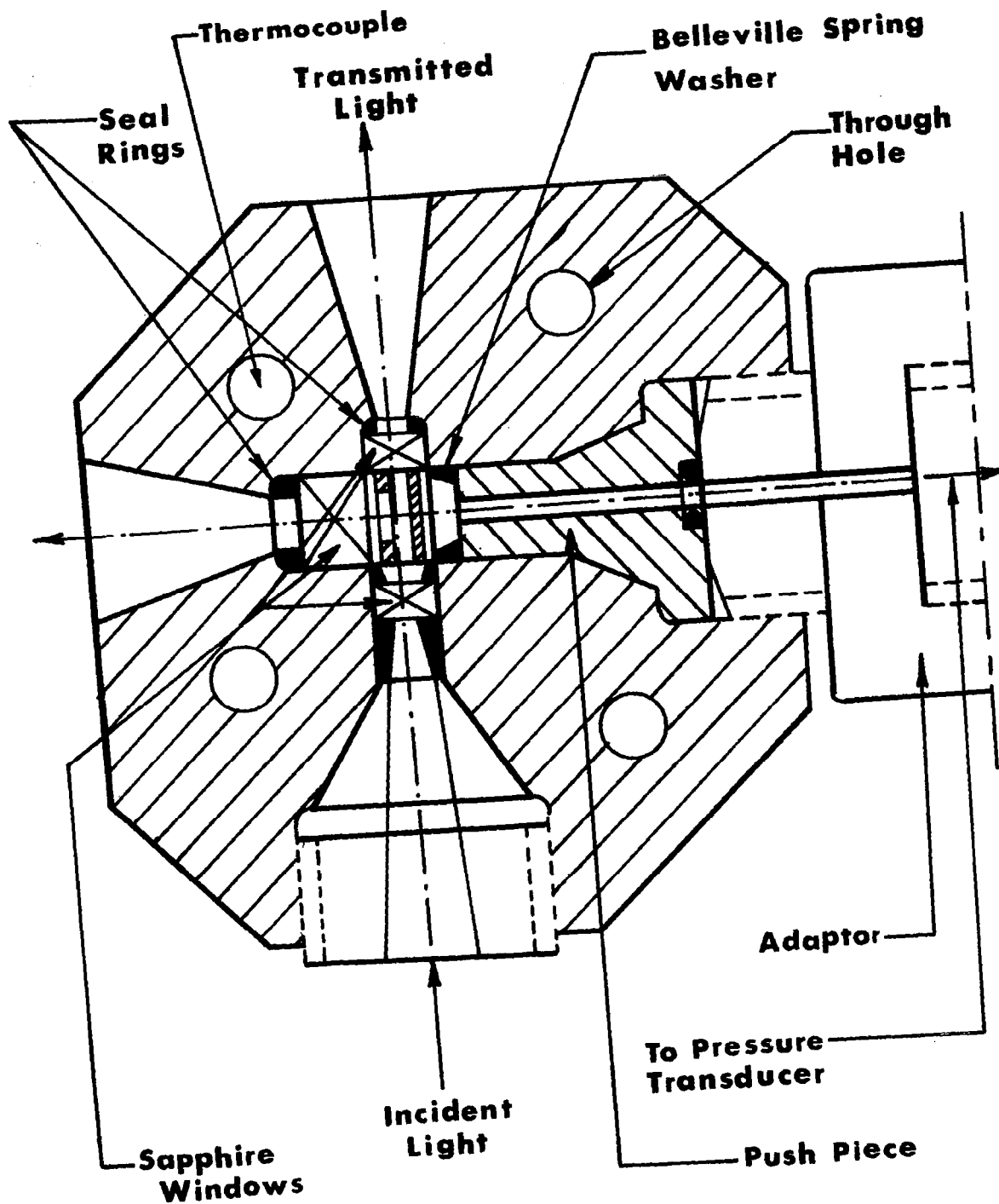


Figure IV-10. Schematic of Light-Scattering Cell. The Intensifier is Attached Perpendicular to the Paper Plane at the Centerline of the Cell.

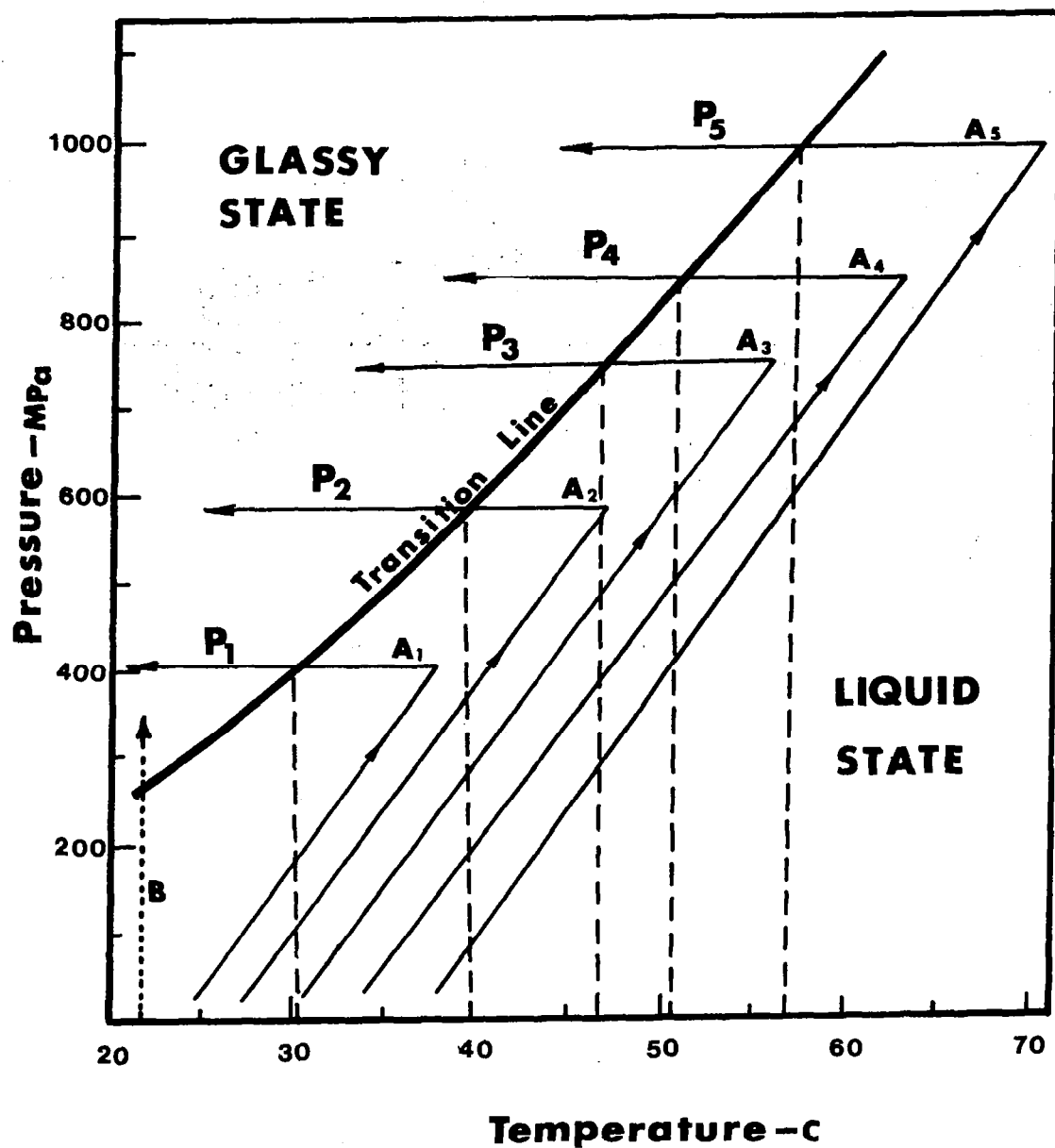


Figure IV-11. Schematic of Formation Histories Used to Form the Glass. A_i and B Represent Constant Formation Histories at Pressure P_i and Room Temperature Respectively.

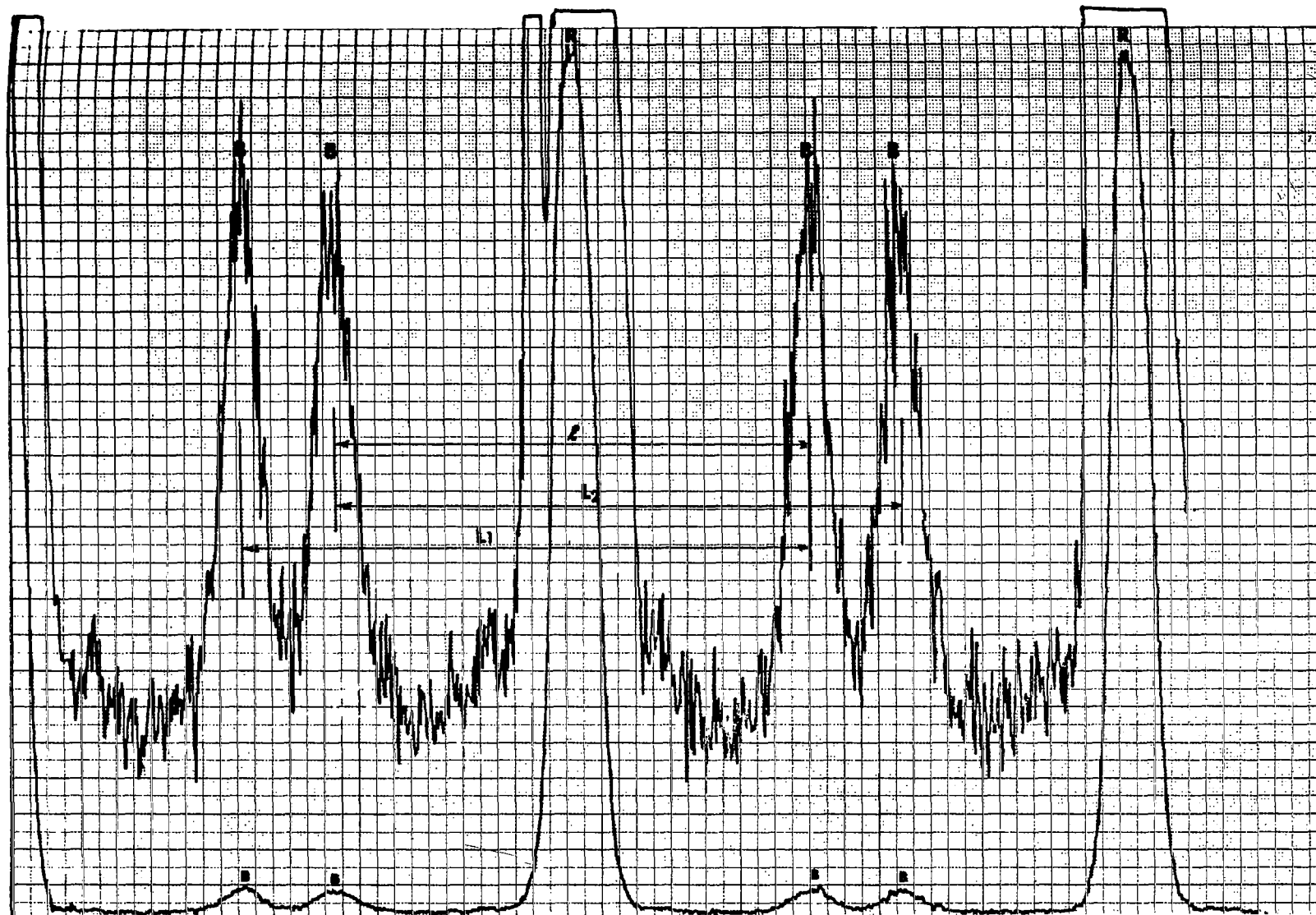


Figure IV-12. Frequency Spectrum for 5P4E Fluid Recorded at 0.19 GPa and 24.4C (History B).
B and R represent the Brillouin and Rayleigh Components Respectively.

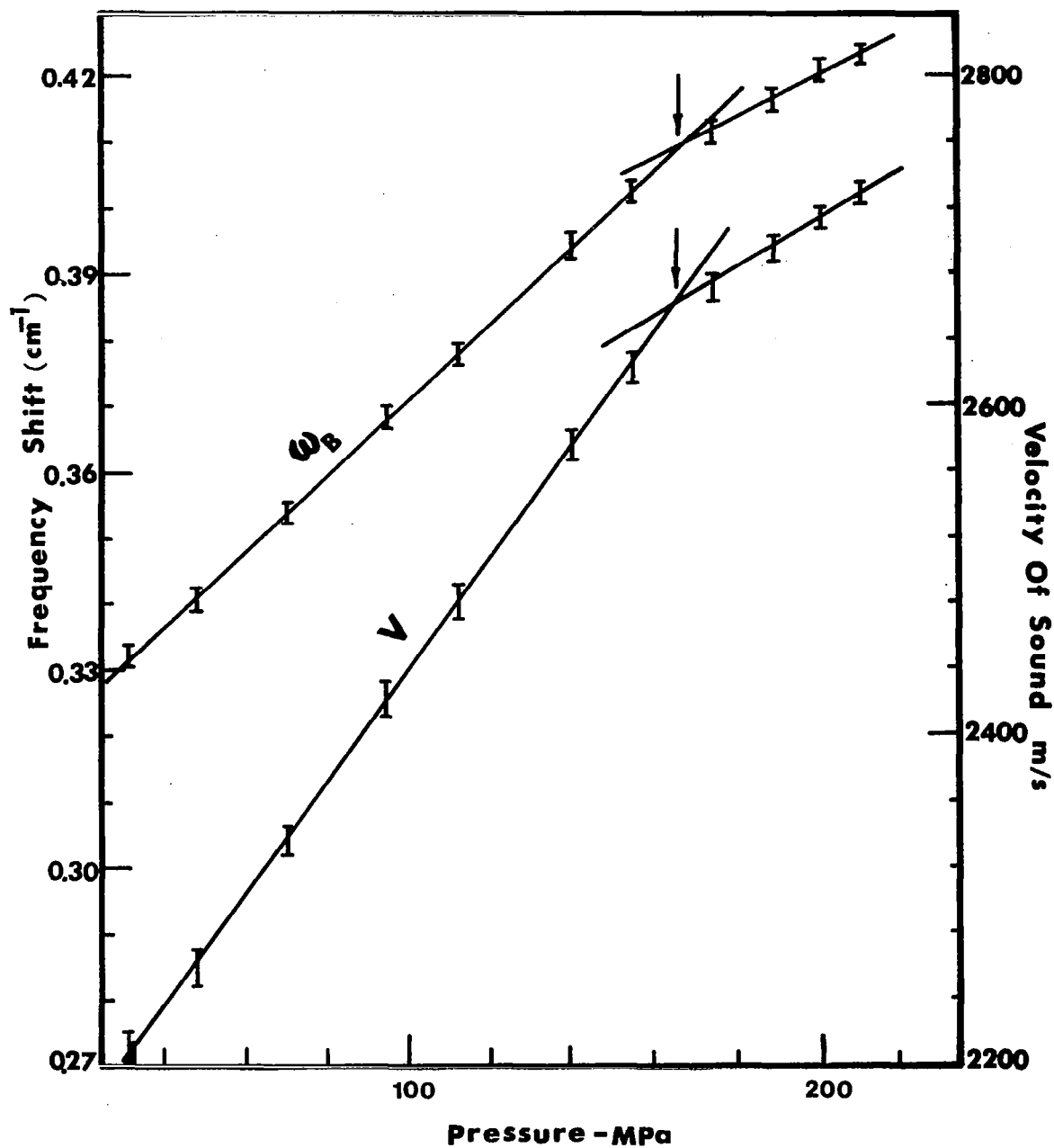


Figure IV-13. Variation of Frequency Shift and Velocity of Sound with Pressure at 24.4C (76 F) for 5P4E Fluid (History B). Arrows Indicate Glass Transition.

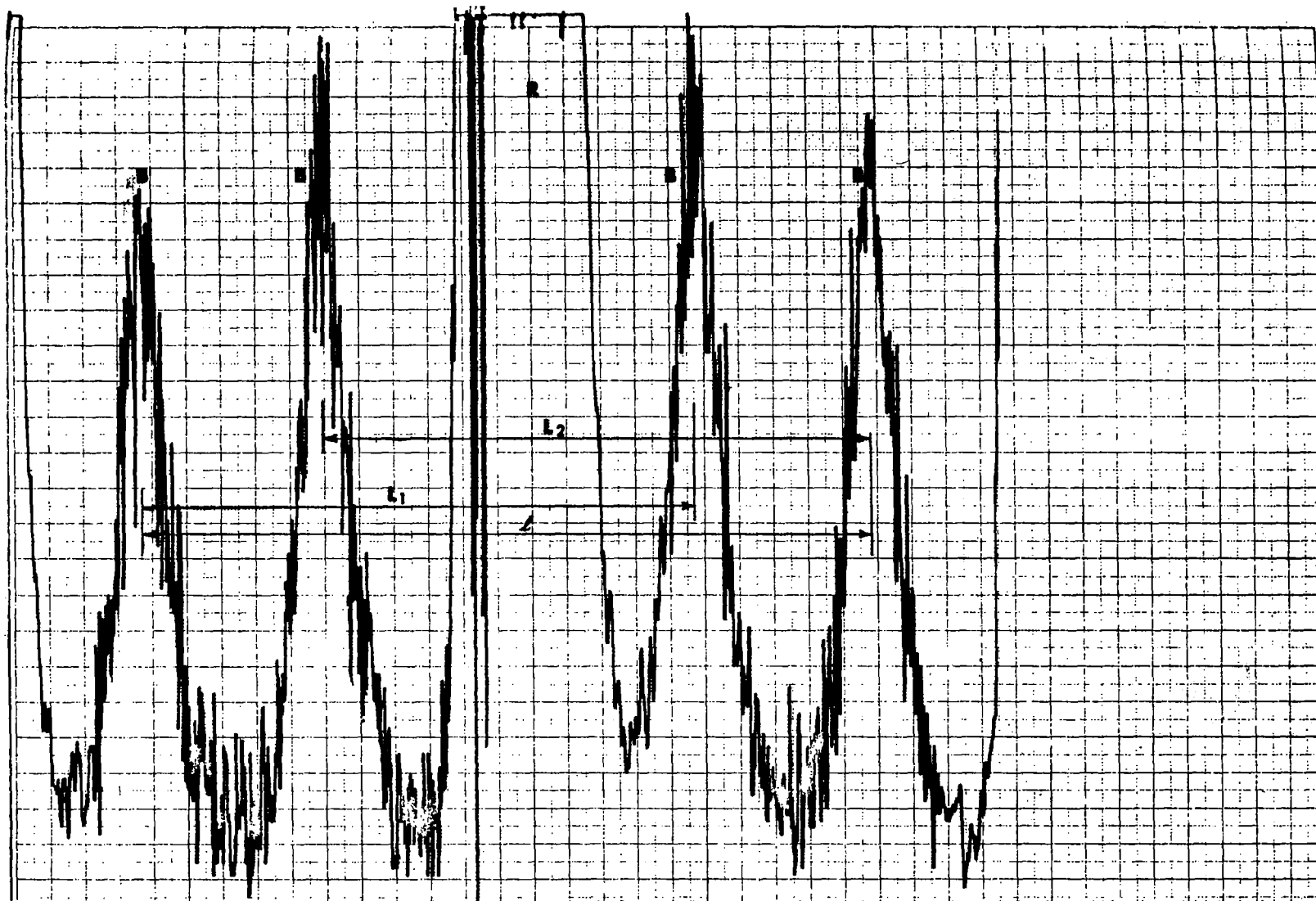


Figure IV-14. Frequency Spectrum for 5P4E Fluid Recorded at 0.40 GPa (59,000 psi) and 64.4C (148F) (History A). B and R Represent the Brillouin and Rayleigh Components Respectively.

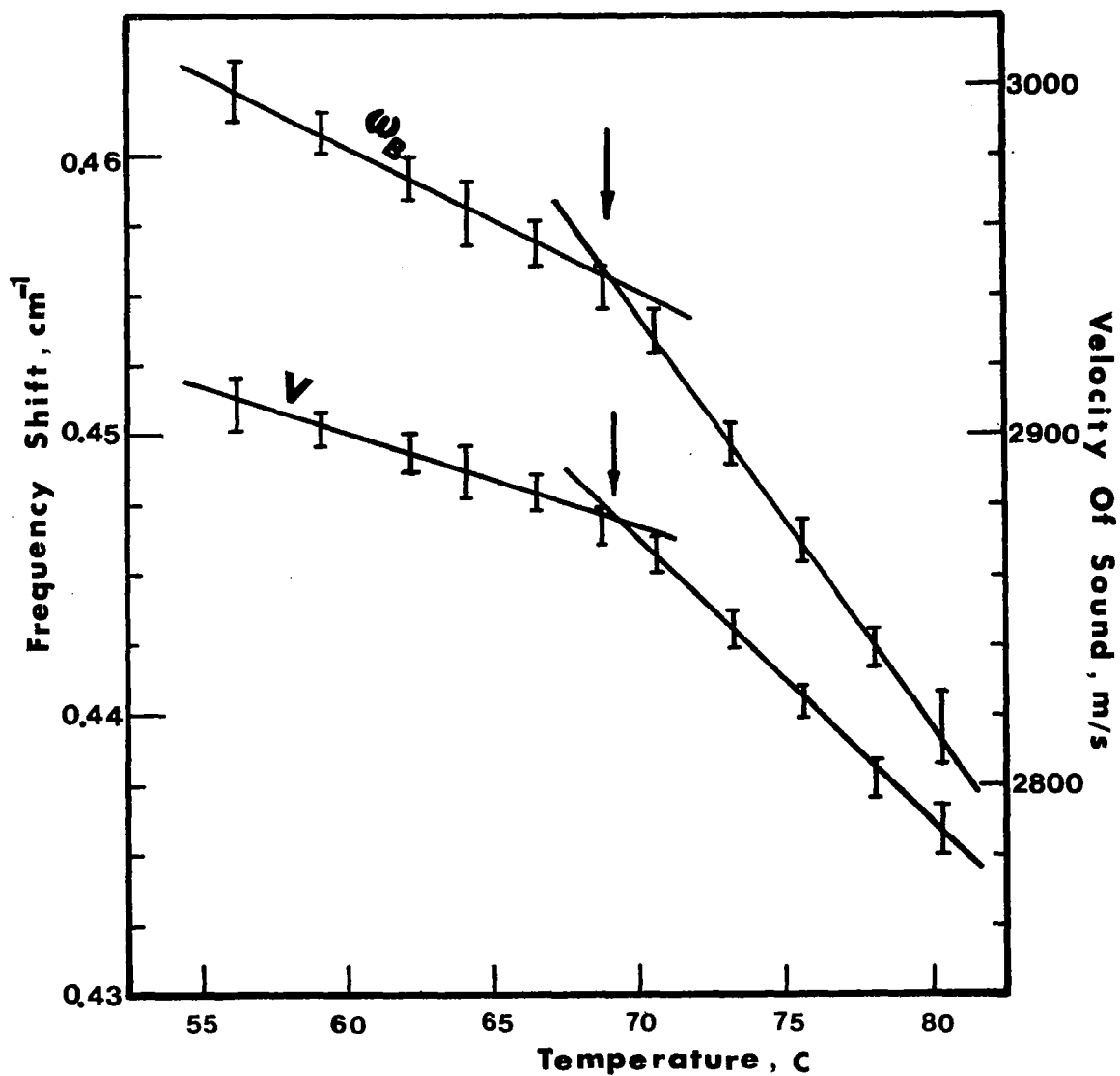


Figure IV-15. Variation of Frequency Shift and Velocity of Sound with Temperature at 0.40 GPa (59,000 psi) for 5P4E (History A). Arrows Indicate Glass Transition.

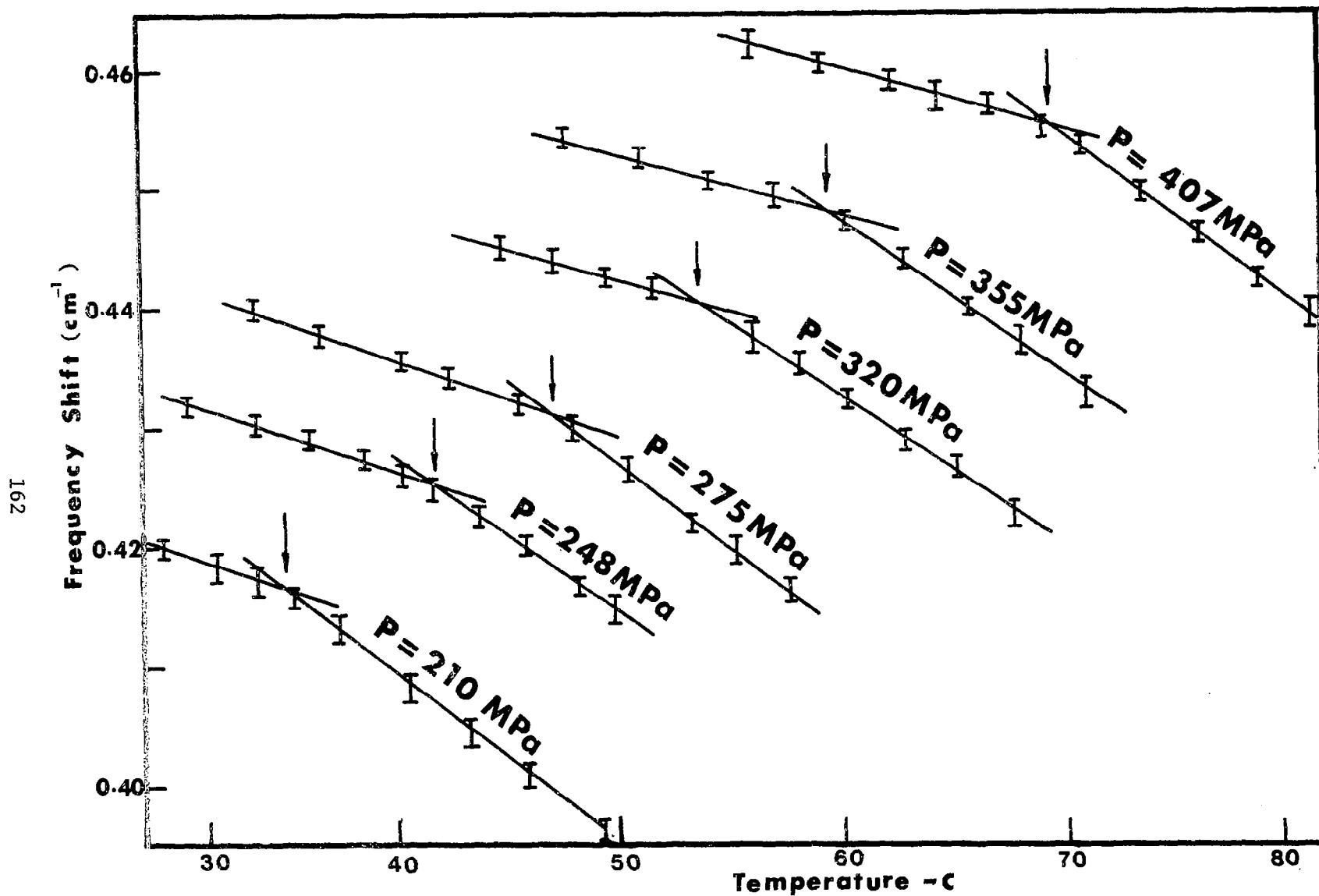


Figure IV-16. Frequency Shift Dependence on Temperature at Different Constant Pressures for 5P4E Fluid (History A). Arrows Indicate T_g .

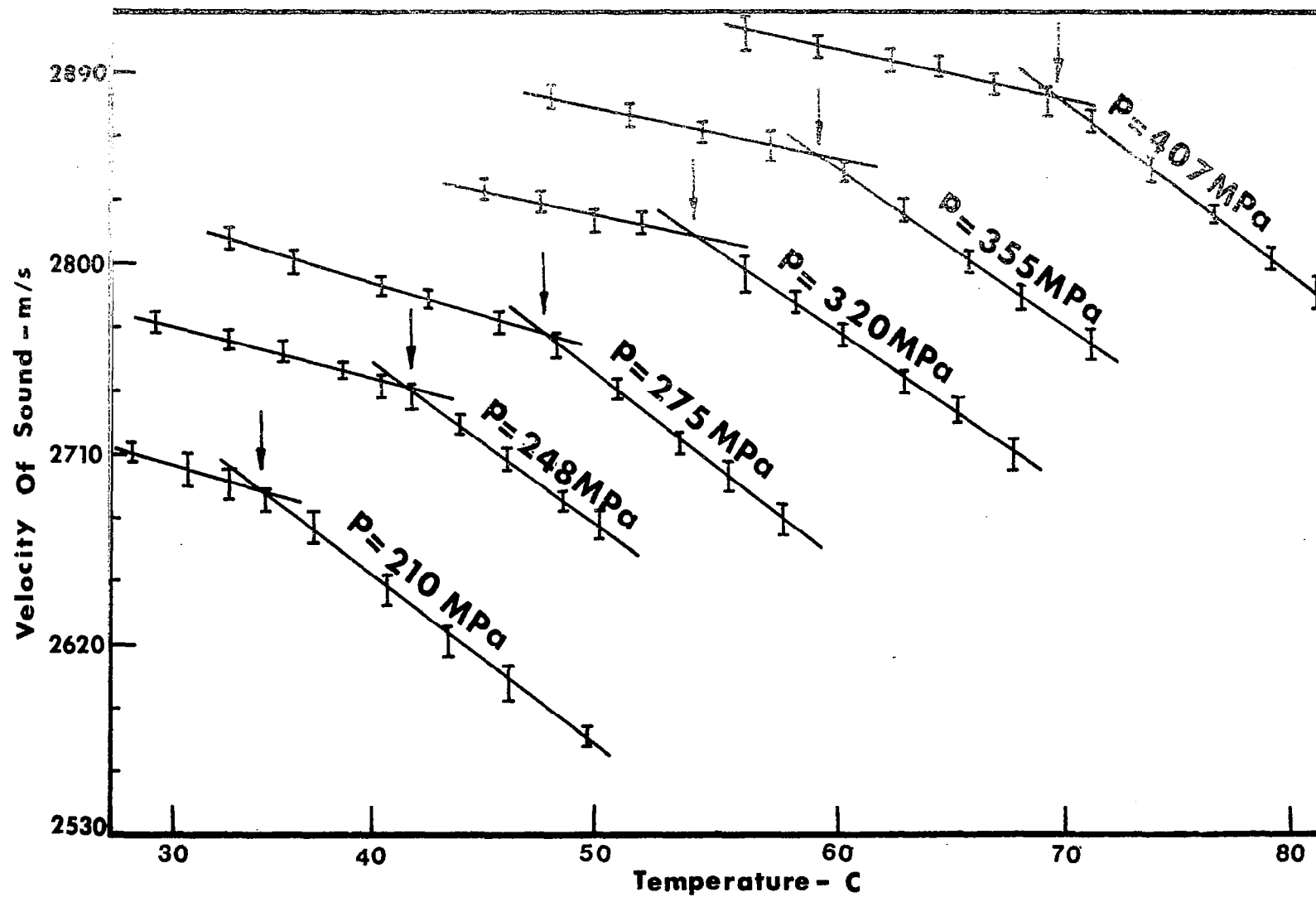


Figure IV-17. Velocity of Sound Dependence on Temperature at Different Constant Pressures for 5P4E Fluid (History A). Arrows Indicate T_q .

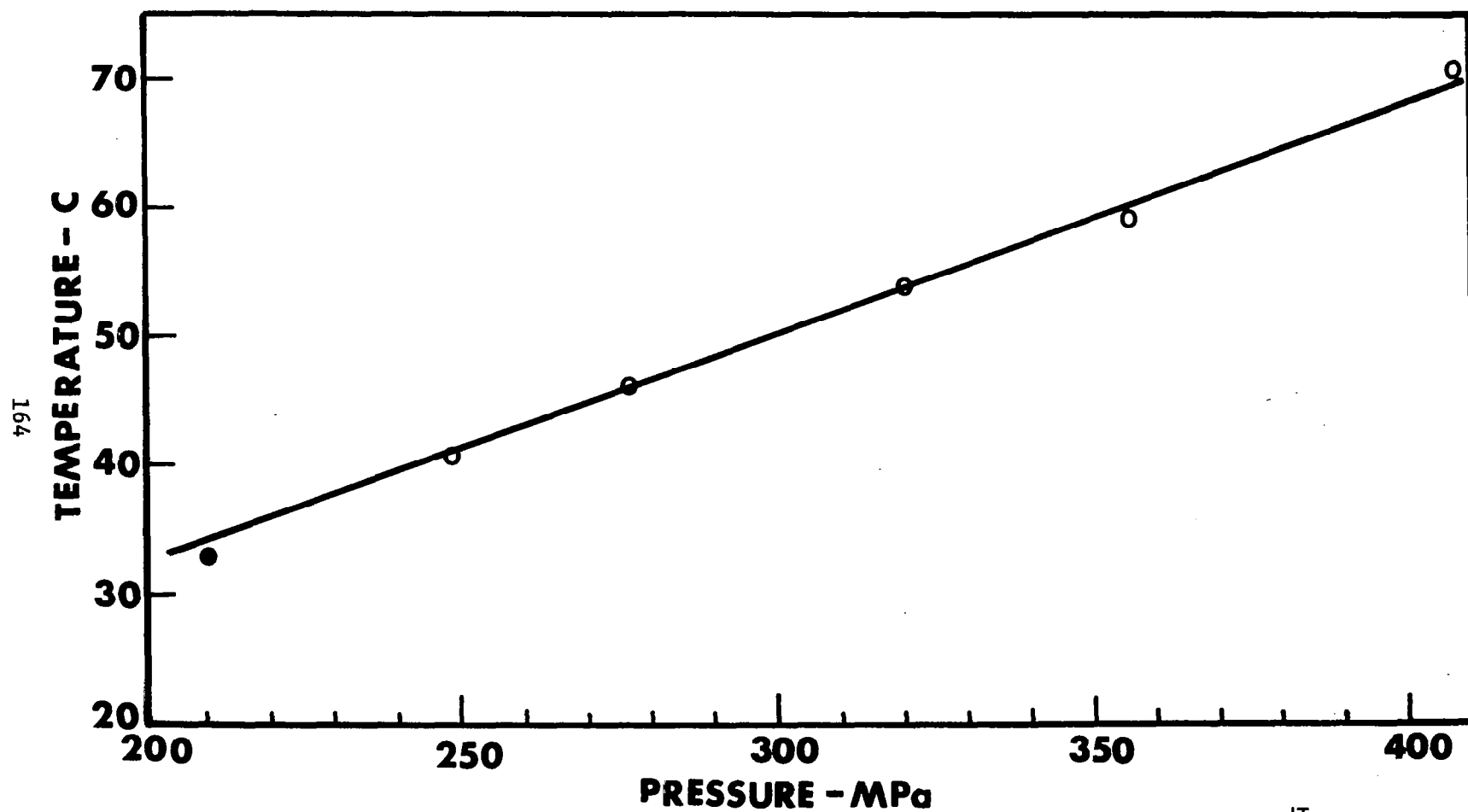


Figure IV-18. Phase Diagram for 5P4E Fluid Based on Light Scattering Experiment. $\frac{dT_g}{dP} = 183 \text{ C/GPa}$.
History A. History B.

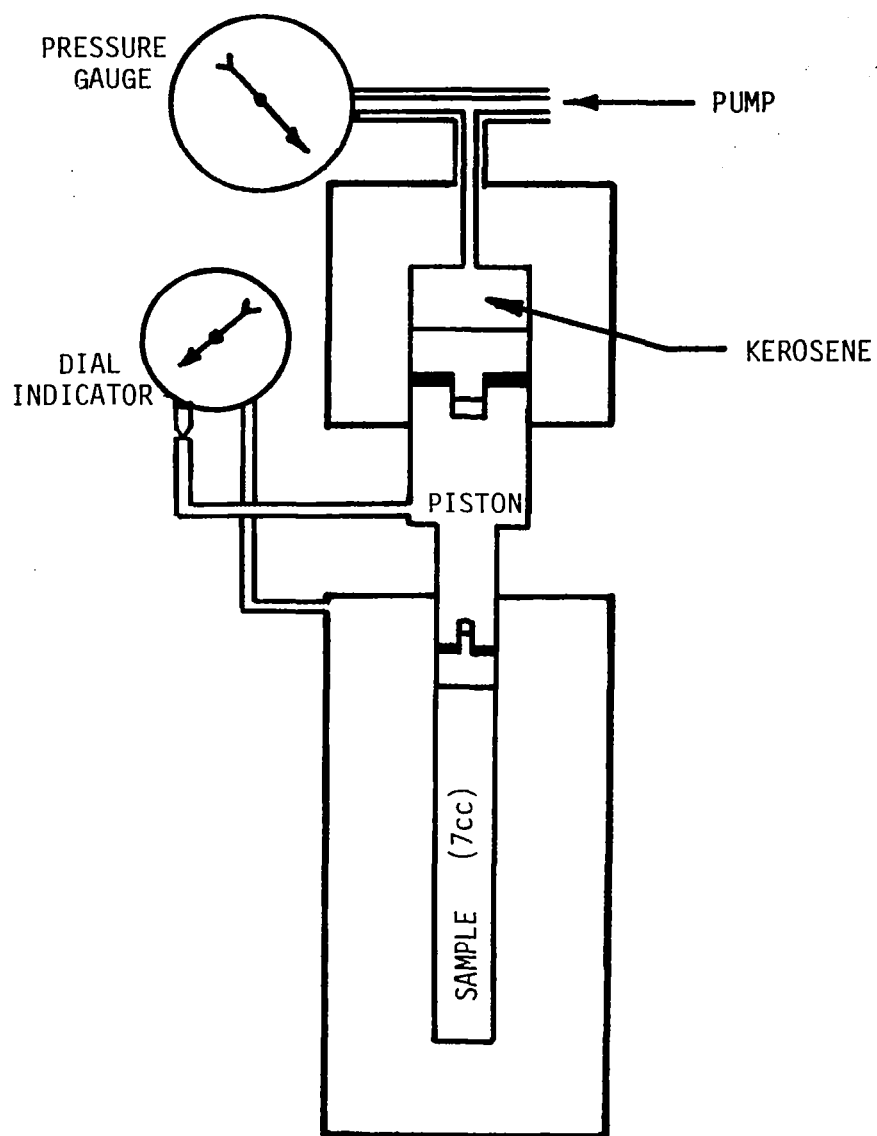


Figure IV-19. High Pressure Dilatometer (.13 to 1.2 GPa).

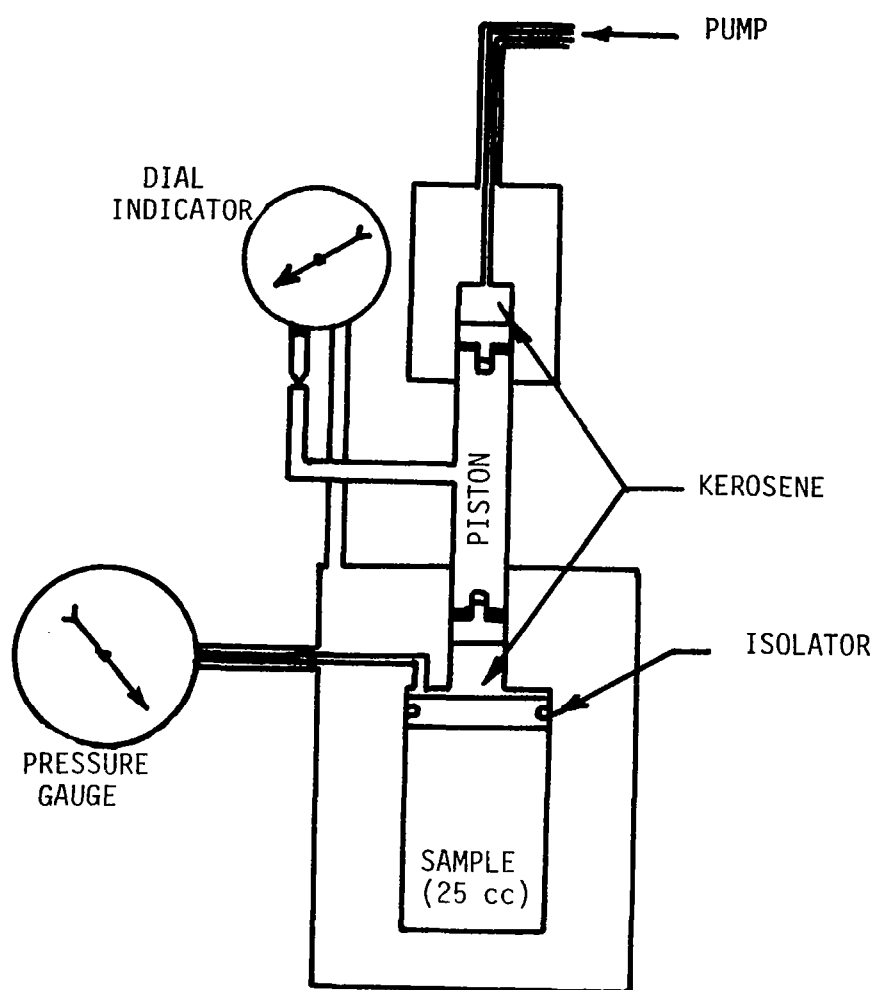


Figure IV-20. Low Pressure Dilatometer.
(.014 to .27 GPa)

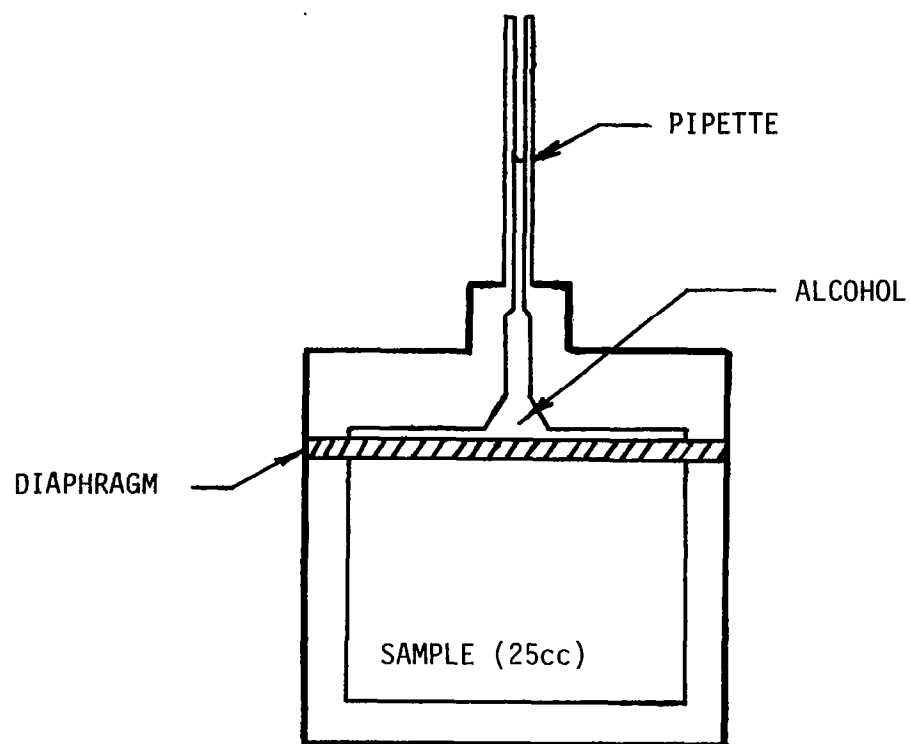


Figure IV-21. Atmospheric Pressure Dilatometer.

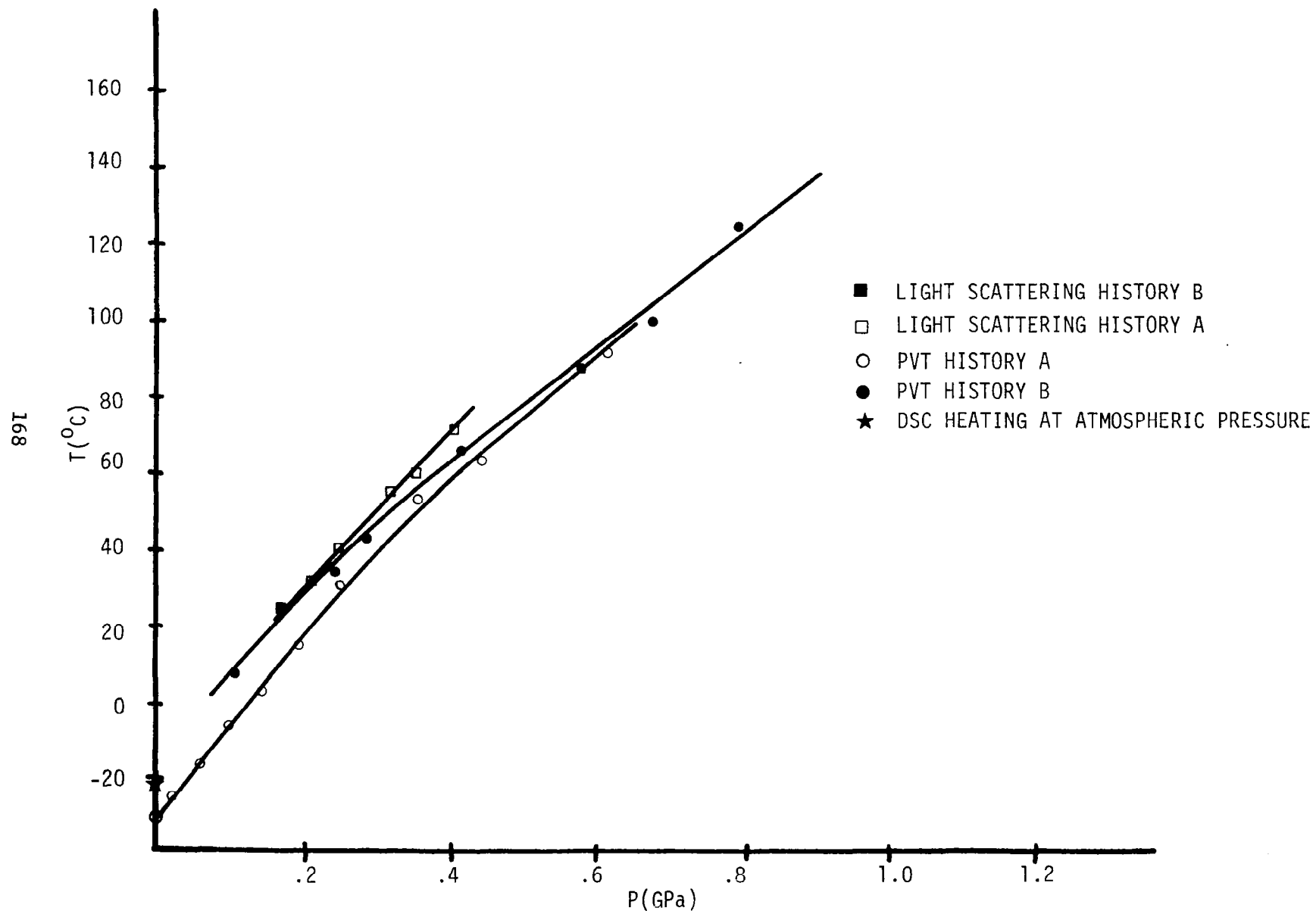


Figure IV-22. Comparison of Glass Transition of 5P4E by Various Methods.

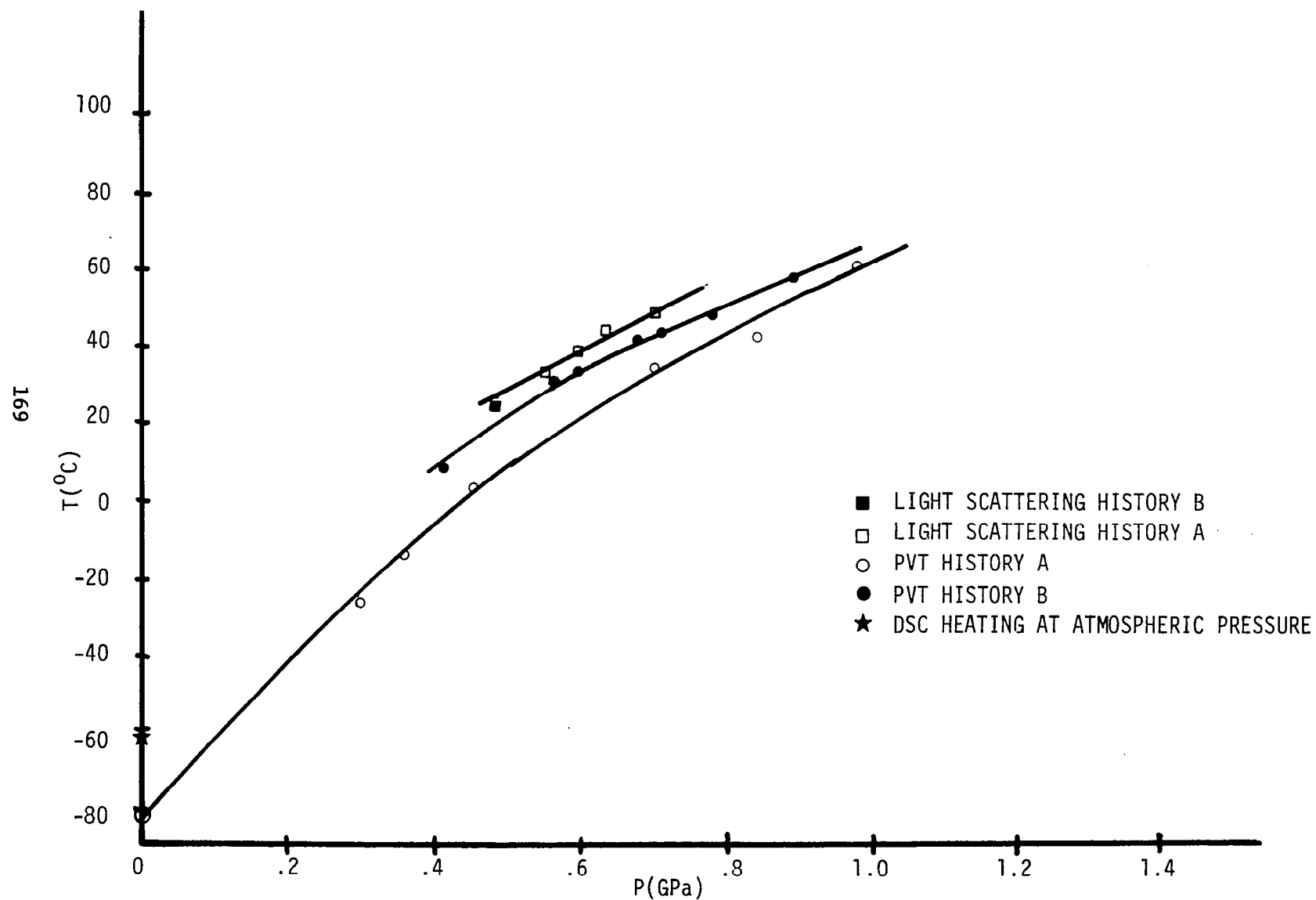


Figure IV-23. Comparison of Glass Transition of N1 by Various Methods.

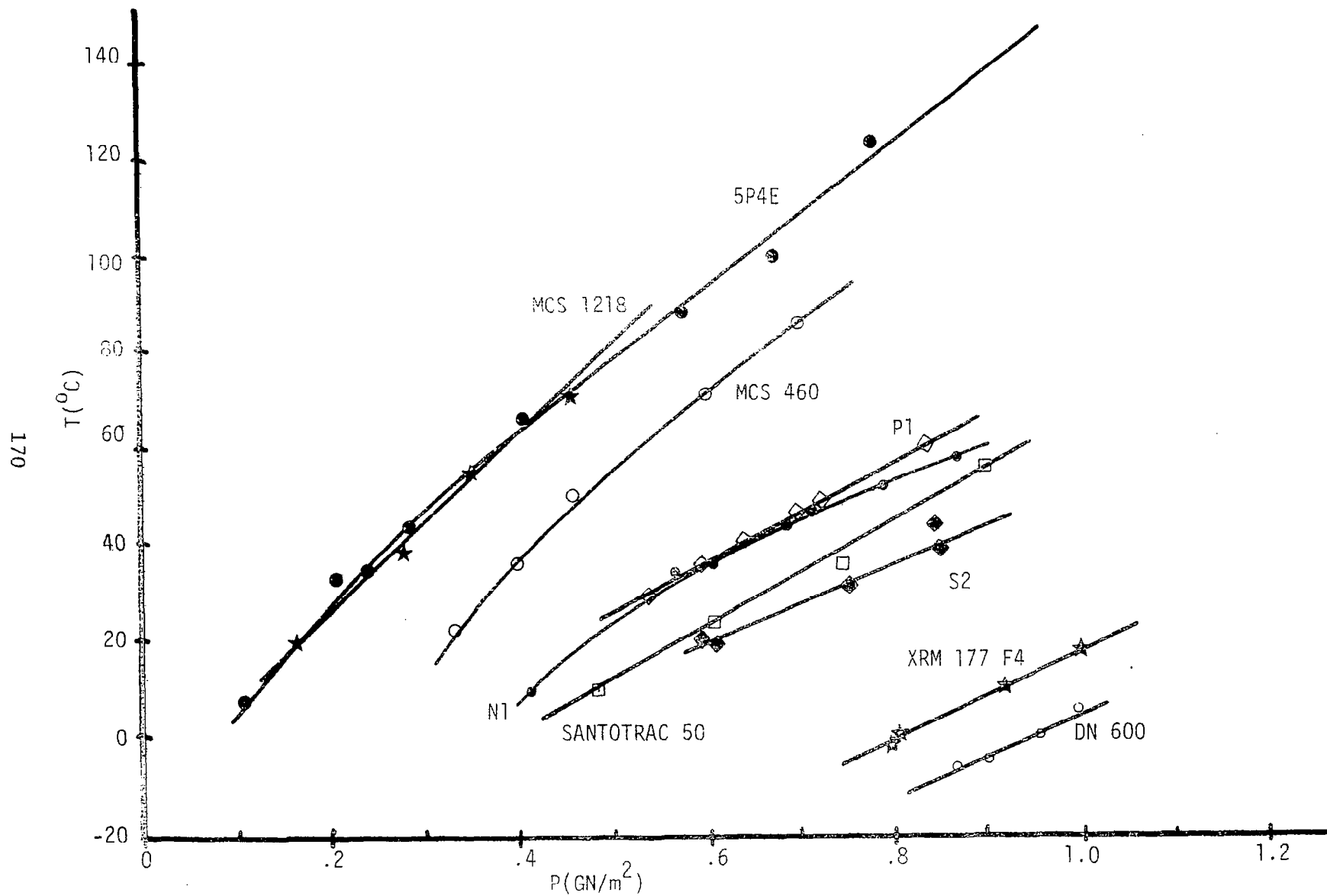


Figure IV-24. Glass Transition by Isothermal Compression from Liquid (Dilatometry).

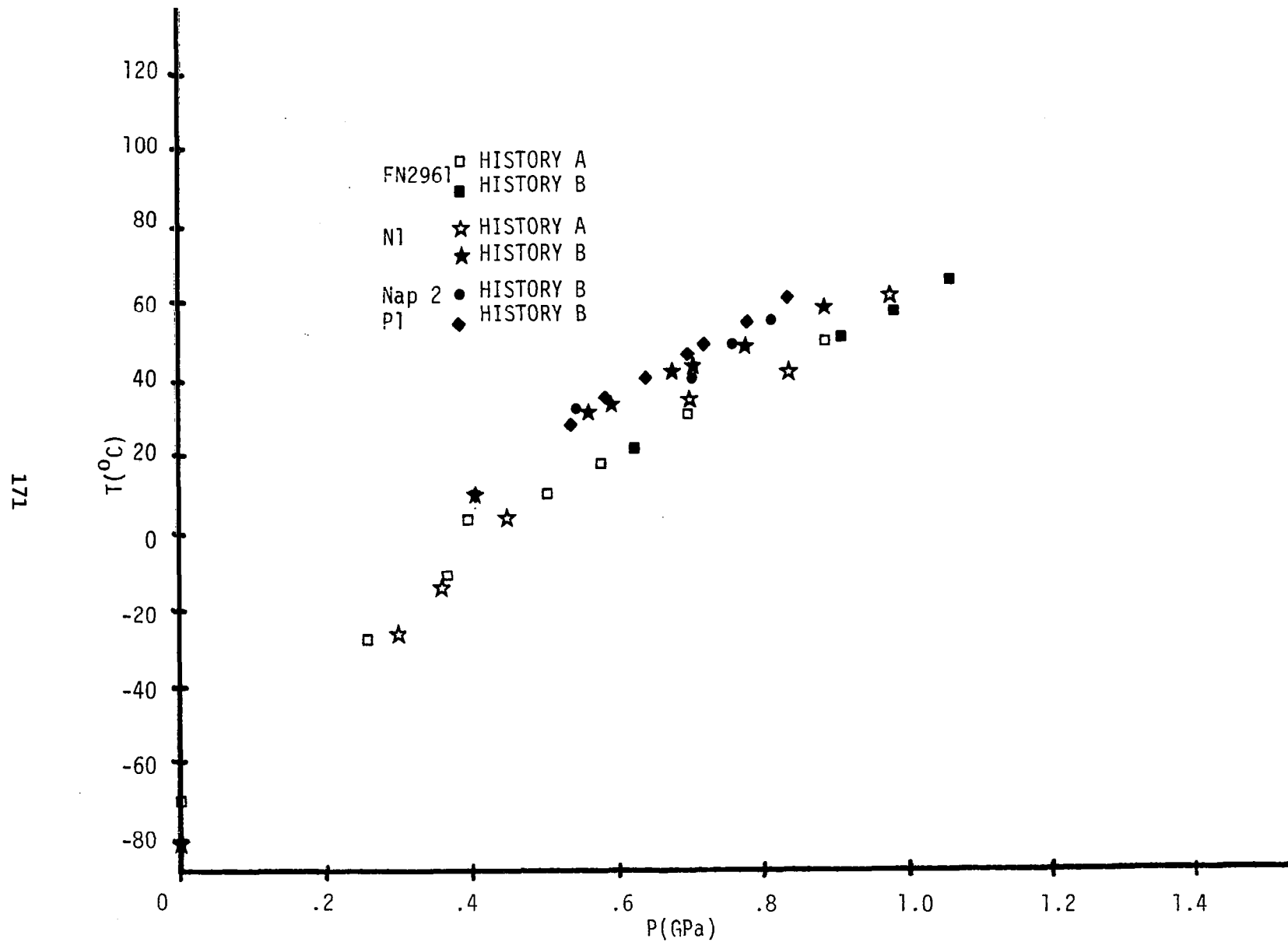


Figure IV-25. Glass Transition of Various Hydrocarbon Oils Determined by Dilatometry.

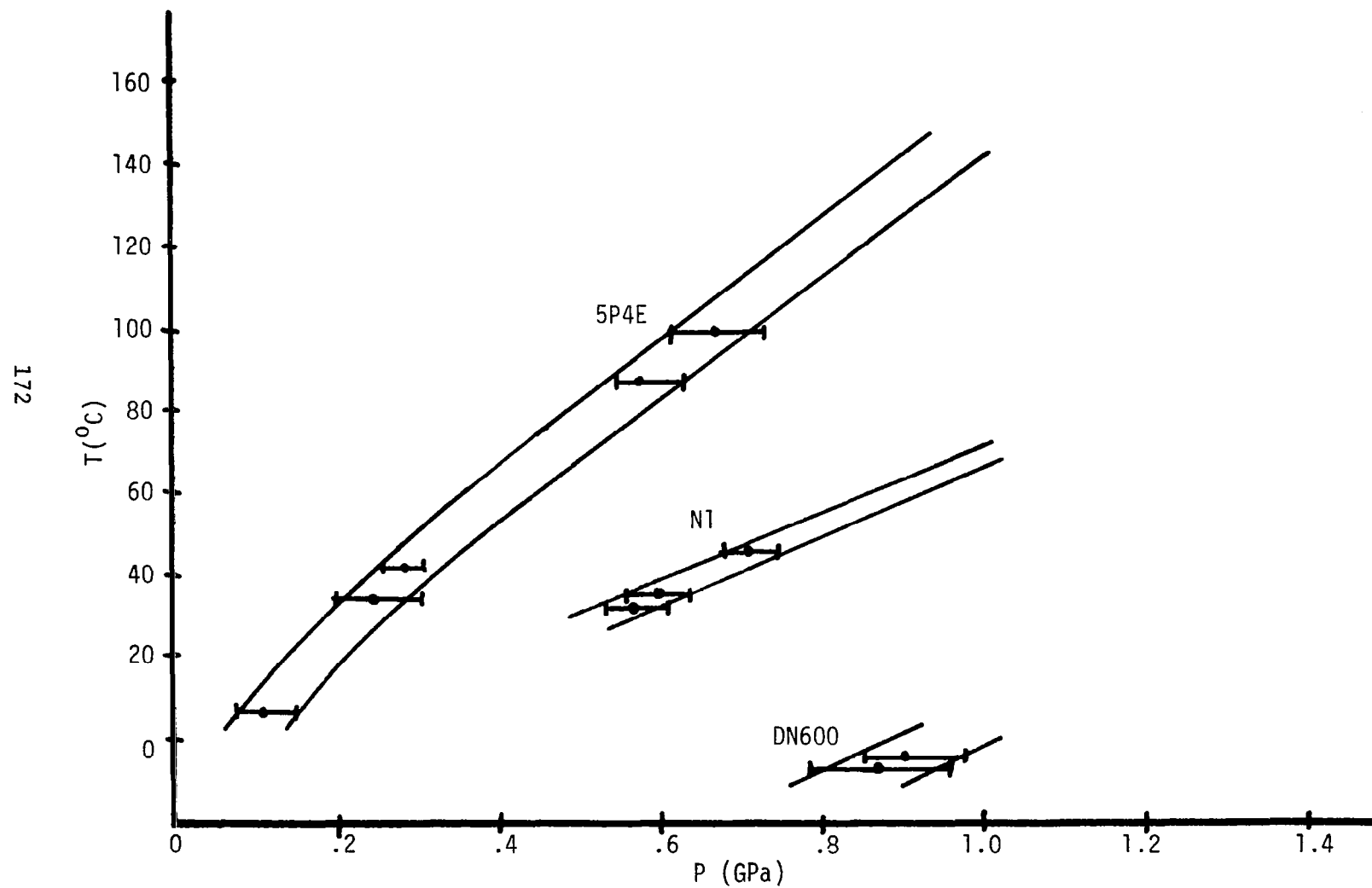


Figure IV-26. Dispersion Region in Isothermal Compression by Dilatometry.

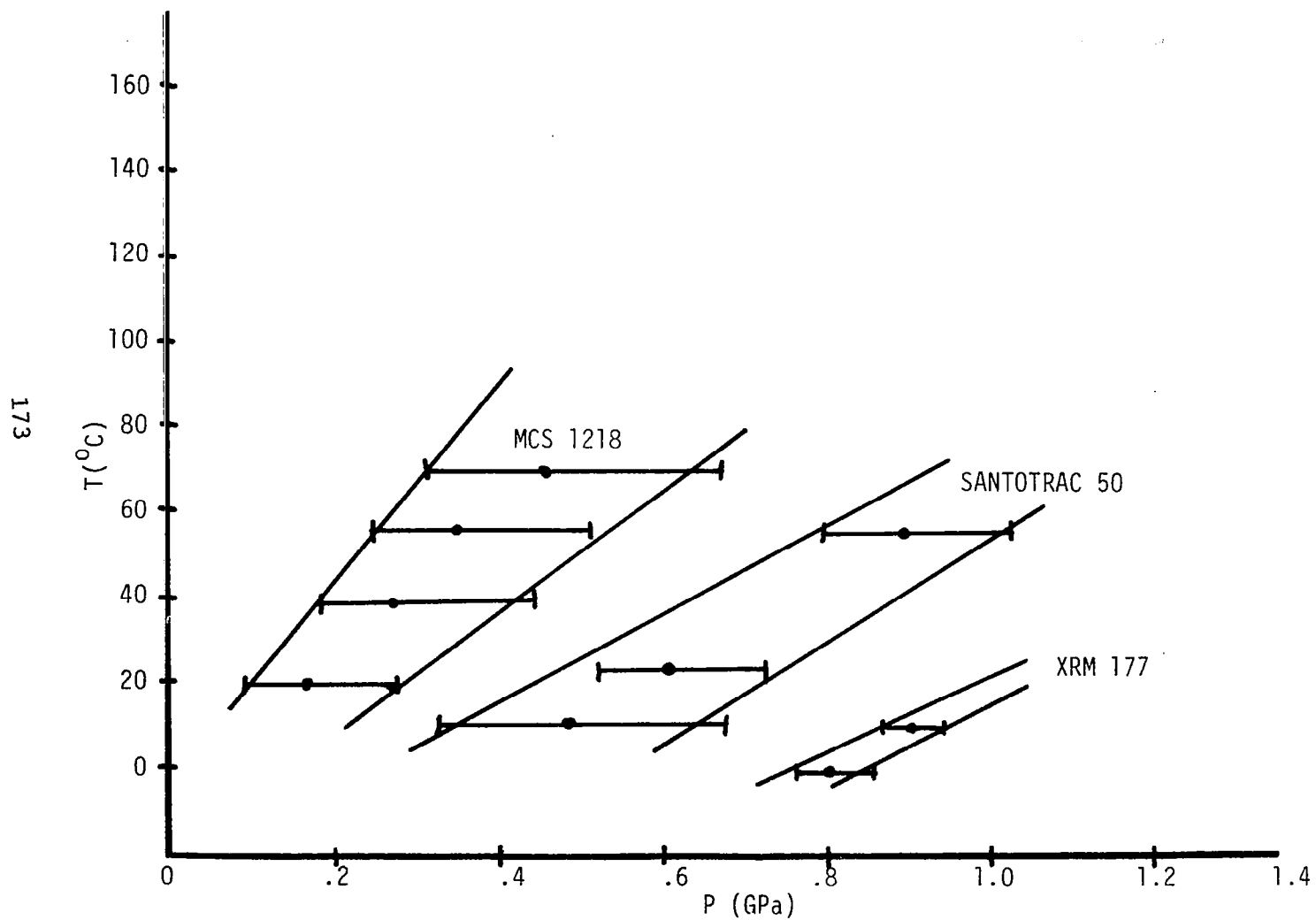
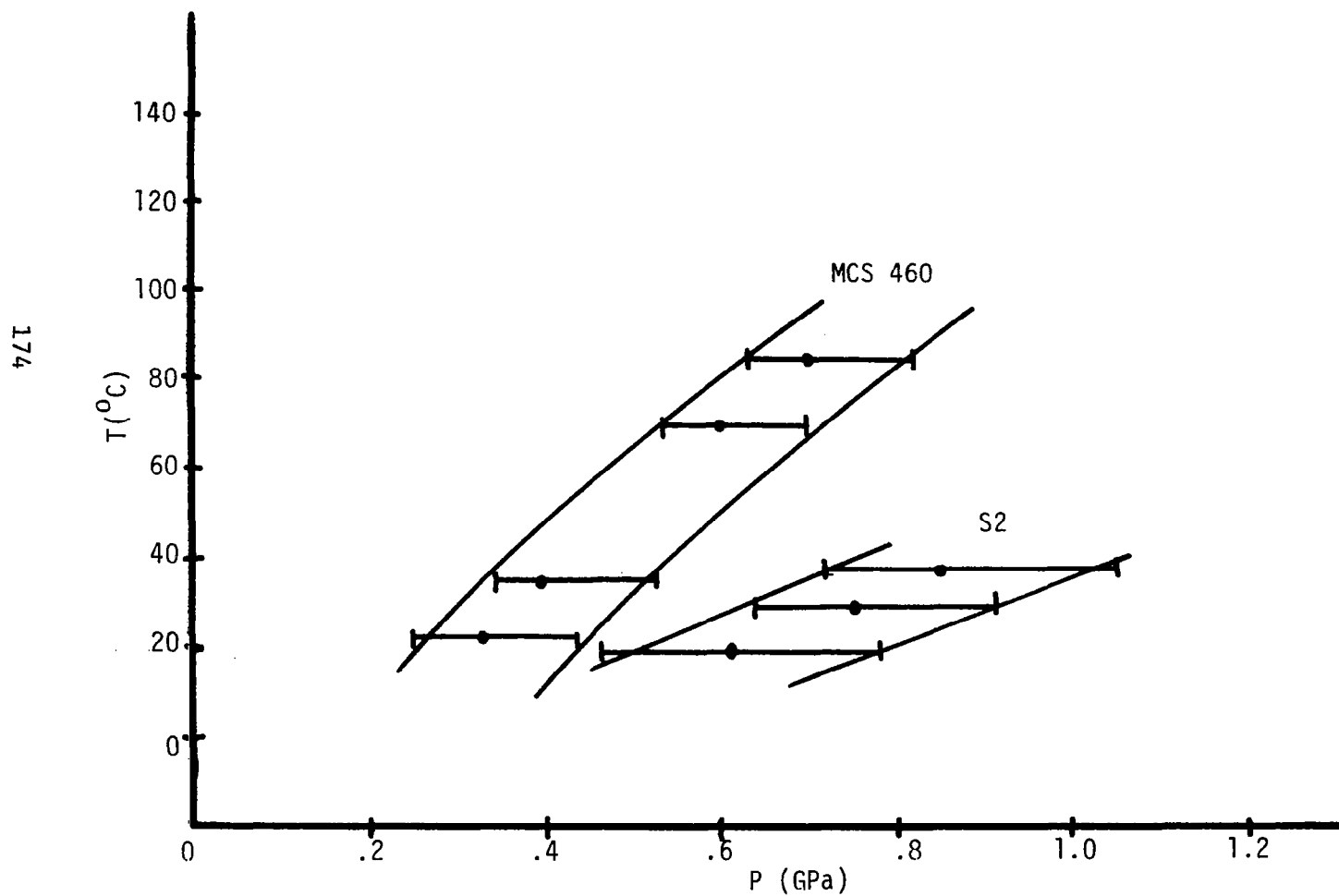


Figure IV-27. Dispersion Region in Isothermal Compression by Dilatometry.



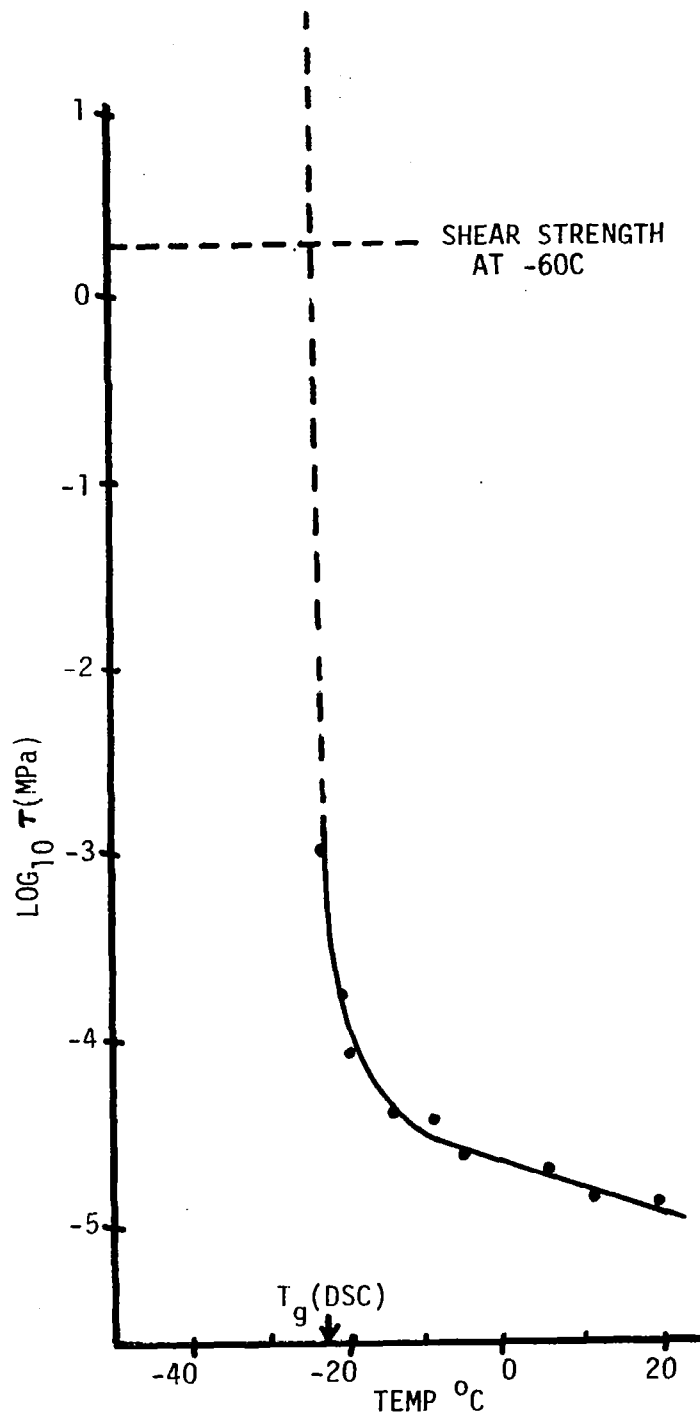


Figure IV-29. Shear Stress Between Concentric Cylinders for 5P4E
Cooled at 2.75 C/min., Shear Rate $\dot{\gamma} = .435 \text{ sec}^{-1}$.

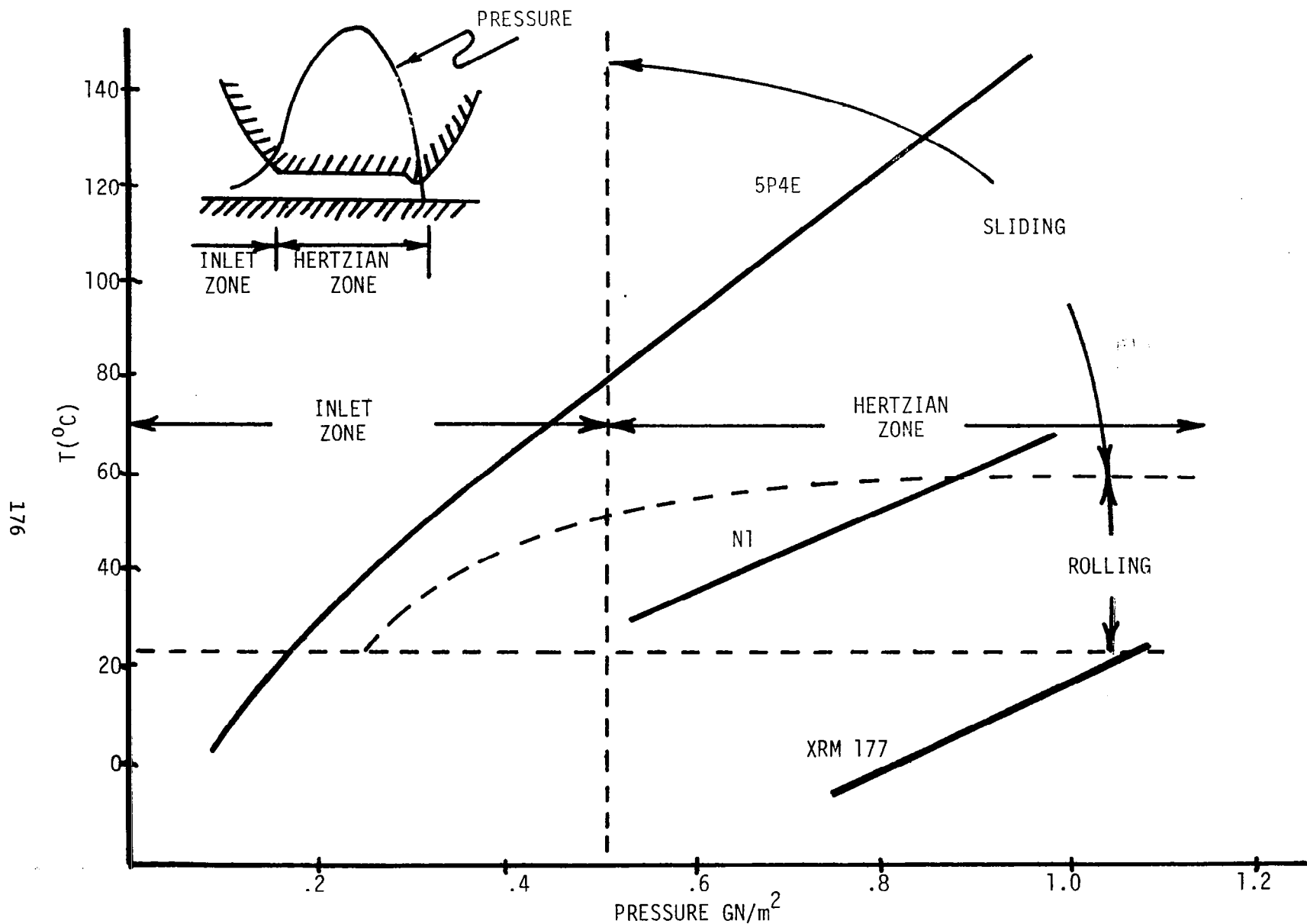


Figure IV-30. Heuristic Estimates of the Relationship Between Conditions in an EHD Contact and Glass-Liquid Phase Diagram of Some Lubricants (Lubricant Supply Temperature about 20°C).

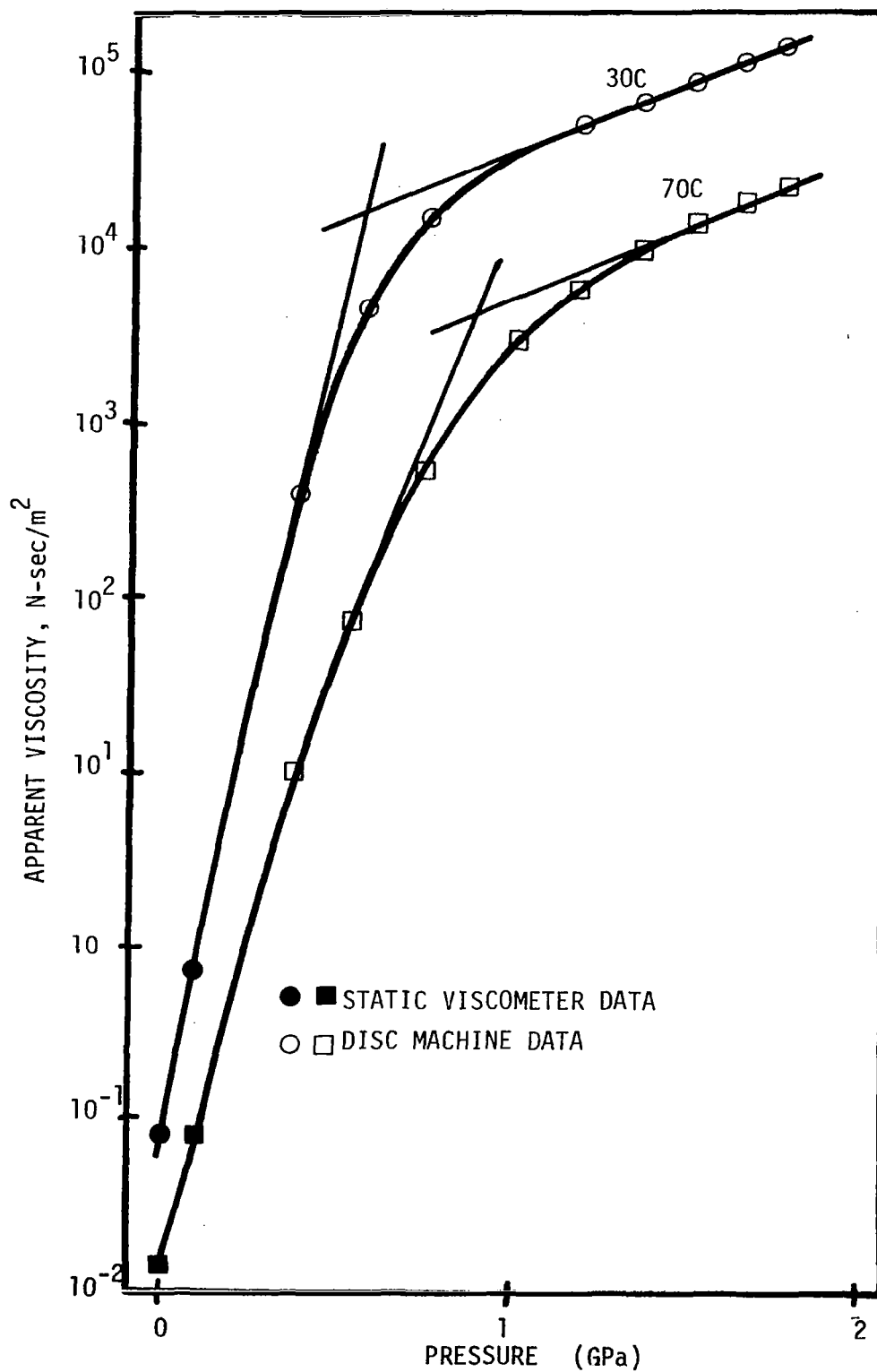


Figure IV-31. The Variation of Apparent Viscosity with Pressure and Temperature.

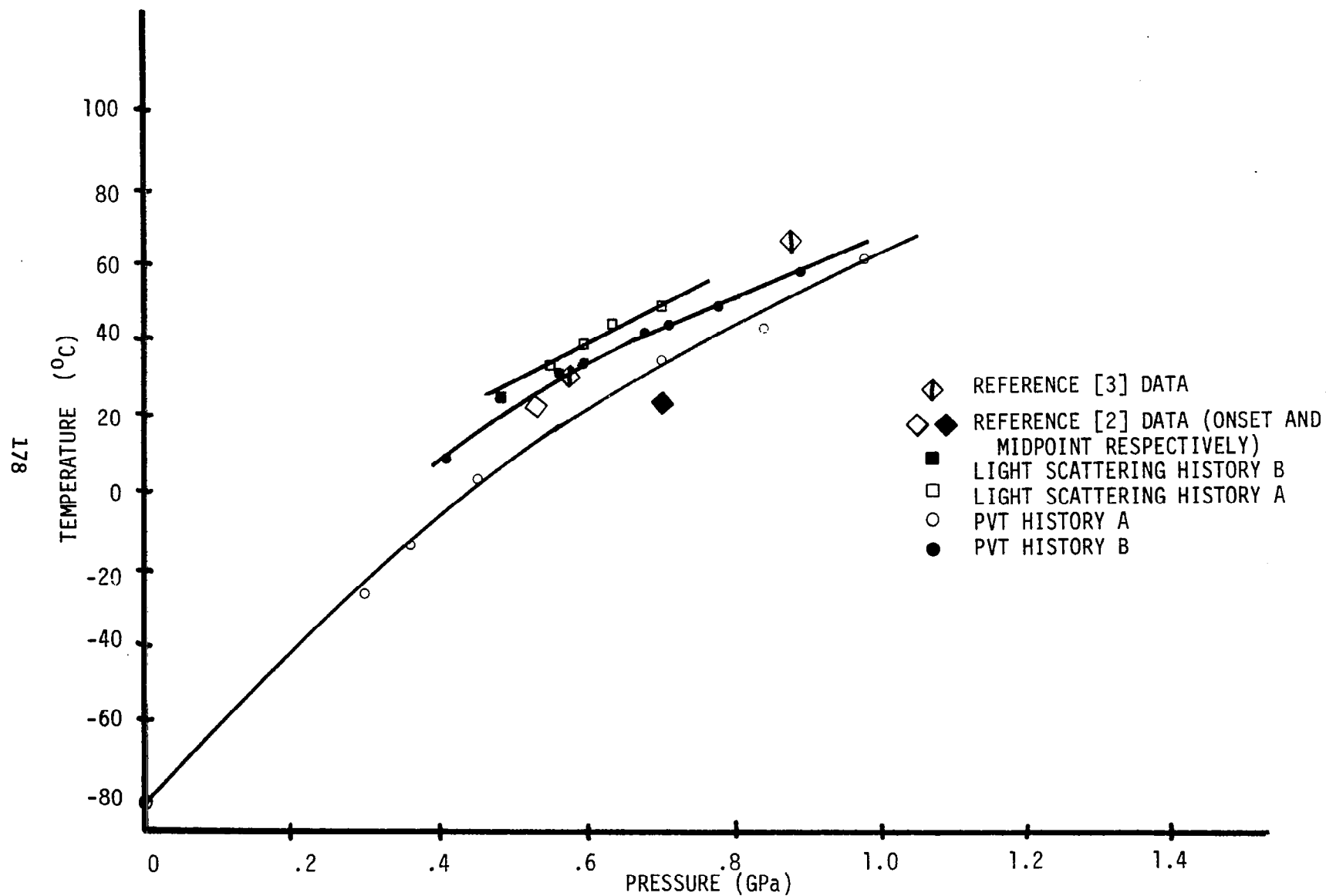


Figure IV-32. Comparison of Glass Transition of NI by Various Methods.

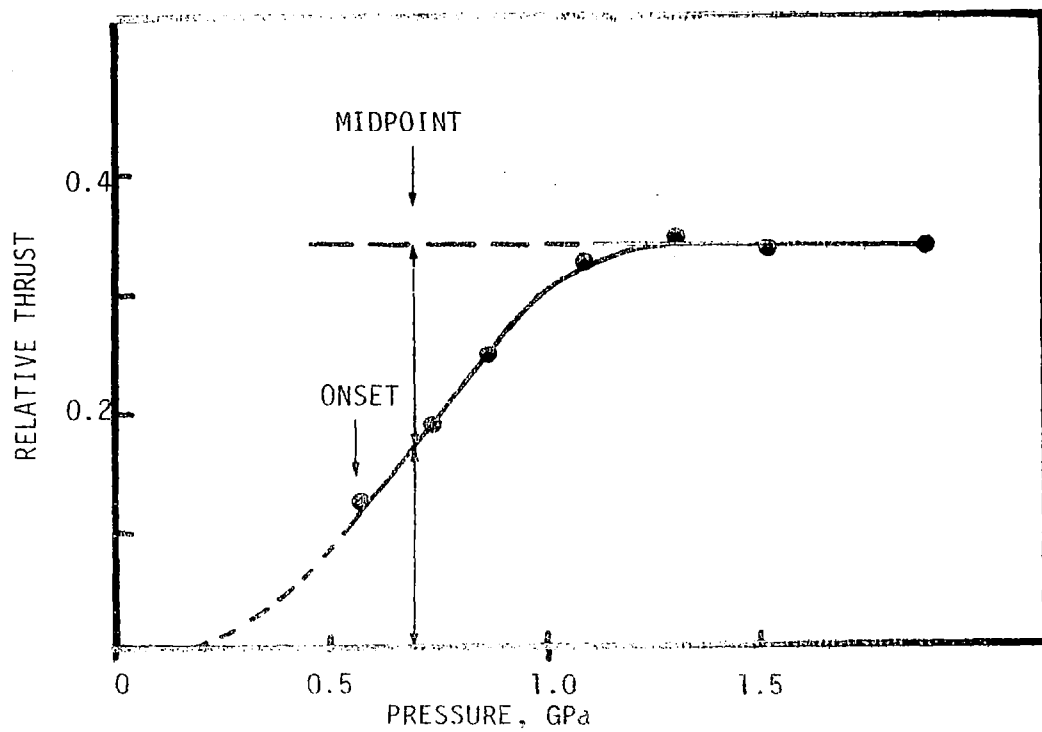


Figure IV-33. Variation of the Relative Side Thrust with Contact Pressure at 23C and 0.1 m/s [26].

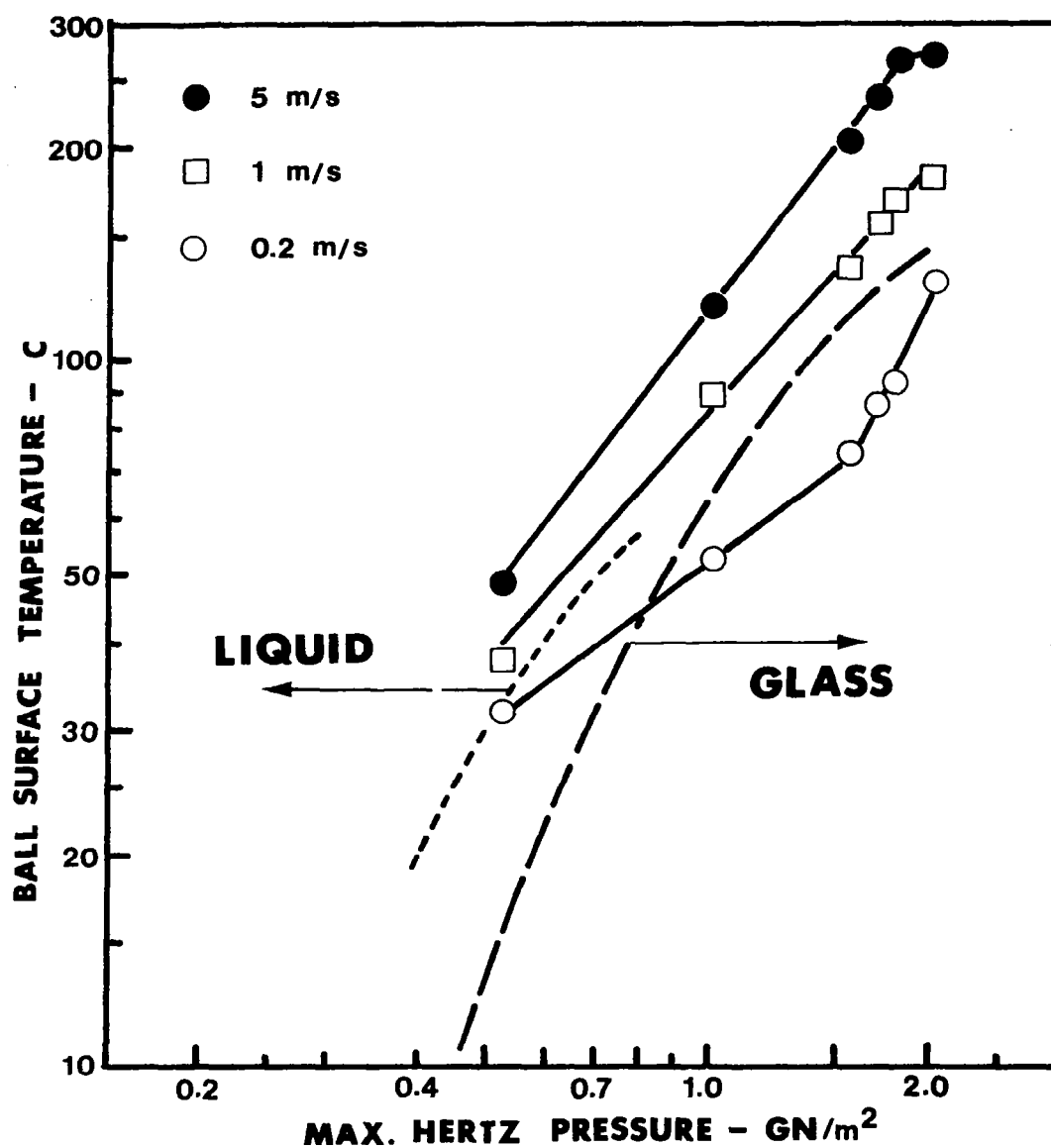


Figure IV-34. The Physical State of N1 Lubricant in the Center of a Sliding Contact at Various Speeds and Hertz Pressures (Reference [9]) ----- and ----- Represent the Light-Scattering and the Volumetric Glass Transition Lines Respectively.

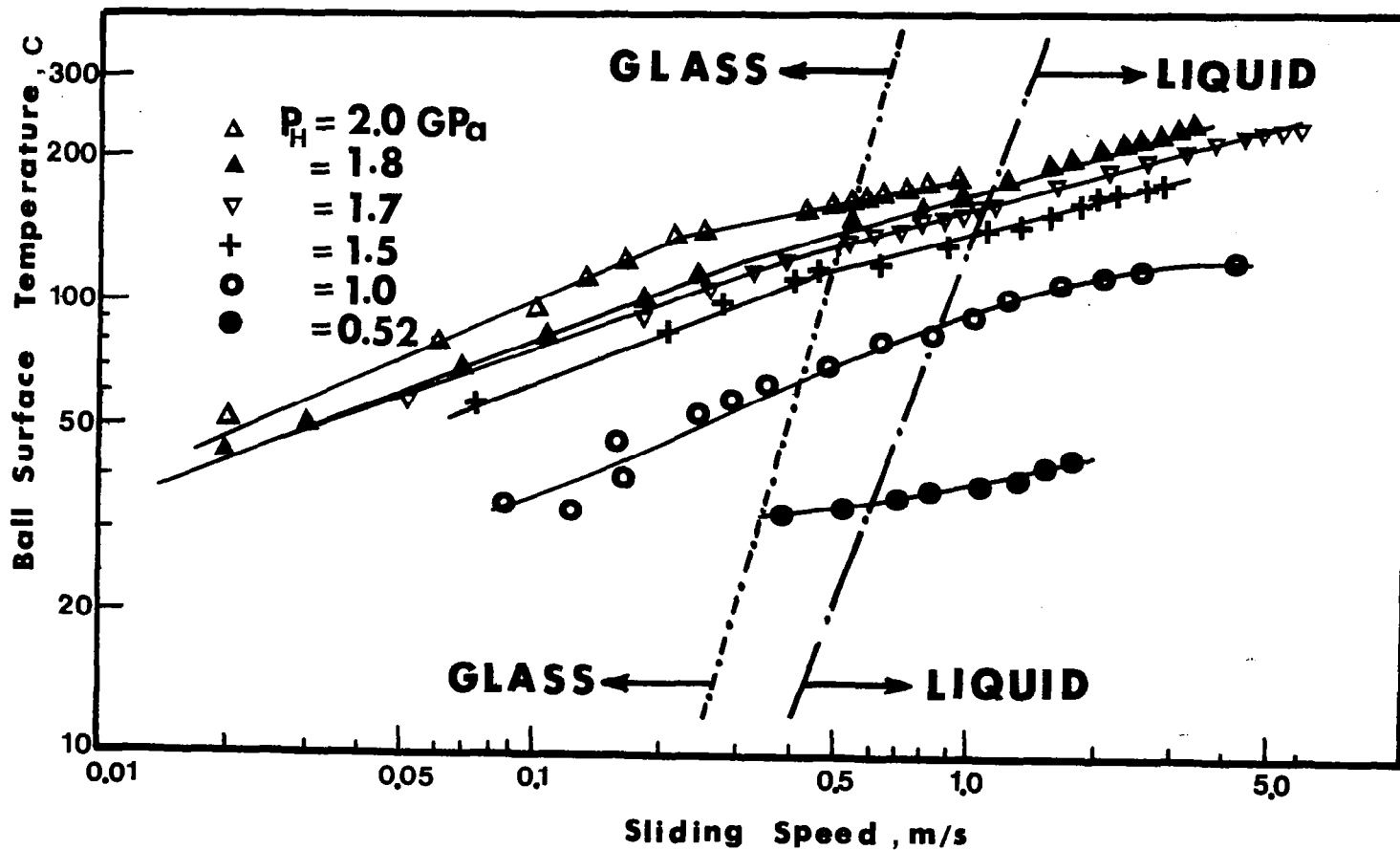


Figure IV-35. The Physical State of NI Lubricant in the Center of a Sliding Contact at Various Speeds and Hertz Pressures and -.-.- Represent the Light-Scattering and the Volumetric Glass Transition Lines.

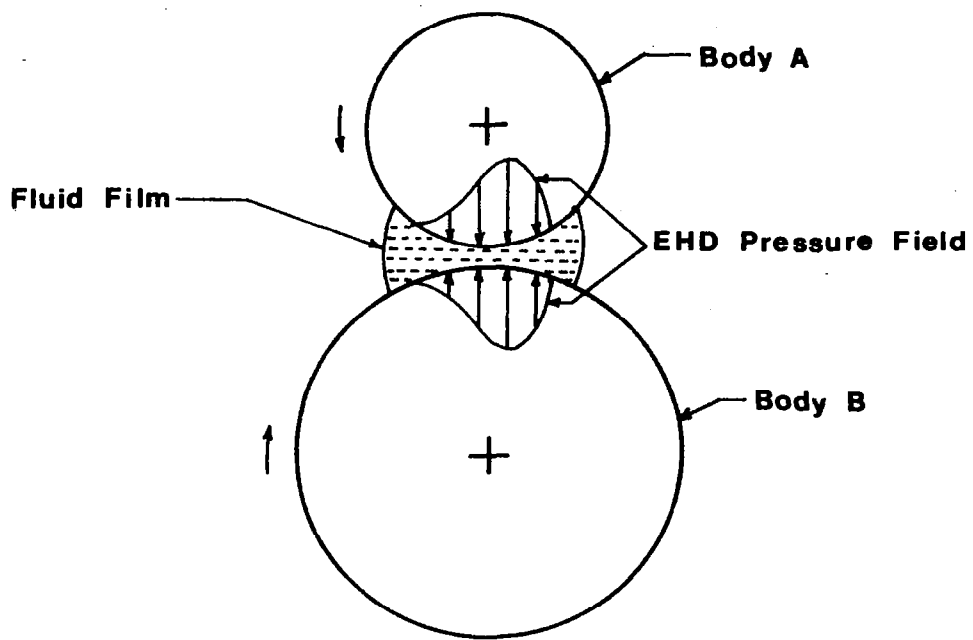


Figure V-1. Two Cylinders.

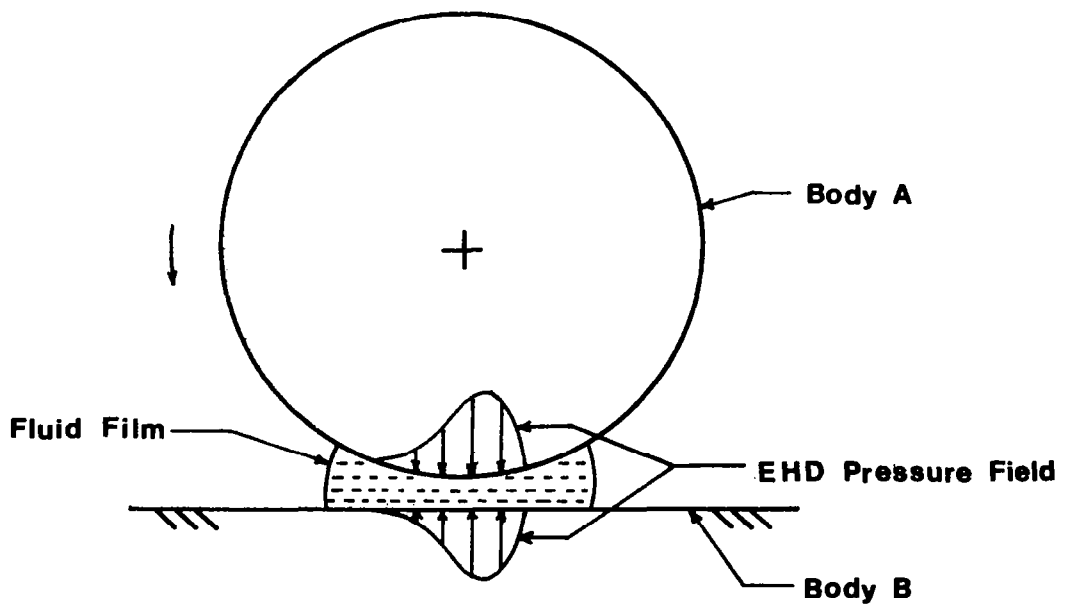
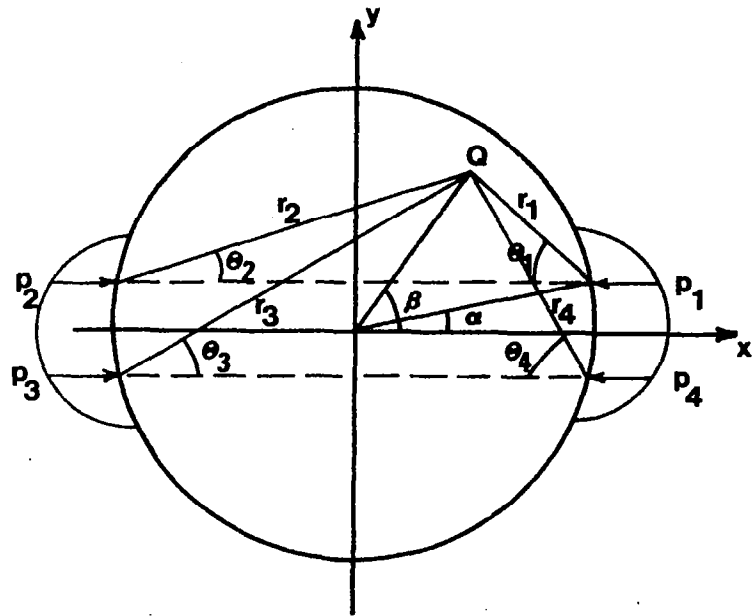
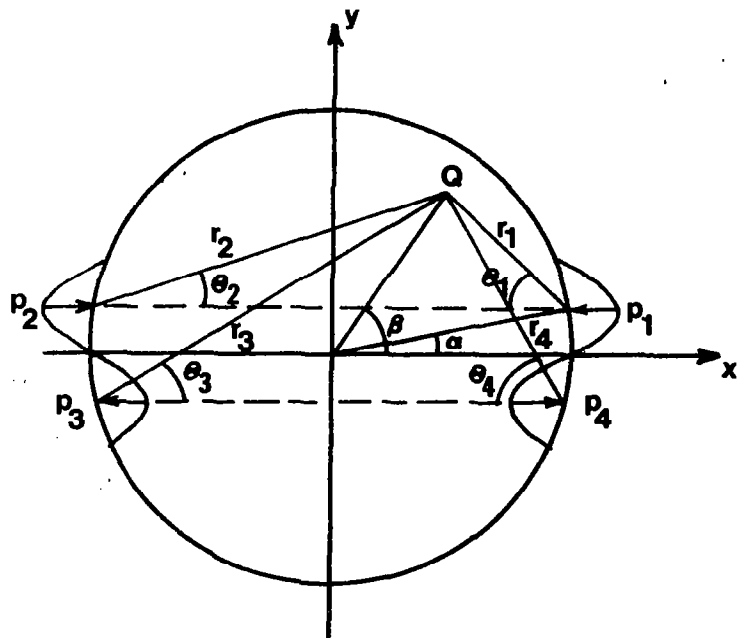


Figure V-2. Cylinder Plate.

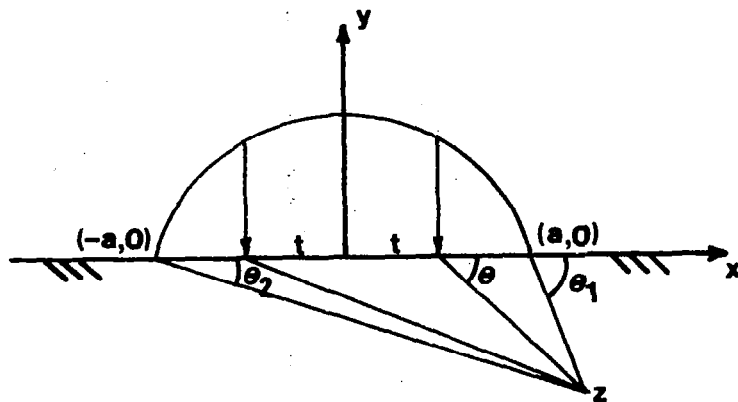


a) Symmetric Pressure Distribution.

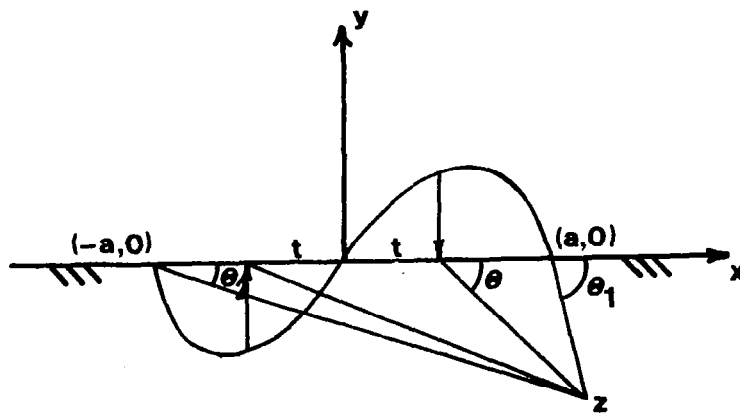


b) Antisymmetric Pressure Distribution.

Figure V-3. Decomposition of the EHD Pressure-Cylinder.



a) Symmetric Pressure Distribution.



b) Antisymmetric Pressure Distribution.

Figure V-4. Decomposition of the EHD-Pressure-The Plate.

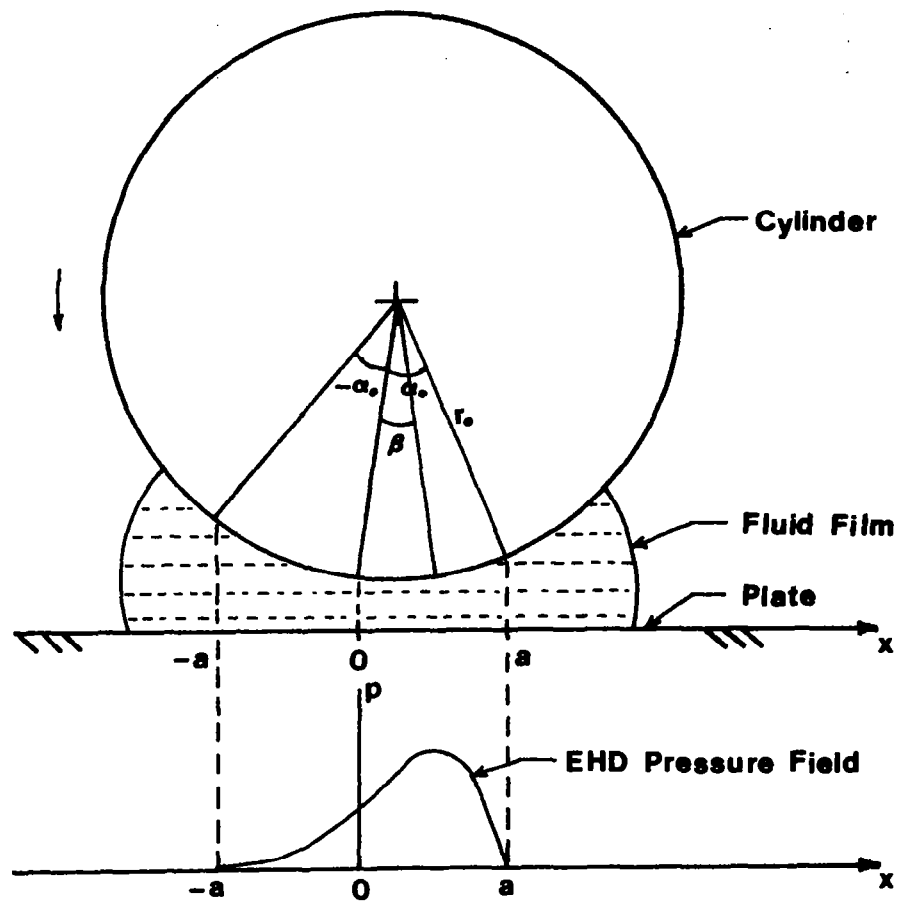


Figure V-5. Schematic Diagram of EHD Contact Zone.

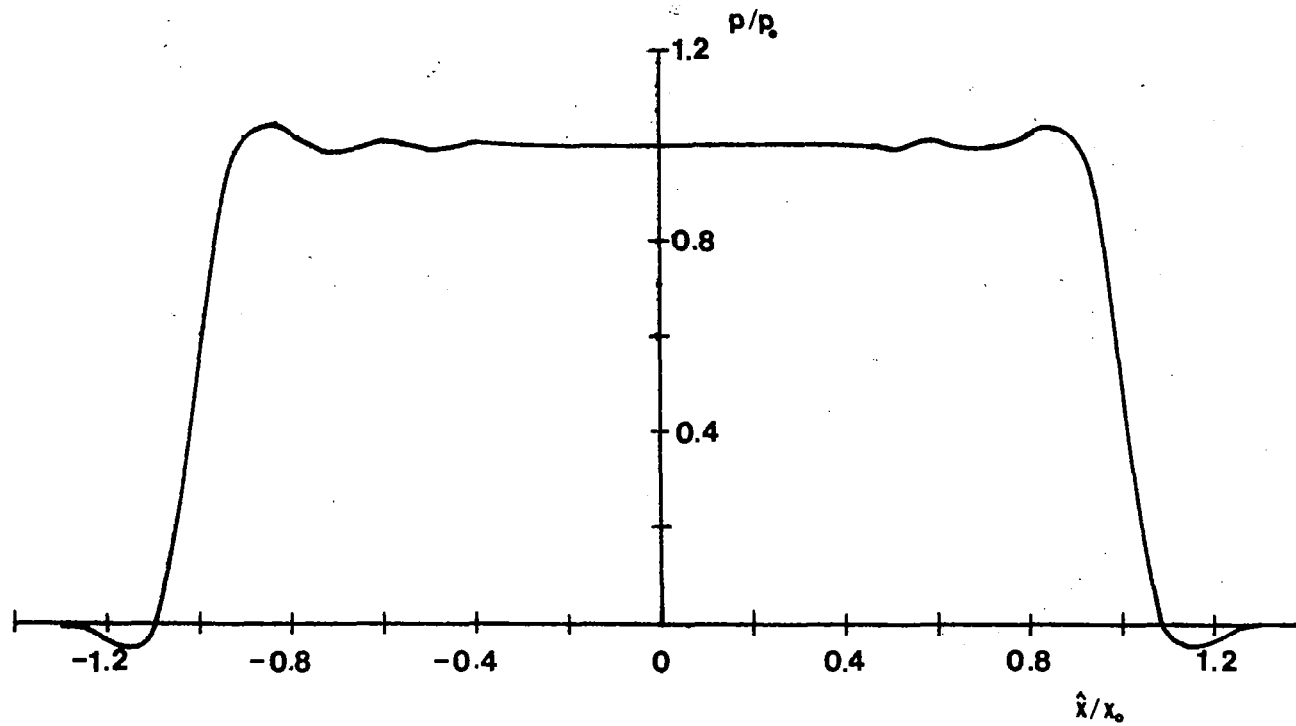


Figure V-6. Test Case 1 - Uniform Pressure Distribution.

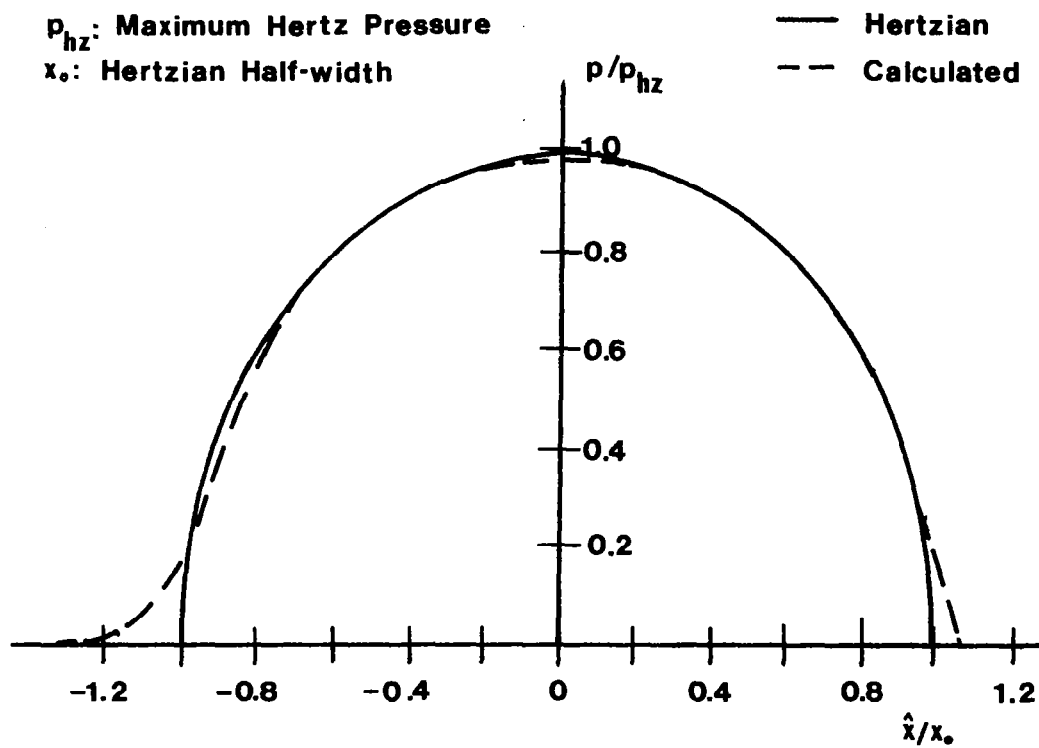


Figure V-7. Test Case 2 - Hertzian Contact.

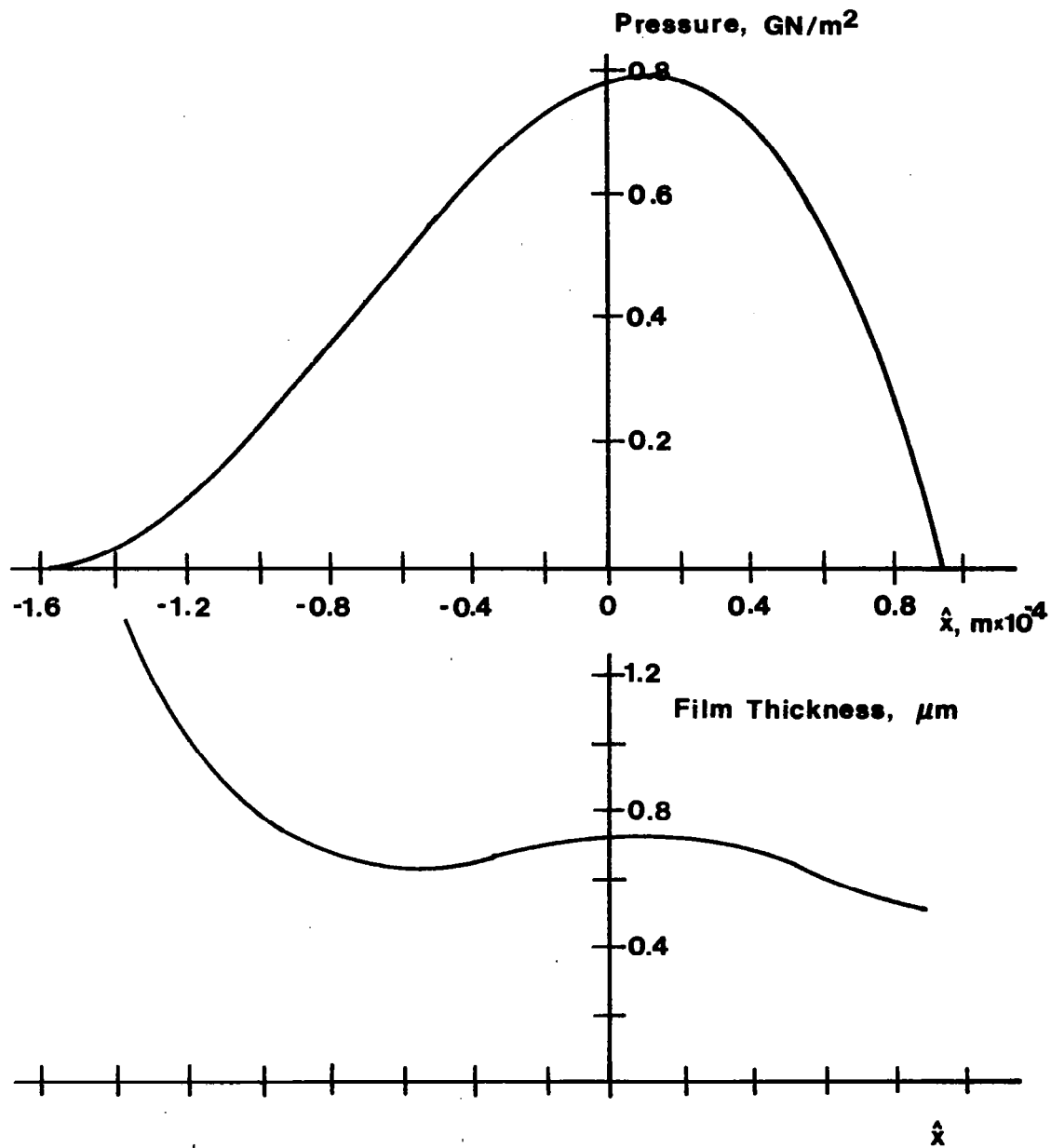


Figure V-8. Test Case 3 - Polynomial Pressure Distribution.

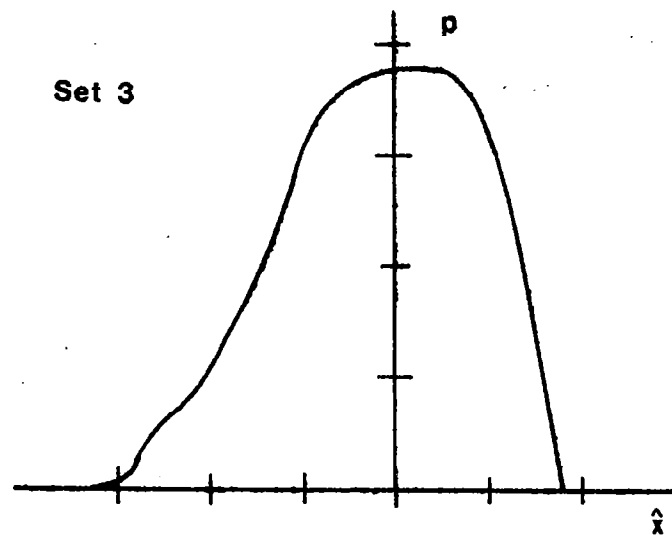
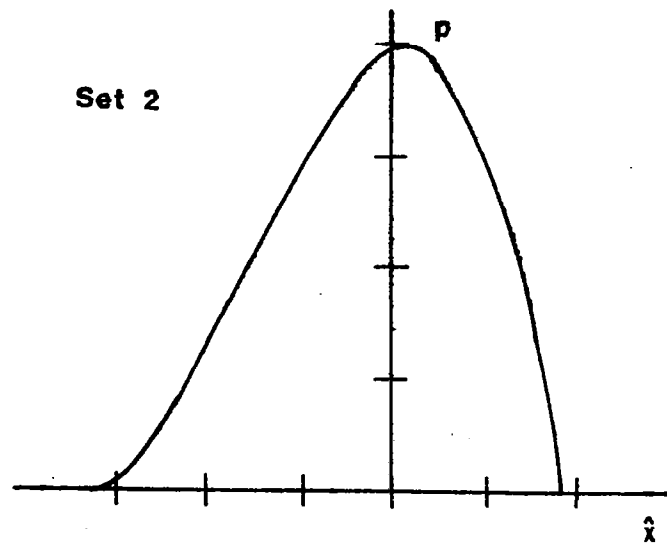
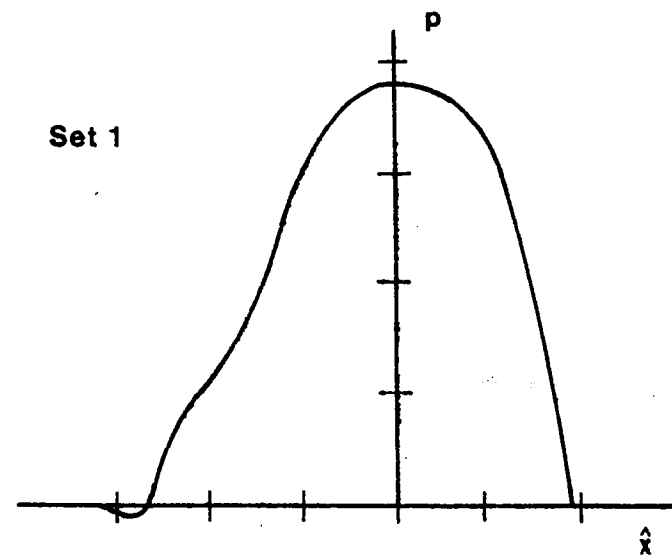
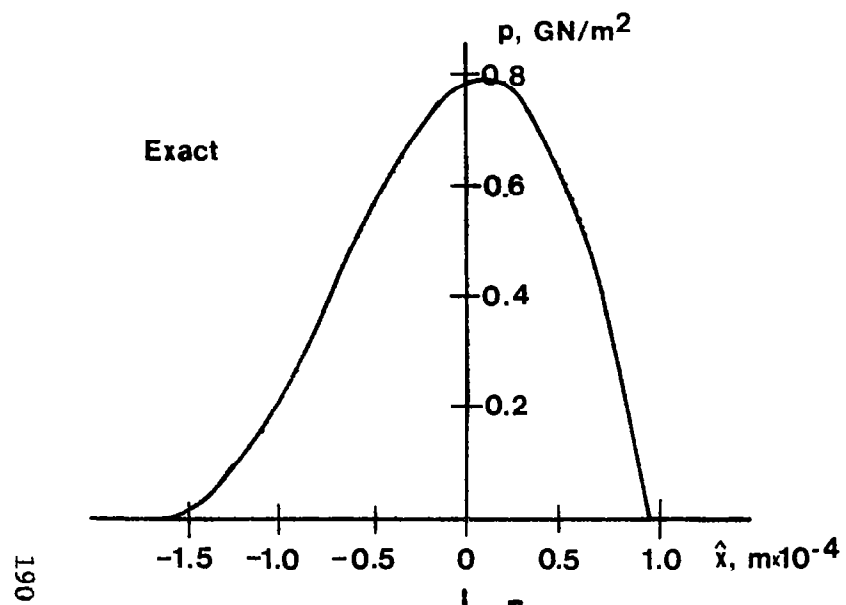


Figure V-9. Test Case 3 - Random Errors Introduced into Film Thickness Values.

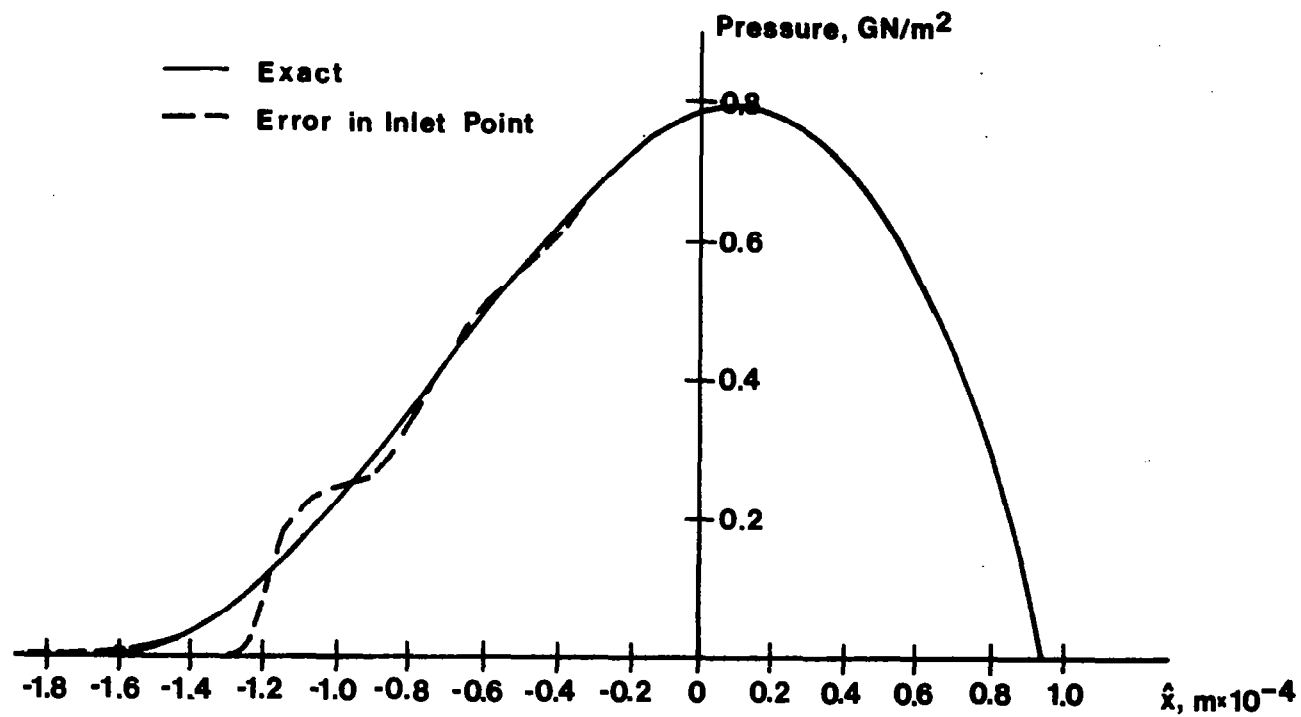


Figure V-10. Test Case 3 - Errors Introduced in Location of Inlet Point.

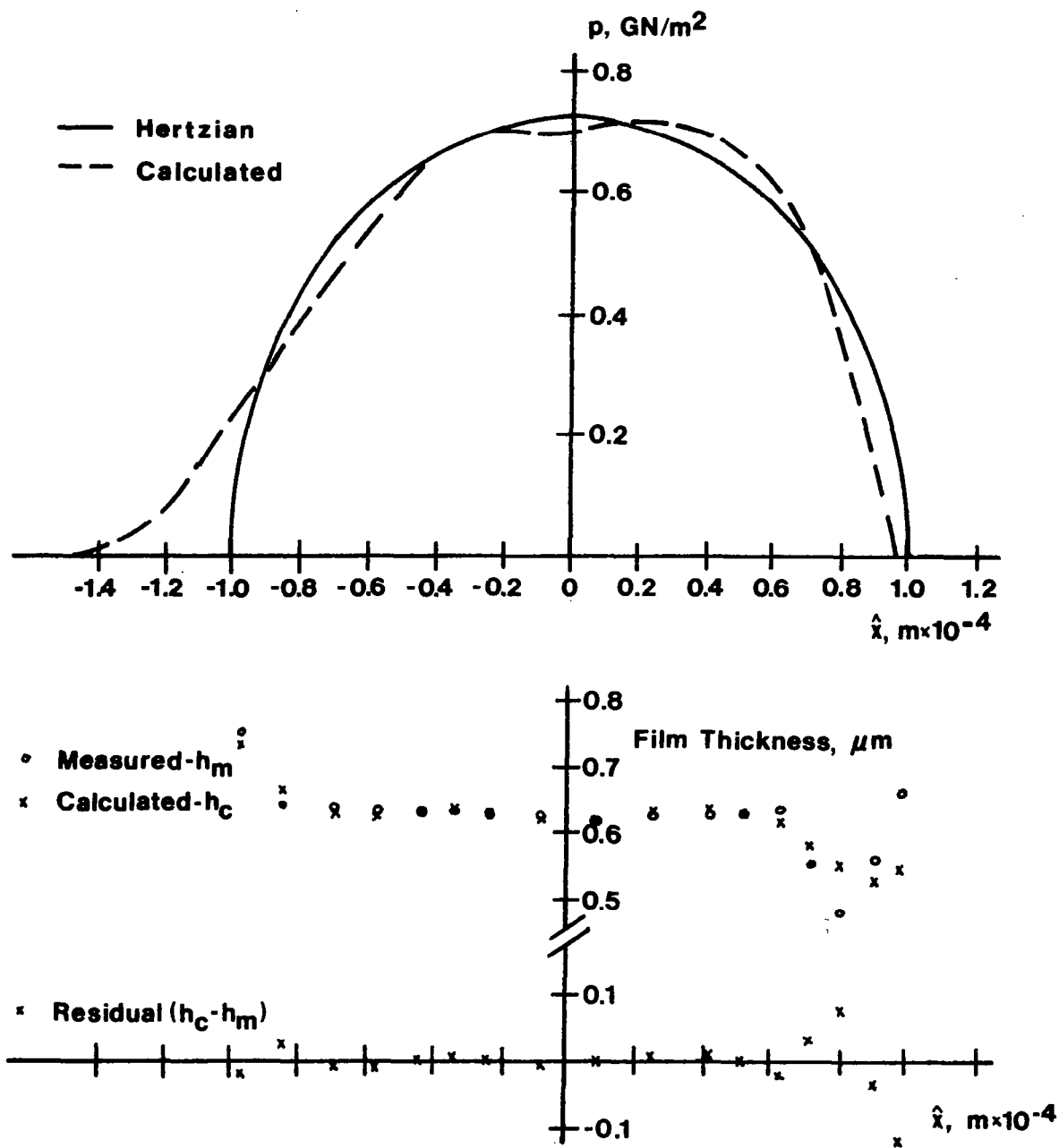


Figure V-11. Calculations Based on Experimental Film Thickness Measurements [71].

APPENDIX A

DESCRIPTION OF EXPERIMENTAL FLUIDS

The following table summarizes the oils investigated in this research and gives characteristic data for each oil.

Experimental Fluids

<u>Symbol</u>	<u>Description</u>
5P4E	Polyphenyl Ether
MCS-1218	Cycloaliphatic Hydrocarbon
MCS-460	Synthetic Hydrocarbon
Santotrac 50	Cycloaliphatic Hydrocarbon Traction Fluid plus additive
N1	Naphthenic Base Oil R-620-15
P1	Paraffinic Base Oil R-620-12
Nap 2	Napthenic Base Oil R-620-16
FN 2961	Super Refined Napthenic Mineral Oil
XRM-177-F4	Synthetic Paraffinic Hydrocarbon plus anti-wear additive
DN-600	Polyalkyl Aromatic
S1	Diester
DC-200-Blend II	Dimethylsiloxane Blend
S3-DC-200-50	Dimethylsiloxane
Advanced Ester	.
S2	Polybutene LF-5193

Fluid Characterization

Symbol:	5P4E	
Type:	Five-ring Polyphenyl Ether	
Source:	Monsanto Company	
Properties:	Viscosity at 37.8C, m^2/s	363×10^{-6}
	Viscosity at 98.9C m^2/s	13.1×10^{-6}
	Density at 22.2C, Kg/m^3	1.205×10^3
	Density at 37.8C, Kg/m^3	1.19×10^3
	Flash Point, C	288
	Pour Point, C	4.4
Symbol:	MCS-1218	
Source:	Monsanto Company	
Type:	Cycloaliphatic Hydrocarbon	
Properties:	It is a combination of two components each have a molecular weight less than 1000.	
	Viscosity at 37.8C, m^2/s	1418×10^{-6}
	Viscosity at 98.9C, m^2/s	18.37×10^{-6}
	Density at 23.9C, Kg/m^3	0.94×10^3

Symbol: MCS-460
Source: Monsanto Company
Type: Synthetic Hydrocarbon
Properties: Viscosity at 37.8C m^2/s 37.2×10^{-6}
 Viscosity at 98.9C m^2/s 4.0×10^{-6}
 Viscosity at 148.9C m^2/s 1.9×10^{-6}
 Pour Point -29 to -32C
 Density 25C Kg/m^3 $.9327 \times 10^3$

Symbol: Santotrac 50
Source: Monsanto Company
Type: Synthetic Cycloaliphatic Hydrocarbon Traction Fluid
Properties: Viscosity at 37.8C m^2/s $.34 \times 10^{-4}$
 Viscosity at 98.9C m^2/s $.056 \times 10^{-4}$
 Pour Point C -37
 Density at 37.8C $.889 \times 10^3 \text{ Kg}/\text{m}^3$
 Flash Point C 163
 Fire Point C 174
 Specific Heat at 37.8C $\text{J}/\text{Kg}\cdot\text{K}$ 0.51

Additive package includes: Antiwear (zinc dialkyl dithiophosphate), Oxidation inhibitor Antifoam, VI Improver (Polymethacrylate).

Symbol: N1
Source: Sun Oil Company
Type: Naphthenic Base Oil R-620-15
Properties: Viscosity at 37.8C, m^2/s 24×10^{-6}
 Viscosity at 98.9C, m^2/s 3.728×10^{-6}
 Viscosity Index (ASTM D-2270) -13
 Flash Point, C 157
 Pour Point -43
 Density at 20C, gm/cc Kg/m^3 0.9157×10^3
 Average Molecular Weight 305

Symbol: P1
Source: Sun Oil Company
Type: Paraffinic Base Oil
Properties: Viscosity at 37.8C m^2/s 33.74×10^{-6}
 Viscosity at 98.9C m^2/s 5.402×10^{-6}
 Density at 25C Kg/m^3 $.8602 \times 10^3$
 V.I. (ASTM D-2270) 103
 Pour Point C -15
 Average molecular weight 404

Symbol: Nap 2
Source: Sun Oil Company
Type: Napthenic Base Oil R-620-16
Properties: Viscosity at 37.8C m^2/s 114.2×10^{-6}
 Viscosity at 98.9C m^2/s 8.076×10^{-6}
 Viscosity Index (D2270) < 0
 Density at 20C Kg/m^3 $.9303 \times 10^3$
 Average Molecular Weight 357
 Refractive Index 1.5173
 Pour Point C -23

Symbol: FN 2961
Source: Humble Oil and Refining Company
Type: Super Refined Napthenic Mineral Oil
Properties: Viscosity at 37.8C m^2/s 78.08×10^{-6}
 Viscosity at 98.9C m^2/s 8.238×10^{-6}
 Viscosity at 148.9C m^2/s 3.3×10^{-6}
 Density at 15.6C Kg/m^3 $.887 \times 10^3$
 Pour Point C -34

Symbol: XRM-177-F4
Source: Mobil
Type: Synthetic Paraffinic Hydrocarbon
 plus antiwear additive
Properties: Viscosity at 37.8C Ns/m^2 376×10^{-3}
 Viscosity at 98.9C Ns/m^2 31.6×10^{-3}
 Pour Point C < -40
 Density 37.8C Kg/m^3 $.8389 \times 10^{-3}$

Symbol: DN-600
Source: Continental Oil Company
Type: Polyalkyl Aromatic
Properties: Viscosity at 37.8C m^2/s 30×10^{-6}
 Viscosity at 98.9C m^2/s 5.0×10^{-6}
 Viscosity at 148.9C m^2/s 2.3×10^{-6}
 Density at 37.8C Kg/m^3 0.851×10^3
 Pour Point C $- 60$
 Specific Heat at 37.8C J/Kg C 1624

Symbol: S1-Diester
 Source: Rohm and Haas Company
 Type: Diester-Plexol 201 bis-2-ethyl hexyl sebecate (PL 5159)
 Properties: Viscosity at -53.9°C m^2/s 7988×10^{-6}
 Viscosity at 37.8°C m^2/s 12.75×10^{-6}
 Viscosity at 98.9°C m^2/s 3.32×10^{-6}
 Cloud Point (ASTM D-2500) below -54°C

Symbol: DC-200-Blend II
 Source: Dow Corning Corporation
 Type: Dimethylsiloxane Blend E1923-49
 Properties: Viscosity at 25°C m^2/s 1060×10^{-6}
 Molecular Weight (GPC) 160,000
 Component Viscosities:
 $50 \times 10^{-6} \text{ m}^2/\text{s}$ 75%
 $11,000 \times 10^{-6} \text{ m}^2/\text{s}$ 12%
 $330,000 \times 10^{-6} \text{ m}^2/\text{s}$ 13%

Symbol:	S3-DC-200-Blend II	
Source:	Dow Corning Corporation	
Type:	Dimethylsilixane DC-200	
Properties:	Viscosity at 37.8C m^2/s	82.6×10^{-6}
	Viscosity at 98.9C m^2/s	33.1×10^{-6}
	Density at 25C Kg/m^3	$.968 \times 10^3$
	Molecular Weight (Average)	7,000

Symbol:	Advanced Ester	
Source:	Shell Oil Company	
Type:	Based on Pentaerythritol (Aeroshell Turbine Oil 555 Base Oil)	
Properties:	Viscosity at 37.8C m^2/s	25.8×10^{-6}
	Viscosity at 98.9C m^2/s	5.1×10^{-6}
	Viscosity at 148.9C m^2/s	2.3×10^{-6}
	Density at 37.8C Kg/m^3	$.979 \times 10^3$

Symbol:	S2	
Source:	American Oil Company	
Type:	Polybutene LF-5193	
Properties:	Viscosity at -17.8C m^2/s	$18,836 \times 10^{-6}$
	Viscosity at 37.8C m^2/s	109×10^{-6}
	Viscosity at 98.9C m^2/s	10.6×10^{-6}
	Density at 25C Kg/m^3	0.8443×10^3
	V.I. (ASTM D-2270)	87
	Polymer Number Average molecular weight	409

APPENDIX B

PUBLICATIONS RESULTING FROM RESEARCH SUPPORTED COMPLETELY OR IN PART BY THE GRANT

- I. Student theses completed. Ph.D. theses are published through University Microfilm and abstracted in Dissertation Abstracts.
 1. Turchina, Valentin Alexandru, "Pressure and Temperature Measurement Techniques in Elastohydrodynamic Contacts", M.S. Thesis, Georgia Institute of Technology, 1973.
 2. Molina-Combita, Manuel A., "Dynamics of Roller Bearings Considering Elastohydrodynamic Forces", M.S. Thesis, Georgia Institute of Technology, 1974.
 3. Jakobsen, Jorgen, "Lubricant Rheology at High Shear Stress", Ph.D. Thesis, Georgia Institute of Technology, 1973.
 4. Alsaad, Mohammed Ahmed, "Light-Scattering Study of the Glass Transition and the Glassy State in Lubricating Oils", Ph.D. Thesis, Georgia Institute of Technology, 1976.
 5. Ausherman, Vernon K., Jr., "Infrared Temperature Mapping in Elastohydrodynamic Lubrication", Ph.D. Thesis, Georgia Institute of Technology, 1975.
 6. Walker, David L., "Polymer Degradation in Sliding Elastohydrodynamic Lubrication", M.S. Thesis, Georgia Institute of Technology, 1973.
 7. Nagaraj, H., "Investigation of Some Temperature-Related Phenomena in Elastohydrodynamic Contacts Including Surface Roughness Effects", Ph.D. Thesis, Georgia Institute of Technology, 1976.

II. Technical Papers

1. Winer, W. O., "A Viscometer for High Pressure Use, and Some Results", Trans. ASME, Vol. 94, No. 3, Series D, The Journal of Basic Engineering, pp. 586-589, 1972.
2. Lee, D., Sanborn, D. M., and Winer, W. O., "Some Observations of the Relationship Between Film Thickness and Load in High Hertz Pressure Elastohydrodynamic Contacts", Trans. ASME, Journal of Lubrication Technology, Vol. 95, pp. 386-390, 1973.
3. Jakobsen, J., Sanborn, D. M., and Winer, W. O., "Simulation of Severe Shear Conditions in Lubrication", Society of Automotive Engineers, SP-382, pp. 59-67, 1973.
4. Turchina, V. A., Sanborn, D. M., and Winer, W. O., "Temperature Measurements in Sliding Elastohydrodynamic Point Contacts", Trans. ASME, Journal of Lubrication Technology, Vol. 96, pp. 410-417, 1974.
5. Winer, W. O., "A Review of Experimental Elastohydrodynamic Lubrication Research", NSF Tribology Workshop Proceedings, 1973.
6. Sanborn, D. M., Jakobsen, J., Carlson, S., and Winer, W. O., "Investigations of Lubricant Rheology as Applied to Elastohydrodynamic Lubrication", NASA CR-121169, NASA Lewis Research Center, June 1972.
7. Sanborn, D. M., Jakobsen, J., Carlson, S., and Winer, W. O., "Investigations of Lubricant Rheology as Applied to Elastohydrodynamic Lubrication", NASA CR-134539, NASA Lewis Research Center, December 1973.
8. Jones, W. R., Johnson, R. L., and Sanborn, D. M., and Winer, W. O.,⁸ "Viscosity-Pressure Measurements for Several Lubricants to 5.5×10^8 N/m² (8×10^4 psi) and 149 C (300F)", NASA TND-7736, August 1974.
9. Jakobsen, J., and Winer, W. O., "Traction of Elastohydrodynamic Contacts with Thermal Shearing Flow", Trans. ASME, Journal of Lubrication Technology, Vol. 97, No. 3, 424-429, 1975.
10. Jakobsen, J., and Winer, W. O., "Dissipative Heating Effects and EHD Corrections for Viscous Newtonian Flow in High Shear Stress Capillary Viscometry", Trans. ASME, Journal of Lubrication Technology, Vol. 97, No. 3, 472-478, 1975.
11. Jakobsen, J., and Winer, W. O., "High Shear Stress Behavior of Some Representative Lubricants", Trans. ASME, Journal of Lubrication Technology, Vol. 97, No. 3, 479-485, 1975.

12. Jones, W. R., Johnson, R. L., Sanborn, D. M., and Winer, W. O., "Viscosity-Pressure Measurements for Several Lubricants to 5.5×10^8 N/m² (8×10^4 psi) and 149 C (300F) (to be published ASLE, Transactions and presented at ASME/ASLE Joint Lubrication Conference, Montreal Canada, October 1974, ASLE Preprint 74LC-4C-1).
13. Carlson, S. F., and Winer, W. O., "The Viscous Lubrication of Rolling and Sliding Rigid Cylinders", ASME Trans., Journal of Lubrication Technology, Vol. 97F, No. 2, 180-186, April 1975.
14. Walker, D., Sanborn, D. M., and Winer, W. O. "Polymer Degradation in Elastohydrodynamic Lubrication", Proceedings of International Colloque on Polymers and Lubrication, C.N.R.S., Brest, France, 1974.
15. Molina-Combita, M. A., Sanborn, D. M., and Winer, W. O., "Dynamics of Roller Bearings Considering Elastohydrodynamic Forces", Proceedings of Japanese Society of Lubrication Engineers/American Society of Lubrication Engineers Joint International Meeting, Tokyo, Japan, June 1975.
16. Winer, W. O., "The Mechanical Properties of Fluids in High Pressure Hydraulic Systems", Proceedings of National Fluid Power Conference, Vol. XXVIII, 412-421, 1974.
17. Walker, D. L., Sanborn, D. M., and Winer, W. O., "Molecular Degradation of Lubricants in Sliding Elastohydrodynamic Contacts", Trans. ASME, Journal of Lubrication Technology, Vol. 97, No. 3, 390-397, 1975.
18. Kunz, R. K., and Winer, W. O., "Prediction of Traction in Sliding EHD Contacts", Trans. ASME, Journal of Lubrication Technology, Vol. 98, Series F, No. 3, 362-365, 1976.
19. Ausherman, V. K., Nagaraj, H. S., Sanborn, D. M., and Winer, W. O., "Infrared Temperature Mapping in Elastohydrodynamic Lubrication", Trans. ASME, Journal of Lubrication Technology, Vol. 98, Series F, No. 2, 236-242, 1976.
20. Sanborn, D. M., and Winer, W. O., "Lubricant Properties in Thin Lubricating Films", presented at ACS Meeting, New York City, 1976.
21. Nagaraj, H. S., Sanborn, D. M., and Winer, W. O., "Effects of Load, Speed and Surface Roughness on Sliding EHD Contact Temperatures", Presented at the Joint ASME-ASLE Lubrication Conference, Boston, Massachusetts, October 1976.